Dissertation

submitted to the

Combined Faculties of the Natural Sciences and Mathematics

of the

Ruperto-Carola-University of Heidelberg, Germany

for the degree of

Doctor of Natural Sciences

Put forward by

Diplom-Physiker *Martin Jürgen Höcker*

born in Clausthal-Zellerfeld

Oral examination: July 26th, 2016

Precision Mass Measurements at THe-Trap and the FSU trap

Referees:

Prof. Dr. Klaus Blaum
Prof. Dr. Markus Oberthaler

Zusammenfassung

Präzisions-Massenmessungen an THe-Trap und der FSU Trap

THe-Trap ist ein Penningfallen-Massenspetrometer am Max-Planck-Institut für Kernphysik in Heidelberg, welches für die Messung des T/^{3}He-Massenverhältnisses mit einer relativen Unsicherheit von 10^{-11} ausgelegt ist. Durch Verbesserungen der Messmethoden, insbesondere in Bezug auf systematische Frequenzverschiebungen, wurden Massenmessungen mit einer relativen Unsicherheit von $7 \cdot 10^{-11}$ erreicht. Dies wurde anhand von Messungen des Zyklotronfrequenzverhältnisses von $^{12}C^{4+}/^{16}O^{5+}$ demonstriert. Die Unsicherheit war durch das Verständnis der Linienform limitiert. Ein verbessertes theoretisches Modell, welches auf einer *rotating wave approximation* basiert, erlaubt es, dynamische Effekte in der Interaktion zwischen Frequenzverschiebungen und Detektionssystem zu beschreiben. Dies kann benutzt werden, um die Linienform zu untersuchen und den damit verbunden systematischen Fehler zu reduzieren.

Die Florida State University Trap ist ein Penningfallen-Massenspektrometer in Tallahassee, Florida (USA). Im Rahmen dieser Arbeit wurden drei neue Massenverhältnisse bestimmt, sowie Daten von 20 weiteren, vorher durchgeführten Messungen ausgewertet. Dadurch konnten die Massen von ^{82,83}Kr, ^{131,134}Xe, $^{86-88}$Sr, and $^{170-174,176}$Yb mit relativen Unsicherheiten von $(0.9 - 1.3) \cdot 10^{-10}$ bestimmt und publiziert werden. Diese Massen dienen als Referenzwerte für weitere Experimente und können in der Messung der Feinstrukturkonstante α mittels der Photon-Rückstoßmethode angewendet werden.

Abstract

Precision Mass Measurements at THe-Trap and the FSU trap

THe-Trap is a Penning-trap mass spectrometer at the Max-Planck-Institute for Nuclear Physics in Heidelberg, Germany, that aims to measure the T/^{3}He mass ratio with a relative uncertainty of 10^{-11}. Improvements of the measurement technique, in particular the measurement of systematic shifts, enabled measurements of mass ratios with relative uncertainties of $7 \cdot 10^{-11}$, as demonstrated by a cyclotron frequency ratio determination on $^{12}C^{4+}/^{16}O^{5+}$. This uncertainty was limited by the lineshape. An improved theoretical model based on a rotating wave approximation can be used to describe dynamical interactions between the detection system and the ion, in order to better understand the lineshape and to further reduce the uncertainty.

The Florida State University trap is a Penning-trap mass spectrometer located in Tallahassee, Florida (USA). In the context of this thesis, three mass ratios were measured, and further 20 mass ratio measurements analyzed, which resulted in the publication of the masses of ^{82,83}Kr, ^{131,134}Xe, $^{86-88}$Sr, and $^{170-174,176}$Yb with relative uncertainties between $(0.9 - 1.3) \cdot 10^{-10}$. These masses serve as reference masses for other experiments and have applications in the determination of the fine-structure constant α via the photon-recoil method.

Contents

List of Figures

List of Tables

1. Introduction

1.1. Mass spectrometry

Mass spectrometry is the art of measuring molecular, atomic, and sub-atomic masses in *unified atomic mass units*, or "u", where 1 u is defined as 1/12 of the mass of a single ^{12}C atom. The origin of mass spectrometry dates back more than 100 years [1, 2] to experiments performed by J.J. Thomson on cathode rays. These first experiments used photographic plates to study the deflection of positive ions ("cathode rays") under different electric and magnetic field configurations. The measured deflection angles were used to compare the relative mass values of the cathode rays' constituents, with approximately 1% uncertainty.

Over the next 100 years, mass spectrometry techniques improved steadily (Table 1.1). Today, the mass measurements with the lowest uncertainty (*high-precision* mass spectrometry) are performed with Penning traps [3]. The detailed measurement principle will be explained in the next chapter, but at its heart a Penning trap uses a strong, homogeneous magnetic field to bend the path of a charged particle into a circle. The period of this circular motion is directly proportional to the mass of the particle, so by measuring the revolution periods of different charged particles in the same magnetic field, the ratio of the particles' masses can be calculated.

Most Penning-trap mass spectrometers are designed to measure the masses of short-lived radioactive nuclei that are produced with nearby particle accelerators or nuclear reactors [4]. These experiments are typically able to obtain relative mass uncertainties in the order of 10^{-8} to 10^{-9}. However, experiments that specialize on stable nuclides[1] are able to reach relative mass uncertainties of 10^{-10} to 10^{-11}. Apart from experiments to determine the mass of the antiproton [5, 6], there are currently two experiments capable of such low uncertainties: The Tritium/Helium-3 Trap (THe-Trap) in Heidelberg, and the Florida State University Penning trap (FSU trap) in Tallahassee. A large portion of this thesis focuses on measurements of the systematic and statistical limitations of both experiments.

Not all nuclear masses need to be known with these low uncertainties, but there are notable exceptions. Relevant in the context of this thesis are the mass values that are used in neutrino-mass determinations, mass values that serve as references for other experiments, and mass values that are needed for measurements of the fine-structure constant α.

1.2. Neutrino mass

Neutrinos are the electrically neutral cousins of the electron, the muon, and the tauon. Their masses are at least five orders of magnitude smaller than the electron mass [19, 20], and they

[1] Or at least *reasonably* stable nuclides. For example, as pointed out by my colleague Jochen Ketter, the 12-year half life of tritium makes it sufficiently stable over the course of a typical PhD thesis.

Table 1.1.: List of mass spectrographs and mass spectrometers that brought significant improvements to the field of high-precision mass measurements.

Year	Method	Uncertainty
1913	Parallel $\vec{E}$- and $\vec{B}$-field [7]	$\sim 10^{-2}$
1919	Crossed $\vec{E}$- and $\vec{B}$-field for energy focusing [8]	$\sim 10^{-3}$
1927	Based on [8], but stronger fields [9]	$\sim 10^{-4}$
1936	New field geometry for simultaneous energy and angle focusing [10]	$\sim 10^{-5}$
1951	Secondary spectrometer to stabilize $\vec{E}$- and $\vec{B}$-field [11]	$5 \cdot 10^{-7}$
1971	Cyclotron-like mass spectrometer [12]	$2 \cdot 10^{-9}$
1978	Ion cloud in Penning trap, axial detection [13]	$2 \cdot 10^{-7}$
1980	Ion cloud in Penning trap, TOF method [14]	$5 \cdot 10^{-8}$
1989	Single ion in Penning trap, continuous axial detection [15]	$3 \cdot 10^{-9}$
1989	Single ion in Penning trap, PnP-method [16]	$4 \cdot 10^{-10}$
2004	Based on [16], with two ions measured simultaneously [17]	$7 \cdot 10^{-12}$
2006	Based on [15], with improved magnet [18]	$1 \cdot 10^{-11}$

only interact with other particles through the *weak nuclear force*, an interaction that is so weak that a lead shield to catch half the neutrinos from a nuclear reactor would have to be light-years thick.

The *standard model* of particle physics includes three types of neutrinos: The electron neutrino, the muon neutrino, and the tau neutrino. In its original form, the standard model assumes the neutrinos to be massless. However, observations have shown that neutrinos of one type (flavor) can turn into neutrinos of another type ("neutrino oscillations") [21, 22]. This can be explained by assuming that the mass eigenstates of neutrinos are different from their flavor eigenstates. Measurements of the neutrino oscillations can be used to infer the squared mass differences of the neutrino types [20], but not the absolute values of the individual masses. However, an upper limit for the neutrino masses can be derived from observations of the cosmic microwave background, combined with galaxy cluster data and cosmological models. This constrains the sum of all neutrino masses to a maximum of $0.39\,\mathrm{eV}/c^2$ (95% confidence interval). Unfortunately, this value is strongly model-dependent [23]. Due to the prohibitively unlikely interaction of neutrinos with matter (and therefore, detectors), a direct measurement of the neutrino masses has so far been impossible and seems highly unlikely in the future.

However, a third, less indirect neutrino-mass measurement method is possible via the study of β-decays. In a β^--decay, a neutron decays into a proton by emitting an electron and an electron antineutrino. One example for such a decay is the β-decay of tritium to helium-3:

$$^3\mathrm{H} \quad \longrightarrow \quad ^3\mathrm{He}^+ + e^- + \bar{\nu}_e + Q \quad . \tag{1.1}$$

The Q-value signifies the decay energy. Unfortunately, the definition of the Q-value subtly differs between the mass spectrometry community and the β-spectrometry community.

In the mass spectrometry community, the Q-value is defined as the difference of the mass energy of mother and daughter *atom* [24]:

$$Q_{\mathrm{ms}} = m(^3\mathrm{H})c^2 - m(^3\mathrm{He})c^2 \quad . \tag{1.2}$$

But in a typical β-decay, the β-electron escapes from the daughter atom, which leaves the daughter atom in an ionized state. Therefore, the β-spectrometry community defines the Q-value as the atomic mass of the mother nucleus minus the masses of the daughter *ion* and the β-electron. Using E_i as the (positive-valued) ionization energy of the ion, we can state the β-spectrometry definition of the Q-value as [25]

$$\begin{aligned} Q_{\beta\mathrm{s}} &= m(^3\mathrm{H})c^2 - \left[m(^3\mathrm{He}^+)c^2 + m(e^-)c^2\right] && (1.3)\\ &= m(^3\mathrm{H})c^2 - \left[m(^3\mathrm{He})c^2 + E_\mathrm{i}\right] \quad . && (1.4) \end{aligned}$$

This definition of the Q-value approximately describes the maximum kinetic energy that the β-electron can have and is accurate to approximately 10 eV. For a better approximation, we have to take into account that the daughter atom is not only left in an ionized state, but generally with an excited electron shell that might even be shared with a molecule. We therefore replace E_i with the slightly more general *binding energy* E_b. Further, the daughter nucleus experiences a recoil force, which leads to the small (a few eV) kinetic energy E_recoil of the nucleus. Finally, and most importantly, we have to consider the rest mass of the electron antineutrino $\bar{\nu}_e$. This lets us state the maximum kinetic energy that the β-electron can have, the *endpoint energy*, as

$$E_\mathrm{endpoint} = m(^3\mathrm{H})c^2 - m(^3\mathrm{He})c^2 - E_\mathrm{b} - m(\bar{\nu}_e)c^2 - E_\mathrm{recoil} \quad . \tag{1.5}$$

In principle, the neutrino mass could be determined with this equation: The first two terms are equal to the Q_ms-value of the β-decay, which is accessible via mass spectrometry. The binding energy E_b can be calculated using input from atomic physics. The average recoil energy E_recoil is known from kinematics [26], and the endpoint energy E_endpoint can be measured with a β-electron spectrometer. This leaves the mass of the electron antineutrino as the only free parameter.

However, the count-rate near the endpoint of the spectrum is so low that the exact determination of the endpoint is confounded by noise. Further, the absolute energy calibration is technically challenging [27]. This makes the determination of E_endpoint a suboptimal method for obtaining the electron antineutrino mass. Instead, the most sensitive method takes advantage of the fact that a finite electron antineutrino mass not only shifts the endpoint of the spectrum, but also distorts the spectrum in a characteristic way, proportional to the square of the neutrino mass (Figure 1.1). The electron antineutrino mass and E_endpoint are then independent fit parameters. But Equation (1.5) still applies. It can be used to test if the fit results are consistent with the mass-spectrometry value of Q_ms, which is an important check for hidden systematic effects.

The most precise measurements of the tritium β-spectrum have been performed in Mainz and Troitsk. These measurements did not reveal the electron antineutrino mass, but yielded (95% confidence interval) upper limits of $2.3\,\mathrm{eV}/c^2$ and $2.05\,\mathrm{eV}/c^2$, respectively [19, 28]. A new experiment, KATRIN, is currently being constructed [29]. It aims to reduce the upper limit to $0.2\,\mathrm{eV}/c^2$ with an absolute energy calibration in the order of 40 meV [30]. In order to examine possible systematical effects, the mass-difference between tritium and helium-3 should be known with a similar uncertainty of $50\,\mathrm{meV}/c^2$. For 9 years, this mass difference was

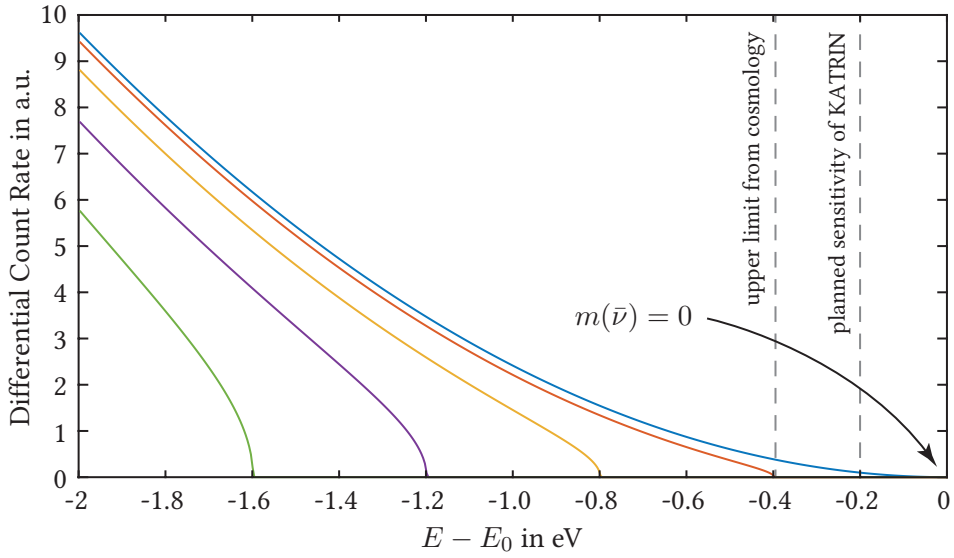

Figure 1.1.: Hypothetical β-electron spectra for different electron antineutrino masses. The electron antineutrino mass shifts the endpoint energy E_{endpoint} away from the hypothetical point of zero mass, E_0, and also bends the spectrum in a characteristic way. The shown spectra are simplified. They do not include background effects, possible inelastic scattering events, different final states of the daughter ion, or effects caused by neutrino oscillations [27].

known with an uncertainty of $1.2\,\text{eV}/c^2$ (measured at SMILETRAP [31]), but it was recently remeasured by the FSU group with an uncertainty of only $70\,\text{meV}/c^2$ [32]. This measurement, which had been planned since the conception of the experiment in the 1980's and is also the main purpose of THe-Trap, showed a 2σ deviation to the previous best measurement, eliciting calls for an independent confirmation.

1.3. Backbone of the AME

The atomic mass evaluation (AME) is a monumental effort to consolidate all mass measurements on the approximately 3000 known nuclei into a table of mean mass values [2]. The most recent mass evaluation is the AME2012 [24, 33]. A typical mass measurement compares the mass of an ion-of-interest with the mass of a reference ion. Ideally, a carbon-12 ion or carbon-12-cluster ion can be used as a reference, in order to relate the measurement directly to the unified atomic mass unit. In other cases, non-carbon ions with accurately known masses are used as secondary standards. The set of high-precision mass values that can serve as secondary standards is known as the "backbone" of the AME. A strong backbone is important to study inconsistencies in the AME itself, and for giving other experiments a wider range of isotopes that can be used as reference masses or for testing new techniques with higher accuracy.

Consolidating all atomic mass measurements into a self-consistent data set is, to say the

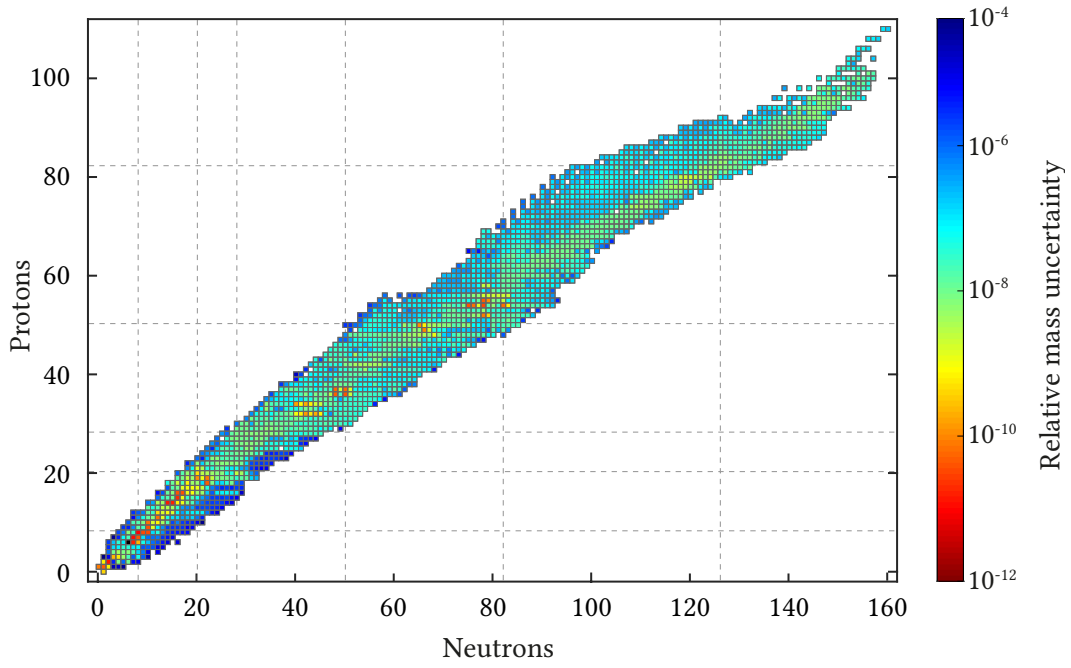

Figure 1.2.: Relative uncertainties of the mass values given in the AME2012 [24]. The relative uncertainty of the ^{12}C mass is 0 and indicated by a black square.

least, a challenge. For example, some measurement methods have historically been shown to yield uncertainties that are bigger than claimed. In the AME, an adjustment factor is assigned to each laboratory that contributed data. This adjustment factor is used to scale the claimed uncertainties of each laboratory, in order to make them consistent with the mean deviations from the final (global) fit values. The scaling factors range between 1 and 4.

But comparing newer AME's to older AME's shows that whenever measurements with a significantly lower uncertainty are available, they typically shift the AME-value by twice the uncertainty computed in the previous AME (Figure 1.3). So even after scaling the individual uncertainties to make the data set self-consistent, with scaling factors that are all larger than 1, the final uncertainty appears to be underestimated by 50%. This is neither meant as a criticism of the AME nor as a criticism of individual experiments, only as an observation that should warrant caution. By and large, we experimenters appear to underestimate our uncertainties. A strong backbone is important for the AME to uncover inconsistencies between different data sets, and low uncertainties help to make errors inconsequential, even when they are underestimated.

1.4. Measurement of fundamental constants

Fundamental constants, such as the fine structure constant and masses of elementary particles, are "important links in the chain of physical theory which binds all of the diverse branches of physics together" [34]. This property — linking different branches — often allows a fundamental

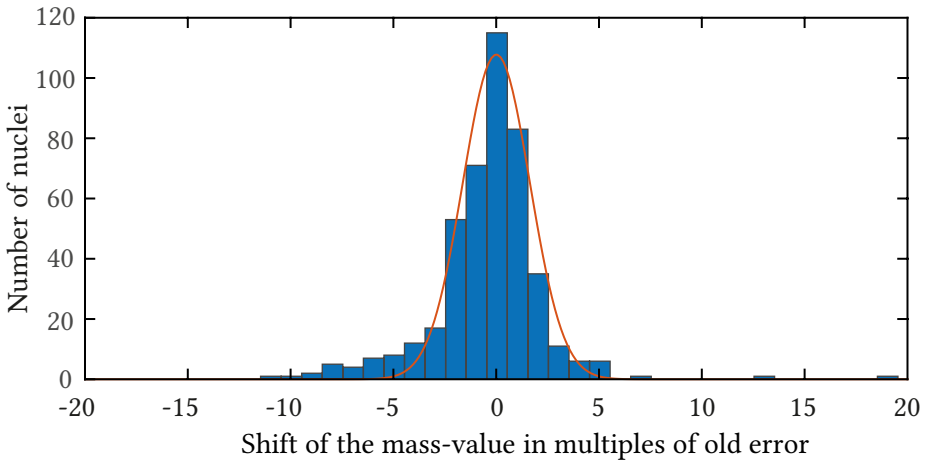

Figure 1.3.: Normalized shifts between AME2012 and AME2003. The data set was limited to the 440 nuclei where new mass measurements reduced the uncertainty by a factor of 3 or more. Masses not based on actual measurements, so-called *inferred values*, were excluded. The root-mean-square of the normalized shifts is 6.9. Fitting the width of a normalized Gaussian distribution yields $\sigma = 1.63(10)$ (red line, shown for comparison), but the thick tails of the histogram make the Gaussian distribution a poor choice. Instead, Student's t-distribution might be more appropriate.

constant to be measured using a wide array of techniques. It also makes independent, high-accuracy measurements so intriguing: If the measured values differ, one of the experiments, or (more interestingly) the underlying theory must be in error.

The fine structure constant α describes the coupling strength between electrons and photons. Currently, the most precise measurement method of determining α is an indirect method: The anomalous magnetic moment of the electron is measured and compared to the value predicted by quantum electrodynamics (QED). The predicted value strongly depends on α. Assuming quantum electrodynamics accurately describes nature, one can adjust the value of α until the prediction of the magnetic moment matches the experiment, with a relative uncertainty of $3.7 \cdot 10^{-10}$ [35].

A different approach, which does not strongly depend on the correctness of quantum electrodynamics, is to measure an atom's recoil velocity v_{recoil} after it absorbs a photon. A photon with wavelength λ carries the momentum $p = h/\lambda$, with h denoting the Planck constant. When the photon is absorbed, its momentum is transferred to the atom. With m_{a} as the atom's mass, the conservation of momentum leads to the recoil velocity

$$v_{\text{recoil}} = \frac{h}{m_{\text{a}}\lambda} \quad . \tag{1.6}$$

This velocity can be measured with a relative uncertainty of 10^{-9} [36] using atom-interferometry techniques, in which the change in Doppler-shift between absorption and (stimulated) emission is determined [37]. Since λ is typically known with even lower uncertainty, the

equation can be rearranged to yield a measurement of h/m_a with a relative uncertainty of 10^{-9}. This quantity can be used to determine α by noting the identity

$$\alpha^2 = 2\frac{R_\infty}{c}\frac{m_\mathrm{a}}{m_e}\frac{h}{m_\mathrm{a}} \quad . \tag{1.7}$$

The Rydberg constant R_∞ can be measured with $5 \cdot 10^{-12}$ uncertainty using hydrogen spectroscopy [38]. The speed of light c is a defined constant, and m_a/m_e can be provided by mass spectrometry. The ratio m_a/m_e is usually not measured directly, but instead calculated from the electron mass measured in atomic units, and m_a in atomic units. The electron's mass was recently determined with $3 \cdot 10^{-11}$ uncertainty[2] [40]. This makes the uncertainty of m_a the limiting factor in the photon-recoil determination of α. The masses of suitable atoms for the recoil method were measured at the FSU trap [43, 44].

1.5. Shifts, errors, and uncertainties

The main goal of precision mass spectrometry is to decrease the uncertainties, shifts, statistical errors, and systematic errors of nuclear masses. However, the definitions of these terms is by no means universal [45]. In this thesis, I use the following definitions:

Statistical error Random errors, for example caused by random $\vec{B}$-field fluctuations during a measurement, give rise to the *statistical error* (sometimes called *precision*). This error can be reduced by taking N measurements under identical conditions, and averaging the results. In this case, the final statistical error is given as the *standard deviation of the mean*. However, in some cases each of the N measurements has its own statistical error, for example, when each measurement is the result of M sub-measurements. In this case, the overall statistical error can alternatively be defined as the combined (propagated) N statistical errors. Ideally, both error-measures agree. To be conservative, the larger of these two errors is taken as the statistical error.

Systematic shift Effects which reproducibly shift the measurement result are called *systematic shifts*. In Penning-trap mass spectrometry, one example is the relativistic shift of the reduced cyclotron frequency at large cyclotron radii. Systematic shifts must be measured or theoretically modeled, so that the end-result can be corrected for them.

Systematic error The correction of systematic shifts often depends on parameters (ion radii, anharmonicity), which are not known exactly. Therefore, the estimate of the systematic shift has some uncertainty. This uncertainty in the systematic shift is the *systematic error*. It is sometimes called *accuracy*.

Unknown systematic shift Although extreme care is taken to find relevant systematic shifts before publication, sometimes they evade discovery until a discrepancy with another

[2] The most precise m_e measurements use indirect techniques that rely on the correctness of QED [39–41]. (The best direct measurement has an uncertainty of $2 \cdot 10^{-9}$ [42].) Therefore, the atomic-recoil method to determine α also relies on QED, but in a different way than the determination via the electron's anomalous magnetic moment.

experiment arises. Such *unknown systematic shifts* could also be called *mistakes*, but the latter word is best reserved for more severe blunders. Examples of later discovered systematic shifts include: day-night fluctuations influencing early results of the UW-PTMS [46, 47], differential filter-heating perturbing early FSU measurements [48], and a polarizability shift of trapped molecules affecting the antiproton/proton mass ratio [49].

Total uncertainty The final measurement uncertainty is calculated by adding the statistical error and the systematic error in quadrature. It is not uncommon to gratuitously round up during every step of the calculation, to account for unknown systematic shifts.

1.6. Overview of my work

I started working at THe-Trap as a diploma student, at a time when the experiment had just been moved to Heidelberg and still carried its temporary name, UW/MPIK-PTMS (University of Washington / Max-Planck-Institut für Kernphysik Penning-Trap Mass Spectrometer). One of the first projects I was involved in was to help cool down the magnet for the first energization attempt, and I later focused on ion-transport-related issues. I enjoyed the work so much that, after graduating in 2010 [50], I gladly accepted Klaus Blaum's offer to continue my work as a PhD student. During my PhD, my role at THe-Trap shifted from ion transport studies to writing the analysis software for the data we took, and to ion work, with the goal of understanding the systematic shifts of our measurements.

In 2011, Edmund Myers from the Florida State University (FSU) was so nice to offer me to conduct parts of my PhD research at the FSU trap — at the time the only operating mass spectrometry experiment that routinely measured masses at relative uncertainties of 10^{-10} or below. During my first four-week visit, he patiently explained the FSU techniques of measuring systematic shifts to me, as we took data on the masses of krypton-82 and krypton-83. During a second, three-month visit in 2012, I performed the data analysis on the krypton data, and on xenon, strontium, and ytterbium data, which had been taken by another student, Raman Rana. This resulted in two papers [44, 51], which are summarized (and partly expanded upon) in this thesis.

In Heidelberg, after we learned how to routinely work with single ions, we realized that many of the FSU calibration techniques were also applicable to THe-Trap. Implementing them allowed us to better understand the frequency shifts that we had observed in our earlier measurements [52, 53], and helped us to reduce all but one systematic errors to a $2 \cdot 10^{-11}$ level or below.

The remaining systematic error at THe-Trap is connected to the complicated lineshape of the resonances. The lineshape is given by an intricate interaction between various frequency shifts, the feedback-based detection system, and different noise sources. The lineshape cannot be described with an analytical function, but instead has to be simulated numerically. This simulation is challenging, since the ion motion (with frequencies of up to 80 MHz) has to be simulated over hundreds of seconds. To find the center frequency of the lineshape, we use a semi-automatic fit procedure that is based on a simplified, linear model [54]. This model has been studied experimentally to rule out a large class of possible systematic shifts. However, to rule out further systematic shifts, a theoretical investigation of the lineshape is necessary.

Discussions with Edmund Myers and with Jochen Ketter helped me to understand the MIT picture of the ion motion, which is based on a Green's function approach to the equations of motion. The Green's function solution is hinted at in MIT papers [55] and theses [56], but to my knowledge was – until now – never written down explicitly. Combined with a treatment of trap imperfections and excitation fields in *Cartesian* coordinates (in contrast to the usually employed cylindrical coordinates), and with a rotating wave approximation, this picture enables efficient numerical simulations of the ion dynamics in an imperfect trap, even over hundreds of seconds. This is the main theoretical contribution of my thesis. It constitutes an important step towards fully understanding the lineshape. Work is continuing to characterize the frequency-spectra of the relevant noise sources and the behavior of the feedback system.

1.7. Layout of this thesis

This thesis was written with the next generation of students in mind, who have taken over the experiment and are already doing an outstanding job. My goal was to document our successes and failures so that they can speed through the inevitable phase of rediscovering old knowledge faster than we did, and move on to new and exciting physics.

Chapter 2 describes the physics of a Penning trap in detail. The novel part of this chapter lies in using Cartesian coordinates for the multipole expansion of the electric (and magnetic) fields, and in using a rotating wave approximation for some of the frequency shifts. To keep the chapter short and relevant to the experiment, some of the mathematical derivations were moved to Appendix A. The interaction between ion and detection circuit is also given in detail, in order to remind the reader that the usually employed model uses simplifications that are not always true.

Chapter 3 and Chapter 4 give a short summary of the experimental setup of THe-Trap and the FSU trap, respectively. Both experiments have been described before and are similar in a lot of ways. My goal was to highlight their differences, and to document recent changes. Chapter 3 also contains notes on preparing a feedthrough-flange, and on servicing our superconducting magnet.

Chapter 5 describes the results obtained at THe-Trap, which include a greatly improved understanding of the systematic frequency shifts, demonstrated on an oxygen-16 to carbon-12 mass ratio measurement.

Chapter 6 summarizes the results of the work at the FSU trap, which include mass measurements of krypton, xenon, strontium, and ytterbium isotopes.

Chapter 7 concludes this thesis with an outlook on the future development at THe-Trap, and how possible lineshape-related systematic errors might be avoided in the future by adopting phase-sensitive techniques as used at the FSU trap.

Appendix A contains some of the math that is needed in the theory chapter, namely the Green's function solution of the ion's equations-of-motion, and the rotating wave approximation.

Appendix B contains a short (1 page), self-contained example of an efficient simulation of Penning-trap ion-dynamics, written in MATLAB. It builds upon the approximations developed in Appendix A and is useful to understand the interaction between frequency shifts and various excitation schemes.

2. Theory

The theory of a Penning trap can be described using a quantum-mechanics-framework [57], but since the quantum numbers of the ion motion in a typical trap can be shown to be large (greater than 1000), a classical treatment is entirely sufficient [55, 56]. The advantage of the classical treatment, which this chapter follows, is that it allows to build an intuitive picture of the ion motion, mode-coupling and frequency shifts. Furthermore, it enables efficient numerical simulation of the ion dynamics in an imperfect trap.

We will begin by reviewing the basic behavior of charged particles in magnetic and electric fields, which allows us to give a qualitative description of the ion motion inside a Penning trap. Subsequently, the equations of motion are solved to give a quantitative description of the ion motion. The ion detection is treated with a particular emphasis on ion-detector interaction, which still holds unsolved mysteries. In the second half of this chapter, the electric potential of the trap is investigated in more detail, and an expansion in harmonic polynomials is given. The expansion in harmonic polynomials, which is more general than the usual expansion in Legendre polynomials, allows a better classification of the electric fields that perturb or drive the ion. The effects of trap imperfections are modeled in a rotating wave approximation, which is derived using a Green's function treatment (Appendix A). A review of relevant frequency shifts concludes the chapter.

2.1. Cyclotron motion

Precision mass spectrometry is based on the motion of charged particles in strong magnetic fields. When an ion with mass m and charge q is moving through a magnetic field $\vec{B}$, it is subject to the Lorentz force

$$\vec{F}_\mathrm{L} = q\,\vec{v} \times \vec{B} \quad . \tag{2.1}$$

In the special case $\vec{v} \perp \vec{B}$, the ion's trajectory is bent into a circle (Figure 2.1, left). In the more general case, $\vec{v}$ has a component parallel to the magnetic field, and the trajectory has the form of a spiral.

By setting $\vec{F}_\mathrm{L}$ equal to the centripetal force, it can quickly be shown that the frequency[1] of the circular motion is independent of the velocity:

$$\omega_\mathrm{c} = \left| \frac{q}{m} \vec{B} \right| \quad . \tag{2.2}$$

This frequency is called the *free-space cyclotron frequency*. At its heart, Penning-trap mass spectrometry measures the free-space cyclotron frequencies of two different ions in the same

[1] I am slightly sloppy in my usage of the term *frequency*. I use it both for "true" frequencies (denoted by f; unit Hz) and for angular frequencies (denoted by ω; unit rad/s). They are related via $\omega = 2\pi f$. Angular frequencies ω are mainly used in discussions of Penning-trap theory, to reduce the number of 2π's in formulas.

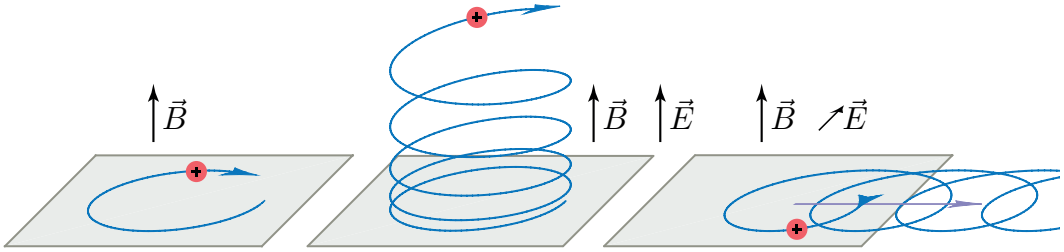

Figure 2.1.: Motion of a charged particle in a magnetic field $\vec{B}$ (left), with an electric field $\vec{E} \parallel \vec{B}$ (center), and with $\vec{E} \perp \vec{B}$ (right).

magnetic field. When the ratio of these frequencies is calculated, the magnetic field (ideally) cancels out and the charge ratio reduces to an integer fraction. The mass ratio can therefore be measured as a frequency ratio:

$$\frac{m_1}{m_2} = \frac{\omega_{c_2}}{\omega_{c_1}} \frac{q_1}{q_2} \quad . \tag{2.3}$$

By using one ion with a well-known or defined mass, such as a $^{12}C^{+}$, the mass of the other ion can be determined.

State-of-the-art superconducting magnets can be carefully tuned to have a magnetic field that changes by only a few parts in 10^8 over a 1 cm^3 region in the center [58]. When a charged particle is inserted into such a field, it orbits around the field lines (in other words, it is trapped radially), but it may drift axially, along the field lines, out of the homogeneous part of the magnetic field. This limits the useful time in which the particle's cyclotron frequency can be determined.

In a Penning trap, this problem is solved by introducing an additional, weak electric field that axially pushes the particles towards the center of the trap.

2.2. *E*-cross-*B* drift

For a qualitative understanding of the Penning trap, it is helpful to review the motion of a charged particle in combined $\vec{E}$- and $\vec{B}$-fields. If the electric field $\vec{E}$ is weak[2] compared to the magnetic field $\vec{B}$, the motion can be separated [59] into a fast cyclotron motion, caused by $\vec{B}$, and a slow drift of the center of the cyclotron motion, caused by $\vec{E}$.

For example: If $\vec{E} \parallel \vec{B}$, the radial motion is unperturbed and the particle is accelerated axially, along the field lines. The trajectory is a spiral that has more and more space between its loops (Figure 2.1, center).

If $\vec{E} \perp \vec{B}$, the particle accelerates and decelerates as it moves on its cyclotron orbit. The radius of the orbit grows as the particle moves in the direction of $\vec{E}$ and shrinks again during the other half of the orbit. This causes the center of the cyclotron motion to drift sideways, orthogonal to both the electric and the magnetic field (Figure 2.1, right). This drift is called the

[2] Weak meaning that the electric forces are much smaller than the magnetic forces.

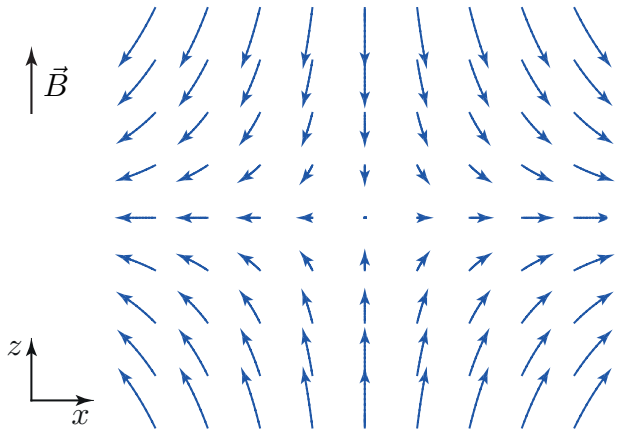

Figure 2.2.: Cut-view of the electric field inside a Penning trap.

E-cross-B drift, and the drift velocity is given by the formula

$$\vec{v} = \frac{\vec{E} \times \vec{B}}{B^2} \quad .$$

The general case can be described by a superposition of $\vec{E}_{\parallel}$ and $\vec{E}_{\perp}$.

2.3. Penning-trap motion

By convention, the magnetic field of the Penning trap defines the z-direction, so that $\vec{B} = B\vec{e}_z$. For a qualitative description of the Penning-trap principle (a quantitative treatment is given in section 2.5), consider an electric field of the form

$$\vec{E} = k \begin{pmatrix} x/2 \\ y/2 \\ -z \end{pmatrix} \quad , \tag{2.4}$$

with some arbitrary constant k. A plot of this field is shown in Figure 2.2. If k is positive, the E_z-component of the electric field pushes positively charged particles[3] towards $z = 0$. This restoring force is proportional to the z-displacement, which makes the z-motion a harmonic oscillation (Figure 2.3).

The radial field is a necessary trade-off, as dictated by Gauss's law: The field lines that come in towards the trap center in the z-direction need to come out somehow. In an ideal Penning trap, the radial components of $\vec{E}$ are chosen such that they point away evenly from the trap center. This electric field pulls the stored particle radially outwards, which leads to a circular E-cross-B drift of the cyclotron motion around the trap center. The frequency of this slow drift is called the *magnetron frequency*.

[3] For this choice of k, negatively charged particles are expelled from the trap. Unlike a Paul trap, a Penning trap cannot store particles of opposite charge simultaneously.

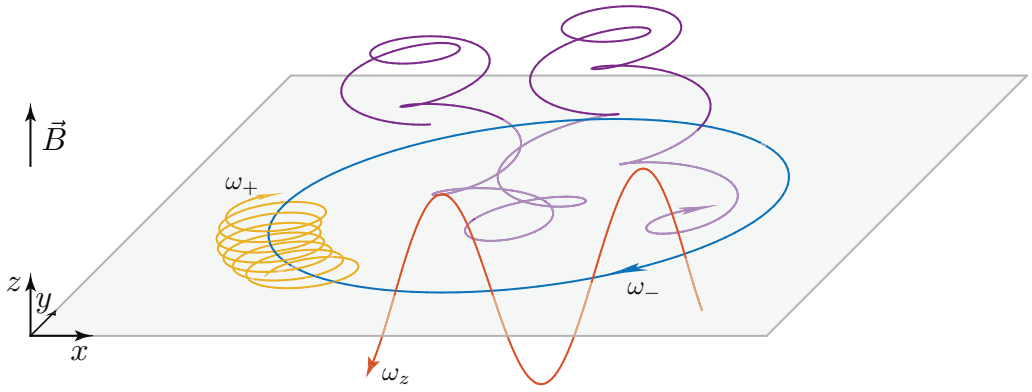

Figure 2.3.: Motion of a positively charged particle in a Penning trap. The motion consists of the slow magnetron drift around the trap center with frequency ω_- (blue), the axial motion with ω_z (red), and the modified cyclotron motion with ω_+ (yellow). The superposition of all three motions is shown in purple.

The E-cross-B drift slightly modifies the frequency of the cyclotron motion, which will be shown in section 2.5.

It is important to point out that the magnetron motion is unstable. The particle sits on a potential hill in the radial plane. If there are any damping processes, such as collisions with background gas, the particle rolls down the potential hill and is lost. In traps that are cooled to 4 K, the vacuum conditions can be so good that particles can be stored for months and longer [57].

2.4. Penning-trap electrodes

The Penning trap's electric field $\vec{E}$ (Equation 2.4) corresponds to the potential

$$\Phi = \frac{c}{2}\left(\frac{-\rho^2}{2} + z^2\right) \quad , \tag{2.5}$$

where $\rho^2 = x^2 + y^2$. This potential can be generated with cylindrically symmetric electrodes that follow the equipotential surfaces of Φ: Two electrodes, the endcaps (Figure 2.4), are implicitly defined via

$$z(\rho) = \pm\sqrt{z_0^2 + \frac{\rho^2}{2}} \quad , \tag{2.6}$$

with z_0 as the closest point to the trap center. Both endcaps are held at the same potential. A third electrode, the ring electrode, follows the contour

$$\rho(z) = \sqrt{\rho_0^2 + 2z^2} \quad , \tag{2.7}$$

with ρ_0 being the distance between trap center and ring electrode.

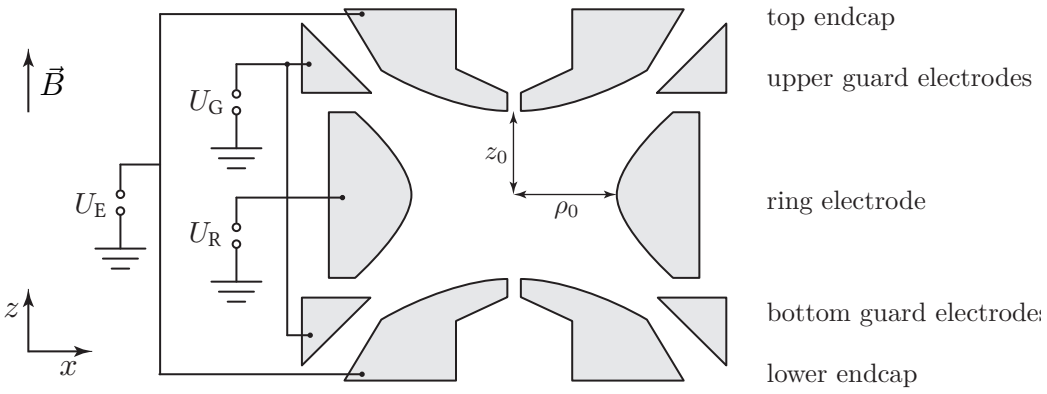

Figure 2.4.: Cross section sketch of THe-Trap. U_E denotes the voltage applied to the (symmetrically biased) endcaps, U_G to the (symmetrically biased) guard electrodes, and U_R to the ring electrode. To allow for radial ion excitation, the guard electrode rings are split in half, for a total of four guard electrodes.

Denoting the voltage difference between the ring electrode and the endcaps[4] as $U_0 = U_E - U_R$, then the potential in the (ideal) trap can be written as:

$$\Phi(\rho, z) = \frac{U_0}{z_0^2 + \frac{1}{2}\rho_0^2}\left(-\frac{1}{2}\rho^2 + z^2\right) \equiv \frac{U_0}{2d^2}\left(-\frac{1}{2}\rho^2 + z^2\right) \tag{2.8}$$

The last step introduces the shorthand $2d^2 = z_0^2 + \frac{1}{2}\rho_0^2$ as a parameter that describes the trap size.

However, in a real trap, the finite electrode size, machining tolerances, surface charges, and endcap holes (used for ion loading and ion transport) lead to field imperfections. Both THe-Trap [53] and the FSU trap [3] use an additional pair of electrodes, called "guard electrodes", to correct these field imperfections. In an "orthogonal trap", the guard electrodes are designed to not influence the quadratic curvature of the trap potential, but instead only the quartic imperfections. The orthogonality of the trap mainly depends on the ratio ρ_0/z_0 [60]. The FSU trap is constructed with a ratio of 1.16, the ideal value for an orthogonal trap. At THe-Trap, a ratio of 1.20 was chosen, because the small deviation from orthogonality can be used to check for unwanted contaminant ions [61]. A comparison of THe-Trap and FSU trap properties is shown at the end of this chapter, in Table 2.1.

2.5. Penning-trap frequencies

To quantify the qualitative understanding of the Penning-trap motion, the equations of motion have to be solved. They can be stated as

$$\ddot{\vec{r}} = \frac{q}{m}\left(\dot{\vec{r}} \times \vec{B} + \vec{E}\right) \quad . \tag{2.9}$$

[4] I follow the German convention and use U rather than V for voltages, so that expressions such as $U_0 = 1\,\mathrm{V}$ look less confusing.

Using $\vec{B} = B\vec{e}_z$ and $\vec{E} = -\vec{\nabla}\Phi$, they can be rewritten as

$$\begin{pmatrix} \ddot{x} \\ \ddot{y} \\ \ddot{z} \end{pmatrix} = \frac{q}{m} B \begin{pmatrix} \dot{y} \\ -\dot{x} \\ 0 \end{pmatrix} + \frac{qU_0}{2md^2} \begin{pmatrix} x \\ y \\ -2z \end{pmatrix} \quad . \tag{2.10}$$

The z-component of this differential equation is independent of the radial components. It has the structure of an undamped, harmonic oscillator, which is solved by

$$z(t) = \hat{z}\cos(\omega_z t + \varphi_z) \quad \text{with} \quad \omega_z = \sqrt{\frac{qU_0}{md^2}} \quad . \tag{2.11}$$

The frequency ω_z is called the *axial frequency*. Using this definition for ω_z and remembering Equation (2.2) for ω_c, the radial equations of motion can be written as

$$\begin{pmatrix} \ddot{x} \\ \ddot{y} \end{pmatrix} = \omega_\mathrm{c} \begin{pmatrix} \dot{y} \\ -\dot{x} \end{pmatrix} + \frac{1}{2}\omega_z^2 \begin{pmatrix} x \\ y \end{pmatrix} \quad . \tag{2.12}$$

These equations can be solved by introducing the function $u(t) = x(t) + iy(t)$, with which the radial equations of motion can be reformulated as

$$\ddot{u} = -i\omega_\mathrm{c}\dot{u} + \frac{1}{2}\omega_z^2 u \quad . \tag{2.13}$$

Guessing a solution of the form $u(t) = u_0 e^{-i\omega t}$ leads to two independent solutions with the frequencies

$$\omega_\pm = \frac{1}{2}\left(\omega_\mathrm{c} \pm \sqrt{\omega_\mathrm{c}^2 - 2\omega_z^2}\right) \quad . \tag{2.14}$$

The frequency ω_+ is the faster frequency. This frequency is often called the *modified cyclotron frequency*, because for typical trap parameters, it is only slightly smaller than the free space cyclotron frequency ω_c. The other frequency, ω_-, is called the *magnetron frequency*. It is the frequency of the slow E-cross-B drift around the trap center.

In order for the trajectory to be stable, the frequencies must be real-valued. This is only the case if $\omega_\mathrm{c}^2 > 2\omega_z^2$, which restricts the ring voltage to a maximum value of $U_{0,\max} = qB^2d^2/(2m)$. This is called the stability limit. In typical Penning traps, $\omega_- \ll \omega_z \ll \omega_+ < \omega_\mathrm{c}$. The magnetron frequency ω_- may become larger than ω_z, but this is only true if the trap is operated dangerously close to the stability limit.

The fact that the particle motion in a Penning trap can be separated into three independent, harmonic modes is important from a practical standpoint. It enables magnetic-field measurements (or rearranged: mass measurements) through the measurement of frequencies, and it ensures that the frequency measurements do not depend on difficult-to-control initial conditions.

By combining Equation (2.11) and Equation (2.14), the general solution can be stated as

$$\vec{r}(t) = \begin{pmatrix} \hat{r}_+\sin(\omega_+ + \varphi_+) + \hat{r}_-\sin(\omega_- + \varphi_-) \\ \hat{r}_+\cos(\omega_+ + \varphi_+) + \hat{r}_-\cos(\omega_- + \varphi_-) \\ \hat{z}\cos(\omega_z + \varphi_z) \end{pmatrix} \quad , \tag{2.15}$$

where $\hat{r}_+$, $\hat{r}_-$, $\hat{z}$ denote the amplitudes of the cyclotron mode, the magnetron mode, and the axial mode; and φ_+, φ_-, φ_z denote the phases. All these parameters are determined by the initial conditions. We can also calculate the energy of the (spinless) trapped ion as [62]

$$E_{\text{tot}} = \frac{1}{2}m|\dot{\vec{r}}|^2 + q\Phi(\vec{r}) \tag{2.16}$$

$$= \underbrace{\frac{1}{2}m\omega_z^2\hat{z}^2}_{E_z} + \underbrace{\frac{1}{2}m\omega_+\left(\omega_+ - \omega_-\right)\hat{r}_+^2}_{E_+} + \underbrace{\frac{1}{2}m\omega_-\left(\omega_- - \omega_+\right)\hat{r}_-^2}_{E_-} \quad . \tag{2.17}$$

Here, we have expressed the total energy as a sum of three terms and identified each term with the energy in the respective mode. Note that the energy of the magnetron mode, E_- is negative (because $\omega_- < \omega_+$), indicating again that the magnetron mode is unstable.

Several relationships can be used to calculate the free space cyclotron frequency ω_c from the trap eigenfrequencies ω_+, ω_-, and ω_z. For example, as follows from Equation (2.14), the sum of the two radial frequencies is equal to the free-space cyclotron frequency ω_c:

$$\omega_c = \omega_+ + \omega_- \quad . \tag{2.18}$$

This is sometimes called the *sideband frequency*, because historically it was measured as a sideband of ω_+. Another relationship between ω_c and the trap eigenfrequencies is given by the *invariance theorem* [63]:

$$\omega_c^2 = \omega_+^2 + \omega_-^2 + \omega_z^2 \quad . \tag{2.19}$$

The name "invariance theorem" alludes to the fact that this equation holds true even when the symmetry axes of the electric and the magnetic field are misaligned, which is the most relevant imperfection for typical Penning traps [64], and also when the electric field has an elliptic component (see subsection 2.10.1). Determining ω_c via the invariance theorem requires measuring all three eigenfrequencies. But since $\omega_+ \gg \omega_z \gg \omega_-$, the uncertainty $\delta\omega_c$ is mainly given by the uncertainty $\delta\omega_+$. The uncertainties $\delta\omega_z$ and $\delta\omega_-$ are suppressed by factors of ω_z/ω_c and ω_-/ω_c, respectively.

The sideband frequency $\omega_+ + \omega_-$ is also invariant under certain imperfections, namely the image charge shift (subsection 2.10.6) and modulation shift (subsection 2.10.8). Furthermore, if the radii $\hat{\rho}_+$ and $\hat{\rho}_-$ are identical during a measurement, then the sideband is also invariant under all electric field imperfections with cylinder symmetry [65]. Furthermore, with a suitable measurement technique, the sideband frequency can be determined in a single measurement. These advantages make the ω_c-determination via the sideband frequency a better choice for mass measurements of short-lived, radioactive ions.

For ideal traps, this equation follows from Equation (2.14) and Equation (2.11). In real Penning traps, neither equation holds true. Various imperfections of the electric and magnetic field, as well as interactions between ion, trap, and detection electronics cause shifts in all eigenfrequencies (section 2.10). But the relationship given by the invariance theorem holds true for a possible misalignment between the symmetry axes of the electric and magnetic field, which is the most relevant imperfection for typical Penning traps [64]. The invariance theorem even holds true for an electric field with added ellipticity, although this is typically a small imperfection.

The following relationship, a direct consequence of Equation (2.14), is useful for calculating one frequency from two measured frequencies:

$$2\omega_+\omega_- = \omega_z^2 \quad . \tag{2.20}$$

2.6. Ion detection

The very first Penning traps used in precision mass spectrometry [13] detected ions by ejecting them from the trap onto an external, charge-multiplying detector. The time of flight [14] or the position of the ions on the detector [66] can be recorded as a function of various excitation parameters, which allows inference of the frequencies of the trapped ions. These destructive measurement techniques require several hundred ions per cyclotron frequency measurement, but they have the advantage that the total measurement time per ion can be as short as a few ten ms. This allows studying short-lived radioactive nuclei [4].

An alternative, more precise detection scheme is to use pick-up electrodes inside the trap to non-destructively monitor the ion-motion via image currents [67]. This is the detection scheme used at THe-Trap and at the FSU trap.

2.6.1. Image current

An electric charge placed near a conducting surface induces an image charge in the surface. If the electric charge moves, so does the image charge. This is called an image current. Both THe-Trap and the FSU trap use one of the endcap electrodes to detect the image current of the axial motion.

The expected magnitude of the axial image current can be calculated using the Shockley-Ramo theorem [68]. To apply the Shockley-Ramo theorem, the electric field $\vec{E}_{\text{test}}$ that is present when the detection endcap is at some test potential U_{test}, and all other electrodes are held at ground, has to be calculated. This can be done numerically. Then the current that is induced in the endcap by a charge q moving with velocity $\vec{v}$ can be calculated as

$$I_{\text{IC}} = q\vec{v} \cdot \frac{\vec{E}_{\text{test}}}{U_{\text{test}}} \quad . \tag{2.21}$$

To first order, the field caused by either endcap can be modeled as an infinite parallel plate capacitor [69], where the plates are separated by the distance $2z_0/\kappa$:

$$\vec{E}_{\text{test}} = -\frac{\kappa U_{\text{test}}}{2z_0}\vec{e}_z \quad . \tag{2.22}$$

The parameter κ is a scale-factor of order unity, which can either be inferred from ion measurements, or from finite element simulations [69, 70]. For THe-Trap and the FSU trap, which both use hyperbolical trap electrodes, $\kappa \approx 0.8$. The image current of the axial motion is then given by

$$I_{\text{IC}} = -\frac{q\kappa\dot{z}}{2z_0} \quad . \tag{2.23}$$

In an ideal Penning trap, all electrodes are held at constant voltages. Possible alternating

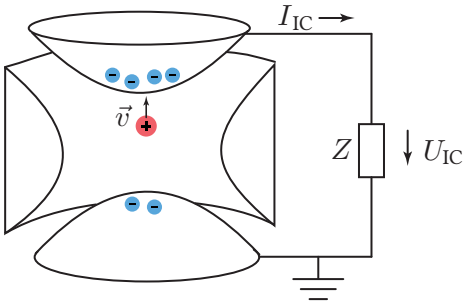

Figure 2.5.: Ion damping. The positive ion is moving upwards and attracts an increasing amount of negative image charge on the upper endcap. The upper endcap has a large impedance Z to its voltage source (here: ground). Consequently, the image current gives rise to the time-dependent voltage U_{IC}.

currents (AC), for example those induced by the axial motion, can flow freely into the respective voltage sources, so that the electrode voltages stay constant. However, when one electrode, for example an endcap, is connected to its voltage source via a large impedance Z (Figure 2.5), the image current gives rise to an endcap voltage[5] $U_{\mathrm{IC}} = -ZI_{\mathrm{IC}}$. This voltage can be amplified and used for detection, but it also back-acts on the ion motion: Using, again, the parallel-plate model for the endcaps, the electric field caused by the voltage U_{IC} can be approximated as

$$(\vec{E})_z = -\frac{\kappa U_{\mathrm{IC}}}{2z_0} = \frac{\kappa Z I_{\mathrm{IC}}}{2z_0} = -\frac{\kappa^2 Z q \dot{z}}{(2z_0)^2} \quad . \tag{2.24}$$

This field acts with the force $F_z = q(\vec{E})_z$ on the axial motion, so that the axial equation of motion is modified to

$$\ddot{z} + \omega_z^2 z = \frac{q}{m}(\vec{E})_z \tag{2.25}$$

$$= -\frac{Z}{m}\left(\frac{\kappa q}{2z_0}\right)^2 \dot{z} \quad . \tag{2.26}$$

If Z is real ($Z = R$), then this equation is analogous to that of a damped, harmonic oscillator

$$\ddot{z} + \gamma_z \dot{z} + \omega_z^2 z = 0 \quad , \tag{2.27}$$

and we can identify the damping term

$$\gamma_z = \frac{R}{m}\left(\frac{\kappa q}{2z_0}\right)^2 \quad . \tag{2.28}$$

It is important to note that $\gamma_z \propto q^2/m$. When a cloud of N ions moves in the trap, their collective (coherent) motion is damped with N times as strongly as the motion of a single ion. This allows measurements of the number of trapped ions.

[5] The minus sign follows from the image-current definition: The image current is the change of the charge on the electrode, $I_{\mathrm{IC}} = \dot{Q}_{\mathrm{electrode}}$. This current is going *into* the electrode. The voltage across Z is determined by the current going *out of* the electrode.

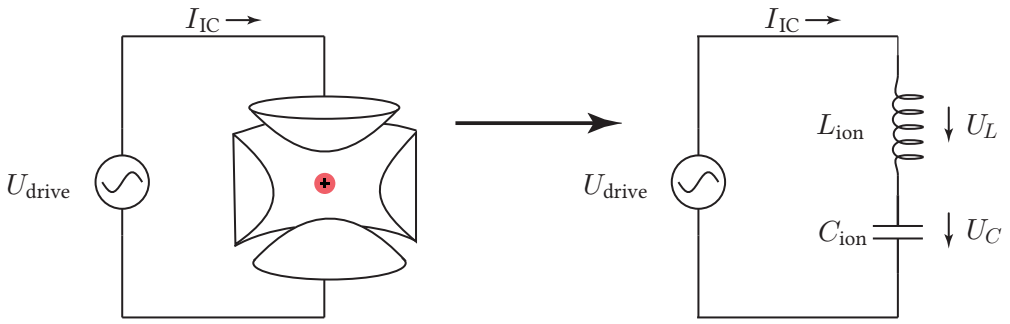

Figure 2.6.: Ion circuit model. The image current as a function of the external drive can be modeled as an equivalent LC-circuit. The DC potentials for trapping are not shown. (DC-wise, the endcaps are typically held at ground potential.)

As a solution of the damped harmonic oscillator shows, the damping term causes the axial energy E_z of an excited particle to decay with $E_z(t) = E_{z,0}\exp(-\gamma_z t)$.

But the motion is not damped to arbitrarily small values. Ultimately, the Johnson noise voltage of the resistor R acts as a heating drive for the ion. Unless other cooling techniques are used, this Johnson noise prevents the ion energy from falling below the thermal limit given by $k_{\mathrm{B}}T$, where T is the effective temperature of R. This temperature depends on external noise, and (when not using feedback methods) is assumed to be approximately 10 K for THe-Trap [52]. At the FSU trap, it was measured to be 40 K [71], which is significantly higher than the 4 K measured at the MIT. It is possible that during the move from the MIT to the FSU, a stronger path for room-temperature noise to the cryogenic detector developed.

2.6.2. Ion equivalent circuit

Before describing the interaction between the ion and the detection circuit (which, as we will learn, cannot be a simple resistor) in more detail, we will introduce a model, in which the ion is treated as a circuit element [56, 72]. To this end, we replace the impedance Z in Figure 2.5 with an AC voltage source (Figure 2.6) and investigate how the image current depends on the frequency and voltage of the AC source. The goal is to describe this dependency using an equivalent LC circuit for the ion.

As in the last section, an electric potential $U_{\mathrm{drive}}(t)$ across the endcaps leads (in the lowest order) to the force, $F_z = -q\kappa U_{\mathrm{drive}}/(2z_0)$, which modifies the axial equation of motion to

$$\ddot{z} + \omega_z^2 z = -\frac{q}{m}\frac{\kappa U_{\mathrm{drive}}}{2z_0} \quad . \tag{2.29}$$

The derivative of this equation, together with the $\dot{z}$–I_{IC} relationship (Equation 2.21), gives the relationship between drive voltage and image current:

$$\ddot{I}_{\mathrm{IC}} + \omega_z^2 I_{\mathrm{IC}} = \frac{q^2\kappa^2}{4mz_0^2}\dot{U}_{\mathrm{drive}} \quad . \tag{2.30}$$

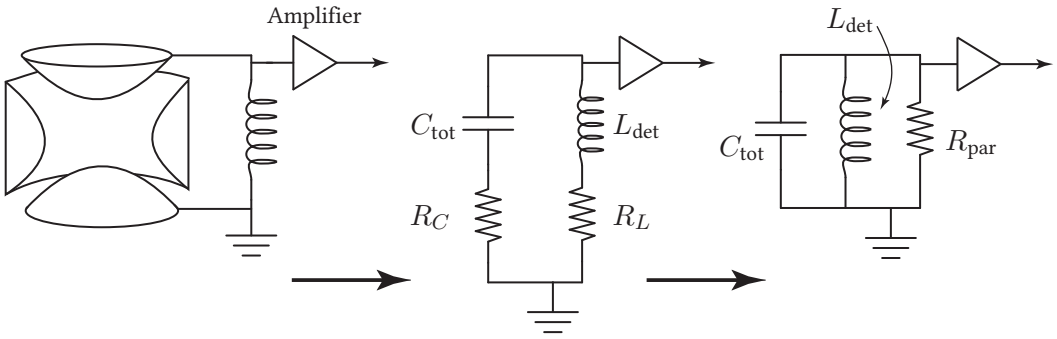

Figure 2.7.: Detection circuit model. The detection circuit, without ion, can be modeled as a lossy capacitor that stands for the total capacitance between the upper endcap and ground, and a lossy detection coil. If the losses are small compared to ωL_{det} and $1/(\omega C_{\text{tot}})$, they can be modeled as an equivalent parallel resistance R_{par}.

For comparison, consider the behavior of a driven series LC-circuit (Figure 2.6). Using $U_L(t) = L_{\text{ion}}\dot{I}$ and $\int I dt = C_{\text{ion}} U_C(t)$, it follows that

$$U_{\text{drive}} = U_L + U_C \tag{2.31}$$

$$= L_{\text{ion}}\dot{I} + \frac{1}{C_{\text{ion}}}\int I dt \tag{2.32}$$

$$\Rightarrow \quad \frac{1}{L_{\text{ion}}}\dot{U}_{\text{drive}} = \ddot{I} + \frac{1}{L_{\text{ion}}C_{\text{ion}}} I \quad . \tag{2.33}$$

The structures of Equation (2.30) and Equation (2.33) are identical. Therefore, the image current as a function of the endcap voltage can be described using a fictional series LC-circuit with the equivalent values

$$L_{\text{ion}} = \frac{4mz_0^2}{q^2\kappa^2} \quad , \tag{2.34}$$

$$C_{\text{ion}} = \frac{1}{\omega_z^2 L_{\text{ion}}} \quad . \tag{2.35}$$

2.6.3. Detection circuit

As was hinted at in the previous sections, the detection circuits at THe-Trap and the FSU trap are based on placing a large impedance (1 MΩ or larger) between the upper endcap and ground, so that the ∼fA image current of the axial motion causes an endcap voltage in the nV-range, which is then picked up by a cryogenic amplifier[6].

However, the electrodes, the cables, and the resonator have a total capacitance to ground of $C_{\text{tot}} \approx 20\,\text{pF}$. If the external detection were based on a simple 1 MΩ-resistor, then at typical axial frequencies (4 MHz at THe-Trap, and 213 kHz at FSU) the resistor would be shorted out

[6]The FSU trap uses a SQUID instead of a traditional amplifier.

by C_{tot}. Instead, the detection circuit uses an inductor L_{det}. This inductor forms an RLC-circuit with the total stray capacitance and the losses of the circuit. As long as the losses are small compared to ωL and $1/(\omega C)$, then near the resonance frequency[7] $\omega_{RLC} = (L_{\text{det}} C_{\text{tot}})^{-1/2}$, they can be modeled as an equivalent parallel resistor [56] with the value

$$R_{\text{par}} = \frac{L}{C_{\text{tot}}(R_L + R_C)} \quad . \tag{2.36}$$

This simplifies the description of the detection system to a parallel RLC-circuit. If this circuit is excited with a current of frequency ω_{RLC}, the reactive components given by L_{det} and C_{tot} cancel each other, so that only R_{par} remains. Near the resonance frequency, the impedance $|Z_{RLC}|^2$ can be approximated by a Lorentzian function that has a center of ω_{RLC} and a full width at half maximum of

$$\Gamma = \frac{1}{R_{\text{par}} C_{\text{tot}}} \quad . \tag{2.37}$$

As customary in the description of resonant circuits, we define the *quality factor* or Q-value of the detection circuit as the ratio of resonance frequency and the full-width-half-maximum:

$$Q \equiv \frac{\omega_{RLC}}{\Gamma} = R_{\text{par}} \sqrt{\frac{C_{\text{tot}}}{L_{\text{det}}}} = \frac{1}{R_L + R_C} \sqrt{\frac{L_{\text{det}}}{C_{\text{tot}}}} \quad . \tag{2.38}$$

The detection system of THe-Trap has a resonance frequency of $\omega_{RLC} \approx 2\pi \cdot 4\,\text{MHz}$ and a Q-value of ≈ 800. At the FSU trap, the resonance frequency is $\omega_{RLC} \approx 2\pi \cdot 213\,\text{kHz}$, and the Q-value, due to a superconducting detection coil, ≈ 30000. When the RLC circuit is excited, the energy dissipates in the resistor R_{par} with a time constant of $1/\Gamma = Q/\omega_{RLC}$. This time constant is $\approx 30\,\mu\text{s}$ at THe-Trap and $\approx 20\,\text{ms}$ at the FSU trap.

Usually, the losses are not known beforehand, and the Lorentzian spectrum of the RLC-circuit is measured to determine its center frequency and width. Together with a separate measurement of L_{det} with an LCR meter, the (fictional) resistance R_{par} can be determined, which can then be used to predict the ion damping.

2.6.4. Ion–detector interaction

As Equation (2.28) shows, a real-valued impedance between the endcaps damps the ion motion. However, the impedance of the detection circuit is only real when the ion is exactly resonant with the detector, and even then the small frequency shift caused by the damping term makes the interaction between the ion and the detection circuit more complex than Equation (2.28).

To fully understand the interaction, the ion's LC-model has to be combined with the parallel RLC-model of the detection circuit (Figure 2.8). Using either an admittance method [56], or a narrow-resonance approximation of the detection circuit impedance [73], it can be shown that for $\gamma_z \ll \Gamma$, the detection circuit damps the ion motion with an effective damping term of

$$\gamma_{z,\text{eff}} = \gamma_z \frac{\Gamma^2}{\Gamma^2 + 4(\omega_z - \omega_{RLC})^2} \quad , \tag{2.39}$$

[7] The shift of the resonance frequency caused by the damping terms is negligible for typical parameters.

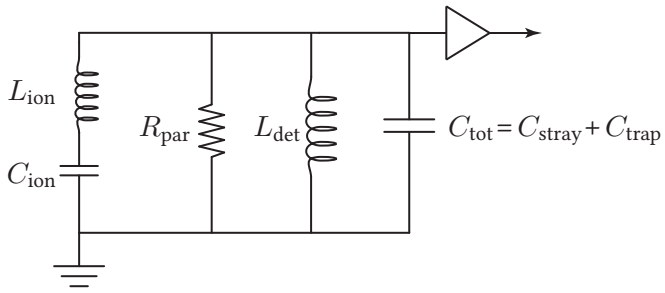

Figure 2.8.: Simplified ion–detector interaction, using a parallel RLC-model for the detector, and an LC-model for the ion.

where Γ is the damping of the detection circuit, and $\omega_z - \omega_{RLC}$ stands for the detuning between the ion and the detection circuit. However, the measured ion damping constants, both at THe-Trap and the FSU trap, are approximately 30% lower than the predicted damping constants. Early Penning-trap experiments measured damping constants that were between 20% to 50% lower than expected [57, 69]. This effect is not yet fully understood, but it appears that a 30% lower damping constant is a common feature of hyperbolic traps[8].

The interaction between ion and detection circuit also shift the ion frequency by an amount

$$\Delta\omega_{z,\text{CP}} = (\omega_z - \omega_{RLC}) \frac{\gamma_z \Gamma}{\Gamma^2 + 4(\omega_z - \omega_{RLC})^2} \quad . \tag{2.40}$$

The frequency shift $\Delta\omega_{z,\text{CP}}$ is called "coil pushing", because the ion frequency is "pushed" further away from the frequency of the detection circuit. The coil-pushing shift has been verified at the FSU trap and was found to be consistent with the theoretical prediction [71, 73], as long as a *measured* (38% lower than calculated) value of the ion width γ_z was used to predict the coil pushing. At THe-Trap, the coil-pushing shift has not been measured because the Q-value of the detection system is lower and the shift can be neglected.

2.7. A detailed look at the electric potential

The following sections on ion manipulation and frequency shifts require a more detailed treatment of the electric potential inside the trap than what was given before. In this section, the electric potential will first be subdivided into potentials "caused" by each electrode, then each of these potentials is separated into a time-dependent and a time-independent part, and finally, the time-independent parts are expanded in a multipole expansion.

2.7.1. Expansion of the potential

The Maxwell equations are linear. Therefore, the total electric potential Φ inside the trap is a superposition of the potentials caused by each electrode. Furthermore, although most of the

[8] This 30% discrepancy is the "unsolved mystery" that was alluded to at the beginning of this chapter. Many systematic frequency shifts are directly or indirectly connected to the damping constant, so the solution of this mystery is long overdue. Unfortunately, I too must leave it to later, smarter students.

electric potentials used for manipulating the ion motion are time dependent, the frequencies are low enough (less than 100 MHz), and the trap small enough, that retardation effects can be neglected. This allows us to factor the time dependence. Let $\Phi_i(x, y, z, U_i(t)$ be the potential inside the trap when electrode i is at the voltage U_i and all other electrodes are at ground potential. Then

$$\Phi(x, y, z, t) = \sum_i \Phi_i(x, y, z, U_i(t)) \quad . \tag{2.41}$$

The space dependence of the Φ_i can be broken down into even smaller parts: Since the sources of the Φ_i are situated on the outside of the trapping region, the Laplace equation $\Delta\Phi_i = 0$ is satisfied *inside* of the trap. This allows us to use a spherical multipole expansion of each Φ_i. In the spherical multipole expansion, each term satisfies the Laplace equation individually. Using spherical coordinates r, θ, ϕ and the spherical harmonics $Y_l^m(\theta, \phi)$, the multipole expansion (with factored-out time dependence) can be stated as

$$\Phi_i(r, \theta, \phi, U_i(t)) = U_i(t) \sum_{l,|m|\leq l} a_{ilm} r^l Y_l^m(\theta, \phi) \quad , \tag{2.42}$$

with $l \in \mathbb{N}$ and $m \in \mathbb{Z}$. The coefficients a_{ilm} have to be found for each electrode i by finite element simulations, or experimentally by carefully studying the particle motion as a function of the electrode's voltage. Note that this particular expansion is the *interior* multipole expansion, which describes the potential of a source-free region *inside* the charge distribution. This is in contrast to the more familiar *exterior* multipole expansion, which describes the potential in a region *outside* of a charge distribution. The interior multipole expansion uses factors of r^l for the base functions, whereas the exterior expansion uses factors of $r^{-(l+1)}$.

The terms $r^l Y_l^m(\theta, \phi)$ can be transformed to Cartesian coordinates, which results in surprisingly simple polynomials. Like the functions Y_l^m, these polynomials are complex, but through linear combinations, all instances of i can be removed and the coefficients of the polynomials can be made real. The resulting polynomials are the *harmonic polynomials* p_{lm} [74–76]. The most relevant polynomials p_{lm} can be stated as (Appendix B):

$$\begin{aligned}
p_{0,0} &= 1 \\
p_{1,0} &= z & p_{1,+1} &= x & p_{1,-1} &= y \\
p_{2,0} &= -\frac{1}{2}(x^2+y^2) + z^2 & p_{2,+1} &= xz & p_{2,-1} &= yz \\
& & p_{2,+2} &= x^2 - y^2 & p_{2,-2} &= xy \\
p_{3,0} &= -\frac{3}{2}(x^2+y^2)z + z^3 & p_{3,+1} &= x^3 + xy^2 - 4xz^2 & p_{3,-1} &= x^2y + y^3 - 4yz^2 \\
& & p_{3,+2} &= zx^2 - zy^2 & p_{3,-2} &= xyz \\
& & p_{3,+3} &= x^3 - 3xy^2 & p_{3,-3} &= y^3 - 3x^2y \\
p_{4,0} &= \frac{3}{8}(x^2+y^2)^2 - 3(x^2+y^2)z^2 + z^4 \\
p_{6,0} &= -\frac{5}{16}(x^2+y^2)^3 + \frac{45}{8}(x^2+y^2)^2 z^2 - \frac{15}{2}(x^2+y^2)z^4 + z^6 \quad .
\end{aligned} \tag{2.43}$$

Since they are linear combinations of the Y_l^m, the p_{lm} each satisfy the Laplace equation $\Delta p_{lm} = 0$, and they are orthogonal to each other with respect to an integral over the unit sphere. The p_{lm} with $l = 1$ describe dipolar components of the potential, those with $l = 2$ quadrupolar components, and those with $l = 3$ octupolar components. All p_{lm} with $m = 0$ are symmetric under rotation around z, since the radial coordinates are only present in powers of $x^2 + y^2 = \rho^2$. They are closely related to the Legendre polynomials:

$$p_{l,0}(x, y, z) = r^l P_l(\cos\theta) \quad . \tag{2.44}$$

On the right hand side of the equation, P_l stands for the l-th Legendre polynomial in spherical coordinates. In most Penning trap theory, the potential is only expanded in Legendre polynomials P_l. In contrast, the expansion in harmonic polynomials p_{lm} has the advantage of allowing a consistent treatment of non-rotationally symmetric potentials. We will use this expansion to examine radial excitation schemes, and for treating the most severe imperfections of the electric field, which are trap tilt and ellipticity (described by $p_{2,m}$ with $m \neq 0$). Further, since the p_{lm} are in Cartesian coordinates, they are a natural choice for simple numerical simulations of the ion dynamics during the excitation pulses in a tilted, anharmonic trap (Appendix B).

For completeness, the expansion of the Φ_i in the p_{lm} is

$$\Phi_i(x, y, z, t) = U_i(t) \sum_{l,|m|\leq l} b_{ilm} p_{lm}(x, y, z) \quad . \tag{2.45}$$

Instead of using numbers for specifying an electrode, we will use $i \in \{\mathrm{R}, \mathrm{E}, \mathrm{G}, \mathrm{H}, \mathrm{B}, \mathrm{T}\}$. The letter R stands for the ring electrode, E for the symmetrically biased endcaps, G for the symmetrically biased guard electrodes, H for one of the lower guard electrodes, B for the bottom endcap, and T for the top endcap. This means that we are double counting the endcaps and one half of the lower guard electrodes, but this will allow us to treat U_T, U_B, and U_H as pure AC potentials, and the rest as pure DC potentials.

The expansion of the DC potentials of the Penning trap can be simplified by exploiting the inherent symmetry of the Penning trap. The field of rotationally symmetric electrodes can be approximated using the rotationally symmetric polynomials $p_{l,0}$. Further, polynomials with odd l are heavily suppressed for all electrodes that are symmetric in z. In normal trap operation, these conditions are true for all DC potentials inside the trap: The endcap electrodes are held at ground, both guard electrodes are biased with the same voltage U_G, and the ring electrode, which is biased with U_R, has inherent symmetry in z. Therefore, the description of the DC potential simplifies to

$$\Phi(x, y, z) = \sum_{l \text{ even}} \left(U_\mathrm{R}\, b_{\mathrm{R},l,0} + U_\mathrm{G}\, b_{\mathrm{G},l,0}\right) p_{l,0}(x, y, z) \tag{2.46}$$

$$\equiv \sum_{l \text{ even}} K_l p_{l,0}(x, y, z) \tag{2.47}$$

$$\equiv \frac{U_0}{2} \sum_{l \text{ even}} C_l \frac{1}{d^l} p_{l,0}(x, y, z) \quad . \tag{2.48}$$

The last equation is only mentioned as a connection to the *standard expansion* that is often used in Penning trap literature. In this standard expansion, the characteristic trap dimension d

is defined such that $C_2 \equiv 1$, and $U_0 \approx -U_\mathrm{R}$ is arbitrarily pulled out of the sum, eliciting the illusion that a change of U_R simply scales the overall potential. This is not true for traps that employ guard electrodes. On a more subtle level, the standard expansion is ambiguous on the definition of U_0 in the presence of guard electrodes.

In this thesis, I therefore chose to summarize the combination of the DC ring potential and the DC guard electrode potential in the coefficients K_l (the units of the K_l are $\mathrm{V/m}^l$). The formulas for the expected frequency shifts are easily converted to this new notation (subsection 2.10.2), and the formula for the axial frequency becomes

$$\omega_z = \sqrt{2\frac{q}{m}K_2} \quad . \tag{2.49}$$

The purpose of the guard electrodes can be seen in Equation (2.46): The potential of an ideal ring electrode can be described by a $p_{2,0}$ term (with the coefficients of all other terms 0). In reality, the ring electrode has a small contribution of $p_{4,0}$. The guard-electrodes, when biased symmetrically, are designed to have a comparably small contribution of $p_{2,0}$, but a large component $p_{4,0}$, so that they can be used to cancel the $p_{4,0}$ term without affecting the axial frequency ("orthogonal" guard electrodes).

In the following sections, we will use Equation (2.47) for describing the DC potential of the trap, and Equation (2.45) for describing the AC potentials that are applied to the bottom endcap ("B"), applied to one half of the lower guard electrodes ("H"), and which is measured on the top endcap ("T").

2.7.2. The values of K_2, K_4, and K_6

For evaluations of frequency shifts formulas, Equation (2.49) can be rearranged to yield a definition of K_2:

$$K_2 = \frac{m}{2q}\omega_z^2 \quad . \tag{2.50}$$

The value of K_4 is most conveniently expressed as

$$K_4 = \Delta U_\mathrm{G}\, b_{\mathrm{G},4,0} \quad , \tag{2.51}$$

with ΔU_G as the difference between the actual guard voltage U_G, and the optimal guard voltage $U_{\mathrm{G},0}$. The optimal guard voltage, which (at a given U_R and U_E) is defined as the voltage where $K_4 \equiv 0$, can be easily found as the guard voltage where an increase of the magnetron radius does not shift the axial frequency (section 5.1). The coefficient $b_{\mathrm{G},4,0}$ is either taken from measurements on light ions, where the relativistic shift can be used to calibrate the absolute amplitudes [77], or from electrostatic simulations [70].

Experimentally, the K_6 measurements often reveal K_6 to be dominated by the ring voltage, so that K_6 is most easily expressed as

$$K_6 = U_0\, b_{\mathrm{R},6,0} \quad , \tag{2.52}$$

with $b_{\mathrm{R},6,0}$ determined from calibration measurements.

2.8. Driving the modes

The ion motion can be influenced applying time-dependent voltages to one or more trap electrodes. The resulting electric fields can either *drive* the ion (increase or decrease the energy of a single mode), or *couple* two modes of the ion (transfer action between two modes).

2.8.1. Axial mode

The axial mode can be driven by applying an alternating voltage $U_\mathrm{B}(t) = \hat{U}_\mathrm{B}\cos(\omega_\mathrm{drive}t + \phi)$ to the bottom endcap. The endcap potential is dominated by its $p_{1,0}$ term, which was earlier approximated using the capacitor model as $b_{\mathrm{B},1,0} = \kappa/(2z_0)$. This first-order approximation leads to a field that can excite (*drive*) the axial motion:

$$\vec{E}_\mathrm{drive}(t) = \vec{E}_\mathrm{B}(t) = -U_\mathrm{B}(t)b_{\mathrm{B},1,0}\vec{e}_z \quad . \tag{2.53}$$

However, when the ion is driven with $\omega_\mathrm{drive} \approx \omega_z \approx \omega_{RLC}$ (which is usually the case), the drive interacts not only with the ion, but also with the detection circuit, which leads to a voltage U_T on the top endcap, and subsequently a field $\vec{E}_\mathrm{T}$ that also acts on the ion [56]. This can lead to effects that are difficult to describe theoretically and challenging to control experimentally[9]. At THe-Trap, this problem is overcome by superimposing a modulation voltage $U_\mathrm{mod} \ll U_\mathrm{R}$ onto the ring voltage, so that

$$U_\mathrm{R}(t) = U_\mathrm{R}(1 + \epsilon\cos(\omega_\mathrm{mod}t)) \quad , \tag{2.54}$$

with $\epsilon = U_\mathrm{mod}/U_\mathrm{R}$. The modulation frequency $\omega_\mathrm{mod} = 2\pi \cdot 100\,\mathrm{kHz}$ is chosen to be larger than the width of the detection circuit Γ, but less than the axial frequency $\omega_z \approx 2\pi \cdot 4\,\mathrm{MHz}$. The modulated ring voltage changes the (undriven) axial equation of motion to

$$\ddot{z} + \gamma_z\dot{z} + \omega_z^2\left[1 + \epsilon\cos(\omega_\mathrm{mod}t)\right]z = \frac{q}{m}E_{\mathrm{drive},z}(t) \quad , \tag{2.55}$$

which is the equation of a frequency modulated oscillator. This oscillator can be excited on its sidebands, for example at $\omega_\mathrm{drive} = \omega_z + \omega_\mathrm{mod}$.

To show this, we can treat ϵ as a perturbation. To zeroth order, the differential equation is that of a driven, damped oscillator. When driven off resonance with $|\omega_\mathrm{drive} - \omega_z| \gg \gamma_z$, the ion responds with a small motion at the drive frequency. In the next order of the perturbation problem, this driven motion interacts with the modulation, which produces terms $\cos[(\omega_\mathrm{drive} \pm \omega_\mathrm{mod})t]$ that can be resonant with the zeroth-order equation when $\omega_\mathrm{drive} = \omega_z \pm \omega_\mathrm{mod}$.

A detailed treatment [56, 57] shows that the drive on the upper sideband $\omega_z + \omega_\mathrm{mod}$ acts as an equivalent resonant drive that is scaled down in amplitude by a factor of $\beta/2$, with

$$\beta = \frac{1}{2}\epsilon\frac{\omega_z}{\omega_\mathrm{mod}} \tag{2.56}$$

[9] The "leakage" of the excitation signal into the high-gain detection system depends on a poorly known and possibly time-dependent stray capacitance. Another complication (which is often overlooked) is that, electrically speaking, the endcap-to-endcap capacitance C_trap is parallel to the ion. So when the lower endcap is not connected to ground, but instead used for driving the ion, C_trap cannot be lumped together with C_stray anymore, and the simple model of Figure 2.8 no longer applies. In [56], it is argued that lumping the capacitances together is a viable approximation for the FSU trap, but simulations show that this is not the case at THe-Trap.

defined as the traditional frequency modulation index. However, it should be noted that this scaling is only true for $\beta \ll 1$. For larger β, the equivalent drive strength is no longer linear in U_{mod}, but instead has several zeroes, the first being at $\beta \approx 2.4$. A second caveat is that the modulation leads to a frequency shift (subsection 2.10.8). Maximum values for ϵ and β at THe-Trap are $4 \cdot 10^{-4}$ and $8 \cdot 10^{-3}$, respectively.

The main advantage of the sideband technique is that the direct interaction between the drive and the detection circuit is non-resonant and can therefore be neglected. The interaction between the detection circuit and the ion can then be described with the familiar damping parameter $\gamma_{z,\text{eff}}$ (Equation 2.39) and the corresponding frequency shift. When detector and ion are resonant, the axial equation of motion becomes

$$\ddot{z} + \gamma_z \dot{z} + \omega_z^2 z = \frac{1}{m} F_{\text{drive},z}(t) \quad , \tag{2.57}$$

where $F_{\text{drive},z}(t)$ is the effective (scaled-down) drive strength. The steady-state solution is most conveniently expressed using complex numbers: Using $\Re$ as the operator that returns the real part of a number, and $F_{\text{drive},z}(t) = \Re\left[\hat{F}_{\text{drive},z} \exp(i\omega_{\text{drive}} t)\right]$, the steady-state solution of the equation of motion can be found to be

$$z(t) = \Re\left[\hat{z} \, \exp\left(i\omega_{\text{drive}} t\right)\right] \quad , \quad \text{with} \quad \hat{z} = \frac{\hat{F}_{\text{drive},z}}{m(\omega_z^2 - \omega_{\text{drive}}^2 + i\gamma_z \omega_{\text{drive}})} \quad . \tag{2.58}$$

As shown in Figure 2.9, $\Re\hat{z}$ has a dispersion shape. This can be used to determine the axial frequency, for example by slowly sweeping the drive frequency across the axial resonance, and identifying ω_z as the zero-crossing of the detected signal.

At the FSU trap, the problematic interaction between drive and detection circuit is circumvented in a different way. Instead of using continuous excitation, a short (~ 1 ms), resonant pulse is used to excite ion. This pulse also excites the detection circuit, but since the detection circuit is more strongly damped than the ion, its excitation decays more quickly, and after a suitable waiting time of a few hundred ms, the detected signal is dominated by the ion motion. This decaying signal is digitally recorded and analyzed to obtain ω_z and γ_z.

An entirely different driving scheme is based on modulating the ring voltage[10] with $2\omega_z$. This is called *parametric excitation*. If the driving strength is larger than a certain threshold given by the axial damping, it leads to exponential energy increase. In practice, the ion energy is limited by trap inhomogeneities, which cause the ion's frequency to shift as a function of its energy, so that it is no longer resonant with the drive. This rather crude driving method can be used to verify that an ion is present, and to roughly gauge the signs of the leading inhomogeneities of the electric field [78–80].

2.8.2. Radial modes

The radial modes are driven using one half of the (split) lower guard electrode ring. The field of this electrode is highly inhomogeneous, and the multipole expansion (Equation 2.45) of its

[10] This drive can also be applied to one of the endcaps, because the $p_{2,0}$ component of one endcap is approximately half as large (with opposite sign) as the $p_{2,0}$ component of the ring electrode. The sizable $p_{1,0}$ component of the endcap is inconsequential for this driving scheme.

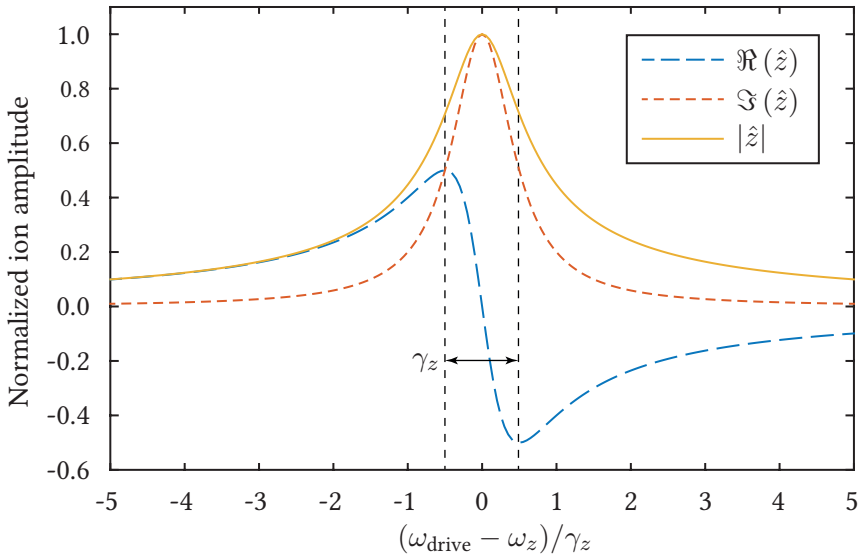

Figure 2.9.: Steady state amplitude z_0 of the driven ion motion as a function of drive frequency ω_{drive}. Here, the axial frequency ω_z is resonant with ω_{RLC}. The distance between the extrema of the $\Re(\hat{z})$ curve is γ_z in the angular frequency plot, or $\gamma_z/(2\pi)$ in a frequency plot.

potential contains terms of many different orders. This makes the guard electrode suitable for many driving and coupling schemes. The strength of the dipolar radial drive is given by the component p_{11}:

$$\vec{E}_{\text{H}} = -U_{\text{H}}\, b_{\text{H},1,1}\, \vec{e}_x \quad . \tag{2.59}$$

At THe-Trap, the coefficient $b_{\text{H},1,1}$ was found with simulations to be $b_{\text{H},1,1} = 1.3\,\text{m}^{-1}$. The coefficient at the FSU trap is of a similar magnitude.

Unlike the axial motion, the radial motion is not a simple harmonic oscillation. However, using a Green's function treatment (Appendix A), it can be shown that for a radial drive with a frequency close to either ω_+ or ω_-, the respective mode can be treated as an undamped[11], one-dimensional harmonic oscillator, where the external force is scaled by a factor of

$$c_\pm = \pm\frac{\omega_\pm}{\omega_+ - \omega_-} \quad . \tag{2.60}$$

The "+" stands for the cyclotron mode, the "-" for the magnetron mode. The most common driving scheme of the radial modes is to use a resonant pulse to excite them. For example, a cyclotron pulse can be realized by applying the voltage $U_{\text{H}}(t) = \hat{U}_{\text{H}} \cos(\omega_+ t + \varphi_{\text{H}})$ for a time t_{pulse} onto one half of the lower guard electrode. Using the Green's function treatment (or,

[11] All modes of the trapped particle are, in principle, damped through rest-gas collisions, synchrotron radiation, and non-zero resistances of the trap electrodes (which interact with the image current). However, for trapped *ions* in a cryogenic trap, the typical radial damping constants are so low that they are inconsequential.

alternatively, solving the inhomogeneous differential equation), the pulse-response of the ion can be found. If the ion starts at rest, then after the pulse its motion is given by

$$x_+(t > t_{\text{pulse}}) = t_{\text{pulse}} \frac{c_+ q \hat{U}_{\text{H}} b_{\text{H},1,1}}{2m\omega_+} \sin(\omega_+ t + \varphi_{\text{H}}) \quad , \tag{2.61}$$

In other words, the pulse increases the amplitude by an amount proportional to t_{pulse}.

When the ion does not start at rest, but instead has some initial motion $x_{+,0}$, for example $x_{+,0}(t) = \hat{x}_{+,0} \cos(\omega_+ t + \phi_+)$, then due to the linearity of the differential equation, we can simply add the pulse response to the original motion. Depending on the phase relationship between the pulse and the original motion, the final amplitude can be bigger or smaller than the amplitude before the pulse. This can easily be shown by treating the amplitudes as vectors (phasors) or complex numbers.

The response to a magnetron pulse can be found accordingly by replacing "+" with "−".

At THe-Trap, the radial modes are not only excited with pulses, but alternatively excited with slow sweeps of the drive frequency across the radial resonance. Such a frequency sweep can be described with

$$(\vec{E}_{\text{drive}})_x(t) = -\hat{U}_{\text{H}} b_{\text{H},1,1} \cos\left[(\omega_{\text{s}} + \frac{\alpha}{2}t)t + \varphi_{\text{H}}\right] \quad , \tag{2.62}$$

where ω_{s} is the starting frequency, and α is the rate with which the excitation frequency is changed (sweep rate)[12]. This field can be added to the radial equations of motion and the resulting system can be solved through numerical integration. Alternatively, we can use the rotating wave approximation Equation (A.50), which greatly simplifies the numerical integration. The main trick is to assume that the frequency sweep happens "at a fixed frequency" with a slowly varying phase $\varphi_{\text{H}}(t) = (\omega_{\text{s}} - \omega_+)t + \alpha t^2/2$. This leads to the equivalent solution

$$x_+(t) = X_+^{\text{s}}(t) \sin(\omega_+ t) + X_+^{\text{c}}(t) \cos(\omega_+ t) \quad , \tag{2.63}$$

$$X_+^{\text{s}}(t) = -\frac{c_+ \hat{U}_{\text{H}} b_{\text{H},1,1}\, q}{2m\omega_+} \int_0^t \cos\left((\omega_{\text{s}} - \omega_+)\, t_0 + \frac{\alpha}{2} t_0^2\right) dt_0 \quad , \tag{2.64}$$

$$X_+^{\text{c}}(t) = -\frac{c_+ \hat{U}_{\text{H}} b_{\text{H},1,1}\, q}{2m\omega_+} \int_0^t \sin\left((\omega_{\text{s}} - \omega_+)\, t_0 + \frac{\alpha}{2} t_0^2\right) dt_0 \quad , \tag{2.65}$$

which is free of fast-oscillating terms in the integrals. The integrals cannot be solved algebraically, but they are readily evaluated numerically, either by transforming them to Fresnel-type integrals (for which efficient look-up tables exist), or by using standard numerical integration algorithms. The total amplitude (assuming the ion started at rest) is given by $\hat{x}_+ = \sqrt{{X_+^{\text{s}}}^2 + {X_+^{\text{c}}}^2}$. This can be used to calculate the cyclotron energy E_+ during the sweep. Figure 2.10 shows E_+ during a typical cyclotron sweep at THe-Trap. The response to a magnetron sweep can be found accordingly.

[12] The instantaneous frequency is given by the time-derivative of the phase evolution. This leads to a factor of $\frac{1}{2}$ [81] in Equation (2.62), which was omitted in some of our earlier work [54, 61].

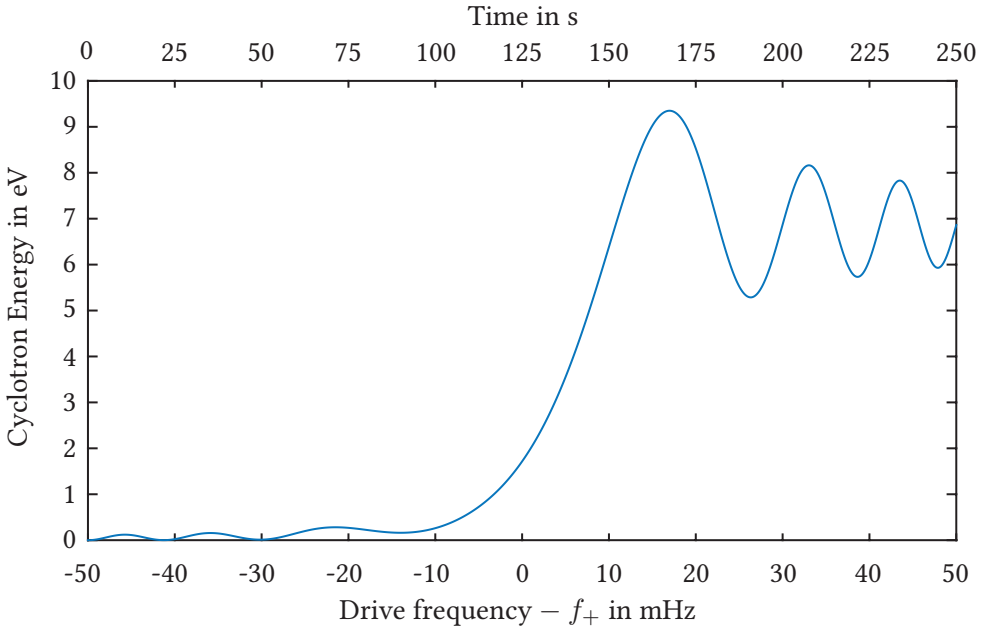

Figure 2.10.: Simulated energy of a $^{12}C^{4+}$ ion during an upsweep of the radial drive. The drive frequency is increased linearly across the reduced cyclotron frequency $f_+ = \omega_+/(2\pi)$. The parameters of this calculation are 0.1 Hz sweep range, 250 s sweep time, and 20 μV_{pp} applied to one half of the lower guard electrode.

2.9. Coupling the modes

The radial modes can be coupled to the axial mode using electric potentials that mix radial and axial coordinates, such as the potential given by $p_{2,1} = xz$. The coupling is only efficient when the potential is modulated with appropriate frequencies.

For example, modulating $p_{2,1}$ with a frequency of $\omega_+ - \omega_z$ leads to energy transfer (*Rabi oscillations*) between the cyclotron mode and the axial mode (section A.6). During the Rabi oscillations, the damping of the axial mode causes the energy in both modes to decrease to a thermal limit. This can be used to cool the cyclotron mode. The same technique can be used to damp the magnetron mode: When using a modulation frequency of $\omega_- + \omega_z$, the Rabi oscillations are between the magnetron mode and the axial mode, and the axial damping cools the magnetron mode[13]. The lowest attainable radial amplitudes are proportional to the thermal axial amplitude $\hat{z}_{th}$. They follow from the scaling factors of the coupling forces:

$$\hat{z}_{th} = \sqrt{\frac{2k_B T}{m\omega_z^2}} \tag{2.66}$$

$$\hat{\rho}_{+,th} = \sqrt{\frac{\omega_z}{\omega_+ - \omega_-}}\hat{z}_{th} \tag{2.67}$$

$$\hat{\rho}_{-,th} = \hat{\rho}_{+,th} \quad . \tag{2.68}$$

[13] Due to the peculiarities of the magnetron mode, the energy of the magnetron mode actually increases, but since the phase-space is reduced for lower amplitudes, the term cooling is appropriate.

The axial damping time constants are typically on the order of seconds. Therefore, the cooling drives have to be applied for tens of seconds, and the coupling frequency has to be known with a precision of much better than 1 Hz for the cooling to be effective. This is impractical, because amplitude-dependent frequency shifts (section 2.10) can, for a radially excited ion, be larger than 1 Hz.

To ensure that the coupling resonance is hit regardless of frequency shifts, the coupling drive can be applied in short (hundred ms) pulses. The Fourier spectrum of such pulses is wide enough to encompass possible frequency shifts. Further, the pulse length can be carefully calibrated to cause half a Rabi oscillation (π-pulse). This pulse swaps the cyclotron action with the axial action (or the magnetron action with the axial action), which in principle allows one pulse to cool the cyclotron (magnetron) mode to the thermal limit. But in practice, the frequency shifts prevent an exact swapping of the action in a π-pulse, so each cooling pulse has to be repeated a few times, with a suitable waiting time in between to let the energy in the axial mode decay.

This is the cooling scheme employed at the FSU trap. The π-pulses are further used to transfer phase information from the radial modes to the axial mode, which is the basis of the cyclotron frequency measurement scheme (the *PnP technique* [16]) at the FSU trap.

At THe-Trap, the imprecise knowledge of the coupling frequency is overcome by sweeping the coupling drive across the coupling resonance. We experimentally observed that, over a wide range of coupling strengths and sweep-rates, these sweeps lead to a complete transfer of cyclotron energy to the axial mode (and back). Effectively, they act as π-pulses, which is surprising, since π-pulses have to be carefully calibrated. We realized[14] that this behavior is the classical analogy of the adiabatic rapid passage [82]: When a coupling force is slowly (compared to the Rabi frequency) increased from zero, held for a few Rabi oscillations, and decreased back to zero, the action of the coupled modes is swapped. Starting with an off-resonant coupling drive and sweeping over the coupling resonance is equivalent to slowly turning the coupling force on and off, and this leads to adiabatic rapid passage. A simulated example, obtained through the rotating wave approximation, is shown in Figure 2.11.

The adiabatic rapid passage allows efficient cooling without having to calibrate the coupling amplitude. However, it requires relatively strong drives. This can be a disadvantage, for example at the FSU trap, where the cryoelectric filters do not have a good thermal connection to the liquid helium bath of the trap, and where differential heating of the filter boards has caused significant frequency shifts in the past [48].

Further coupling schemes are employed at other traps: When the field given by $p_{2,-2} = xy$ is modulated at the *sideband frequency*[15] $\omega_+ + \omega_-$, it causes Rabi oscillations between the two radial modes. This allows convenient cyclotron frequency measurements, because in the absence of trap imperfections (and even in the presence of many significant imperfections!) the sideband frequency is equal to the free space cyclotron frequency ω_c.

Yet other spatial field configurations can be used to couple modes. The octupolar potential $p_{3,3} = x^3 - 3xy^2$ is being investigated as an alternative to $p_{2,-2}$ for sideband-frequency

[14] All credit is due to Jochen Ketter, who immediately saw the connection to the Landau–Zener–Stückelberg effect in two-level quantum systems.

[15] The name *sideband frequency* can be misleading: There are of course many sideband frequencies, but most of them have other names. At THe-Trap, we call the frequency $\omega_+ - \omega_z$ *cyclotron coupling frequency*, and $\omega_- + \omega_z$ *magnetron cooling frequency*.

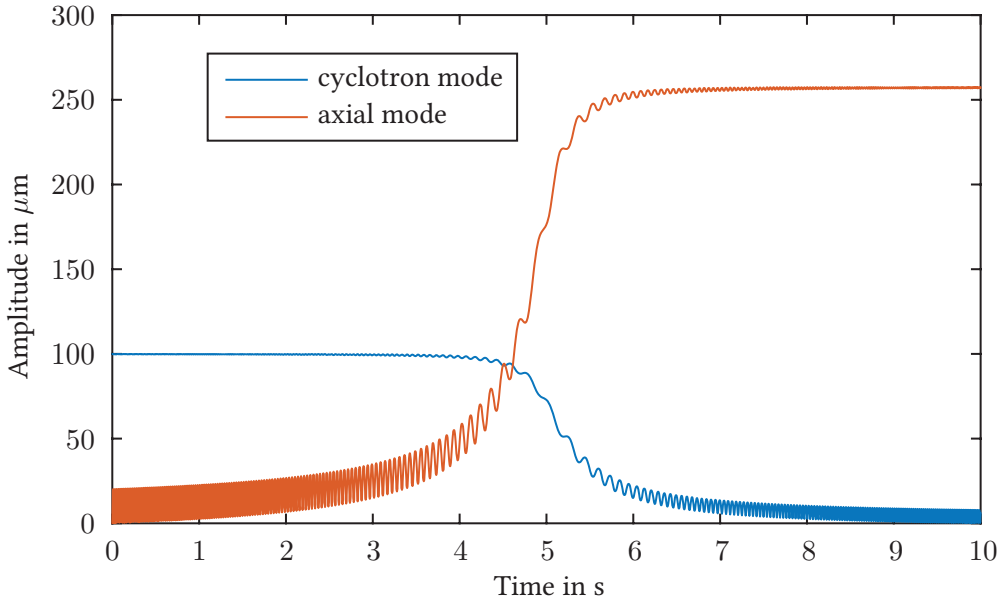

Figure 2.11.: Simulation of adiabatic rapid passage between the cyclotron mode and the axial mode. The coupling drive is swept linearly across the coupling resonance, starting 50 Hz below the resonance and increasing in frequency with 10 Hz/s. For a more realistic simulation that includes damping and anharmonicity, see Figure B.1.

measurements [75]. The octupolar potential given by $p_{3,-2} = xyz$ could even be used to couple all three modes together simultaneously, but the rotating wave approximation quickly shows that the resulting evolution of the ion motion is strongly nonlinear, which makes practical applications doubtful.

2.10. Trap imperfections

In a real Penning trap, the magnetic field is not perfectly homogeneous, and the electric field is not an ideal quadrupolar field. The axes of the fields may be slightly misaligned, and the ion motion (even at the low energies typical for Penning traps) is perturbed by relativistic effects. As this section will show, imperfections lead to systematic shifts of the ion frequencies. While all shifts can be estimated and corrected for, the uncertainties in the shift corrections give rise to the *systematic error* of the measurement. This fundamentally limits the measurement uncertainty[16].

As will be described in section 3.6, THe-Trap employs a feedback loop that changes the ring voltage to keep the axial frequency constant ("frequency lock"). Therefore, shifts of the axial frequency change the ring voltage, which in turn changes the radial frequencies. More generally,

[16] Most systematic effects can be reduced by using lower ion amplitudes, which leads to a lower signal-to-noise ratio and therefore to an increased statistical error. Typically, the optimal settings make the statistical error of a measurement as large as the systematic error.

if a systematic effect causes the ion frequencies to shift by $\Delta\omega_z$, $\Delta\omega_+$, and $\Delta\omega_-$, then under axial frequency lock, the shifts of the radial frequencies can be shown to be

$$\Delta\hat{\omega}_\pm = \Delta\omega_\pm \pm \frac{\omega_z}{\omega_+ - \omega_-}\Delta\omega_z \quad . \tag{2.69}$$

2.10.1. Trap tilt and ellipticity

Tilting the trap electrodes around the y-axis by an angle θ can be approximated as changing the electric field by

$$\Delta\vec{E} = -3K_2\,\theta \begin{pmatrix} z \\ 0 \\ x \end{pmatrix} - 3K_2\,\theta^2 \begin{pmatrix} x \\ 0 \\ -z \end{pmatrix} + \mathcal{O}(\theta^3) \quad . \tag{2.70}$$

Both field terms can be shown to shift the ion frequencies by amounts proportional to θ^2.

The first term does so via back-action. Consider the modified cyclotron motion of the ion: It leads to a non-resonant force in the axial direction. This causes a forced z-motion with frequency ω_+ and an amplitude of order θ (Equation A.22). This motion back-acts with a force of order θ^2 on the modified cyclotron mode. Using the rotating wave approximation, the back-action can be shown to shift the modified cyclotron frequency. The argument can be expanded to all modes, and the resulting frequency shifts stated as

$$\begin{aligned}
\Delta\omega_{z,\theta_1} &= -\frac{9}{4}\frac{\omega_-}{(\omega_+ - 2\omega_-)}\omega_z\theta^2 && \approx 0 \\
\Delta\omega_{+,\theta_1} &= \frac{9}{2}\frac{\omega_-^2}{(\omega_+ - \omega_-)(\omega_+ - 2\omega_-)}\omega_+\theta^2 && \approx 0 \\
\Delta\omega_{-,\theta_1} &= \frac{9}{2}\frac{\omega_+^2}{(\omega_+ - \omega_-)(2\omega_+ - \omega_-)}\omega_-\theta^2 && \approx \frac{9}{4}\omega_-\theta^2 \\
\Delta\hat{\omega}_{+,\theta_1} &= 0 \\
\Delta\hat{\omega}_{-,\theta_1} &= \frac{9}{2}\frac{\omega_+(\omega_+ + \omega_-)}{(\omega_+ - 2\omega_-)(2\omega_+ - \omega_-)}\omega_-\theta^2 && \approx \frac{9}{4}\omega_-\theta^2 \quad .
\end{aligned} \tag{2.71}$$

The final approximation neglects terms of $\mathcal{O}(\omega_-/\omega_+)$ to show that the electric field of order θ mainly shifts the magnetron frequency.

The second term in Equation (2.70) directly causes resonant forces of order θ^2, which shift the frequencies by

$$\begin{aligned}
\Delta\omega_{z,\theta_2} &= -\frac{3}{4}\,\omega_z\theta^2 \\
\Delta\omega_{\pm,\theta_2} &= \pm\frac{3}{2}\frac{\omega_+\omega_-}{\omega_+ - \omega_-}\theta^2 \approx \pm\frac{3}{2}\,\omega_-\theta^2 \\
\Delta\hat{\omega}_{\pm,\theta_2} &= 0 \quad .
\end{aligned} \tag{2.72}$$

This is mainly due to an effective reduction of the trapping field strength[17]. When the ring voltage is adjusted (by the frequency lock) to account for the effective reduction in the trapping field strength, the shifts of the radial frequencies vanish.

Combined, the frequency shifts can be stated as

$$\begin{aligned}
\Delta\omega_{z,\theta} &= -\frac{3}{4}\frac{\omega_+ + \omega_-}{\omega_+ - 2\omega_-}\omega_z\theta^2 && \approx -\frac{3}{4}\omega_z\theta^2 \\
\Delta\omega_{+,\theta} &= \frac{3}{2}\frac{\omega_-(\omega_+ + \omega_-)}{(\omega_+^2 - 3\omega_+\omega_- + 2\omega_-^2)}\omega_+\theta^2 && \approx \frac{3}{2}\omega_-\theta^2 \\
\Delta\omega_{-,\theta} &= \frac{3}{2}\frac{\omega_+(\omega_+ + \omega_-)}{(2\omega_+^2 - 3\omega_+\omega_- + \omega_-^2)}\omega_-\theta^2 && \approx \frac{3}{4}\omega_-\theta^2 \\
\Delta\hat{\omega}_{+,\theta} &= 0 \\
\Delta\hat{\omega}_{-,\theta} &= \frac{9}{2}\frac{\omega_+(\omega_+ + \omega_-)}{(\omega_+ - 2\omega_-)(2\omega_+ - \omega_-)}\omega_-\theta^2 && \approx \frac{9}{4}\omega_-\theta^2 \quad .
\end{aligned} \tag{2.73}$$

At typical angles of $0.05^\circ - 0.50^\circ$, the shifts due to trap-tilt are the most severe shifts in high-precision Penning traps [83]. Assuming other shifts are negligible or already corrected for, the tilt angle θ (often called the *magnetron angle*) can be conveniently calculated from the measured (shifted) frequencies $\bar{\omega}_+, \bar{\omega}_-, \bar{\omega}_z$ [56, 57] as

$$\sin\theta \approx \frac{2}{3}\sqrt{\frac{2\bar{\omega}_+\bar{\omega}_-}{\bar{\omega}_z^2} - 1} \quad . \tag{2.74}$$

A shift of a similar nature arises when the trap is elliptic instead of cylindrical. To first order, the trap ellipticity can be parametrized as [57]

$$\Delta\vec{E} = -\frac{m}{2q}\omega_z^2\epsilon\begin{pmatrix} -x \\ y \\ 0 \end{pmatrix} \quad . \tag{2.75}$$

The ellipticity mainly affects the magnetron mode and shifts its frequency by [57]

$$\Delta\omega_{-,\epsilon} = \Delta\hat{\omega}_{-,\epsilon} = -\frac{1}{2}\epsilon\omega_- \quad . \tag{2.76}$$

Trap tilt and ellipticity are special cases of frequency shifts that are caused by the quadrupolar polynomials $p_{2,m}$. These frequency shifts, although all second order in the imperfection size, are the most severe shifts in a Penning trap. However, a general (and exact) treatment [57] shows that when the shifted eigenfrequencies $\bar{\omega}_+, \bar{\omega}_-, \bar{\omega}_z$ are summed in quadrature, the result is equal to the (unshifted) free-space cyclotron frequency:

$$\bar{\omega}_+^2 + \bar{\omega}_-^2 + \bar{\omega}_z^2 = \omega_c^2 \quad . \tag{2.77}$$

This equation, called the Brown–Gabrielse invariance theorem [63], is true for *any size* of the quadrupolar imperfections, as long as they are small enough to allow stable trapping.

[17] The second term in Equation (2.70) is derived from a potential that is proportional to $\theta^2\left(\frac{1}{2}p_{2,2} - p_{2,0}\right)$. The polynomial $p_{2,2}$ is equivalent to trap ellipticity. Ellipticity can be shown to lead to a quadratic shift (also via back-action), which here is a shift of order θ^4 and can be neglected. The term $p_{2,0}$ has the same spatial configuration as the main trapping field. It therefore changes the trapping field strength.

2.10.2. Other electric field imperfections

In the parametrization of the electric field given by Equation (2.47), trap tilt and ellipticity can be thought of as the lowest-order imperfections. Higher order imperfections lead to frequency shifts that depend on the ion's amplitudes [57].

For typical imperfection magnitudes and ion amplitudes, the frequency shifts caused by higher order imperfections are smaller than those caused by lower order imperfections. Using a symmetry argument [84], imperfections of the form $p_{l,m}$ with l odd can be shown to be heavily suppressed and inconsequential. Imperfections with $m \neq 0$ are minimized through trap construction techniques (the electrodes are turned on a lathe, which ensures good rotational symmetry). In practice, the only relevant shifts left are those caused by $p_{4,0}$ and $p_{6,0}$. The frequency shifts caused by these imperfections are typically stated using the C_l parametrization (Equation 2.48). But, noting that both parametrizations are connected via

$$K_l = \frac{U_0}{2}\frac{C_l}{d^l} \quad , \tag{2.78}$$

the well-known frequency shift formulas [57, 85] can be reformulated using the more suitable K_l parametrization:

$$\Delta\omega_{z,K_4} = \frac{3K_4}{4K_2}\omega_z\left(-2\hat{\rho}_+^2 - 2\hat{\rho}_-^2 + \hat{z}^2\right) \tag{2.79}$$

$$\Delta\omega_{\pm,K_4} = \pm\frac{3K_4}{2K_2}\frac{\omega_-\omega_+}{\omega_+ - \omega_-}\left(\hat{\rho}_\pm^2 + 2\hat{\rho}_\mp^2 - 2\hat{z}^2\right) \tag{2.80}$$

$$\Delta\hat{\omega}_{\pm,K_4} = \mp\frac{3K_4}{2K_2}\frac{\omega_-\omega_+}{\omega_+ - \omega_-}\left(\hat{\rho}_\pm^2 + \hat{z}^2\right) \tag{2.81}$$

$$\Delta\omega_{z,K_6} = \frac{45K_6}{48K_2}\omega_z\left(3\hat{\rho}_+^4 + 12\hat{\rho}_+^2\hat{\rho}_-^2 + 3\hat{\rho}_-^4 - 6\hat{\rho}_+^2\hat{z}^2 - 6\hat{\rho}_-^2\hat{z}^2 + \hat{z}^4\right) \tag{2.82}$$

$$\Delta\omega_{\pm,K_6} = \mp\frac{45K_6}{24K_2}\frac{\omega_+\omega_-}{\omega_+ - \omega_-}\left(\hat{\rho}_\pm^4 + 6\hat{\rho}_+^2\hat{\rho}_-^2 + 3\hat{\rho}_\mp^4 - 6\hat{\rho}_\pm^2\hat{z}^2 - 12\hat{\rho}_\mp^2\hat{z}^2 + 3\hat{z}^4\right) \tag{2.83}$$

$$\Delta\hat{\omega}_{\pm,K_6} = \pm\frac{45K_6}{12K_2}\frac{\omega_+\omega_-}{\omega_+ - \omega_-}\left(\hat{\rho}_\pm^4 + 3\hat{\rho}_+^2\hat{\rho}_-^2 + 3\hat{\rho}_\mp^2\hat{z}^2 - \hat{z}^4\right) \tag{2.84}$$

In these formulas, K_2 can be approximated as $K_2 = \frac{m}{2q}\omega_z^2$. Note that these formulas are a special case of a general treatment that allows to find a closed formula for the frequency shifts caused by *all* rotational symmetric imperfections [86, 87].

2.10.3. Magnetic field imperfections

As with the electric field, the magnetic field inside the trap is source-free, so that $\vec{\nabla}\cdot\vec{B} = 0$ and $\vec{\nabla}\times\vec{B} = 0$. Therefore, the magnetic field can be expressed using a scalar potential Ψ with $\Delta\Psi = 0$ and $\vec{B} = -\vec{\nabla}\Psi$.

Similar to the electric potential Φ, the magnetic potential Ψ can be expanded using harmonic polynomials. However, since the non-rotationally symmetric polynomials can be shown to not

lead to first-order frequency shifts [84], it suffices to only consider the rotationally symmetric polynomials $p_{l,0}$:

$$\Psi(x,y,z) = -\sum_l B_l \frac{1}{l+1} p_{l+1,0}(x,y,z) \quad . \tag{2.85}$$

The scaling factor and the offset in the indexing are due to historical reasons. The B_1 term does not lead to a first-order frequency shift, since the effects on the cyclotron phase average out over an axial period[18]. Typically, only B_2 leads to significant frequency shifts, which can be shown to be [57, 85]

$$\Delta\omega_{z,B_2} = \frac{B_2}{2B_0}\frac{\omega_+ + \omega_-}{\omega_z}\left(\omega_+\hat{\rho}_+^2 + \omega_-\hat{\rho}_-^2\right) \tag{2.86}$$

$$\Delta\omega_{\pm,B_2} = \pm\frac{B_2}{2B_0}\frac{\omega_+ + \omega_-}{\omega_+ - \omega_-}\left(\omega_\pm\hat{z}^2 - \omega_\pm\hat{\rho}_\pm^2 - (\omega_+ + \omega_-)\,\hat{\rho}_\mp^2\right) \tag{2.87}$$

$$\Delta\hat{\omega}_{\pm,B_2} = \pm\frac{B_2}{2B_0}\frac{\omega_+ + \omega_-}{\omega_+ - \omega_-}\left(\omega_\pm\hat{z}^2 - \omega_\pm\hat{\rho}_\mp^2\right) \tag{2.88}$$

Again, these formulas are special cases of a general formula that can be derived in a perturbation theory approach [86, 87].

2.10.4. Mixed effects

The lowest odd-order effects, which were neglected in the previous sections, can become significant when they interact with each other. For example, a small surface charge on one of the endcaps can lead to a small, (approximately) linear gradient K_1 superimposed with the main trapping field. In an ideal trap, this gradient only shifts the axial center of the ion motion by

$$z_{\text{offset}} = -\frac{q}{m\omega_z^2}K_1 \quad . \tag{2.89}$$

However, when the magnetic field also has a gradient in the z-direction, signified by B_1, the combination of these effects shifts the free-space cyclotron frequency by

$$\Delta\omega_{c,K_1\cdot B_1} = -\frac{q^2}{m^2\omega_z^2}K_1 B_1 \tag{2.90}$$

Another shift, often called $C_1 \cdot C_3$-shift ($K_1 \cdot K_3$-shift in the notation of this thesis), arises when electrodes are intentionally biased asymmetrically [57]. In the ideal case, the axial frequency changes by an amount that is proportional to the square of the asymmetric bias voltage [57]. Deviations from the ideal case can be used to measure unintentional voltage offsets caused by contact potentials or thermal potentials [56, 89], but in the presence of localized surface patch potentials, the results can be difficult to interpret.

[18] See section 2.6.2 in [88] for an estimate of the second-order shift.

2.10.5. Relativistic shifts

Considering how small typical ion amplitudes are (a few ten μm for an excited ion), the significance of relativistic shifts may seem surprising. However, combined with the reduced cyclotron frequency (tens of MHz), the typical speed of an excited ion can be on the order of 10 km/s, so that due to the high measurement precision, relativistic effects become relevant.

As an intuitive model, the relativistic effects can be treated as increase of the ion mass. This leads to shift-formulas that are correct within a factor of two [90]. A full treatment, using either a quantum-mechanical [57] or classical [90] framework, leads to first-order shift formulas

$$\Delta\omega_{z,\mathrm{rel}} = -\frac{\omega_z}{4c^2}\left(\omega_+^2\hat{\rho}_+^2 + \omega_-^2\hat{\rho}_-^2 + \frac{3}{4}\omega_z^2\hat{z}^2\right) \tag{2.91}$$

$$\Delta\omega_{\pm,\mathrm{rel}} = \mp\frac{1}{2c^2}\frac{\omega_\pm^2}{\omega_+ - \omega_-}\left(\omega_\pm^2\hat{\rho}_\pm^2 + 2\omega_\mp^2\hat{\rho}_\mp^2 + \frac{1}{2}\omega_z^2\hat{z}^2\right) \tag{2.92}$$

$$\begin{aligned}\Delta\hat{\omega}_{+,\mathrm{rel}} = -\frac{1}{2c^2}\frac{\omega_+^2}{\omega_+ - \omega_-}\Bigg[&\omega_+^2\hat{\rho}_+^2\left(1 + \frac{\omega_-}{\omega_+}\right) + 2\omega_-^2\hat{\rho}_-^2\left(1 + \frac{\omega_-}{2\omega_+}\right) + \\ &\frac{1}{2}\omega_z^2\hat{z}^2\left(1 + \frac{3\omega_-}{2\omega_+}\right)\Bigg]\end{aligned} \tag{2.93}$$

$$\begin{aligned}\Delta\hat{\omega}_{-,\mathrm{rel}} = \frac{1}{2c^2}\frac{\omega_+\omega_-}{\omega_+ - \omega_-}\Bigg[&\omega_-^2\hat{\rho}_-^2\left(1 + \frac{\omega_-}{\omega_+}\right) + \omega_+^2\hat{\rho}_+^2\left(1 + 2\frac{\omega_-}{\omega_+}\right) + \\ &\frac{3}{4}\omega_z^2\hat{z}^2\left(1 + \frac{2\omega_-}{3\omega_+}\right)\Bigg] \quad .\end{aligned} \tag{2.94}$$

2.10.6. Image charge shift

An ion inside the trap induces image charges in the trap electrodes. The image charges, in turn, attract the ion towards the nearest electrode (and therefore away from the trap center). This leads to frequency shifts that depend mainly on the trap geometry and the total charge of the trapped ion [15, 91]. A more detailed treatment gives the formulas

$$\Delta\omega_{z,\mathrm{i.c.}} = -\frac{q^2}{me}\frac{E_z'}{2\omega_z} \tag{2.95}$$

$$\Delta\omega_{\pm,\mathrm{i.c.}} = \mp\frac{q^2}{me}\frac{E_\rho'}{\omega_+ - \omega_-} \approx \mp\frac{q}{e}\frac{E_\rho'}{B_0} \tag{2.96}$$

$$\Delta\hat{\omega}_{\pm,\mathrm{i.c.}} = \mp\frac{q^2}{2me}\frac{2E_\rho' + E_z'}{\omega_+ - \omega_-} \approx \mp\frac{q}{e}\frac{2E_\rho' + E_z'}{2B_0} \quad , \tag{2.97}$$

where e is the elementary charge, B_0 the strength of the magnetic trapping field, and E_ρ' and E_z' are constants that depend on the trap geometry. These constants can be found with finite element simulations [70] or a series-solution of the image charge problem [91]. They strongly depend on the trap size d, approximately scaling with $1/d^3$. For THe-Trap, a finite element simulation resulted in [70]

$$E_\rho' = 0.0423(9)\,\mathrm{V/m^2} \tag{2.98}$$

$$E_z' = 0.0804(13)\,\mathrm{V/m^2} \quad . \tag{2.99}$$

For the FSU trap, the constants were found with a series-solution as [91] (converted to the notation used in this thesis):

$$E'_\rho = 0.002572(9)\,\mathrm{V/m^2} \tag{2.100}$$
$$E'_z = 0.004699(9)\,\mathrm{V/m^2} \quad . \tag{2.101}$$

2.10.7. Ion–ion interaction

At the FSU trap, two ions are trapped simultaneously: one ion in the center of the trap (for precision measurements), and the other ion parked on a large cyclotron radius $\hat{\rho}_{+,\mathrm{k}}$. The interaction between the inner ion and the outer ion can be treated in two parts: Resonant interactions, and non-resonant interactions.

A first, possible resonant interaction is the cyclotron motion of the outer ion acting as dipolar drive on the inner ion. Since the frequency difference between the two ions' cyclotron modes is typically large, the resulting driven cyclotron motion of the inner ion has negligible amplitude [92].

Another resonant interaction is that the magnetron motion of the outer ion acts on the magnetron motion of the inner ion. The magnetron frequency is only a weak function of m/q, therefore the magnetron frequencies of the two trapped ions typically differ by less than 1 Hz. However, since the magnetron *amplitudes* of both ions are ideally near the cooling limit, the effective forces between the ions, and therefore any associated frequency shifts, are typically inconsequential[19].

Other interactions are second-order. For example, the motion of the *inner* ion can non-resonantly excite the outer ion, which leads to that ion back-acting on the inner ion. Again, due to the strong dependence on the frequency difference, this effect is heavily suppressed in the cyclotron mode and axial mode. For the magnetron mode, the shift can be neglected as long as magnetron radius of the inner ion is small [92].

The non-resonant interactions can be summarized by modeling the outer ion as a continuous *ring-of-charge*. This ring-of-charge modifies the potential near the center of the trap. Using standard techniques from classical electrostatics, the modification of the potential can be expressed using the rotationally symmetric harmonic polynomials $p_{l,0}$. Due to axial reflection symmetry, only the even polynomials have to be considered. The effect of $p_{0,0}$ is inconsequential to the ion motion, and the effect of $p_{2,0}$ is equivalent to a change of the ring voltage. It therefore does not influence the measurement of the free space cyclotron frequency ω_c. Only higher order effects, such as $p_{4,0}$ and $p_{6,0}$, affect the cyclotron frequency determination. The most relevant[20]

[19] This is not always true: The magnetron frequency of the outer ion is shifted by anharmonic effects coupling to $\hat{\rho}_{+,\mathrm{k}}$. In the worst case, these shifts can cancel the natural frequency difference, which leads to further resonant enhancement of the coupling between the ions. This is one of the reasons why at the FSU trap, every mass measurement is repeated several times, using different reference ions, different trap parameters, or both.

[20] These formulas are tailored to the measurement method employed at the FSU trap, where the magnetron frequency is calculated from trap parameters, and where the axial mode and the reduced cyclotron mode are measured by only exciting the respective mode.

ion-ion shifts (the index "ii" stands for ion-ion) are given by

$$\Delta\omega_{z,\mathrm{ii}} = \Omega_z \left[\frac{9}{16} \left(\frac{\hat{z}_\mathrm{i}}{\hat{\rho}_{+,\mathrm{k}}} \right)^2 - \frac{75}{128} \left(\frac{\hat{z}_\mathrm{i}}{\hat{\rho}_{+,\mathrm{k}}} \right)^4 \right] \tag{2.102}$$

$$\Delta\omega_{+,\mathrm{ii}} = \frac{\omega_{z,\mathrm{i}}}{\omega_{+,\mathrm{i}}} \Omega_z \left[\frac{9}{16} \left(\frac{\hat{\rho}_{+,\mathrm{i}}}{\hat{\rho}_{+,\mathrm{k}}} \right)^2 + \frac{75}{128} \left(\frac{\hat{\rho}_{+,\mathrm{i}}}{\hat{\rho}_{+,\mathrm{k}}} \right)^4 \right] \quad , \tag{2.103}$$

with a single i denoting the inner ion, a single k denoting the outer ion, and with Ω_z defined as

$$\Omega_z = \frac{1}{\omega_{z,\mathrm{i}}} \frac{q_\mathrm{i}\, q_\mathrm{k}}{4\pi\epsilon_0 m_\mathrm{i}\, \hat{\rho}_{+,\mathrm{k}}^3} \quad . \tag{2.104}$$

2.10.8. Ring modulation

The axial frequency depends on the $p_{2,0}$ component of the electric field, which in turn mainly depends on the ring voltage. For hyperbolic traps, the simplification

$$\omega_z \propto \sqrt{U_0} \tag{2.105}$$

is often used, with U_0 denoting the ring voltage. A small (compared to U_0) and slow (compared to ω_z) modulation of the ring voltage (which is part of the detection at THe-Trap, subsection 2.8.1) acts as a frequency modulation of the axial frequency. However, the non-linearity of the square-root lowers the *average* axial frequency. This is a second order effect, and it can be shown to be [57, 87]

$$\Delta\omega_{z,\mathrm{mod}} = -\omega_z \frac{\epsilon^2}{16} \quad , \tag{2.106}$$

with $\epsilon = U_\mathrm{mod}/U_0$ as the ratio of the modulation amplitude U_mod and the ring voltage.

If the ring voltage is modulated with a frequency that is much higher than the motional frequencies of the ion, the modulation can act as a pseudo-potential, comparable to a Paul trap [56].

2.10.9. Ion detection

Shifts caused by the ion detection depend on the detection method. At the FSU trap, the coil-pushing shift given by Equation (2.40) has to be considered, and another, subtle effect can be caused by differential voltage drifts subsection 4.5.3. At THe-Trap, the coil-pushing shift is negligible, but the *locked loop* that stabilizes the axial frequency can lead to shifts. This is described in more detail in section 3.6.

2.10.10. Shifts of the cyclotron frequency ratio

The individual frequency shifts can be used to calculate the ω_c-shift of each ion. Subsequently, the shift of the the cyclotron frequency ratio $R = \omega_{\mathrm{c}_1}/\omega_{\mathrm{c}_2}$ can be calculated, which (up to an integer fraction) determines the shift of the mass ratio (see Equation 2.3). The size of the R-shift

Table 2.1.: Comparison of THe-Trap and the FSU trap. (B_0 of THe-Trap is the pre-quench value.)

Property	Symbol	THe-Trap	FSU trap
magnetic field strength	B_0	5.258 T	8.530 T
ring voltage range	U_R	0 V to -100 V	0 V to -24 V
trap size	d	2.11 mm	5.49 mm
endcap-to-center distance	z_0	2.29 mm	6.00 mm
ring-to-center distance	ρ_0	2.77 mm	6.96 mm
axial frequency	f_z	4.058 MHz	213 kHz
detector Q-value	Q	800	30 000
m/q range		1 u/e to 3 u/e	10 u/e to 42 u/e

strongly depends on the nature of the ω_c shift. For example, if only one of the frequencies is shifted, e.g. $\bar{\omega}_{\mathrm{c}_1} = \omega_{\mathrm{c}_1} + \Delta\omega$, then R is shifted to

$$\bar{R} = \frac{\omega_{\mathrm{c}_1} + \Delta\omega}{\omega_{\mathrm{c}_2}} = R\left(1 + \frac{\Delta\omega}{\omega_{\mathrm{c}_1}}\right) \quad . \tag{2.107}$$

Fortunately, the frequencies ω_{c_1} and ω_{c_2} are often shifted by similar amounts (*common mode* shifts). Using a Taylor series, it can be shown that for $R \approx 1$, the effect of a common-mode shift $\Delta\omega$ is suppressed by a factor $R - 1$:

$$\bar{R} = \frac{\omega_{\mathrm{c}_1} + \Delta\omega}{\omega_{\mathrm{c}_2} + \Delta\omega} \approx R\left(1 + \frac{\Delta\omega}{\omega_{\mathrm{c}_2}}(R-1)\right) \quad . \tag{2.108}$$

On the other hand, an exceptionally troublesome class of shifts is given by those shifts that are proportional to the charge of the ion, such as the image-charge shift. Modeling these shifts as $\Delta\omega = q \cdot \xi$, the shift to R can be shown to be

$$\bar{R} = \frac{\omega_{\mathrm{c}_1} + q_1\xi}{\omega_{\mathrm{c}_2} + q_2\xi} = \frac{\frac{q_1}{m_1}B\left(1 + \frac{m_1\xi}{B}\right)}{\frac{q_2}{m_2}B\left(1 + \frac{m_2\xi}{B}\right)} \tag{2.109}$$

$$\approx R\left(1 + \frac{\xi}{B}(m_1 - m_2)\right) \quad . \tag{2.110}$$

This shift is proportional to the mass difference of the ions. This is troubling, because a standard test of a spectrometer's precision is to measure the well-known R of two charge states of the same ion, for example $^{12}\mathrm{C}^{4+}$ vs $^{12}\mathrm{C}^{5+}$ [93]. In those measurements, the $q \cdot \xi$ shifts are zero, and therefore easily overlooked.

3. The THe-Trap Experiment

THe-Trap was originally designed and built at the University of Washington under the name UW-PTMS [47]. It was moved to the Max-Planck-Institute for Nuclear Physics in Heidelberg in 2008, where it was modified and commissioned [52]. The experimental setup has been described before [47, 52, 53, 94], so only a brief description is given here. Emphasis is placed on those components that were modified since the last description [94].

3.1. Superconducting magnet

The 5.9 T superconducting magnet system (Figure 3.1) was designed by R. S. Van Dyck Jr. [58] and built by Nalorac Cryogenic Corporation. The magnet exhibited an exceptional temporal stability better than 2 parts in 10^{12} per hour (2 ppt/h) when it was installed in Seattle [95]. In 2009, the magnet was energized in Heidelberg to approximately 5.258 T. Due to the absence of a suitable NMR-probe, the magnet was not shimmed [54]. Instead, the shim-settings used in Seattle were scaled down to the reduced main field. Unfortunately, air-ice blocked the cryogenic connector to the superconducting magnet coils, and it was not possible to shim the magnet without quenching it. The relative homogeneity was later determined to be $1 \cdot 10^{-5}$ over a 1 cm^3 sample volume, a factor of 500 worse than the design specification of the magnet [96]. After the magnetic field had settled in 2010, magnetic field measurements carried out with ions showed a $\vec{B}$-field stability in the order of 10 ppt/hr. While this was slightly worse than the Seattle value, it was still excellent compared to other magnets. However, the measurements revealed a pronounced dependence on external pressure (1.8 ppb/mbar) [53], which may be caused by movement of the trap structure in the inhomogeneous $\vec{B}$-field.

One design feature that enables the exceptional $\vec{B}$-field-stability is the magnet's self-shielding coil [58, 97, 98]. Changes of the overall magnetic field, either due to flux-creep of the main coil [99], or due to changes of the z-component of the ambient $\vec{B}$-field[1], induce a current in the self-shielding coil, such that field variations in the center of the magnet are suppressed, in this case, by a factor of 180 [94]. This passive shielding system is augmented by an external, active system, which has an additional shielding factor of 3 [94].

Another design feature is the *cold bore* of the magnet: The liquid helium (LHe) that cools the superconducting magnet coils also cools the inside of the bore, and thereby the experimental apparatus. The level and pressure of the LHe in the bore are stabilized with an external system. This keeps the temperature in the bore constant [94], which in turn reduces $\vec{B}$-field variations caused by temperature-dependent susceptibilities of materials near the magnet center. However,

[1] To first order, changes in the x- or y-component of the $\vec{B}$-field only tilt the field, but don't change the magnitude. Variations of the ambient $\vec{B}$-field can be caused, for example, by ferromagnetic material being moved in adjacent labs, or by changes in the ionosphere currents [100].

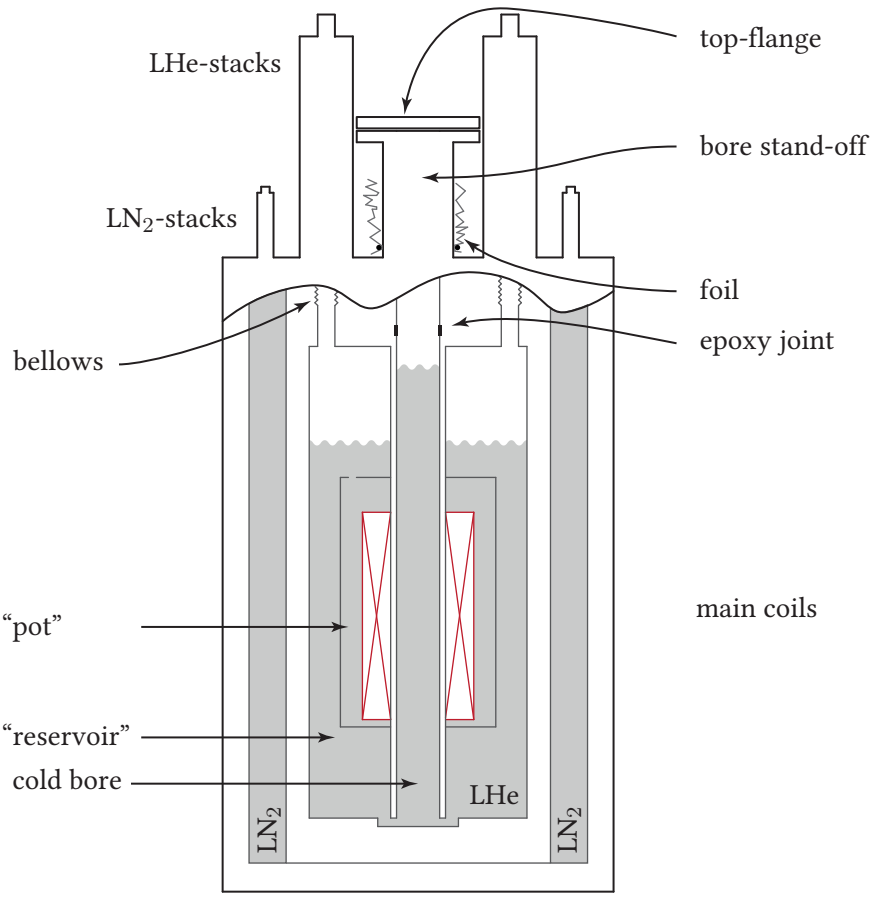

Figure 3.1.: Sketch of the magnet used at THe-Trap. The LHe level and pressure inside the bore are stabilized with an external feedback system (not shown). A tube made from cryogenic-rated foil is attached to the bore stand-off. It can be partly pulled above the top flange, pressed closed (by hand), and inflated with helium gas to prevent air from entering the bore when the top flange is open.

when the top-flange of the cold bore is opened, air can fall into the bore and form *air ice*. In 2011, the accumulated air-ice blocked part of the bore, and the ice had to be chiseled out[2]. We later installed cryogenic-rated NOWOFLON FEP foil [102] on the bore stand-off (see Figure 3.1), so that we can establish a helium-atmosphere around the top of the bore.

In early 2015, the magnet's cryogens were not refilled in time, which led to a quench. During the subsequent servicing and leak-checking of the magnet, the LHe-reservoir and the bore had to be temperature cycled between 77 K and room-temperature. Unfortunately, the cold bore is

[2] Air ice is paramagnetic [101] and floats near the point of strongest $\vec{B}$-field. The chiseled air-ice chips can be conveniently fished out with an aluminum cup on a long rod. PENTATRAP uses a similar magnet design and faced the same problem [80, 102].

constructed from two tubes that are epoxied together, and the temperature cycling caused a leak to develop at the epoxy-joint. Subsequent tries to close the leak with additional epoxy were successful at room temperature, but the leak opened up again at 77 K. At the end of the second attempt, as the magnet was warming up, the joint finally broke off completely. The lower end of the bore, and everything attached to it (the magnet coils, the LHe-reservoir), crashed down onto the 20 K shield inside the magnet. Fortunately, it was possible to repair the joint using the original epoxy (Armstrong A12). During the lengthy repair-process, we were also able to replace most of the O-Rings of the magnet system with new VITON O-Rings. Further, the bolts of the bottom access flange of the magnet (not shown in Figure 3.1) were replaced with spring-loaded studs to serve as an additional overpressure relief path for the vacuum space.

During the repair process we realized how badly the brown anodization layer of the magnet's top-surface was corroded. The reason for the corrosion was that this surface had not been kept dry after cryogen filling. The corroded patch was sanded down and coated with a spray-on epoxy. Unfortunately, the corroded patch extended to contact area between the LN_2-stacks and the top surface. The vacuum-tight seal between the LN_2 stacks and the top surface is made with a multi-O-ring assembly just below the magnet's top surface, and the innermost O-rings are likely damaged by the corrosion. These O-rings were not replaced, because the replacement would have required to cut weld-seams at the top of the LHe-stacks[3]. It is crucial to avoid further corrosion by making sure the top surface of the magnet stays dry. Should the magnet vacuum deteriorate in the future, the problematic O-rings can be leak-checked by pumping on the magnet vacuum, and spraying He gas around the bottom of the LN_2-stacks[4].

In the summer of 2015, the magnet was re-energized to 5.721 T, and shimmed to a relative homogeneity of approximately $1 \cdot 10^{-7}$ over a 1 cm^3 volume.

3.2. Vacuum setup and ion sources

THe-Trap features an external ion source to create low-charged ions from gases [47]. The ion source is located outside of the magnet's cryostat, approximately 1.6 m above the trap region (Figure 3.2). The barium dispenser cathode of the ion source was replaced with a tungsten filament [96], and a movable Faraday-cup was installed to monitor the beam-quality [70].

The ion-beam can be aligned mechanically by rotating the beamline along a ball-joint (inside the box that houses the room-temperature electrical connections), and by rotating and translating the traps inside the magnet using a translation/rotation stage. The ion-source is pumped with a turbomolecular pump, backed by a scroll pump. When the ion source is not used, two valves (one computer-controlled pneumatic valve, and another manual valve) can be closed to separate the cryopumped trap vacuum from the ion source vacuum. Typically, the vacuum conditions in the trap are sufficient that we see no unintentional ion loss over the course of weeks and even months.

In addition to the external ion source, ions can also be loaded via a field emission point (FEP) at the bottom of the trap tower. The FEP can emit an electron beam (a few nA) through the trap

[3] This is not an error. Full access to the top plate underside requires cutting weld seams at the top of the LHe-stacks.
[4] If a leak is found, make sure to find the disassembly procedure proposed by James Carolan in 2015, specifically for our magnet. The SPECTRAP group closed similar leaks temporarily with Armstrong A12 epoxy [103].

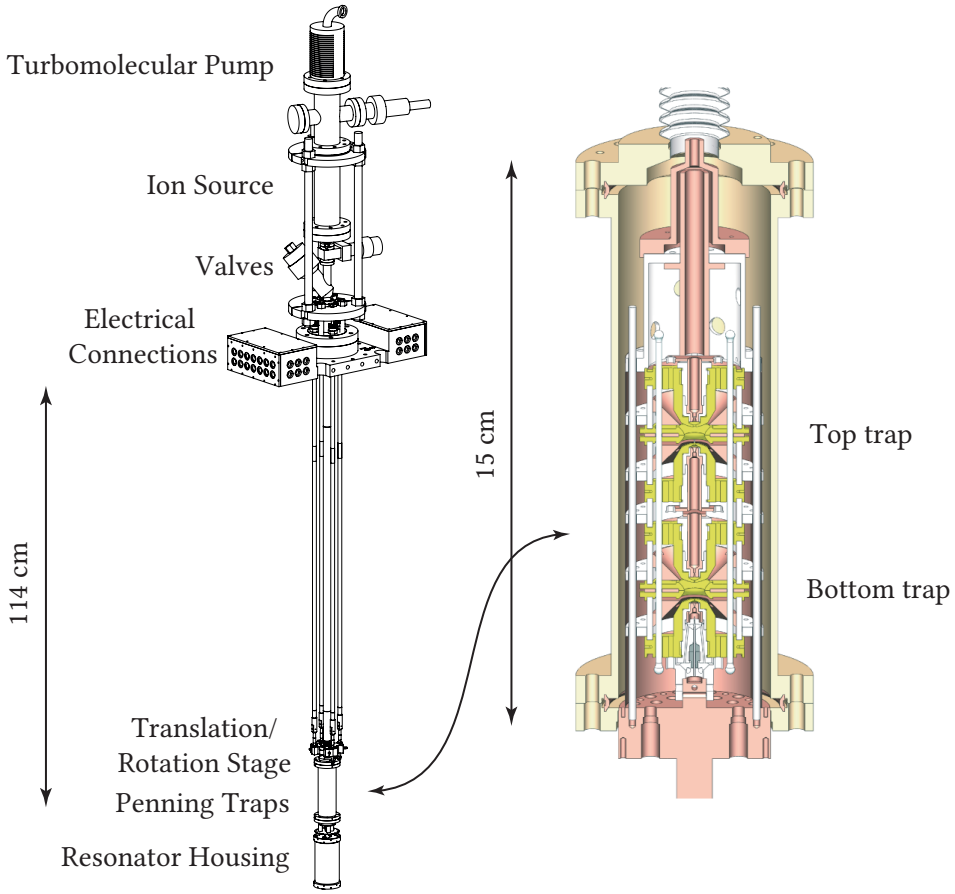

Figure 3.2.: Vacuum system and double traps, courtesy of David Pinegar [47].

region, along the magnetic field lines. The electron beam can be reflected on the other end of the traps and thereby folded back onto itself, in the style of a miniature electron-beam-ion-trap [104]. The multiple reflections increase the electron beam diameter until the electrons hit the inside of the endcap-holes, where surface atoms are released and ionized. This allows the production of hydrogen, oxygen, carbon, fluorine, and other ions [52], with charge-states up to $6+$. The ion most often used at THe-Trap is $^{12}C^{4+}$, because its charge-to-mass ratio is close to $^{3}H^{+}$ and $^{3}He^{+}$, with the quadruple charge giving a stronger axial detection signal.

3.3. Feedthrough flange

The electrical signals are fed into and out of the traps' vacuum envelope through a feedthrough flange. The flange must stay leak-tight even when it is cooled down within minutes from room

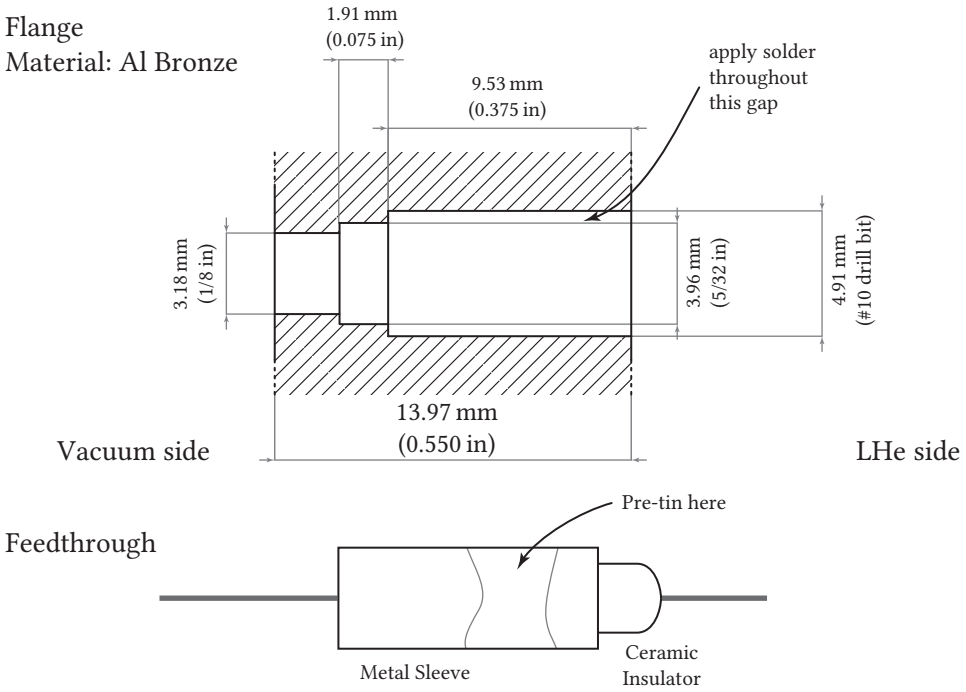

Figure 3.3.: Detail of the feedthrough holes. The dimensions are a consequence of the fractional inches, decimal inches, and drill-bit-gauges used in the original drawing. Only the 3.96 mm (5/32 in) hole diameter is critical, since it is designed for a tight fit with the feedthrough sleeve. The 4.91 mm hole serves as an approx. 0.5 mm gap between sleeve and flange, which is filled with solder after the feedthrough is inserted.

temperature to LHe temperature[5]. This requirement can be challenging to meet, especially when many feedthroughs are needed [80]. The original flange was designed and built at the University of Washington, but it developed leaks over time. We assembled an almost identical flange from spare parts, the main difference between the flanges being the assembly procedure. Until now, (after approximately 10 cool-downs), this replacement flange has not developed any leaks.

The flange contains 24 single-pin feedthroughs made by CERAMASEAL. The dimensions of the holes for the feedthroughs are shown in Figure 3.3. The feedthroughs' inner conductors are made from copper, and the sleeves around the ceramic feedthrough bodies are made from a non-ferromagnetic 70%–30% copper nickel alloy[6]. The original flange consisted of feedthroughs that were hard-soldered into a copper plug, which was then soft-soldered into an aluminum bronze ring. However, the hard soldering damaged some of the feedthroughs [47], and over the

[5]Due to the air-ice problems of the cold bore, the experiment cannot be pre-cooled with LN_2 or cooled down slowly.

[6]It is possible that the sleeves consist of 304 stainless steel, which also has suitable properties.

course of a few thermal-cycles, the flange developed additional leaks that became too difficult to close. We had two spare aluminum bronze pieces in the shape of the original plug-and-ring assembly. We gold plated these pieces, and soft-soldered new feedthroughs into them. The soft-soldering procedure consisted of the following steps:

1. Pre-tin the feedthroughs. Use aggressive flux, if necessary. We used LAVAR21 flux and Sn96Ag4 solder that had a standard flux-core.
2. Place the feedthroughs into the flange and heat the flange on a hot-plate to 225 °C.
3. Apply solder around the feedthroughs until the gap indicated in Figure 3.3 is completely filled. It might help to use solder without a flux-core for the bulk of the filling process, since the boiling flux can cause channels in the gap that are difficult to close.

We chose Sn96Ag4 due to its melting point of 221 °C. This allowed us to install additional material on the flange using Sn63Pb37 (melting point 183 °C). Both new flanges were leak-tight on the first try, and appear to be quite robust. The one flange in use did not develop leaks over several thermal cycles of the experiment, and even soldering directly to the body of a feedthrough where the wire had broken off did not introduce leaks. Unfortunately, for the second flange we used a set of feedthroughs where the inner conductor is made from CONSTANTAN instead of copper. At 4 K, CONSTANTAN is slightly ferromagnetic [101]. The feedthroughs used in the Seattle experiment had a nickel flash between the sleeve and the ceramic. This caused sizable B_1 and B_2 gradients [105]. The new feedthroughs do not have this nickel flash, but they are expensive and difficult to order. (On our last try, the suppliers denied that the nickel flash can be omitted). When not many cryogenic feedthroughs are needed, they can be home-made using epoxy and a thin-walled metal tube [73]. For this feedthrough design it is crucial that the epoxy is applied in a single blob that encloses the inside and the outside of the tube simultaneously [101].

3.4. Trap tower

The trap tower consists of two almost identical, hyperbolic traps, and additional electrodes to create, catch, and transport ions (Figure 3.4). The characteristic size of both traps is $d = 2.11$ mm, with a ring-electrode distance of $\rho_0 = 2.77$ mm and an endcap-electrode distance of $z_0 = 2.29$ mm.

The endcap electrodes and ring electrodes are made of phosphor-bronze, the other electrodes are made of OFHC copper. All electrodes are gold-plated and separated by MACOR spacers [47]. The endcaps of the bottom trap each have a central hole with a diameter of 300 μm for ion-transport and for the electron beam created by the FEP. The only difference between top and bottom trap is that the respective holes in the top trap endcaps are 500 μm in diameter, to facilitate ion transport. All endcap holes are countersunk on the trap-side to ensure that possible electron-strikes occur inside the holes, instead of on surfaces facing the trap [70]. Furthermore, outside of each endcap are the *skimmer electrodes*, which have slightly smaller holes than the corresponding endcaps, so that during ion loading or ion transport, stray ions or electrons are more likely to be caught inside the holes of the skimmers, instead of the holes in the endcaps[7].

[7] The quality of the gold plating inside the holes is not well known, and charges hitting the inside surfaces of the holes may lead to *patch potentials*, which can degrade the quality of the main trap potential.

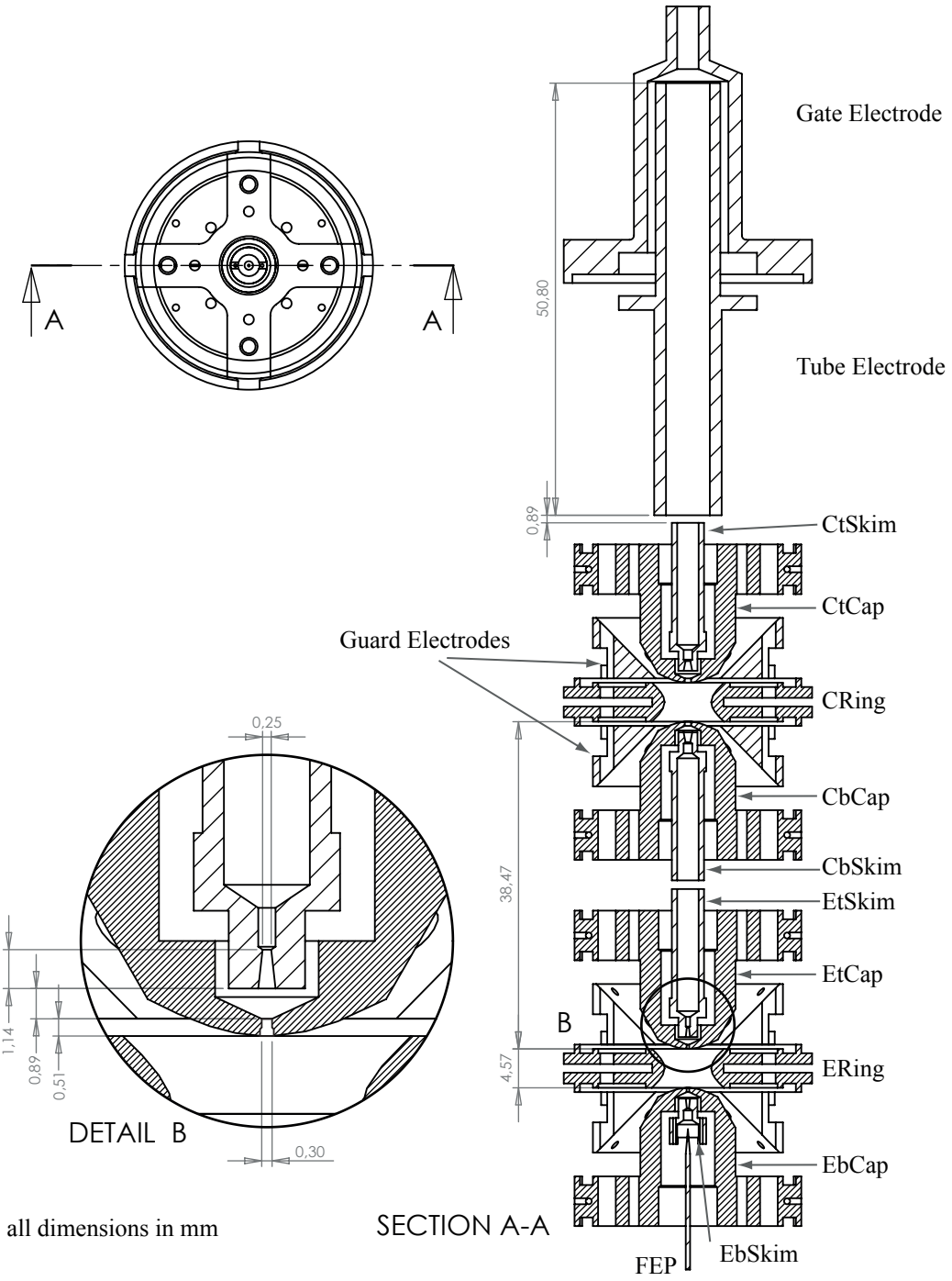

Figure 3.4.: Cut-view of the electrodes used at THe-Trap. The *gate electrode* and the *tube electrode* can be used to catch ions from the external ion source. The two hyperbolic traps are identical, except for larger hole diameters in the top trap. Not shown are spacers, alignment rods, and screws. Figure adapted from [50], with corrected endcap-detail.

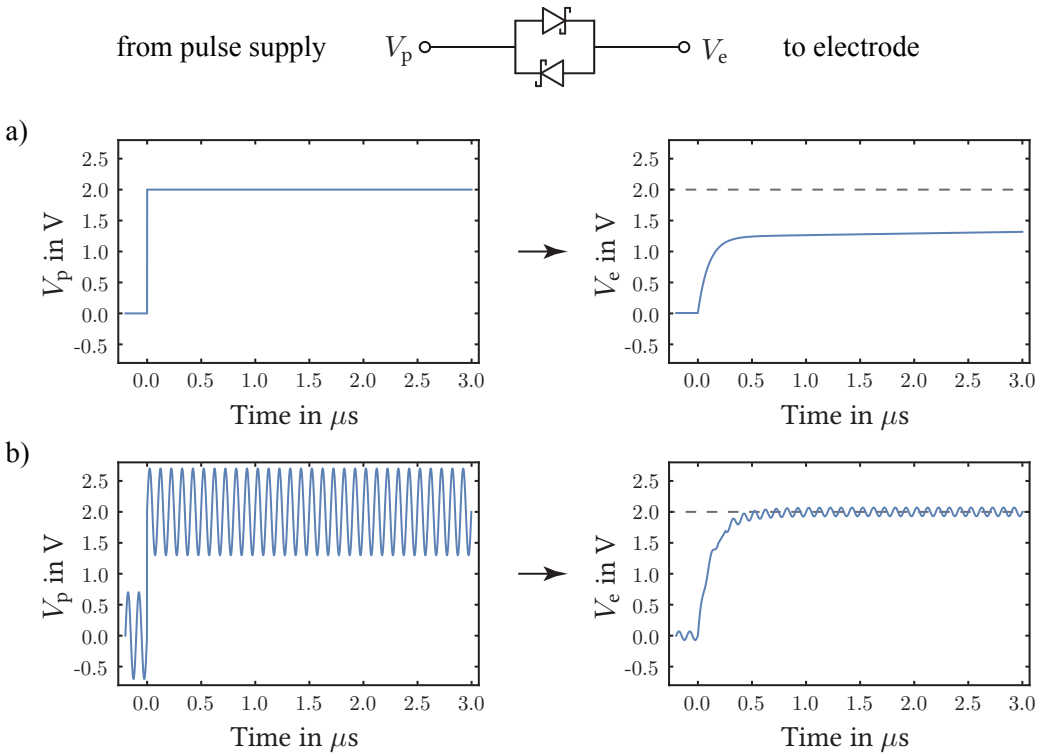

Figure 3.5.: A diode pair can be used as an impedance switch for electrodes that must be high impedance to ground, e.g. electrodes used for detection [47, 50]. Typical electrode voltages V_e during detection are in the nV-range, which is much smaller than the forward voltage of the diodes (0.7 V). Therefore, the diodes are high-impedance with respect to the ion signal. On the other hand, typical pulse voltages V_p are several volts. Up to a difference given by the forward voltage, such a pulse is transmitted rapidly (a). The final 0.7 V can also be transmitted rapidly by superimposing a *diode-drive RF* signal onto the pulse: A 40 MHz signal with an amplitude of 1.4 V_{pp} ensures that each diode is conductive once during each RF-cycle (b). This results in a faster pulse response, at the expense of some leakage of the diode-drive-RF on the electrode. The frequency of 40 MHz was chosen to not interfere with any ions of interest. These sketches are based on [50], which also includes measurements.

The bottom trap is used for precision measurements. It is placed into the region of the magnetic field that is most homogeneous and most stable. The top trap can be used for ion capture and ion storage, and additionally for monitoring drifts of the magnetic field or the trapping voltages. The transport between the traps is challenging, since the endcaps are used for detection and all connections from the outside must be of high impedance (tens of MΩ). However, the voltage pulses for the ion transfer must change the endcap voltage within μs. This requires a low impedance connection. The original solution was to use anti-parallel diode pairs and a *diode-drive-RF*-signal as an impedance switch (Figure 3.5). While the effectiveness of the diodes has not been disproved, the diodes introduced additional complexity into the system and were not installed in the latest measurement runs, and ion transport between the trap has not been attempted since. Alternative transport schemes might be implemented in the future, for example pulsing the ring electrodes instead of the endcaps, or switching to adiabatic transfer in cylindrical traps.

However, during the very first run of the experiment in Heidelberg, it was serendipitously discovered that when the diode pairs are cooled to 4 K, they exhibit exceptionally low conductance for voltage differences smaller than 500 mV. It was possible to keep the endcaps (which were connected via diode-pairs) charged by a few hundred mV relative to the applied DC voltage, with no appreciable drift of the axial frequency over several days. This corresponds to an impedance of $10^{21}\,\Omega$ or higher. In the future, it might be possible to use the diode pairs as an impedance switch to stabilize the ring-voltage, in a system comparable to the cryogenic optocoupler used in the latest runs of the UW-PTMS [106].

3.5. Loading single ions

The loading procedure at THe-Trap [54] begins by running one of the ion-sources (typically the FEP) to load a small cloud of ions into the trap. Then the ring voltage U_R is ramped up to $U_\mathrm{drop} = -50\,\mathrm{mV}$, which reduces the well-depth of the trap and lets hot ions evaporate into the endcaps[8]. At THe-Trap, this procedure is called a "drop" of the ring voltage. After a few seconds, the ring-voltage is reduced back to the value that brings the axial frequency of the ions-of-interest into resonance with the detection circuit (typically $-30\,\mathrm{V}$ to $-97\,\mathrm{V}$, depending on the ion species of interest). This cools the axial motion of the ions-of-interest, and indirectly (through electrostatic coupling with cooled ions) all other ions.

The unwanted ion species are then excited with a broad sweep of an axial excitation signal, which is applied to the bottom endcap. This is called a "broom". Unfortunately, this excitation signal can also excite the magnetron mode of the ion-of-interest through the "magnetron heating" resonance at $f_z - f_-$. Therefore, the ions-of-interest must be cooled with an appropriate sweep across their magnetron cooling resonance $f_z + f_-$.

This drop/broom/cool procedure is repeated a few times, each time increasing U_drop by approximately 10 mV. The presence of an ion-of-interest can be verified periodically using an axial excitation, for example a parametric excitation (subsection 2.8.1). U_drop is increased until the magnetron radius of the ion-of-interest noticeably grows during the drop. This is a clear

[8] One of the advantages of a hyperbolic trap is that the ions *can* crash into the endcaps. Cylindrical traps, with their open endcaps, are more difficult to clean of contaminant ions.

sign that the maximum U_{drop} is reached (typically at $U_{\text{drop}} = -20\,\text{mV}$), and that any further increase in U_{drop} would likely lead to complete ion loss. At this point, there is usually only one ion left. However, if a measurement of the axial ion width suggests that there are two ions, the ions are expelled from the trap by reversing the polarity of the ring voltage, and the loading procedure is repeated from the beginning.

Frequent reloading of the trap, especially when loading ions with a charge state of $5+$ and higher, can lead to the formation of patch potentials on the endcap electrodes. Over time, this modifies the maximal voltage U_{drop} that the ions can survive by a few ten mV. It also modifies the ring voltage needed for locking the ion by a few mV, and there are indications that the optimal guard voltage $U_{\text{G},0}$ can also be shifted by tens of mV.

3.6. Axial detection

The original detection system designed in Seattle featured a differential amplifier to measure the voltage across the endcaps of the traps, with both traps connected in parallel [47]. This enabled measurements of the image currents in both traps simultaneously using only one cryogenic amplifier, while keeping the capacitance of the LC-resonance circuit low. However, the differential detection required that all four endcaps are connected to the amplifier, which poses a challenge for applying the pulsed voltages that are needed for transporting ions *through* the endcaps. Ultimately, noise problems of the original amplifier led us to evaluate a non-differential amplifier [107], based on a design that is used at the Mainz electron-g-factor experiment [108]. This new amplifier was tested in a simplified trap setup, where only the precision trap was fully wired for ion work. (Filter details are shown at the end of this chapter, in Figure 3.9 and Figure 3.10.) This system worked so reliably that it was used for high-precision mass measurements.

The detection system is based on continuously driving the axial motion (instead of pulses, which are used at the FSU trap), to measure the phase of the ion-response. The overall layout is shown in Figure 3.6. (Since the new amplifier is only connected to one trap, instead of both traps simultaneously, this detection system no longer requires the complexity of the beat-frequency-oscillators [47], and instead uses the traditional heterodyne detector design of earlier Penning-trap work performed in Seattle [109, 110] (Figure 3.6.)

The ring voltage is chosen such that the axial resonance of the ion is at 4 MHz. The ring voltage is modulated by a few parts in 10^4, with a frequency of 100 kHz (MOD). This creates ± 100 kHz sidebands in the axial motion. The axial motion is driven on the 4.1 MHz sideband, using a *local oscillator* (LO) set to 4.1 MHz. The detection circuit picks up and amplifies the 4 MHz component of the axial ion motion. This signal is mixed down to DC, using first the local oscillator, and then a phase-shifted copy of the modulation signal.

When the phase-shift is chosen appropriately, the resulting signal (as a function of the ring voltage) has a dispersion shape. This can be used to construct a feed-back loop, in which the ring voltage is automatically adjusted to keep the ion's axial motion resonant with the (fixed) driving frequency (see Figure 3.7): The dispersion-shaped signal is integrated, divided by a large factor a_{div} (currently set to 100 000), and subtracted from the ring voltage. This feedback system ensures that the ion's axial motion is frequency locked to the drive created by the synthesizers.

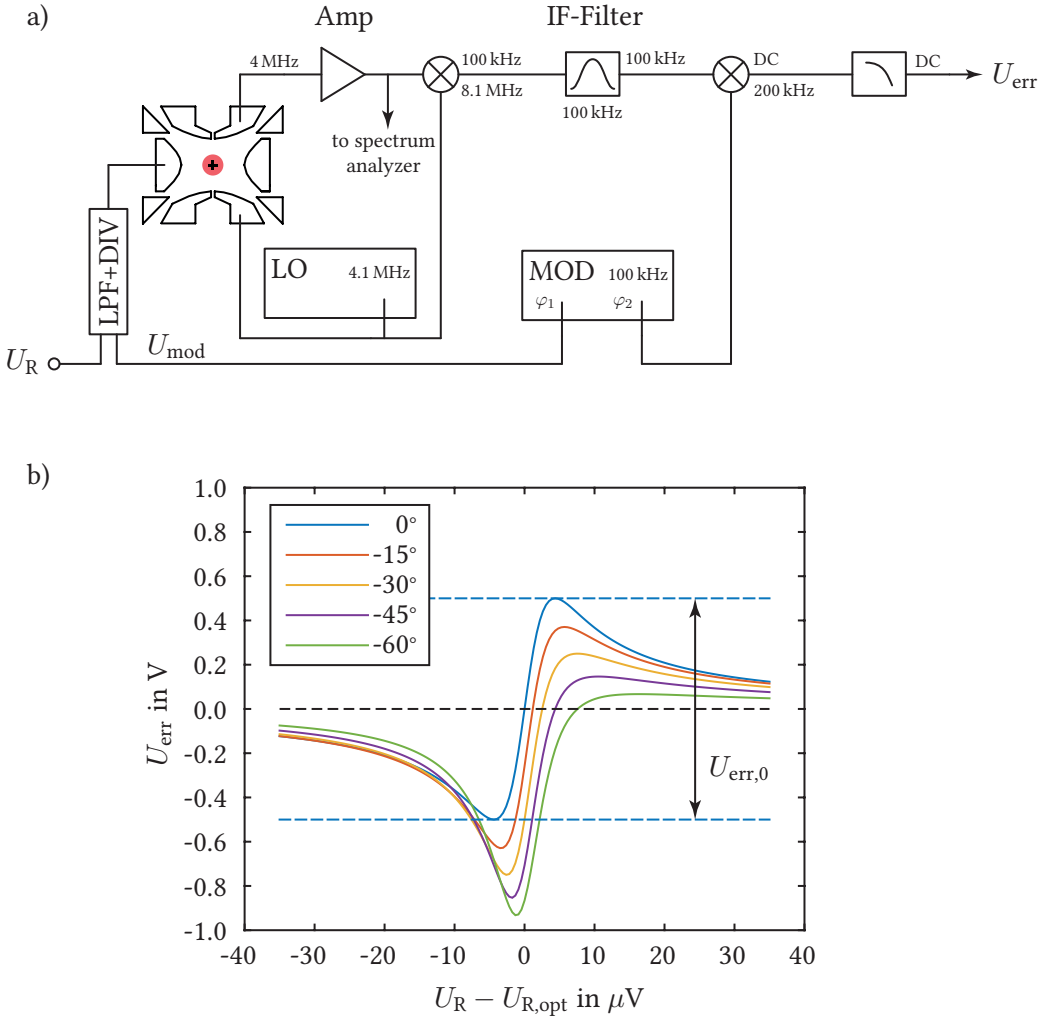

Figure 3.6.: Layout of the THe-Trap detection system. a) The ring voltage U_{R} is set to a value such that $f_z = 4\,\mathrm{MHz}$. A 100 kHz signal U_{mod} from the "modulation synthesizer" (MOD) is added to U_{R} through a cryogenic filter board (Figure 3.9). This modulates f_z, creating $\pm$ 100 kHz sidebands of the axial ion motion. Another synthesizer, the "local oscillator" (LO) drives the upper (4.1 MHz) axial sideband. The 4 MHz ion-response is amplified and mixed down to DC in two stages. By using a 2-channel MOD synthesizer, the phase in the last mix-down step can be set arbitrarily. b) At the optimal phase setting (shown as $\varphi = 0$ in the plot), the output signal U_{err}, as a function of ring-voltage offset, has a dispersion-shape (see subsection 2.8.1). Near $U_{\mathrm{R,opt}}$, the output U_{err} is directly proportional to the ring voltage offset, or equivalently, the f_z offset. This is used as the error signal in the feedback loop shown in Figure 3.7.

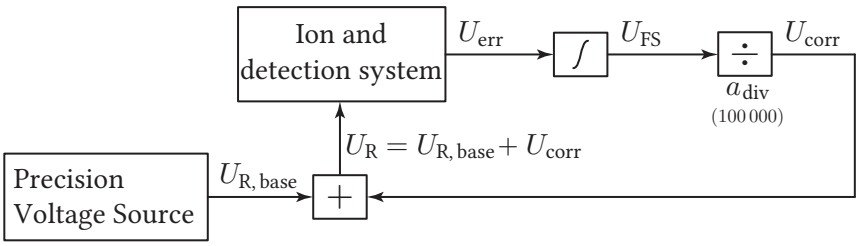

Figure 3.7.: The axial feedback loop used at THe-Trap is best understood in terms of the DC-voltages. The ring-voltage U_{R} is mostly given by $U_{\text{R, base}}$, which is provided by a stable reference source [111] and set to a value that makes the ion resonant with a fixed-frequency, axial drive (not shown). Small frequency shifts $\Delta\omega_z$ or voltage shifts $\Delta U_{\text{R, base}}$ lead to a non-zero error voltage U_{err}, which is integrated, divided by a large factor a_{div}, and then added to $U_{\text{R, base}}$. This forms a feedback-loop, which ensures that the ion's axial mode is frequency locked to the axial drive.

However, imperfections of the detection-system can cause the ion's axial frequency to be slightly different than the frequency that the feed-back loop locks on to. If, for instance, the last mixer in the chain superimposes a DC-offset U_{offset} onto U_{err}, the zero-crossing is shifted and the locked frequency differs from the true axial frequency by

$$\Delta\omega_{z,\text{offset}} = -\frac{1}{2}\gamma_z \frac{U_{\text{offset}}}{U_{\text{err},0}} \quad , \tag{3.1}$$

where $U_{\text{err},0}$ is the amplitude of the axial resonance in the U_{err} vs. U_{R} diagram (Figure 3.6).

Another error arises if the phase-difference of the two MOD-channels is not chosen appropriately. A phase error of $\Delta\varphi$ shifts the frequency by [18]

$$\Delta\omega_{z,\varphi} = -\frac{1}{2}\gamma_z \Delta\varphi \quad . \tag{3.2}$$

The optimal phase-difference of the two MOD-channels has to be determined experimentally. To this end, and for general troubleshooting, we monitor the 4 MHz ion signal (just before it enters the first mixer, see Figure 3.6) with a general purpose spectrum analyzer. This allows us to see noise-spikes on our detection circuit, to monitor the strength of the excitation signal, and to measure the amplitude of the ion response. By maximizing the ion-response as a function of the MOD channel phase difference, the optimal phase can be determined (see section 5.2).

The optimal phase difference is subtly influenced by the detection system. This is similar to the coil-pushing effect: If ω_{RLC} does not coincide with ω_z, the frequency and phase of the ion's axial motion are shifted. The change in phase causes the zero-crossing of the resonance to shift, and subsequently leads to an error in ω_z. The magnitude of both effects can be shown to be equal[9]. However, at THe-Trap the coil-pushing shift is insignificant, therefore both effects can be neglected.

[9] In my calculations, which I do not include here, I found the coil-pushing and "phase-turning" effects to be equal in magnitude and sign. However, when trying to measure their combined effect by using deliberate, large offsets between f_z and f_{RLC}, we could not observe any shift at all. It is possible that I made an error in sign and that the effects cancel out.

3.7. Radial detection

At THe-Trap, the frequencies of the radial modes are detected indirectly through frequency shifts of the axial mode. The ion is continuously excited *axially* using the bottom endcap and kept in axial frequency lock. Then, a simultaneous radial excitation is applied to one of the guard electrodes. The frequency of this drive is swept linearly across one of the radial resonances. This causes the radius of the respective mode to increase, which to lowest order changes the axial frequency by

$$\Delta\omega_z = \left(-\frac{3K_4}{2K_2}\omega_z + \frac{B_2}{2B_0}\frac{\omega_+ + \omega_-}{\omega_z}\omega_+ - \frac{\omega_z}{4c^2}\omega_+^2\right)\hat{\rho}_+^2 \;\propto\; E_+ \tag{3.3}$$

for a sweep of the reduced cyclotron mode, and by

$$\Delta\omega_z = \left(-\frac{3K_4}{2K_2}\omega_z + \frac{B_2}{2B_0}\frac{\omega_+ + \omega_-}{\omega_z}\omega_- - \frac{\omega_z}{4c^2}\omega_-^2\right)\hat{\rho}_-^2 \;\propto\; E_- \tag{3.4}$$

for a sweep of the magnetron mode. Under axial frequency lock, the $\Delta\omega_z$-shift is compensated through a proportional response of U_{FS} (which is divided by a large factor and added to the ring voltage to keep the axial frequency constant). Since $\Delta\omega_z \propto E_+$ (or $\Delta\omega_z \propto E_-$, in case of a sweep over the magnetron mode), the changes of U_{FS} can directly be mapped to changes of the cyclotron (magnetron) energy. In an idealized trap, where the radial modes have no frequency shifts, the U_{FS} response is instantaneous, and where the noise is negligible, a U_{FS} vs. drive frequency plot would be equivalent to the E_+ vs. drive frequency plot shown in Figure 2.10.

In a real trap, anharmonic frequency shifts, noise sources, and the lag of the axial frequency lock can skew the expected lineshape significantly. However, by choosing an appropriate value of the guard voltage U_{G}, we can set K_4 to a value that at least cancels some of the low-order frequency shifts, to make the cyclotron mode harmonic with respect to its own energy. (This makes the magnetron mode *less* harmonic with respect to its own energy, but since errors in the magnetron frequency are suppressed by the invariance theorem, this trade-off is tolerable.) The required guard voltage for such a cancellation can be calculated by summarizing the $\hat{\omega}_+(\hat{\rho}_+^2)$-shifts, given by Equation (2.81) and Equation (2.93):

$$\Delta\hat{\omega}_+ = \left(-\frac{3K_4}{2K_2}\frac{\omega_-\omega_+}{\omega_+ - \omega_-} - \frac{\omega_+^3}{2c^2}\frac{\omega_+ + \omega_-}{\omega_+ - \omega_-}\right)\hat{\rho}_+^2 \quad . \tag{3.5}$$

(Note that under axial frequency lock, there is no $B_2 \cdot \hat{\rho}_+^2$ shift in the cyclotron mode.) The "magic" K_4 that (to lowest order) makes the cyclotron mode harmonic with respect to its own energy is given by the K_4 that eliminates this $\Delta\hat{\omega}_+$-shift. With K_2 given by Equation (2.50), and K_4 by Equation (2.51), the difference between the optimal guard voltage $U_{\mathrm{G},0}$ and the "magic" guard voltage can be approximated as

$$\Delta U_{\mathrm{G}} = -\frac{m\omega_+^4}{3qc^2 b_{\mathrm{G},4,0}} \quad . \tag{3.6}$$

For typical ions, ΔU_{G} is in the order of a few hundred mV. Using this deliberate guard-voltage offset is the main difference in the detection methods of THe-Trap and its predecessor, the

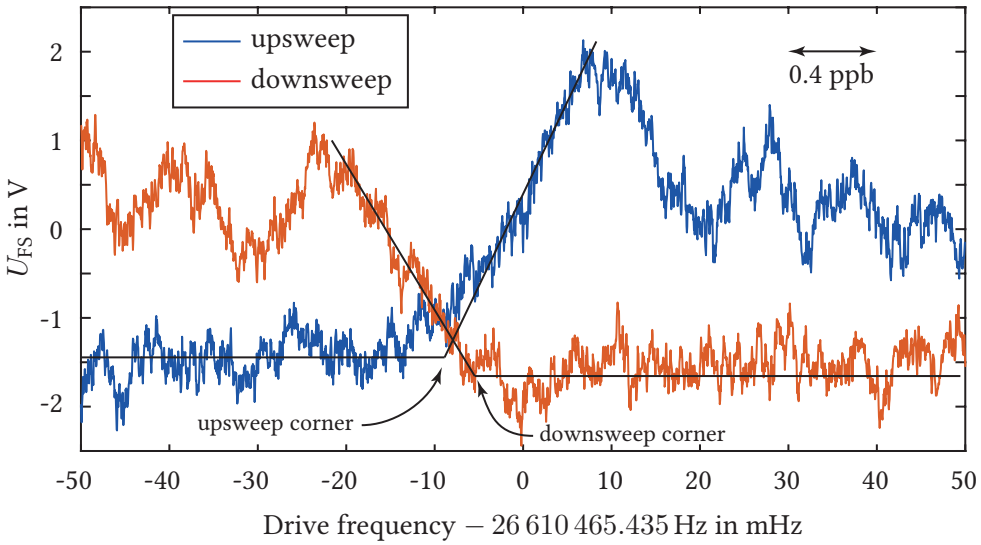

Figure 3.8.: Typical sweep over the f_+-resonance of a $^{12}C^{4+}$ ion. The duration of each linear sweep is 250 s. The signal U_{FS} is proportional to the frequency shift $\Delta\omega_z$, which in this sweep is mainly influenced by ρ_+^2, and therefore E_+ (compare Figure 2.10 and section 2.10). The black lines show linear fits over parts of the resonance. The "sweep corners" indicate the fit results of the sweeps.

UW-PTMS. It has the advantage of making the measured cyclotron lineshape closer to the theoretically expected lineshape, which helps in finding adequate linearized fit models. Furthermore, the upsweep and downsweep become symmetric, so that a possible, systematic fit error cancels out when averaging the results of the upsweeps and downsweeps (Figure 3.8). The fit model used at THe-Trap is similar to the fit model employed at the UW-PTMS [18], only that the fit-range is chosen semi-automatically [54, 94]. Some remarks about the lineshape are given in section 5.4.

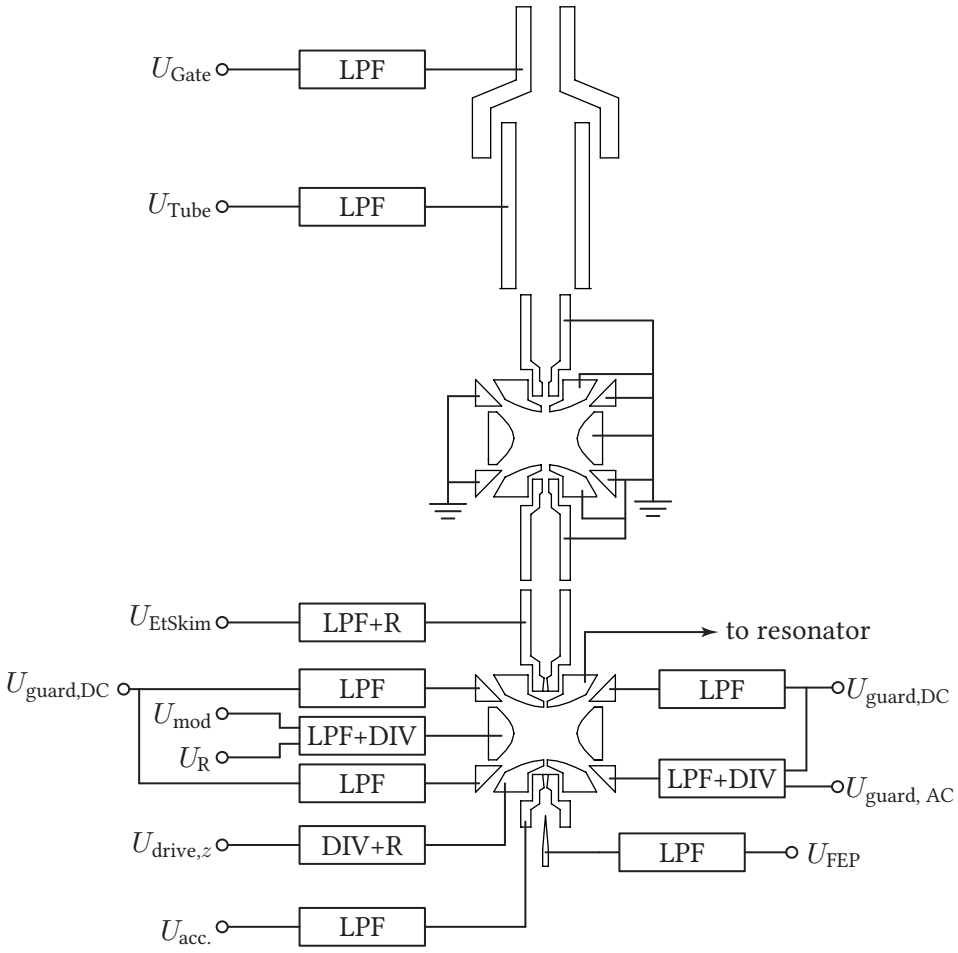

Figure 3.9.: Overview of the cryogenic filters used at THe-Trap. The filters are built on individual boards and installed between the vacuum envelope of the traps and the resonator housing. They are in direct contact with LHe. Board details are given in Figure 3.10.

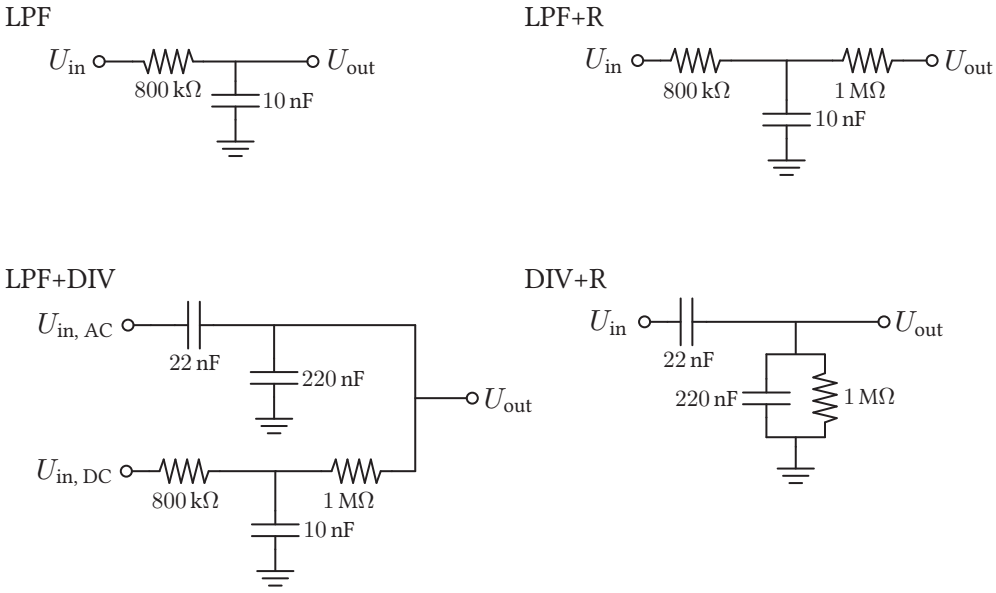

Figure 3.10.: Filter details. “LPF” is a low-pass-filter with a time constant of 8 ms. “LPF+R” is a low-pass-filter with an additional 1 MΩ resistor to decouple the filter-capacitance from the output. This is only needed for the EtSkim electrode, due to its strong capacitive coupling to the detection circuit. “LPF+DIV” is based on LPF+R, with an additional 1:10 capacitive voltage divider that adds AC onto the filtered DC (needed for the driving guard electrodes and the ring electrode). “DIV+R” is a 1:10 capacitive voltage divider. Its DC output is pulled to ground with a 1 MΩ resistor (used on the bottom endcap). The capacitors are Johanson Technology S-Series multilayer ceramic capacitors with NP0 characteristics. They show no significant change in capacitance when cooled to 4 K.

4. The FSU-Trap Experiment

The FSU trap was originally designed and built at the Massachusetts Institute of Technology (MIT) in the group of David Pritchard[1]. In 2003, the experiment was moved to the Florida State University in Tallahassee [71], where Edmund Myers and his group have been using it for measuring masses of over 30 nuclides [3].

The general architectures of THe-Trap and the FSU trap are similar. The ion detection is based on measuring the image current of the ion's axial motion, and the detection circuit and trap are cooled by LHe. The main difference lies in the detection of the radial frequencies. The approach used at THe-Trap is based on slowly exciting the radial modes with RF-sweeps across the radial resonances, which (through anharmonicities) changes the *axial* frequency. Typically, a resolution of approximately 3 mHz (out of 30 MHz, corresponding to a relative resolution of 10^{-10}) can be obtained with a sweep-bracket of two 250 s sweeps, plus additional 400 s for cooling and relocking (total measurement time 900 s). But as explained in the previous chapter, imperfections of the trap and the detection system result in a complicated lineshape that is difficult to fit.

At the FSU trap, however, the radial detection is sensitive to the *phase evolution* of the radial modes, and the frequency is determined as $\omega = \Delta\varphi / t_{\mathrm{msr}}$ (see section 4.5). The typical resolution that can be obtained in a 600 s measurement cycle is 0.5 mHz (out of 3 MHz, corresponding to a relative resolution of $5 \cdot 10^{-10}$). This includes the time needed for cooling. It is worth noting that this resolution is three times smaller than the Fourier limit. Without including the time needed for cooling, the resolution is a simple function of the phase uncertainty. Assuming a phase uncertainty of $\delta\varphi \approx 20^{\circ}$ [71], the theoretical resolution is $\delta f = \delta\varphi / (2\pi\, t_{\mathrm{msr}}) \approx 1/(18 \cdot t_{\mathrm{msr}})$, which is approximately 18 times smaller than the Fourier limit[2].

Another advantage of this method is that the radial frequency is determined while the ion is not actively driven. This avoids the complex interaction between the phase of the driven motion and the phase of the excitation, and the effect of possible frequency drifts is reduced to a phase-evolution at the average radial frequency.

The phase-sensitive detection method relaxes the constraints on the stability of the magnetic field. Furthermore, a method was developed to simultaneously measure the cyclotron phase evolutions of two ions stored in the same trap [113]. This essentially decouples the measurement precision from the stability of the magnet, but due to technical challenges, it has not been widely used. Instead, a variant of the two ion technique was developed, where two ions are stored in a single trap, but measured sequentially (see section 4.6).

The setup of the FSU trap has been described before, for example in the PhD theses of the

[1] The early history of the MIT trap is summarized in the PhD-thesis of Vasant Natarajan [112].

[2] In principle, the sweep-method that is used at THe-Trap also allows measurements beyond the Fourier limit. Numerical simulations show a best case resolution of $\delta f \approx 1/(7 \cdot t_{\mathrm{msr}})$ for a measurement time of t_{msr}. In practice, noise limits our resolution to a value close to the Fourier limit $\delta f_{\mathrm{FL}} \approx 1/t_{\mathrm{msr}}$.

FSU students Matt Redshaw [71] and Brianna Mount [114]. Schematics of the electronic filters can be found in Michael Bradley's PhD thesis [73]. Due to the similarities between THe-Trap and the FSU trap, the following, brief description of the FSU trap focuses on areas where the two experiments differ.

4.1. Superconducting magnet

The superconducting magnet used at the FSU trap is an 8.530 Tesla magnet made by Oxford instruments. Its vertical bore is not part of the main cryostat, but instead houses a separate cryostat with additional LN_2 and LHe reservoirs (Figure 4.1). The bore's LN_2-reservoir has a hold time of approximately 15 hours. Shortly before running empty, the low LN_2-level in the bore causes the resonance frequency of the axial detection system to shift, which limits a typical measurement run to 12 hours. The bore's LN_2 reservoir is refilled by an automated system. The hold time of the LHe-reservoir of the bore is approximately 3 days. The bore's LHe cryostat is shaped such that a SQUID detector can be installed in a region where the residual field of the main coils is only 10 mT. For optimal SQUID-operation, this fringe field can be temporarily nulled with external bucking coils, and then permanently shielded using a superconducting niobium box.

4.2. Vacuum system and traps

The vacuum enclosure of the FSU Penning trap is connected to a beam-tube, which allows sending a neutral gas beam into the trap region (see Figure 4.1). The top of the beam tube can be connected to a gas injection system, which consists of several "holding chambers" for different gases, computer controlled valves, and a digital manometer to accurately monitor the amount of gas that is injected into the trap system [115]. The gas injection system allows switching quickly between gases, and fully automating the ion loading procedure [71]. It is augmented by a metal vapor loader for measurements on alkali metals [73, 114]. The vacuum enclosure and the beam-tube, together with attached heat-shields and the ion detection circuitry, can be lifted out of the magnet bore for servicing the experiment.

With the exception of the wire carrying the axial signal, all electrical connections to the trap are routed through the beam-tube, so that almost all vacuum feedthroughs are at the room-temperature end of the trap's vacuum system. The single cryogenic feedthrough is made of Stycast epoxy [73]. Since the excitation signals are routed through the beam tube, the cryogenic filters for the excitation signals are installed inside the trap's vacuum enclosure. This protects the filters from condensation when warming up the apparatus, but it makes the filter components more difficult to exchange. It also reduces the thermal coupling of the filters to the LHe bath, which can lead to a subtle systematic shift: The filters are slightly heated by the excitation signals, which changes their magnetic susceptibilities and consequently shifts the cyclotron frequency of the measured ion. If in a cyclotron frequency ratio measurement the drive power (or drive time) differs between the two ions, the resulting differential frequency shift can significantly affect the measurement [48].

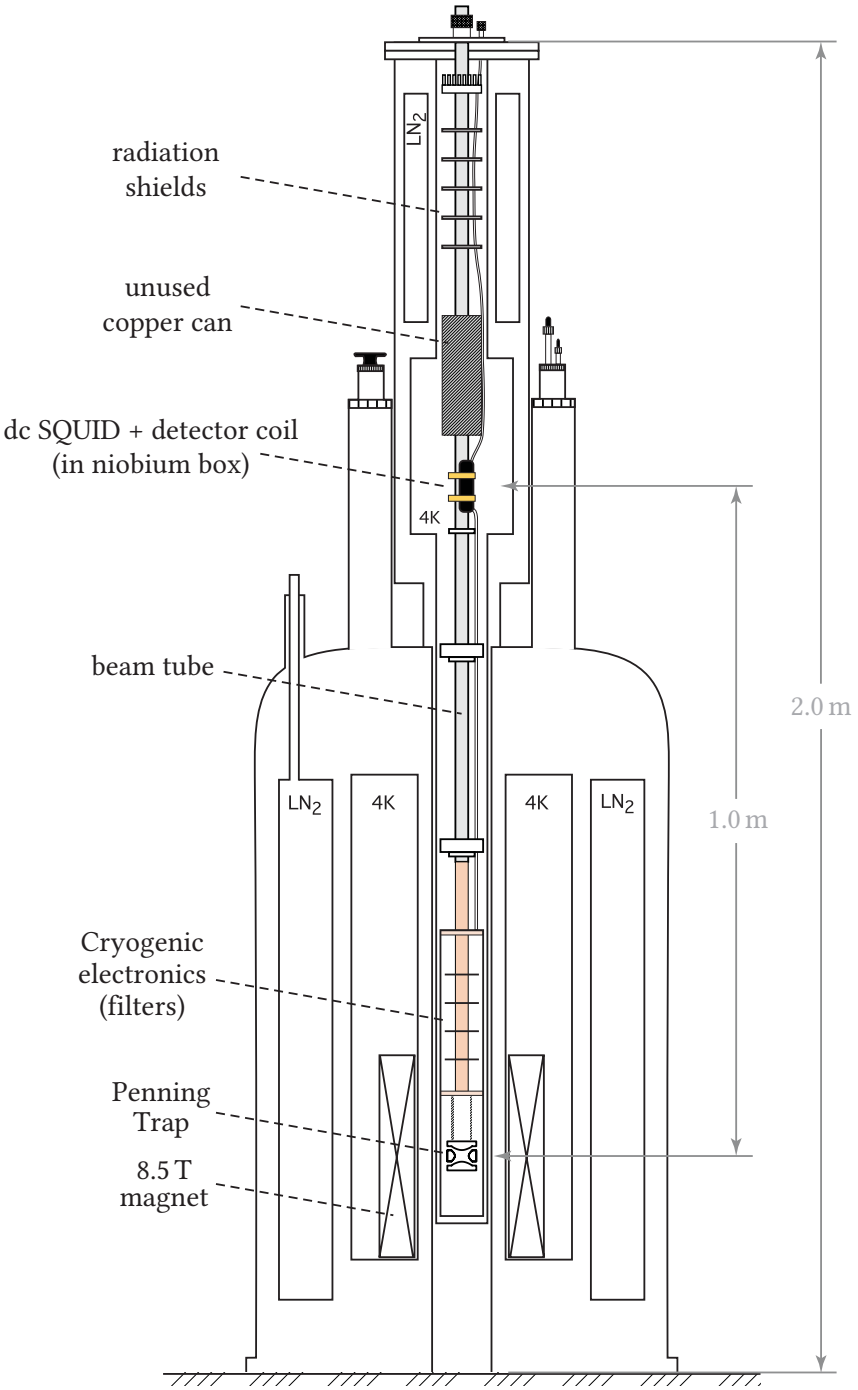

Figure 4.1.: Sketch of the magnet and cryostat used at the FSU trap. Picture adapted from [17].

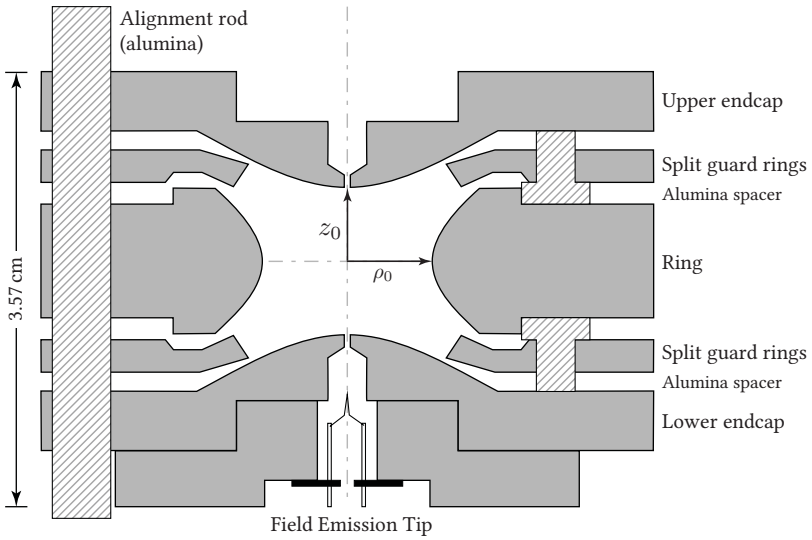

Figure 4.2.: Cross section of the FSU trap. The FSU trap is more than twice as big as THe-Trap and more orthogonal ($\rho_0/z_0 = 1.16$). The dimensions are $z_0 = 6.00\,\text{mm}$ and $\rho_0 = 6.96\,\text{mm}$, which leads to $d = 5.49\,\text{mm}$. Since the FEP current is never folded back into the trap, there are no "skimmer electrodes". Picture adapted from [17].

The trap tower of the FSU trap contains one hyperbolic trap with split guard electrode rings (Figure 4.2).

4.3. Ion loading

The gas or vapor beam that is sent down the beam tube can be ionized inside the trap with electrons from a FEP. The FEP is situated at the bottom of the trap tower. Compared to the external ion source used at THe-Trap, the neutral gas beam system has the advantage of being more robust and easier to set up. However, it potentially introduces more gas into the trap region than an ion source. For radioactive tritium, where trap contamination can be problematic [61], the gas beam must be collimated externally before it enters the trap cryostat [32].

Unwanted ions are excited with a series of specific RF pulses[3] to excite their axial motion, and expelled from the trap by ramping the potential of one of the endcaps close to the potential of the ring electrode[4]. After a single ion is loaded, another ion can be loaded (only relevant for the two-ion techniques, see section 4.6). The first ion is pulsed to a large "cyclotron parking"

[3] These are called "kills" in the parlance of the FSU trap, and "specific brooms" in the parlance of THe-Trap.

[4] This is called a "dip" at the FSU trap. Dips are similar, but not equivalent to the "drops" at THe-Trap, where the ring-electrode is ramped. A drop keeps the trap more symmetric (and harmonic) than a dip. From limited personal experience, this seemed more efficient for reducing the ion number to a single ion, possibly through more effective evaporative cooling as the ion number is reduced.

radius $\hat{\rho}_{+,\mathrm{k}}$, and the loading procedure is repeated for the second ion. During preparation of the second ion, it is important to avoid exciting the first ion with the specific RF pulses, and to cool the axial motion of both ions before ramping the endcap potential close to the ring potential.

4.4. Axial detection

As at THe-Trap, the detection system is based on detecting the image current of the axial ion motion using a resonant LC-circuit attached to the upper endcap. However, the ions are not continuously driven in the axial mode, but instead excited with an RF-pulse. This pulse simultaneously excites the resonator and the ion, but after a suitable waiting period (100 ms), the resonator's excitation has decayed far enough that the signal is dominated by the ring-down of the axial ion motion [56]. This ring-down is amplified, mixed to approximately 250 Hz and digitized with a sampling rate of 1 kSample/s. The frequency, amplitude and damping parameter of the ring-down signal are estimated using a fast Fourier transform (FFT). The frequency, amplitude, and phase are subsequently determined more precisely with a least-squares estimate, in which a damped sinusoid (with fixed damping parameter) is fitted to the ring-down data[5] [112].

Unlike THe-Trap, which uses a normally conducting coil and a transistor-based amplifier, the FSU trap uses a superconducting coil and a SQUID detector [116]. This detection circuit has, compared to the THe-Trap, an exceptionally high Q-value of 30 000. This enables the FSU trap to detect and cool singly-charged ions with masses of up to 42 u. However, the strong interaction between ion and detection circuit can give rise to frequency shifts (coil pushing, see subsection 2.6.4). Given the detector's resonance frequency of $f_{\mathrm{det}} = 213$ kHz and the ring voltage source range from 0 V to -24 V [71], the FSU trap is optimally suited[6] for m/q-ratios between 10 u/e and 42 u/e.

The detector's effective noise temperature was measured to be approximately 5 K at MIT and 40 K at FSU [71]. For the measurement of the tritium/helium-3 mass ratio, the coil of the detection system was recently changed to a smaller coil, giving a resonance frequency of 685 kHz, a Q-value of 28 000, and a temperature of 28 K [32].

4.5. Radial detection

There are two radial detection methods used at the FSU trap [16]. The first measures the radial-to-axial coupling frequencies ($f_+ - f_z$ and $f_- + f_z$), which together with a measurement of f_z, determines the radial frequencies f_+ and f_-. This method is called *cyc-splitting* for the cyclotron mode, and *mag-splitting* for the magnetron mode. The second, and more precise method, is based on measuring the phase evolution of the radial modes. This is called the *Pulse-and-Phase* (PnP) method [115].

[5] As shown in [112], this least-squares fit is equivalent to multiplying the data with an exponential decay and then finding the frequency that maximized the squared-sum of a Discrete Time Fourier Transform of the data.

[6] Towards the lower end of this range, the relative stability of the voltage source becomes limiting.

4.5.1. Cyc-splitting and mag-splitting

A cyc-splitting measurement starts with a determination of the axial frequency: An RF pulse is applied to the bottom endcap, and the frequency of the axial ring-down signal is determined. In the next step, a coupling drive with a frequency near the axial-to-cyclotron resonance is continuously applied to one half of the bottom guard electrode, and the axial mode of the ion is excited with another RF pulse to the bottom endcap. Due to the coupling drive, the resulting axial energy oscillates between the axial and cyclotron mode, which effectively amplitude-modulates the axial motion. In the frequency spectrum of the axial ring-down, this amplitude modulation splits the single axial peak into two separate peaks. The peak separation (the *splitting*) indicates the Rabi frequency of the coupling, and the average frequency of the two peaks, together with the earlier measurement of the true axial frequency, indicates the offset between the applied coupling frequency and the actual coupling frequency. By adjusting the frequency of the coupling drive until the average peak frequency coincides with the true axial frequency, the coupling frequency can be measured with an uncertainty of typically 0.1 Hz. The splitting of the peaks (the Rabi frequency) can typically be determined with an accuracy of 1–2%. This can be used to calculate the amplitude and duration of a coupling pulse that completely swaps the action between the respective radial mode and the axial mode (a π-pulse, see section A.6).

The mag-splitting works analogously, and has a similar accuracy of 0.1 Hz. When the free-space cyclotron frequency is determined via the invariance theorem, a 0.1 Hz uncertainty of the magnetron frequency is typically accurate enough for mass ratio measurements with relative uncertainties of 10^{-11}.

4.5.2. Pulse-and-phase

The PnP method is used to determine the reduced cyclotron frequency with lower uncertainty. A PnP measurement starts with an ion that has been cooled in all modes. Then, an RF-pulse with a frequency near the reduced cyclotron frequency is applied to one half of the bottom guard electrode. This RF-pulse acts as a resonant, dipolar drive on the reduced cyclotron mode. It increases the amplitude of the reduced cyclotron mode to $\hat{\rho}_{+,i}$ and sets a defined phase. This phase is allowed to evolve for a time T_{evol}, after which a π-pulse is used to write the phase into the axial mode, where the ring-down is measured and the phase determined via a least-squares fit of a damped sinusoid. The phase measurement typically has an accuracy of 20° or better. By plotting the measured phase as a function T_{evol}, the cyclotron frequency can be determined as

$$f_+ = \frac{1}{2\pi}\frac{\Delta\varphi}{\Delta T_{\text{evol}}} \quad . \tag{4.1}$$

Since the phase can only be measured modulo 2π, it is necessary to *unwrap* the phase by adding an appropriate number of 2π's for longer and longer evolution times. Typically, one starts with an initial estimate of the reduced cyclotron frequency from the cyc-splitting measurement. By choosing an appropriately short evolution time, the phase can be unwrapped unambiguously. The difference between expected phase and measured phase can be used to calculate a new, more precise value of the reduced cyclotron frequency. This can then be used to unwrap the

phase of a measurement with a longer T_{evol}. The evolution time is successively increased until the random drift of the magnetic field prevents unambiguous unwrapping of the cyclotron frequency. For typical ions with a reduced cyclotron frequency of 3 MHz, the longest useful evolution times are on the order of 1 minute, and approximately 10 different evolution times are used. This is called a PnP cycle. The total duration of a PnP-cycle is on the order of 10 minutes.

The least-squares fit of the axial ring-down yields not only the initial phase, but also the axial frequency. Thereby, the axial frequency can be determined simultaneously with each phase measurement.

4.5.3. Determining the free space cyclotron frequency

The free-space cyclotron frequency f_c is obtained via the invariance theorem, using PnP measurements of the reduced cyclotron frequency f_+ and the axial frequency f_z, and calculated values of the magnetron frequency f_-. The magnetron mode is sufficiently stable that f_- only needs to be measured once per ion species. This measurement is used to determine the trap angle θ using Equation (2.74). Since f_z and, to a lesser extent, f_+ drift during the measurement, subsequent values of f_- are calculated from θ, f_+ and f_z by rearranging Equation (2.74) to

$$f_- = \frac{f_z^2}{2f_+}\left(1 + \frac{9}{4}\sin^2\theta\right) \quad . \tag{4.2}$$

The typical relative uncertainty in a f_c-determination using a 10-minute PnP cycle is $5 \cdot 10^{-10}$ or less.

In the PnP measurement method, the result of the f_+ measurement is mostly determined by the phases of the measurements with the shortest and longest evolution times. However, f_z is determined as the average frequency of all ring-downs. This can lead to a subtle, systematic error [48]: The "average time" of the f_+ determination may be different from the average time of the f_z determination. If the voltage source drifts during the measurement, then the f_c determination via the invariance theorem will be shifted. In a ratio measurement, this error is negligible for typical drift rates, as long as the voltage drifts are the same for both ions. However, when the ring-voltages for the two ions are different enough to require a (computer-controlled) switch between voltage-dividers, the voltage drift can be different for the two ions (*differential* voltage drift), in which case the error in the f_c determination can be significant.

As a counter-measure against differential linear drifts, the sequence of different T_{evol} is shuffled such that the average times of the reduced cyclotron frequency measurements and of the axial frequency measurements coincide. However, since the troublesome drift-rates are often exponential decays, the individual f_z measurements have to be analyzed to exclude non-linear drifts.

4.6. Two ion technique

Early in the development of the spectrometer, it was hypothesized that when two ions form a mass doublet (fractional mass difference of a few 10^{-4}), their cyclotron frequencies can be measured simultaneously in a single trap [113, 117]. This technique is based on the fact that the

magnetron frequencies of mass-doublet ions are almost degenerate, which causes the magnetron modes to become strongly coupled. The ions therefore share a magnetron trajectory (with 180° phase difference), and sample the same average magnetic field. This elegant method relaxes the requirements for the magnetic field stability, and it enables mass comparisons of m/q doublets with unprecedented precision and accuracy (total relative uncertainty less than 10^{-11}). However, this technique requires rigorous knowledge and control of systematic effects, which makes it technically challenging. It took more than 10 years for the first mass measurement to be performed with the shared-magnetron-orbit technique [17]. This measurement still stands today as the most accurately determined cyclotron frequency ratio [3]. Unfortunately, the increased detector temperature prevented this technique from being applied at FSU. Instead, the group around Edmund Myers adapted a two-ion technique from an antiproton/proton mass comparison experiment [5], in which two ions are kept in the trap simultaneously, but only one ion is measured at a time, with the other ion parked on large cyclotron radius [92]. This allows switching the measured ion species rapidly (within minutes, instead of tens of minutes for reloading the trap).

For a typical mass measurement at the FSU, three PnP cycles (each lasting approximately 10 minutes and using 10 different T_{evol}) are performed on the inner ion, and then the inner and outer ion are swapped. This is repeated for 12 hours (until LN_2 needs to be refilled), and yields a ratio of the cyclotron frequencies with a relative statistical uncertainty of $1 \cdot 10^{-10}$ or less. Several such 12 hour runs are performed, with various trap parameters (amplitudes, parking radii, pulse radii), in order to measure or exclude systematic effects.

5. Results at THe-Trap

Previous mass measurements at THe-Trap were limited by systematic errors, mainly the amplitude dependent errors connected with K_4, K_6, B_2, and special relativity [53]. Our method of measuring these effects was to observe ω_+, ω_-, ω_z as a function of the axial ion amplitude $\hat{z}$. At THe-Trap, $\hat{z}$ is the only amplitude that leads to appreciable K_4, K_6, B_2, and relativity related shifts in the ω_c determination, so measuring the eigenfrequencies as a function of $\hat{z}$ allows a straightforward interpolation to $\hat{z} = 0$. However, as we learned to work with lower axial amplitudes, additional shifts caused by the detection system (section 3.6) became more relevant. Especially the shift $\Delta\omega_{z,\text{offset}}$, which is inversely proportional to $\hat{z}$, interfered with the extrapolation to $\hat{z} = 0$. Furthermore, our measurement method did not allow us to reliably determine the K_6 or B_2 parameters of our trap, and gave conflicting results for the optimal guard voltage $U_{\text{G},0}$.

We therefore implemented a shift-measurement technique that was originally developed at MIT/FSU[1]: Instead of measuring ω_+, ω_-, ω_z as a function of $\hat{z}$, we now measure ω_z as a function of $\hat{\rho}_+$, $\hat{\rho}_-$, $\hat{z}$, and U_G. As will be shown below, this method is faster and allows fitting the trap parameters more reliably. Additionally, we improved our measurements of shifts related to the detection system. This chapter demonstrates our improved understanding of the systematic shifts on an oxygen-carbon mass measurement.

5.1. Trap characterization

5.1.1. Preparation

The first step in characterizing the trap is to ensure that there is only a single ion in the trap: the ion-of-interest. Otherwise, contaminant ions can change the effective anharmonicity of the trap through non-resonant interactions, which depend on the amplitudes of both ions (see the ring-of-charge model, subsection 2.10.7). If the contaminant ions are interacting resonantly with the ion-of-interest, the ion behavior is even more difficult to understand, which makes all efforts in tuning the trap moot.

When the contaminant ion is of the same species as the ion-of-interest, the most obvious warning sign is an increased axial ion width, which grows proportional with the number of trapped ions (Equation 2.28). If the width is not measured, the presence of multiple ions (of the same species) can be inferred from lock voltage changes after each radial cooling: Since the "breathing modes" of the coupled ion motion do not induce an image current in the trap, they are uncooled. The cooling drives only swap the action of the breathing modes between the radial and the axial motion, leading to changed amplitudes and, through typical anharmonic

[1] I am extremely grateful to Edmund Myers who, during my visit to FSU, patiently explained this technique to me and showed me how to apply it in practice.

shifts, to a relative axial frequency change in the order of 10^{-7}. This corresponds to lock voltage changes of several volts.

If the contaminant ion is of a different species than the ion-of-interest, a typical warning sign is a changed "orthogonality" of the trap. Normally, the electrostatic properties of THe-Trap dictate that for every 750 mV change of the guard voltage U_{G}, the ring voltage U_{R} has to be changed by -1 mV in order to keep f_z constant[2]. A non-resonant contamination ion, however, also reacts to ring voltage changes and guard voltage changes. This changes the coupling between the ion-of-interest and the contaminant ion, which in turn changes the effective ratio of $\Delta U_{\mathrm{G}}/\Delta U_{\mathrm{R}}$ from 750 to a value that is typically lower by $100 - 300$. If such effects cannot be observed, then either there is truly only one ion present, or the contaminants are at such large amplitudes that their effects are immeasurably small. However, in the latter case the contaminant ions can slowly (over the course of days and weeks) cool in by weakly coupling to the cooled ion-of-interest. This has occasionally been observed.

The last step before characterizing the trap is to ensure that both radial modes of the ion are thoroughly cooled. Otherwise, residual radial motion, together with the mixing-terms in the K_6-shift formula, can lead to frequency-shifts that mimic K_4-effects. This can lead to an erroneous tuning of the guard voltage.

5.1.2. Rough trap tuning: Guessing $U_{\mathrm{G},0}$

The optimal guard voltage $U_{\mathrm{G},0}$ is defined as the guard voltage that leads to a vanishing electrostatic anharmonicity K_4. The process of finding $U_{\mathrm{G},0}$ is called "trap tuning", and the ratio $U_{\mathrm{G},0}/U_{\mathrm{R}}$ (sometimes its inverse) is called the "tuning ratio" and is a constant of the trap[3]. Therefore, having found $U_{\mathrm{G},0}$ for one ion allows guessing $U_{\mathrm{G},0}$ of a different ion species with typically 100 mV accuracy. If the initial value is less well known, for example when tuning a trap for the first time, it can help to bring the ion into parametric resonance (see subsection 2.8.1), and to record the change of the ion amplitude as a function of the ring voltage. This can be repeated at different guard voltages. Near the optimum guard voltage, the signal amplitude is very sensitive to small changes of the *ring* voltage [78–80].

5.1.3. Minimizing the trap angle θ

The next step in trap optimization is to minimize the trap angle θ. The most sensitive technique is to observe the axial frequency (in lock) as a function of the mechanically adjusted trap angles via control rods of the xy-translation/rotation stage (a tripod mechanism with two adjustable distances). One full turn of a control rod corresponds to approximately 1° of trap tilt. We routinely optimize the trap tilt within a sixteenth $(1/16)$ turn of the control rods, which allows us to set $\theta < 0.1^\circ$. The final trap angle θ can be calculated from the measured ion frequencies with the help of Equation (2.74). Using the calibration data (Table 5.1) and correcting it for the modulation shift and the image charge shift leads to $\theta^2 = 7(8) \cdot 10^{-9}$ for the $^{12}\mathrm{C}^{4+}$ ion, and $\theta^2 = 8(7) \cdot 10^{-9}$ for the $^{16}\mathrm{O}^{5+}$ ion. This corresponds to a magnetron angle $\theta < 0.01^\circ$, which is ten times smaller than the sensitivity of the lock-optimization technique. This is likely

[2] Using the expansion Equation (2.46), $\Delta U_{\mathrm{G}}/\Delta U_{\mathrm{R}}$ can be identified with the ratio $b_{\mathrm{R},2,0}/b_{\mathrm{G},2,0}$.
[3] Again, using Equation (2.46), the ratio $U_{\mathrm{G},0}/U_{\mathrm{R}}$ can be identified with the ratio $b_{\mathrm{G},4,0}/b_{\mathrm{R},4,0}$.

a serendipitous result. Previous measurements at THe-Trap and its predecessors obtained a small *negative* value of θ^2, which corresponds to a small trap ellipticity (see subsection 2.10.1). We cannot rule out that a true magnetron angle of 0.1° remains, which might be masked by a minute amount of trap ellipticity. Fortunately, neither the ellipticity nor the trap angle are of any significance in the ω_c determination via the invariance theorem [57].

5.1.4. Fine trap tuning: Measuring $U_{\mathrm{G},0}$, K_6, and $\hat{\rho}_-$

The most accurate determination of the optimal guard voltage $U_{\mathrm{G},0}$ is based on increasing the magnetron radius with a resonant RF pulse, and recording the resulting shift of the axial frequency (indirectly, by recording the shift of the lock voltage U_{FS}). The ion is then cooled and the measurement repeated, using different RF pulse amplitudes and different guard voltages U_{G}. As will be shown below, the optimal guard voltage $U_{\mathrm{G},0}$ can be found as the voltage where the axial frequency, up to second order, is independent of the pulse amplitude (Figure 5.1). The magnetron pulse measurement shown in Figure 5.1 can also reveal the absolute magnetron radius after a given pulse, and the K_6 parameter of the trap. To derive the appropriate formulas, let us describe the pulse measurements in more detail.

The magnetron-pulse measurements begin by setting U_{G} to the desired value, cooling the radial modes of the ion to the thermal limits $\hat{\rho}_{-,\mathrm{th}}$, $\hat{\rho}_{+,\mathrm{th}}$, and bringing the ion into axial frequency lock at the lowest convenient amplitude $\hat{z}_{\mathrm{det}}$. Then the magnetron radius $\hat{\rho}_-$ is increased by applying a pulse with frequency ω_-, amplitude U_{pulse}, and duration t_{pulse} to one half of the lower guard electrode. Assuming the pulse is strong enough to increase $\hat{\rho}_-$ well above $\hat{\rho}_{-,\mathrm{th}}$, the final amplitude of the magnetron mode is given by

$$\hat{\rho}_- = \hat{\rho}_{-,\mathrm{cal}}\, U_{\mathrm{pulse}}\, t_{\mathrm{pulse}} \quad . \tag{5.1}$$

Here, $\hat{\rho}_{-,\mathrm{cal}}$ is an unknown calibration factor. In principle, this calibration factor can be calculated from the guard electrode's electric potential component $b_{\mathrm{G},1,1}$, the ion's charge-to-mass ratio, and the properties of the cryogenic filter that the excitation signal has to pass through. However, since the properties of the cryogenic filters are difficult to measure, and since parasitic coupling between the trap electrodes modifies the electric field strength inside the trap, $\hat{\rho}_{-,\mathrm{cal}}$ has to be determined experimentally (shown below).

Using the formulas from section 2.10, we can state the expected shift of the axial frequency as a function of the magnetron radius up to fourth order:

$$\Delta\omega_{z,\rho_-} = -\frac{3}{2}\frac{K_4}{K_2}\omega_z\hat{\rho}_-^2 + \frac{45}{16}\frac{K_6}{K_2}\omega_z\hat{\rho}_-^4 \quad . \tag{5.2}$$

This formula is the result of several simplifications: We exploit the fact that $\hat{\rho}_{+,\mathrm{th}}$ and $\hat{z}_{\mathrm{det}}$ are not changed by the pulse, so that their K_4, B_2 and relativity shifts cancel out. Furthermore, $\hat{\rho}_{-,\mathrm{th}}$ and $\hat{z}_{\mathrm{det}}$ are small enough so that mixing terms in the K_6-related formula can be neglected. And finally, the B_2 shift (Equation 2.86) and the relativistic shift (Equation 2.91) caused by the magnetron radius are dropped, because they can be shown to be negligible for typical trap parameters.

The axial frequency shift causes a change of the lock-voltage U_{FS}. Using Equation (2.49) and $\Delta U_{\mathrm{R}} = \Delta U_{\mathrm{FS}}/a_{\mathrm{div}}$ (see section 3.6), the voltage shift can be related to the axial frequency shift

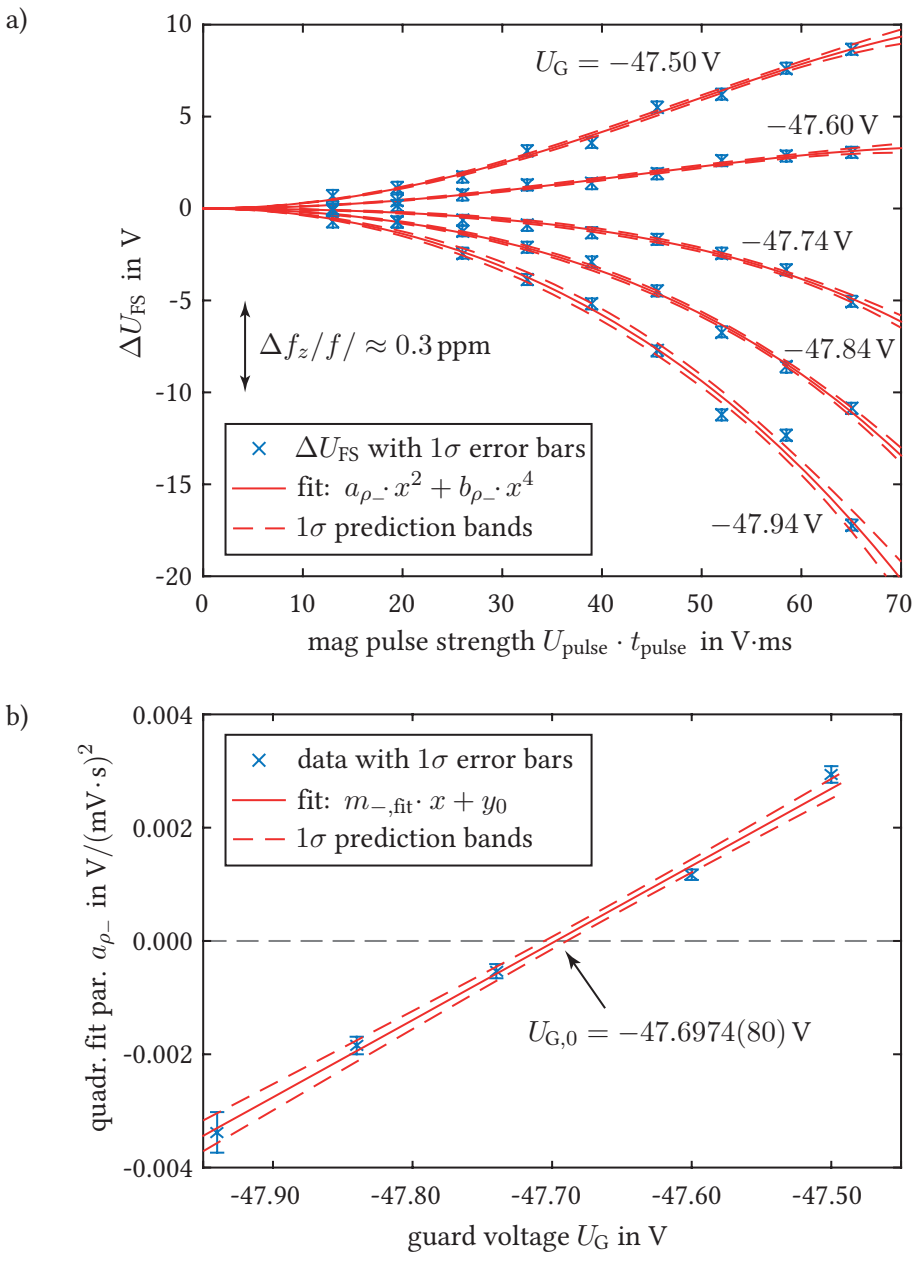

Figure 5.1.: Magnetron pulse measurement on a $^{12}C^{4+}$ ion. a) At different guard voltages U_G, the magnetron amplitude is increased with various pulse strengths, and the resulting shifts in the lock voltage U_{FS} are recorded. The curves are fitted with functions of the form $y = a_{\rho_-} \cdot x^2 + b_{\rho_-} \cdot x^4$. b) Plotting the quadratic fit parameter a_{ρ_-} vs. U_G, the optimal guard voltage $U_{G,0}$ can be extrapolated as the value where $a_{\rho_-} \equiv 0$.

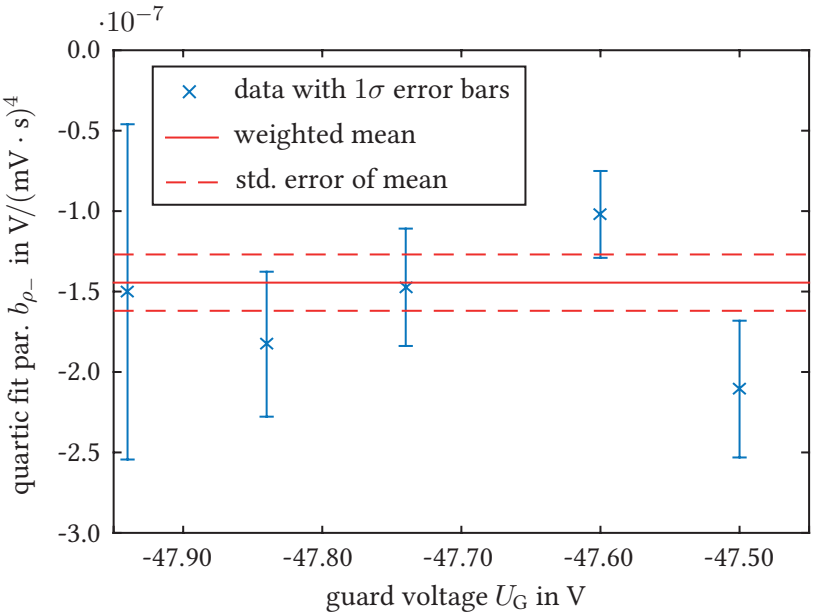

Figure 5.2.: K_6 from magnetron pulse measurement (Figure 5.1). The fitted quartic parameter b_{ρ_-}, which corresponds to a K_6-shift of the axial frequency, is independent of the guard voltage. Repeating this measurement with different ions reveals that K_6 scales with the ring voltage U_R.

by the formula

$$\Delta\omega_z = -\frac{1}{a_{\text{div}}}\frac{\omega_z}{2U_R}\Delta U_{FS} \quad . \tag{5.3}$$

Finally, the K_2 and K_4 parameters of the trap can be expressed as (subsection 2.7.2)

$$K_2 = \frac{m}{2q}\omega_z^2 \quad , \tag{5.4}$$

$$K_4 = (U_G - U_{G,0})\, b_{G,4,0} \quad , \tag{5.5}$$

with $b_{G,4,0} = -5.34(36) \cdot 10^{-4}\,\text{mm}^{-4}$ known from finite element simulations of the trap's electrostatic properties (see Table 4.3 in [70]). These formulas can be combined to express the shift of the lock voltage as a function of the magnetron pulse strength and guard voltage:

$$\begin{aligned}\Delta U_{FS} =& \frac{6\,q\,a_{\text{div}}\,U_R\,b_{G,4,0}}{m\omega_z^2}\hat{\rho}_{-,\text{cal}}^2\,(U_G - U_{G,0})\,\left(U_{\text{pulse}}\,t_{\text{pulse}}\right)^2 \\ &- \frac{45\,q\,a_{\text{div}}\,U_R}{4m\omega_z^2}K_6\,\hat{\rho}_{-,\text{cal}}^4\,\left(U_{\text{pulse}}\,t_{\text{pulse}}\right)^4 \quad .\end{aligned} \tag{5.6}$$

This formula looks complicated, but isn't. Almost all constants in it are known, only $U_{G,0}$, $\hat{\rho}_{-,\text{cal}}$, and K_6 are unknown. On the experimental side, each of the ΔU_{FS} vs. U_{pulse} curves (one for

each guard voltage U_G) can be fit with a function of the form

$$\Delta U_\mathrm{FS} = a_{\rho_-} \left(U_\mathrm{pulse}\, t_\mathrm{pulse}\right)^2 + b_{\rho_-} \left(U_\mathrm{pulse}\, t_\mathrm{pulse}\right)^4 \tag{5.7}$$

Comparing both formulas, it becomes obvious that a_{ρ_-} must be a linear function of the guard voltage:

$$a_{\rho_-}\left(U_\mathrm{G}\right) = \underbrace{\frac{6\, q\, a_\mathrm{div}\, U_\mathrm{R}\, b_{\mathrm{G},4,0}}{m\omega_z^2}\hat{\rho}_{-,\mathrm{cal}}^2}_{=\, m_{\text{-,fit}}} \left(U_\mathrm{G} - U_{\mathrm{G},0}\right) \tag{5.8}$$

Plotting a_{ρ_-} against U_G shows this linear dependence (Figure 5.1, b). The optimal guard voltage $U_{\mathrm{G},0}$ can be read off as the zero-crossing of the line, and the slope $m_{\text{-,fit}}$ of the line can be used to determine $\hat{\rho}_{-,\mathrm{cal}}$:

$$\hat{\rho}_{-,\mathrm{cal}} = \sqrt{\frac{m\,\omega_z^2\, m_{\text{-,fit}}}{6\, q\, a_\mathrm{div}\, U_\mathrm{R}\, b_{\mathrm{G},4,0}}} \quad . \tag{5.9}$$

With this knowledge of $\hat{\rho}_{-,\mathrm{cal}}$, the fit parameters b_{ρ_-} can be used to calculate K_6:

$$K_6 = \frac{-4\, m\, \omega_z^2\, b_{\rho_-}}{45\, q\, a_\mathrm{div}\, U_\mathrm{R}\, \hat{\rho}_{-,\mathrm{cal}}^4} \quad . \tag{5.10}$$

The resulting values are summarized in Table 5.1.

5.1.5. Measuring B_2 and $\hat{\rho}_+$

A pulse measurement can also be performed by pulsing the cyclotron mode instead of the magnetron mode. As with the magnetron pulse, the cyclotron pulse response can be modeled as

$$\hat{\rho}_+ = \hat{\rho}_{+,\mathrm{cal}}\, U_\mathrm{pulse}\, t_\mathrm{pulse} \quad . \tag{5.11}$$

The axial frequency shift $\Delta\omega_z$ as a function of $\hat{\rho}_+$ is slightly more complicated than the corresponding $\hat{\rho}_-$ shift, because the B_2-term and the relativistic term cannot be neglected. Assuming, however, that there is no relevant B_4-term, the shift can be stated as

$$\Delta\omega_{z,\rho_+} = \left(-\frac{3}{2}\frac{K_4}{K_2}\omega_z + \frac{1}{2}\frac{B_2}{B_0}\frac{\omega_c\omega_+}{\omega_z} - \frac{1}{4}\frac{\omega_+^2\omega_z}{c^2}\right)\hat{\rho}_+^2 + \frac{45}{16}\frac{K_6}{K_2}\omega_z\hat{\rho}_+^4 \quad . \tag{5.12}$$

The general structure of this equation is equivalent to the magnetron pulse shift in Equation (5.2), only that there are extra terms in the quadratic $\hat{\rho}_+$-dependence. These terms modify the guard voltage at which the quadratic dependence vanishes. Instead of being at the guard voltage that makes $K_4 \equiv 0$, the "optimal cyclotron guard voltage" $U'_{\mathrm{G},0}$ leads to a non-zero K_4 that cancels the relativistic and the B_2 terms. The difference between $U'_{\mathrm{G},0}$ and $U_{\mathrm{G},0}$ can be used to calculate B_2:

$$B_2 = \frac{6\, b_{\mathrm{G},4,0}}{\omega_+ - \omega_-}\left(U'_{\mathrm{G},0} - U_{\mathrm{G},0}\right) + \frac{\omega_z^2}{2c^2}B_0 \quad . \tag{5.13}$$

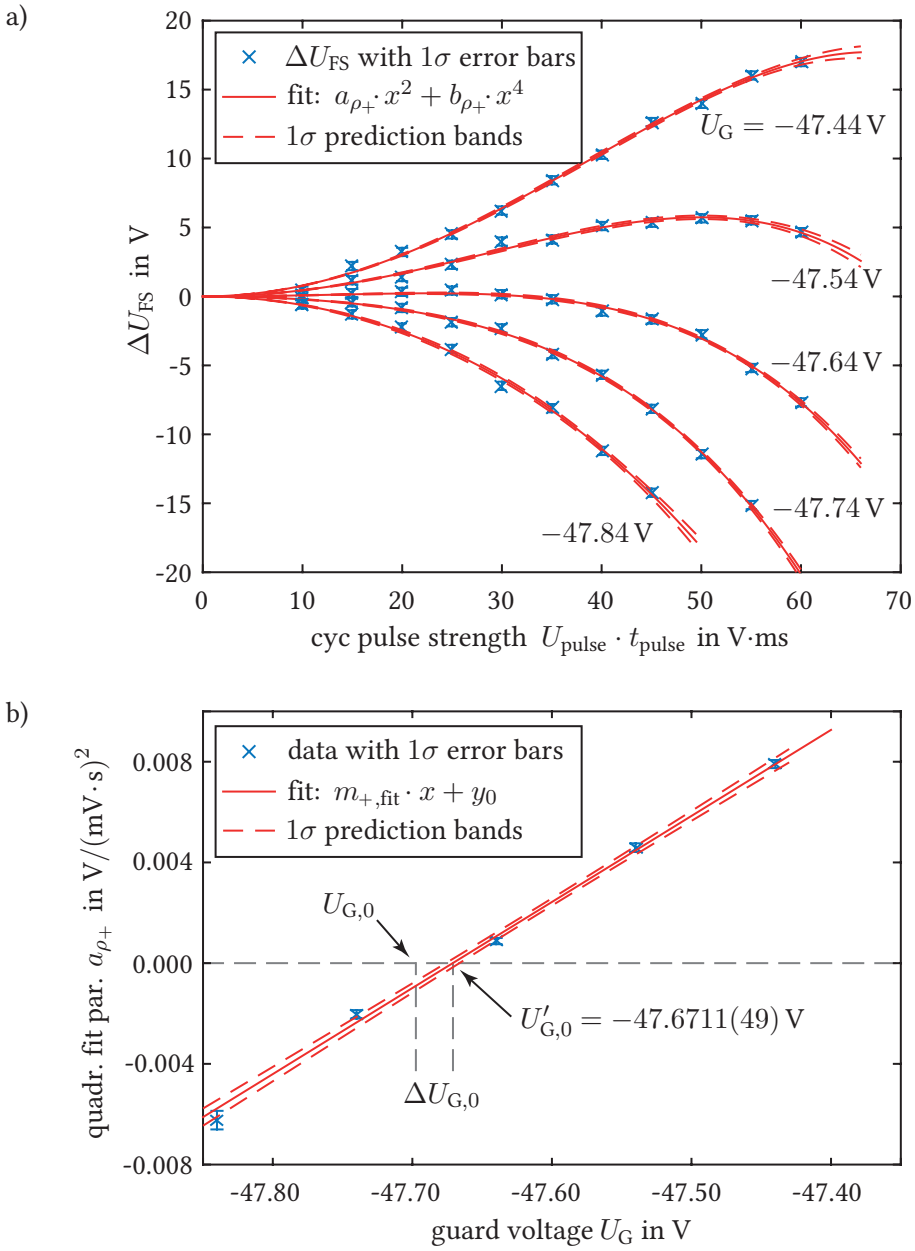

Figure 5.3.: Cyclotron pulse measurement on a $^{12}C^{4+}$ ion. This measurement is equivalent to the magnetron pulse measurement shown in Figure 5.1, only that here the cyclotron mode is pulsed. Since the quadratic dependence of $\Delta\omega_z$ on $\hat{\rho}_+$ is not only given by K_4, but also by B_2 and relativity, the "optimal guard voltage" in the plot b) is shifted by $\Delta U_{\mathrm{G},0}$. This can be used to determine B_2.

This formula follows from comparing Equation (5.12) with Equation (5.2)[4]. The analysis of $\hat{\rho}_{+,\mathrm{cal}}$ and K_6 is analogous to the magnetron pulse measurement. The experimental data is fit in the same way as the magnetron pulse measurements, and $\hat{\rho}_{+,\mathrm{cal}}$, K_6 can be calculated from the fit parameters as

$$\hat{\rho}_{+,\mathrm{cal}} = \sqrt{\frac{m\,\omega_z^2\,m_{+,\mathrm{fit}}}{6\,q\,a_{\mathrm{div}}\,U_{\mathrm{R}}\,b_{\mathrm{G},4,0}}} \quad , \tag{5.14}$$

$$K_6 = \frac{-4\,m\,\omega_z^2\,b_{\rho_+}}{45\,q\,a_{\mathrm{div}}\,U_{\mathrm{R}}\,\hat{\rho}_{+,\mathrm{cal}}^4} \quad . \tag{5.15}$$

The K_6-measurements of the magnetron mode and the cyclotron mode fortunately agree very well with another, validating that the assumption $B_4 = 0$ is true within the uncertainty of the measurement. Alternatively, the difference can be analyzed to yield $B_4 = 0.2(1.7)\cdot 10^{-6}\,\mathrm{T/mm^4}$. The results of the cyclotron pulse measurements are shown in Table 5.1.

5.1.6. Practical considerations for the pulse measurements

The effective "pulse strength" is given by $t_{\mathrm{pulse}} \cdot U_{\mathrm{pulse}}$. There are practical limits for t_{pulse}, U_{pulse}, and for the overall pulse strength. In order for the linear pulse-response model of Equation (5.1) and Equation (5.11) to be true, the overall pulse strength must neither be too weak nor too strong. If it is too weak, then the final radius is confounded by the thermal amplitude. If it is too strong, the electric field that drives the mode can no longer assumed to be homogeneous. At THe-Trap, however, simulations of the electrostatic properties have shown that the assumption of homogeneity holds true within 1% for ion amplitudes up to 500 μm.

The pulse time t_{pulse} must be chosen short enough, such that uncertainties of the excitation frequency (for example, caused by anharmonic frequency shifts) are well within the Fourier spectrum of the pulse. At THe-Trap, an excitation time of 50 ms is used.

The pulse amplitude U_{pulse} is limited by the amplifier, which can be damaged if too strong excitation signals are used. For pulses that are not resonant with the detection circuit, applying $3\,\mathrm{V_{pp}}$ at the experiment header (the input of the cryogenic filters) is safe. This limit implies that at THe-Trap, pulses much shorter than 50 ms are impractical.

In principle, it is possible to speed up the pulse measurements by only pulsing the ion once for each amplitude value, and measuring U_{FS} for different values of U_{G} without cooling and pulsing the ion in between. We tried this method extensively, but slow, random drifts of the ring voltage make this shortcut unfeasible.

5.1.7. Calibrating the axial mode

Due to the continuous damping by the tuned circuit, the axial amplitude is not increased through pulses, but by using a stronger, continuous drive. The resulting axial amplitude can be modeled as

$$\hat{z} = \hat{z}_{\mathrm{cal}} U_{\mathrm{drive}} \quad , \tag{5.16}$$

[4] To be more precise, the comparison was done with a version of Equation (5.2) that still had the B_2 shift and the relativity shift in it. This makes the result shorter and easier to evaluate.

with unknown calibration factor $\hat{z}_{\text{cal}}$. Within the easily-accessible axial amplitude regime, the axial frequency shifts are typically not very pronounced compared to the typical scatter of U_{FS}. Therefore, the axial amplitude calibration takes considerably longer than the equivalent radial pulse measurements (12 hours vs. 2 hours).

The relativity shift is insignificant in this case, so the relevant terms of the axial frequency shift can be simplified to

$$\Delta\omega_{z,\hat{z}} = \frac{3}{4}\frac{K_4}{K_2}\omega_z\hat{z}^2 + \frac{15}{16}\frac{K_6}{K_2}\omega_z\hat{z}^4 \quad . \tag{5.17}$$

The K_6 effect is too subtle to be fitted directly. Another difficulty, from an experimental standpoint, is that the lowest convenient axial drive[5] $U_{\text{drive},0}$ for the axial frequency lock already corresponds to an amplitude $\hat{z}$ that can cause appreciable frequency shifts. But modeling the lock voltage as $U_{\text{FS}}(U_{\text{drive}}) = U_{\text{FS},0} + a_{\hat{z}} \cdot U_{\text{drive}}^2$ allows us to fit the *changes* of the lock voltage as

$$\Delta U_{\text{FS}} = a_{\hat{z}} \left(U_{\text{drive}}^2 - U_{\text{drive},0}^2\right) \quad , \tag{5.18}$$

with $a_{\hat{z}}$ as the fit parameter. These fits are shown in Figure 5.4. These fits showcase one major problem of the measurements, where the axial amplitude is varied: For low axial amplitudes, the fits do not match the data well. One possible reason is the $\Delta\omega_{z,\text{offset}}$ shift, which is inversely proportional to $\hat{z}$. It can skew the measurements at low amplitudes enough to interfere with the simple quadratic and quartic fit models. Still, as a first measure, the fits can be analyzed and the $\Delta\omega_{z,K_6}$ and $\Delta\omega_{z,\text{offset}}$ problems can be fixed later.

Despite the $\Delta\omega_{z,K_6}$ and $\Delta\omega_{z,\text{offset}}$ problems, the fit parameter $a_{\hat{z}}$ appears to depend linearly on the guard voltage U_{G}, as expected. But the zero-crossing of the $a_{\hat{z}}$ vs. U_{G} plot (the "axially optimal guard voltage" $U''_{\text{G},0}$) is offset from the $\hat{\rho}_-$-pulse result by approximately 30 mV. Still, the slope $m_{z,\text{fit}}$ of this plot can be compared to the theoretically expected value, to obtain the axial amplitude calibration factor $\hat{z}_{\text{cal}}$:

$$\hat{z}_{\text{cal}} = \sqrt{\frac{-m\,\omega_z^2\,m_{z,\text{fit}}}{3\,q\,a_{\text{div}}\,U_{\text{R}}\,b_{\text{G},4,0}}} \quad . \tag{5.19}$$

Finally, this value of $\hat{z}_{\text{cal}}$ can be used to predict the K_6 effect and correct the data for it. This only slightly changes the fit, and moves the axially optimal guard voltage $U''_{\text{G},0}$ approximately 5 mV closer to the expected value $U_{\text{G},0}$. However, when assuming a suitable DC-offset[6] in the feedback loop, and correcting the data for it, the fits start to match the data, and the axially optimal guard voltage becomes equal to the expected value. Fortunately, neither correction changes the slope in the $a_{\hat{z}}$ vs. U_{G} plot, so the value of $\hat{z}_{\text{cal}}$ stays unchanged.

The corresponding measurements on a $^{16}O^{5+}$ ion did not show such a shift, suggesting that the DC offset had drifted to a more favorable level. The results of the calibrations are shown in Table 5.1.

[5] The axial drive strength is given by the ring modulation U_{mod} and the drive applied to the endcap U_{drive}. Both signals pass through attenuators, filters, and splitters. We defined a certain setting of the synthesizers and attenuators as "1 V axial drive", but this is completely arbitrary.

[6] The assumption was $U_{\text{offset}} = -12$ mV (a wrong setting of -0.03 mV in our "Controller" program), which is three times bigger than the measurement uncertainty of the optimal U_{offset}.

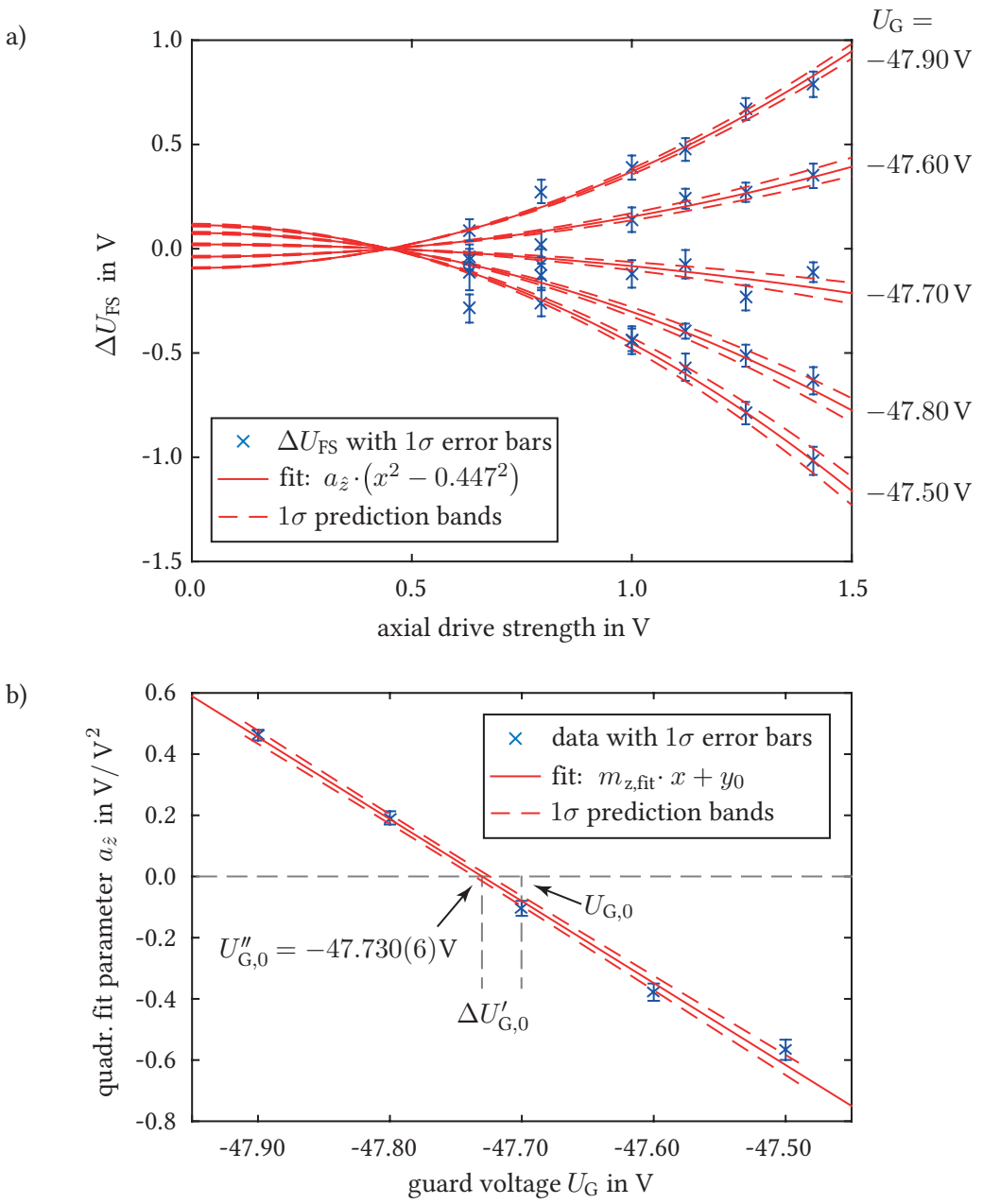

Figure 5.4.: Axial amplitude calibration of a $^{12}C^{4+}$ ion. These shifts caused by easily accessible $\hat{z}$ are less pronounced than in the $\hat{\rho}_-$ and $\hat{\rho}_+$ pulse measurements. At low amplitudes, the fits don't match the data well. Further, the axial "optimal" guard voltage $U''_{G,0}$ is offset from the $\hat{\rho}_-$ pulse result by 33(7) mV (b). This offset disappears when correcting for the K_6-shift and by assuming a small DC-offset error.

Table 5.1.: Results of a typical trap calibration. The uncertainty of f_z is given by the uncertainty in the $\Delta\omega_{z,\text{phase}}$ and $\Delta\omega_{z,\text{offset}}$ shifts. The K_6 parameter is given as K_6/K_2, so that it can be compared more easily to the result at the FSU trap in Table 6.1.

Property	Symbol	$^{12}C^{4+}$	$^{16}O^{5+}$
f_z	f_z	4 057 520.000(7) Hz	4 057 520.000(7) Hz
f_- extrapolated to $\hat{z}=0$	f_-	309 342.018(5) Hz	330 397.266(5) Hz
f_+ extrapolated to $\hat{z}=0$	f_+	26 610 465.45(3) Hz	24 914 658.77(2) Hz
magnetron radius calibration	$\hat{\rho}_{-,\text{cal}}$	3.11(11) μm/(mV·s)	3.10(11) μm/(mV·s)
cyclotron radius calibration	$\hat{\rho}_{+,\text{cal}}$	4.84(18) μm/(mV·s)	4.97(17) μm/(mV·s)
axial radius calibration	$\hat{z}_{\text{cal}}$	66.0(2.8) μm/V	44.4(2.9) μm/V
ring voltage	U_R	−91.096 40(10) V	−97.143 17(5) V
optimal guard voltage	$U_{G,0}$	−47.693(8) V	−50.949(5) V
K_6 (aver. $\hat{\rho}_-$ and $\hat{\rho}_+$ meas.)	K_6/K_2	$-3.0(5)\cdot 10^7/\text{m}^4$	$-3.0(5)\cdot 10^7/\text{m}^4$
magnetic bottle	B_2	−0.43(19) T/m^2	−0.50(13) T/m^2
trap misalignment angle	θ	$< 0.01°$	$< 0.01°$
measured modulation amp.	U_{mod}	33.3(1.5) mV	34.3(1.5) mV
typ. axial signal strength	$U_{\text{err},0}$	166(20) mV	224(50) mV
DC-offset uncertainty	δU_{offset}	4 mV	
opt. detection phase	$\varphi_2-\varphi_1$	284.1(2.0)°	

5.1.8. Comparison with old characterization method

We did extensive calibration measurements with the old method as well to compare the two methods. For example, we measured f_+ as a function of the axial amplitude, or more precisely, as a function of U_{drive}. Using the known values of K_4, K_6, B_2, and the axial calibration constant $\hat{z}_{\text{cal}}$, we can predict the shift and compare it to the data. This is shown in Figure 5.5 for f_- and f_+ measurements on a $^{12}C^{4+}$ ion, where only the frequency offset was fit. In all our measurements, the predicted shifts were in excellent agreement with the measured shifts.

We used both shift measurement methods to extrapolate f_+, f_-, and ultimately f_c to zero axial amplitude. The accuracies of both methods are approximately the same. The main advantage of the new shift measurement method is that it allows measuring of the optimal guard voltage, K_6 and B_2 more reliably than the old method. Another advantage is its speed (4 hours vs. 24 hours), which allows for devoting more measurement time to gaining statistics of the frequency measurements at the optimal settings of the trap. Furthermore, the new shift measurement method allows us to calculate the "magic guard voltage" $U_{\text{G, magic}}$, at which the cyclotron mode is harmonic with respect to its own radius $\hat{\rho}_+$. This is important, since it makes the upsweeps and downsweeps become symmetric, which results in reduced systematic fitting errors. Using Equation (2.81) and Equation (2.93), the value of the magic guard voltage can be calculated as

$$U_{\text{G, magic}} = U_{G,0} - \frac{B_0}{3c^2}\frac{\omega_+^3}{b_{G,4,0}} \quad , \tag{5.20}$$

with B_0 signifying the strength of the magnetic field. Typical differences between $U_{\text{G, magic}}$ and

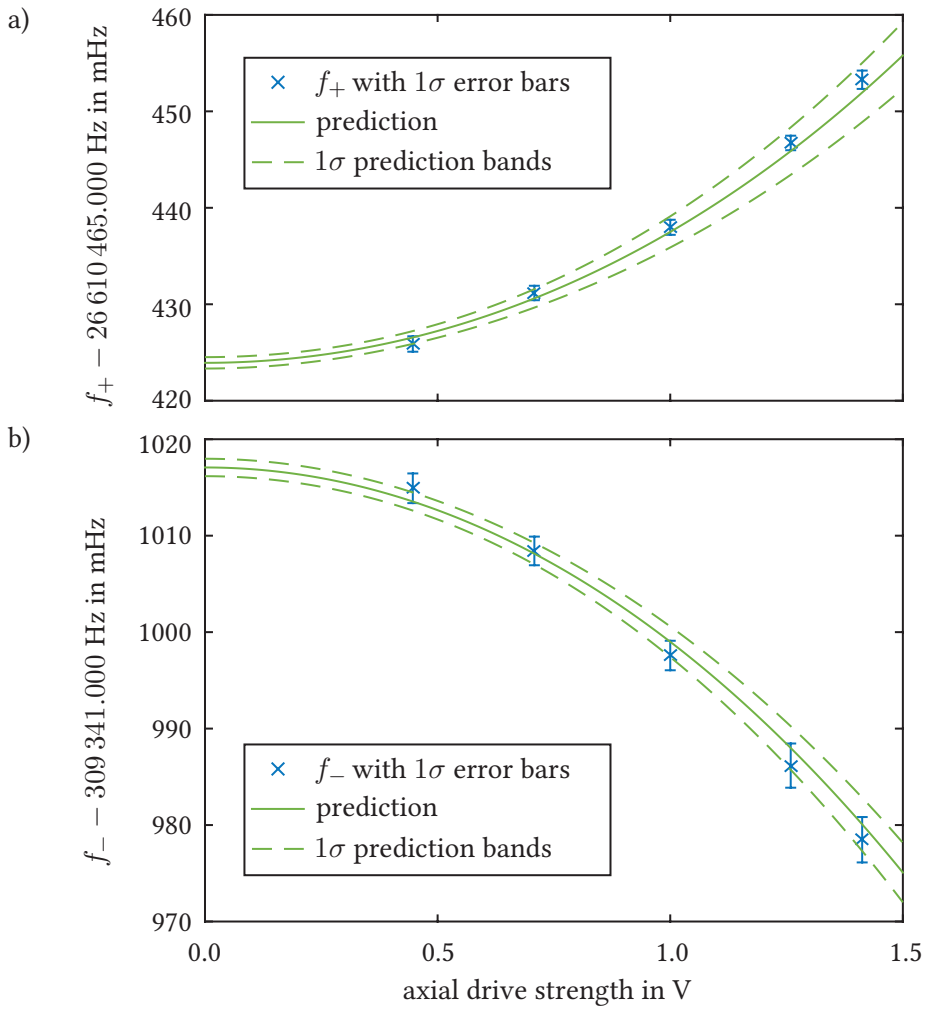

Figure 5.5.: Prediction of the f_+, f_- vs. $\hat{z}$ shifts for a $^{12}C^{4+}$ ion. Using the results of the pulse measurements, the radial frequency shifts can be predicted. In these curves, only a constant frequency offset was fit to the data, with the curvature given through the predictions of K_4, K_6, B_2 and relativity shifts.

$U_{G,0}$ are 200 mV. In the past, we determined $U_{G,\,\mathrm{magic}}$ by adjusting the guard voltage until the sweeps appeared symmetric [94]. However, once the calibration measurements allowed us to calculate $U_{G,\,\mathrm{magic}}$, we had to learn that the old method was a lot less sensitive than initially assumed, and that we often used values for $U_{G,\,\mathrm{magic}}$ that were wrong by as much as 100 mV.

5.2. Improved measurements of other shifts

The quadratic $\Delta\omega_{z,\mathrm{mod}}$ shift was used to calibrate the absolute magnitude of the ring modulation signal U_{mod} at the ring electrode. The measurement was carried out by observing the lock voltage U_{FS} while increasing the strength of U_{mod}. The strength of U_{drive} was simultaneously decreased to keep the overall axial drive strength, and thereby the axial amplitude, constant. The results are summarized in Table 5.1. The value stated in the table corresponds to the typical U_{mod} used in most measurements. We used the same U_{mod} for both ions, which leads to slightly different ϵ parameters for both ions, and a serendipitous cancellation of the modulation shift in the cyclotron frequency ratio [118]. As a consistency check, we used a 10 dB stronger modulation signal for some of the measurements.

In order to rule out possible coil-pushing shifts, we used the spectrum analyzer to monitor the resonator's frequency f_{RLC} during the f_+ measurements. We observed that every few hours, f_{RLC} jumped down by 300 Hz, only to return to the nominal value approximately one hour later. A possible cause of these jumps are helium bubbles, which form at the amplifier, and which might get trapped inside the resonator housing. Since gaseous helium and liquid helium have different dielectric properties[7], the bubbles change the parasitic capacitance of the RLC-circuit, and thereby shift its frequency. Since the jumps were random in nature, and not long in duration, we accounted for them by assigning a common 100 Hz uncertainty to f_{RLC} in our coil-pushing shift estimates.

We further used the spectrum analyzer to optimize the phase offset $\varphi_2 - \varphi_1$ between the two channels of the modulation synthesizer (Figure 3.6). We measured the ion signal strength in lock as a function of $\varphi_2 - \varphi_1$. At the optimal phase difference, the signal strength is maximal. We determined the maximum using a quadratic fit. This measurement typically took 4 hours per ion and resulted in an uncertainty of approximately 1°. However, on repeated measurements, the scatter was twice as large as the uncertainty. This might have been caused by jumps of f_{RLC}, but could also have been caused by temperature-dependent phase-delays of the filters, mixers, and amplifiers used in the driving/detection hardware. We therefore assume an uncertainty of 2° in the optimal phase setting.

The DC-offset in the feedback loop was optimized by observing the drift of U_{FS} when no ion was present in the trap. In this case, the integrator in the feedback loop integrates noise (and a possible DC-offset). Our detection electronics allow adding or subtracting a small DC-offset in front of the integrator, and by measuring the drift velocity of U_{FS} as a function of the DC-offset setting, the optimal setting can be found with approximately 5 mV accuracy. This can be compared with the typical signal amplitudes of $U_{\mathrm{err},0} = 200$ mV to calculate the expected frequency shift $\Delta\omega_{z,\mathrm{offset}}$ (Equation 3.1).

[7] This effect is exploited in the level sensor that is part of the LHe-level-stabilization loop [106].

5.3. Mass measurements

Before and after each measurement run, we decided to do a full calibration routine to catch possible drifts of the relevant parameters. This calibration routine consisted of (with typical measurement times in parentheses):

- Taking an axial resonance (comparable to Figure 2.9) to measure the axial damping γ_z, which can be used to rule out multiple ions of the same species (1 hour)
- Measuring the optimal DC-offset, which should be the same for both ions (2 hours)
- Measuring the optimal detection phase difference $\varphi_2 - \varphi_1$ (4 hours)
- Doing a magnetron pulse calibration (4 hours)
- Doing a cyclotron pulse calibration (4 hours)
- Doing an axial amplitude calibration (12 hours)
- For comparisons: Measuring f_+ and f_- as a function of $\hat{z}$ (12 hours each)

A typical measurement run consisted of loading a single ion (25 minutes), measuring f_+ with four sweep-brackets[8], then expelling the ion from the trap and repeating the procedure with the other ion species. These steps were performed automatically by procedures described in our domain-specific language THe-Script [94]. The runs lasted between $10 - 50$ hours. We limited the runs to approximately 50 hours, because we had observed that the frequent trap reloading changed the effective K_2 and K_4 of the trap, prompting recalibrations. The fundamental limit of a measurement run is given by the 3 weeks hold time of the magnet's LN_2 reservoir.

We took several runs with different values for the axial drive and ring modulation amplitudes (see Table 5.2) to exclude systematic effects. The data was analyzed in the manner of a blind analysis, by doing the comparison of the measured cyclotron frequency ratio R to the expected literature value as the very last step in the analysis.

Each f_+ sweep-bracket was fitted with a semi-automatic fit procedure [54, 94], as showin in Figure 3.8. The fitted f_+ values were combined with measurements of f_- and the value of f_z given by the detection system (the axial frequency lock) to calculate f_c values via the invariance theorem (Equation 2.77). The drift of the f_c values over time was then fitted with an Nth-degree polynomial of the form

$$f_c(t) = f_0 + f_1 t + \cdots + f_N t^N \; + \; f_{\text{diff}} \cdot \delta(\text{ion}) \quad , \tag{5.21}$$

where $\delta(\text{ion}) = 0$ for the $^{12}C^{4+}$ data and $\delta(\text{ion}) = 1$ for the $^{16}O^{5+}$ data (see Figure 5.6). This model assumes a common drift for the cyclotron frequencies of both ions, which is adequate, since the cyclotron frequencies only differ by approximately 6%. Inspired by the FSU experiment, the optimal degree of the polynomial was determined using an F-test [115, 119]. At the FSU, it was found that the exact degree of the fit polynomial has little influence on the ratio R, and our results agree with this assessment. One fit example is shown in Figure 5.6.

[8] Each sweep-bracket consists of a four-minute upsweep, a three-minute cooling period, a four-minute downsweep, and another three-minute cooling period. The total f_+ measuring time per ion is approximately 1 hour.

Table 5.2.: Parameters used for the $^{12}C^{4+}/^{16}O^{5+}$ mass ratio measurements at THe-Trap. The axial drive signal and modulation signal are routed through variable attenuators, with 20 dB of axial drive attenuation and 10 dB of modulation attenuation defined as a nominal drive voltage of 1 V. The results are given in Table 5.4.

Run	A	B	C	D
Ax. drive attenuation	26 dB	17 dB	15 dB	10 dB
Mod. attenuation	10 dB	20 dB	20 dB	20 dB
$U_{G,0}$ of $^{12}C^{4+}$	$-47.699(5)$ V	$-47.697(5)$ V	$-47.692(5)$ V	$-47.686(5)$ V
$U_{G,\,set}$ of $^{12}C^{4+}$	-47.500 V	-47.500 V	-47.500 V	-47.500 V
$U_{G,0}$ of $^{16}O^{5+}$	$-50.956(5)$ V	$-50.955(5)$ V	$-50.945(5)$ V	$-50.934(5)$ V
$U_{G,\,set}$ of $^{16}O^{5+}$	-50.820 V	-50.820 V	-50.820 V	-50.820 V
Measurement time	53 h	23 h	26 h	9 h
Number of f_+ brackets	134	64	68	28
δR_{stat}	23 ppt	34 ppt	33 ppt	50 ppt

The cyclotron frequency ratio $R = f_{c_1}/f_{c_2}$ can be calculated from the fit-parameters f_0 and f_{diff} via

$$R = \frac{f_0}{f_0 + f_{diff}} \quad . \tag{5.22}$$

5.3.1. Statistical uncertainty

The semiautomatic fit-procedure of the f_+ sweep brackets does not yield an estimate of the statistical uncertainty $\delta f_{+,stat}$. Therefore, the statistical uncertainty of R is determined via the *scatter* of the f_+ brackets, which is reflected in the uncertainties δf_0 and δf_{diff} of the fit parameters. Using standard error propagation, δR_{stat} can be calculated as

$$\delta R_{stat} = \sqrt{\left(\frac{f_{diff}}{(f_0 + f_{diff})^2}\delta f_0\right)^2 + \left(\frac{f_0}{(f_0 + f_{diff})^2}\delta f_{diff}\right)^2} \tag{5.23}$$

$$\approx \frac{f_0}{(f_0 + f_{diff})^2}\delta f_{diff} \quad . \tag{5.24}$$

The last simplification makes use of the fact that $f_{diff} \ll f_0$ and $\delta f_{diff} \approx \delta f_0$. A typical statistical uncertainty of a 24-hour measurement run is $\delta R_{stat} \approx 30$ ppt (parts per 10^{12}).

5.3.2. Systematic uncertainty

The systematic shifts and the shift-uncertainties (the *systematic errors*) of the eigenfrequencies f_+, f_-, f_z were calculated for each run, using the run-parameters given in Table 5.2. The shifts of the eigenfrequencies were then used to calculate the shift of the free-space cyclotron frequency f_c of each ion, and subsequently used to calculate the shift of the the measured cyclotron frequency ratio R. Many of the shifts share a dependence on the same set of parameters. For

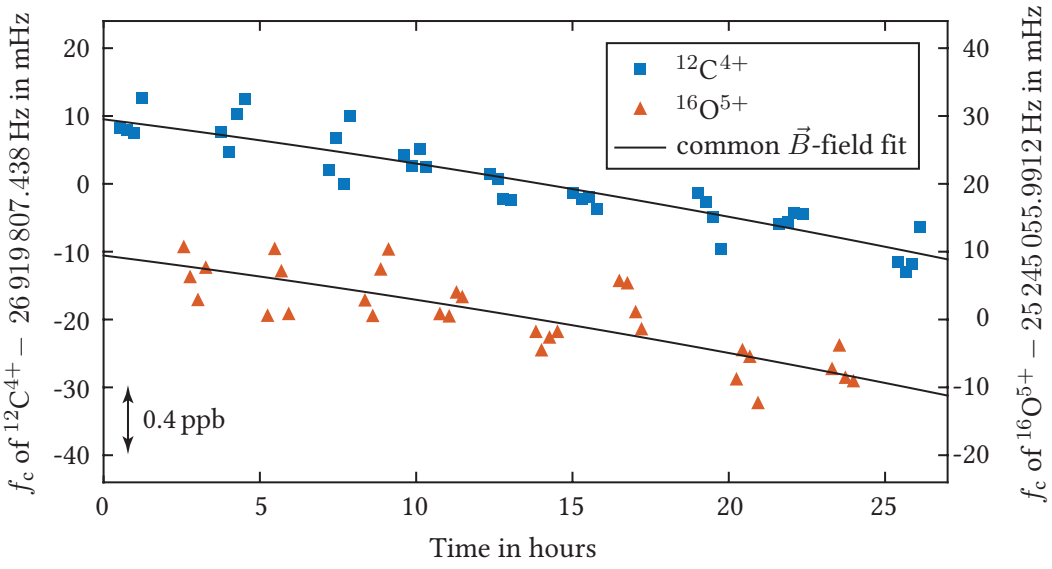

Figure 5.6.: Typical frequency ratio measurement on a $^{12}C^{4+}/^{16}O^{5+}$ ion pair. The cyclotron frequencies were fitted with a model that assumes a common B-field drift. In this measurement run (Run C from Table 5.2), the F-test suggested a second order polynomial to describe the B-field drift.

example, $\hat{z}_{\text{cal}}$ is needed for evaluating the K_4 and K_6-related shifts of f_z and f_+. Therefore, the uncertainties of the shifts (the systematic errors) can be strongly correlated.

These correlations were treated using the Monte-Carlo method [120]: The shifts were calculated using parameters that were drawn from appropriate random distributions, corresponding to the values given in Table 5.1 and Table 5.2. The calculation was repeated a large number of times, each time drawing the parameters anew from the random distributions. The calculation results were recorded and analyzed. The mean value and the standard deviation of the calculated shifts determine the shifts and their uncertainties, respectively. The calculations showed that most shifts were negligible on a 10^{-11}-level. The relevant shifts are given in Table 5.3. These shifts were caused by:

DC-Offset The uncertainty in optimal DC-offset of the error-signal (see section 3.6) leads to a relative uncertainty of f_z of up to 2 ppb. This results in a relative f_c uncertainty of up to 50 ppt. However, since the optimal DC-offset for both ions is the same, the shifts are mostly common mode, so that the resulting systematic error of R was, at most, 13 ppt.

Coil pushing The jumps of the coil-frequency (see section 5.2) lead to a small "coil-pushing" effect (see subsection 2.6.4) and "phase-turning" effect (section 3.6), which can shift f_z by up to 1 ppb, leading to a relative f_c uncertainty of approximately 30 ppt. However, since the probability of the coil-frequency jumps is the same for both ions, the shift is mostly common mode. Furthermore, since less than a quarter of the data points are affected,

the average shift is suppressed even more. To be cautious, we assign an uncertainty of $\delta R = 10$ ppt to this shift.

Ring modulation The ring modulation shifts all eigenfrequencies by considerable amounts, and if f_c is determined via the invariance theorem, it can be shifted significantly. For run A, which used a stronger modulation signal, the cyclotron frequencies f_c were shifted by 200 ppt, in the other runs by 20 ppt. However, this shift is common mode. Furthermore, we used the same modulation amplitude for both ions, which meant that the modulation indexes were slightly different (since the ions are trapped with different ring voltages). In this case, the relative shift of the ratio R is fortuitously suppressed by a factor of 200, which makes this shift irrelevant.

$\boldsymbol{K_4}$ The K_4-parameter was deliberately detuned to make the cyclotron mode harmonic with respect to its own energy. The "magic" K_4-parameter (see Equation 5.20) scales with f_c^3, leading to different K_4 parameters for the two ions. The uncertainty of K_4 is approximately 5 mV, which includes possible drifts caused by frequent reloading of the trap. The main amplitude that causes appreciable K_4-shift is the continuously driven axial amplitude $\hat{z}$. This amplitude is also different for the two ions, which leads to f_c-shifts that are significantly different for the two ions: Typically 200 ppt for $^{12}C^{4+}$, and 70 ppt for $^{16}O^{5+}$. The resulting ratio shift is approximately 100 ppt, with an uncertainty of 15 ppt. Run D, which used larger axial amplitudes, was affected even more severely.

$\boldsymbol{B_2}$ The main B_2-shift is given by the $B_2 \cdot \hat{z}^2$-shift of f_+. Since the axial amplitudes are different for the ions, the shifts are quite dissimilar, with a relative f_c-shift of -40 ppt for the $^{16}O^{5+}$ ion, and -20 ppt for the $^{12}C^{4+}$ ion. The overall shift of R is in the order of $-20(5)$ ppt for the runs A−C.

$\boldsymbol{B_1 \cdot K_1}$ In the current configuration of the experiment, the endcaps cannot be DC-biased to move the electrostatic trap center along the z-axis. This prevents us from measuring B_1 and K_1 directly, but using a generous upper limit for the B-field gradient of $B_1 \leq 10^{-3}$ T/m (from measurements of the $\vec{B}$-field with an NMR probe [96] and simulations of expected gradients introduced by the trap material [70]), and assuming that the voltage offset of the endcaps is at most 100 mV (from observations of the maximum drop-voltage), the relative shifts of the cyclotron frequencies can be shown to be less than 200 ppt. Since this shift is mostly common mode, the ratio shift is less than 12 ppt.

Image charge The image charge effect leads to relative f_c-shifts of $-371(5)$ ppt for $^{12}C^{4+}$, and $-495(7)$ ppt for $^{16}O^{5+}$. The absolute ratio shift is 132(2) ppt. These shifts are large, but since the prediction of the image charge effects, which is based on electrostatic simulations [121], has a low uncertainty, the systematic error caused by the image charge effect is negligible on a 10^{-11} level.

Unfortunately, the analysis revealed that the average difference between upsweep and downsweep corner of the f_+ sweeps was 6 mHz for $^{16}O^{5+}$, but less than 1 mHz for $^{12}C^{4+}$. This difference between the upsweep and downsweep corner is mainly influenced by the amplitude of the f_+ excitation signal ("power broadening"). Usually, the excitation amplitude is chosen

such that the power broadening is minimal, a procedure that was accidentally omitted for the measurements. At the predecessor experiment of THe-Trap, the UW-PTMS, it was shown that the power broadening displaces the sweep-corners of the up- and downsweep symmetrically. Because up- and downsweeps are averaged, the power broadening does not shift the fitted value of the f_+ resonances. We confirmed these findings experimentally at THe-Trap, but did not take enough data to rule out influences on a 2 mHz level. Therefore, we must assign a 2 mHz systematic uncertainty to the f_+ measurements on $^{16}O^{5+}$, which leads to an additional systematic uncertainty of $\delta R_{\text{fit}} = 70$ ppt in the cyclotron frequency ratio. This, unfortunately, is the dominating uncertainty of our result, since the magnet quench prohibited us from taking additional data at the optimal setting of the f_+ excitation signal.

5.3.3. Final cyclotron frequency ratio

Table 5.4 shows the results of the individual runs, with the systematic shift-corrections applied. The statistical error, the systematic error, the fit error, and the total error are shown in parentheses, with the total error calculated by adding the other errors in quadrature.

The runs A—C were used to the calculate an average ratio, using the number of f_+ sweep-brackets as weights. The result is in excellent agreement with the literature value. Run D was used to confirm our understanding of the axial-amplitude related systematic shifts (see Table 5.4) and is also in excellent agreement with the literature value.

The uncertainty caused by the erroneously set upsweep/downsweep level unfortunately leads to an overall uncertainty that prevents the new measurement from being used in the next atomic mass evaluation. However, our greatly improved understanding of the systematic shifts prove that THe-Trap is ready for high-precision mass measurements.

5.4. About the lineshape

Even if the radial excitation power, which caused the 6 mHz difference between the upsweep and downsweep corners of the $^{16}O^{5+}$ cyclotron resonances, had been set correctly, a discussion of the validity of the fit-model employed at THe-Trap and, to some extent, the predecessor experiment, UW-PTMS) is warranted.

At the UW-PTMS, the linewidth of the cyclotron resonances was defined as the difference between the upsweep and the downsweep corners of the linear fits applied to the data [18]. By choosing appropriate excitation amplitudes, this linewidth was reduced to approximately 1 part in 10^{10}, which helped to build confidence that, by averaging over a large number of resonances, the center frequency can be determined with a relative uncertainty of $1 \cdot 10^{-11}$. However, since the linear fits use a large portion of the sweep-data to determine the corner frequencies, it could also be argued that the linewidth is given by, typically, one third of the sweep range (approximately 20 mHz, or 10^{-9} in relative terms). In this case, the lineshape has to be understood fairly well, if the center frequency is to be determined with 10^{-11} accuracy.

When comparing the theoretically expected lineshape (Figure 2.10) to the fit shown in Figure 3.8, the linear fit model can seem overly simplistic. For example, the horizontal line that is fitted to first part of the resonance (before energy is transferred) is biased by the “wiggles”: The wiggles all point in the same direction, so the line will be shifted (upwards, in the plot), with

Table 5.3.: Systematic shifts of the $^{12}C^{4+}$ (ion 1) and $^{16}O^{5+}$ (ion 2) measurements. The f_c shifts are given as relative shifts, while the R shifts are given as absolute shifts. All shifts are stated in parts-per-10^{12}. The systematic errors are given in parentheses. These shifts have to be subtracted from the measured values.

	A	B	C	D
$\Delta f_{\text{c, offset, 1}}$	0(39)	0(43)	0(35)	0(19)
$\Delta f_{\text{c, offset, 2}}$	0(40)	0(45)	0(36)	0(20)
ΔR_{offset}	0(12)	0(13)	0(10)	0(6)
$\Delta f_{\text{c, CP, 1}}$	0(30)	0(30)	0(30)	0(30)
$\Delta f_{\text{c, CP, 2}}$	0(40)	0(40)	0(40)	0(40)
ΔR_{CP}	0(10)	0(10)	0(10)	0(10)
$\Delta f_{\text{c, mod, 1}}$	$-204(18)$	$-20(2)$	$-20(2)$	$-20(2)$
$\Delta f_{\text{c, mod, 2}}$	$-206(18)$	$-21(2)$	$-21(2)$	$-21(2)$
ΔR_{mod}	1(0)	0(0)	0(0)	0(0)
$\Delta f_{\text{c},K_4,1}$	195(14)	154(11)	233(17)	717(52)
$\Delta f_{\text{c},K_4,2}$	66(8)	52(7)	74(9)	216(28)
ΔR_{K_4}	106(16)	84(13)	130(19)	413(56)
$\Delta f_{\text{c},B_2,1}$	$-40(10)$	$-32(8)$	$-50(12)$	$-159(39)$
$\Delta f_{\text{c},B_2,2}$	$-22(6)$	$-17(5)$	27(7)	$-87(23)$
ΔR_{B_2}	$-19(6)$	$-15(5)$	$-24(8)$	$-77(25)$
$\Delta f_{\text{c},B_1\cdot K_1,1}$	0(188)	0(188)	0(188)	0(188)
$\Delta f_{\text{c},B_1\cdot K_1,2}$	0(176)	0(176)	0(176)	0(176)
$\Delta R_{B_1\cdot K_1}$	0(12)	0(12)	0(12)	0(12)
$\Delta f_{\text{c, IC, 1}}$	$-371(5)$	$-371(5)$	$-371(5)$	$-371(5)$
$\Delta f_{\text{c, IC, 2}}$	$-495(7)$	$-495(7)$	$-495(7)$	$-495(7)$
ΔR_{IC}	132(2)	132(2)	132(2)	132(2)
ΔR_{syst}	220(20)	200(19)	238(20)	477(48)

Table 5.4.: Measurement results. The measured ratios were corrected for systematic shifts (Table 5.3), and the statistical, systematic, fit, and total errors are given in parentheses.

Measurement	$R = f_c(^{12}C^{4+})/f_c(^{16}O^{5+})$
Run A	$1.066\,339\,779\,250(23)_{\text{stat}}(20)_{\text{syst}}(70)_{\text{fit}}(76)_{\text{tot}}$
Run B	$1.066\,339\,779\,196(34)_{\text{stat}}(19)_{\text{syst}}(70)_{\text{fit}}(80)_{\text{tot}}$
Run C	$1.066\,339\,779\,212(33)_{\text{stat}}(20)_{\text{syst}}(70)_{\text{fit}}(80)_{\text{tot}}$
Run D	$1.066\,339\,779\,203(50)_{\text{stat}}(48)_{\text{syst}}(70)_{\text{fit}}(99)_{\text{tot}}$
Average A–C	$1.066\,339\,779\,227(17)_{\text{stat}}(20)_{\text{syst}}(70)_{\text{fit}}(75)_{\text{tot}}$
Lit. [18, 94]	$1.066\,339\,779\,186(17)_{\text{tot}}$

the shift depending on the fit-range. Furthermore, the curve shape just after the resonance has an inflection point. When fitting a line to an inflection point, the fitted slope strongly depends on the range that is considered. (The best fully automated fit-model that we found did not fit a line to the curve near the inflection point, but instead smoothed the data and then laid a tangent to the the point with maximum slope, i.e. the inflection point. However, the semi-automatic linear fits turned out to be superior in practice.)

At the UW-PTMS, these problems were circumvented in several ways. For example, the detection system used much longer filter times, which averages out some of the "wiggles" and helps to make the data conform better to the linear fit model shown in Figure 3.8. Further, the cyclotron sweeps were *not* made symmetric with a guard-voltage offset, such that the expected shapes of the downsweeps and the filtered upsweeps are even closer to the linear fit model (see Figure 1 in [18]). The validity of the fit model was confirmed by repeatedly measuring the same masses using different calibration ions (for example, different charge-states of ^{12}C ions), different anharmonicity parameters, and different sweep settings. Lastly, the cyclotron frequency ratios of different charge-states of the same atom where compared to the expected values. All these measurements agreed with each other on a 10^{-11} level.

At THe-Trap, we used the guard-voltage offset to make the upsweeps and downsweeps (to second order[9]) symmetric, so that a possible systematic fit error is canceled out when averaging the upsweeps with the downsweeps. Furthermore, we compared different fit-models to each other, and found no difference on a $3 \cdot 10^{-11}$ level.

However, there is a small chance that, despite all efforts to validate the fit-model, a systematic fit-error remains. First simulations using a model that was built upon the code given in Appendix B and expanded to include the ion dynamics in all three modes, in an imperfect trap and under the influence of a realistic axial feedback loop, show that there are subtle effects that can shift the fitted center of a resonance on a few times 10^{-11}-level. Some of these shifts are, unfortunately, the dreaded shifts that are proportional to the ion charge (see subsection 2.10.10). These shifts depend on a wealth of parameters and are difficult to predict in practice. Therefore, we chose to modify the experiment to be able to take measurements with the pulse-and-phase method. This will allow us to compare both methods in the same trap.

Fortunately, in our ultimate measurement – the tritium to helium-3 mass ratio – possible systematic errors introduced by the fit-routine are negligible. Both ions will carry the same charge, and the ionic masses differ by less than 1 part in 10^5. Therefore, the resonance-shapes are almost identical, which means that the fit error will be mostly common mode, and will be heavily suppressed in the cyclotron frequency ratio.

[9] The K_6-related shifts remain, but they only cause the sweeps to become asymmetric when large excitation amplitudes are used.

6. Results at the FSU trap

This chapter contains details on the mass measurements performed at the FSU trap that I was involved in. Most of the data (the measurements on ^{131,134}Xe, $^{86-88}$Sr, $^{170-174,176}$Yb) were taken by a previous student, Raman Rana. The mass measurements on ^{82,83}Kr were taken during my first visit to FSU. I did most the data analysis for these measurements during my second visit to FSU. The results have been published to be included in a future atomic mass evaluation [44, 51].

6.1. Motivation

The masses of the three most abundant strontium isotopes and of the six most abundant ytterbium isotopes were measured to enable their use in photon recoil measurements of the fine-structure constant α (see section 1.4). Currently, the best photon recoil measurement of α was performed on ^{87}Rb atoms [36], with a relative uncertainty of 0.62 ppb [122]. It might be possible to reduce this uncertainty by repeating the measurement on strontium [123, 124] or ytterbium [125] isotopes. The outer electron shell of strontium and ytterbium consists of two valence electrons in a spin-singlet ground state. The shell offers several laser-accessible transitions with various line-widths. In the latest mass evaluation, the AME2012, the masses of the most abundant strontium and ytterbium isotopes are given with fractional uncertainties of more than 10 ppb [24], which limits their use in a determination of α via the photon-recoil method. The mass measurements that were performed and/or analyzed in the context of this thesis reduce the relative uncertainties of the masses of $^{86-88}$Sr, and $^{170-174,176}$Yb to below $2 \cdot 10^{-10}$. The strontium and ytterbium ions were loaded with the help of the metal vapor loader, from samples that had a natural abundance of isotopes. Since the stable isotopes ^{84}Sr and ^{168}Yb have abundances of only 0.56% and 0.14%, respectively, it was not attempted to load them into the trap.

The measurements on ^{82,83}Kr and ^{131,134}Xe complement earlier mass measurements on krypton and xenon performed at the FSU trap [48, 126, 127], so that the masses of all krypton and xenon isotopes with a natural abundance of $> 3\%$ are now available with a relative uncertainty $< 2 \cdot 10^{-10}$. Krypton and xenon ions are readily produced in typical online Penning traps and serve as convenient reference ions [66, 128, 129]. However, care has to be taken when using helium-buffer gas for cooling ions in a pre-trap: The high ionization energies of krypton and xenon lead to a risk of charge-exchange with impurities in the buffer gas [130], which can lead to systematic frequency shifts.

The reference ions used for these measurements were ^{84,86}Kr^{2+} and ^{129,132}Xe^{3+}. Their masses had been determined with earlier measurements at the FSU trap [48] with relative uncertainties of less than $1 \cdot 10^{-10}$.

6.2. Trap calibration

6.2.1. Initial calibration

The initial calibration is performed for every ion species that is loaded into the trap, in order to determine the three eigenfrequencies to within 0.1 Hz, and to find the amplitude and duration parameters of the magnetron-to-axial and cyclotron-to-axial π-pulses.

The initial step of this calibration procedure is finding the optimal ring voltage U_{R}, and setting the guard voltage U_{G} to the value that earlier calibrations of the trap predict to be optimal. This prediction is typically within 5 mV of $U_{\mathrm{G},0}$. Subsequently, a magnetron splitting measurement and a cyclotron splitting measurement are performed (see subsection 4.5.1) in order to determine the magnetron-to-axial and cyclotron-to-axial coupling frequencies and coupling strengths. Together with the value of f_z, these coupling frequencies can be used to calculate f_- and f_+ with approximately 0.1 Hz uncertainty. These frequencies are in turn used to calculate the magnetron angle via Equation (2.74). The magnetron angle has proven to be an effective parametrization of the magnetron frequency, so that in later PnP measurements, f_- can be calculated via Equation (4.2).

For each ion species investigated in the context of this thesis, the magnetron angle was approximately $\theta = 0.52(2)^\circ$, with the uncertainty dominated by the uncertainty of the f_- measurement. The fact that θ shows no dependence on the m/q of the ions suggests that the magnetron angle is dominated by a physical misalignment of the trap electrodes with respect to the magnetic field, instead of by a large, asymmetrical patch potential in the trap.

The coupling strengths that are determined in the splitting measurements are used to calculate the π-pulse times for swapping the magnetron/axial and cyclotron/axial actions.

6.2.2. Measuring $U_{\mathrm{G},0}$, $\hat{\rho}_-$, K_6, B_2, and $\hat{\rho}_+$

On eight of the ion species, the trap calibration was continued by performing a "magnetron pulse calibration" and a "cyclotron pulse calibration". These calibrations are analogous[1] to those described in subsection 5.1.4 and subsection 5.1.5, only that, instead of having the ion in an axial-frequency lock, Δf_z is observed directly by measuring f_z with axial pulses before and after the radial mode is excited. An example pulse calibration is shown in Figure 6.1 and Figure 6.2.

The fit-results of the magnetron pulse calibration are analyzed to find the optimal guard voltage $U_{\mathrm{G},0}$, the magnetron excitation calibration $\hat{\rho}_{-,\mathrm{cal}}$, and the K_6 parameter. Likewise, the cyclotron pulse calibration is analyzed to find the size of the magnetic bottle term B_2, the cyclotron excitation calibration $\hat{\rho}_{+,\mathrm{cal}}$, and an additional measurement of K_6. Example results of two calibration measurements are summarized in Table 6.1. The analysis of all calibration measurements led to the following results:

$U_{\mathrm{G},0}$: As a technical detail, the guard voltage is derived from the ring-voltage via a voltage-divider. Then, a small (less than 200 mV), computer controlled voltage offset is added for fine-adjustments. Determining of $U_{\mathrm{G},0}$ is therefore equivalent to finding the optimal

[1] The FSU/MIT pulse calibrations precedes the THe-Trap pulse calibrations by many years. The procedure performed at THe-Trap was, in fact, modeled after the FSU trap procedure.

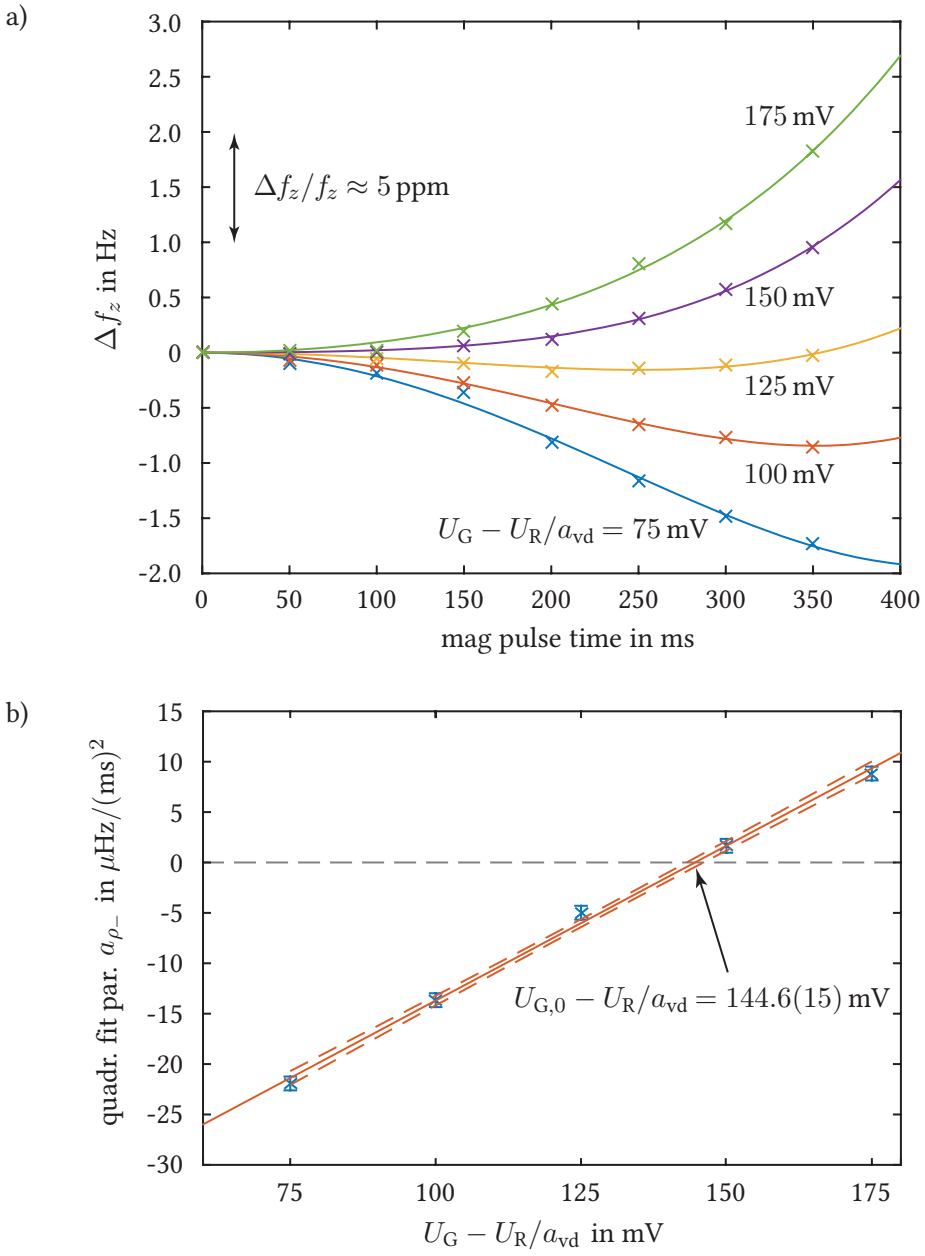

Figure 6.1.: Example of a magnetron pulse calibration performed at the FSU trap. This is analogous to the procedure shown in Figure 5.1. The differences are that Δf_z is recorded directly, and that the guard voltage U_G is not set absolutely, but relative to $U_\mathrm{R}/a_\mathrm{vd}$, with the voltage-division factor $a_\mathrm{vd} \approx 2$. As at THe-Trap, these shifts are fitted with even, fourth-order polynomials, and the fit coefficients are used to calculate, among other parameters, the optimal guard voltage $U_{\mathrm{G},0}$.

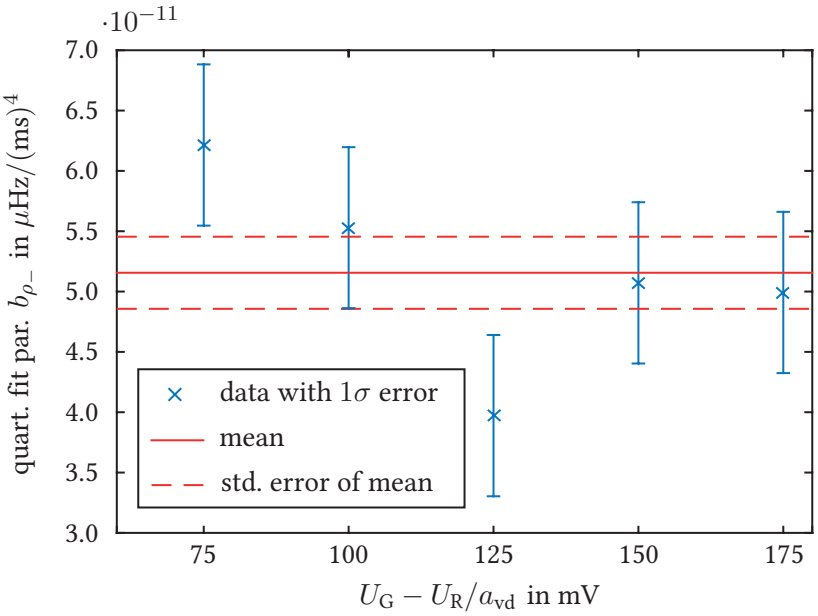

Figure 6.2.: Quartic fit parameter determined in the magnetron pulse measurement shown in Figure 6.1. This parameter is proportional to K_6. As at THe-Trap, it shows no dependance on the guard voltage setting.

fine-adjust voltage. Surprisingly, the calibrations showed that this fine-adjust voltage has no m/q dependence. In the final data analysis, we used $U_{G,0} = 139(6)$ mV for all ions, which is the average (and scatter, i.e. standard deviation) of all measurements. To account for a *possible* m/q dependence, a linear fit of the $U_{G,0}$ vs. m/q data was performed, and the uncertainty of the fitted (and negligible) slope was used to calculate possible systematic errors arising from an m/q dependence of $U_{G,0}$.

$\hat{\rho}_{-,\mathrm{cal}}$: The results for $\hat{\rho}_{-,\mathrm{cal}}$ show a small m/q dependence, but the exact values are unimportant, since magnetron pulses are not used in the PnP cycles. A typical value for m/q in the vicinity of 43 u/e was 2.2(2) μm/(V · ms).

K_6: As at THe-Trap, the results of the magnetron pulse measurements and cyclotron pulse measurements of K_6 agree, and the values scale with m/q as expected ($K_6/K_2 \equiv$ const). Although the uncertainty of the K_6 determination via the magnetron pulse measurement is worse than via the cyclotron pulse measurement, only the magnetron pulse results are used in the analysis, because the cyclotron results are potentially shifted by a B_4 term. The average value of all K_6/K_2 magnetron pulse results was $1.37(21) \cdot 10^{-6}/\mathrm{mm}^4$, with the uncertainty taken from the standard deviation of all measurements.

B_2: As at THe-Trap, this value is calculated from the difference of the "optimal guard voltages" determined by the magnetron pulse and the cyclotron pulse calibrations. The scatter of

the measurements with the usual ions of interest, which all had m/q ratios in the range of $(42-44)\,\mathrm{u}/e$, was approximately as large as the the average value. Therefore, we used the results of three measurements performed with $^{84}\mathrm{Kr}^{3+}$, which have a lower m/q ratio and allowed a more reliable measurement of B_2. The value used in the final analysis was $B_2 = -0.043(26)\,\mathrm{T/m}^2$.

$\hat{\rho}_{+,\mathrm{cal}}$: This parameter is used for the correction of the most relevant amplitude-dependent shifts. For example, in the f_+ measurement, the radius $\hat{\rho}_+$ is pulsed to $\hat{\rho}_{+,\mathrm{i}}$, which can be large enough to cause relevant frequency shifts. The correction of these frequency shifts depends on $\hat{\rho}_{+,\mathrm{cal}}$. During the measurement of f_z (in the axial ring-down), the amplitude $\hat{z}$ is large and leads to frequency shifts. Since $\hat{z}$ is the result of a cyclotron-to-axial π-pulse, the correction of the $\hat{z}$-related shifts also depends on $\hat{\rho}_{+,\mathrm{cal}}$.

The measurements of $\hat{\rho}_{+,\mathrm{cal}}$ show a clear m/q-dependence, mostly caused by the frequency dependence of the cryogenic filter boards. To account for this dependence, the $\hat{\rho}_{+,\mathrm{cal}}$ vs. m/q data was fit with a linear model

$$\hat{\rho}_{+,\mathrm{cal}} = a + b \cdot (m/q - \overline{m/q}) \quad , \tag{6.1}$$

with $\overline{m/q} = 39.53\,\mathrm{u}/e$ as the average m/q value of the data, in order to remove correlations between the fit coefficients. This resulted in $a = 14.65(14)\,\mu\mathrm{m}/(\mathrm{V}\cdot\mathrm{ms})$ and $b = -0.514(20)\,\mu\mathrm{m}/(\mathrm{V}\cdot\mathrm{ms})\cdot(e/\mathrm{u})$.

In the data analysis, the coefficient a leads to *common-mode* shifts, while the coefficient b leads to much more severe, differential frequency shifts. In order to ensure that the m/q dependence was not underestimated in the cyclotron frequency ratio measurements, the signal amplitudes of the ring-downs of each PnP cycle were recorded. The ratio of the average axial signal amplitudes $\overline{U}_{\mathrm{s},1}/\overline{U}_{\mathrm{s},2}$ of ion 1 and ion 2 was calculated and compared to the expected value[2] $(\sqrt{f_{+,1}/f_{+,2}})\cdot(\hat{\rho}_{+,1}/\hat{\rho}_{+,2})\cdot(q_1/q_2)$.

This comparison confirmed the measured m/q-dependance of $\hat{\rho}_{+,\mathrm{cal}}$. However, the uncertainty of the measured axial signal amplitude ratio was much greater than the uncertainty of the predicted ratio based on the calibration of $\hat{\rho}_+$. To be on the safe side, the uncertainty of the fit-coefficient b was increased by a factor of 8, so that the measured signal ratios were mostly within the uncertainty band of the predicted signal ratios.

Lastly, the value of $\hat{\rho}_{+,\mathrm{cal}}$ determines the expected cyclotron radius $\hat{\rho}_{+,\mathrm{k}}$ after a "parking pulse" that moves the inner ion onto the outer parking orbit ($\hat{\rho}_{+,\mathrm{k}} \approx 2\,\mathrm{mm}$). For such large $\hat{\rho}_+$, the excitation pulse is not 100% effective, because the anharmonic frequency shifts become too severe, and because the strength of the driving field (from one half of a guard electrode) falls off at large ion radii. The effectiveness of a typical parking pulse was measured as 80(10)%. Therefore, for the parking pulses, $\hat{\rho}_{+,\mathrm{cal}}$ was scaled by a factor of 0.8(1).

In the data analysis, these calibration parameters were always determined from fits to *all* calibration measurements, even if the particular ion species had been used in such a calibration measurements.

[2] The factor in the square-root is due to the conservation of *action* in a π-pulse, see Equation (A.87).

Table 6.1.: Example results of a full trap calibration at the FSU trap. The uncertainties of $U_{\mathrm{G},0}$, $\hat{\rho}_-$, K_6/K_2, B_2, and $\hat{\rho}_+$ were estimated from the scatter of repeated measurements on similar ions. The uncertainty of the ring voltage was below 1 mV. For the data analysis, the ring voltage is not needed more accurately. The agreement of the K_6/K_2 results is typically better than in this comparison.

Property	Symbol	$^{86}\mathrm{Kr}^{2+}$	$^{129}\mathrm{Xe}^{3+}$
f_z	f_z	213 364.00(10) Hz	213 367.00(10) Hz
f_-	f_-	7 484.53(10) Hz	7 486.88(10) Hz
f_+	f_+	3 041 837.04(10) Hz	3 040 915.37(10) Hz
magnetron-to-axial π-pulse	$t_{\mathrm{mcp}} \cdot U_{\mathrm{mcp}}$	4.59(32) V·ms	4.65(39) V·ms
cyclotron-to-axial π-pulse	$t_{\mathrm{ccp}} \cdot U_{\mathrm{ccp}}$	0.204(5) V·ms	0.202(5) V·ms
magnetron radius calibration	$\hat{\rho}_{-,\mathrm{cal}}$	2.22(22) μm/(mV·s)	2.43(22) μm/(mV·s)
cyclotron radius calibration	$\hat{\rho}_{+,\mathrm{cal}}$	13.6(6) μm/(mV·s)	12.3(6) μm/(mV·s)
ring voltage	U_{R}	-24.177 V	-24.187 V
optimal guard voltage	$U_{\mathrm{G},0,\mathrm{diff}}$	144.6(4.0) mV	140.1(4.0) mV
K_6/K_2 from $\hat{\rho}_-$ meas.	K_6/K_2	$1.76(21) \cdot 10^6/\mathrm{m}^4$	$1.08(21) \cdot 10^6/\mathrm{m}^4$
magnetic bottle	B_2	$-0.025(55)$ T/m^2	$-0.124(55)$ T/m^2
trap misalignment angle	θ	$0.544(18)^\circ$	$0.520(18)^\circ$

6.2.3. Shifts due to the decaying axial amplitude

The axial frequency is measured by fitting an exponentially decaying sinusoid to the axial ring-down data. This determines the *average* axial frequency during the time t_{meas} of the recorded ring-down. (Typically, a t_{meas} of 8.192 s is used.) Because the axial amplitude changes during the ring-down, the anharmonic shifts of f_z change as well.

The axial amplitude at the beginning of the ring-down is given by the cyclotron amplitude $\hat{\rho}_+$ and by the effectiveness of the cyclotron-to-axial coupling pulse. Assuming a 100% effective coupling pulse, the initial axial amplitude can be calculated as (see Equation A.87)

$$\hat{z}_0 = \sqrt{\frac{f_+ - f_-}{f_z}}\hat{\rho}_+ \quad . \tag{6.2}$$

If this value were used to calculate the correction of the anharmonic frequency shifts, the shifts would be over-corrected. Instead, it is necessary to calculate the average frequency shifts. The decay of the axial amplitude during the ring-down can be described as $\hat{z}(t) = \hat{z}_0 \exp(-\gamma_{z,\mathrm{eff}}\, t/2)$, with $\gamma_{z,\mathrm{eff}}$ given by Equation (2.39). The most severe shift, the K_4-related shift, is proportional to $\hat{z}^2$, so the average frequency shift can be calculated by determining the average $\langle \hat{z}^2 \rangle$ during the measurement time t_{meas}:

$$\begin{aligned} \langle \hat{z}^2 \rangle &= \frac{1}{t_{\mathrm{meas}}} \int_0^{t_{\mathrm{meas}}} [z(t)]^2 \, dt \\ &= \frac{\hat{z}_0^2}{\gamma_{z,\mathrm{eff}}\, t_{\mathrm{meas}}} \left(1 - e^{-\gamma_{z,\mathrm{eff}}\, t_{\mathrm{meas}}}\right) \quad . \end{aligned} \tag{6.3}$$

For convenience, we can define $\hat{z}_{\text{eff}} = \sqrt{\langle \hat{z}^2 \rangle}$ and write

$$\hat{z}_{\text{eff}} = F \cdot \hat{z}_0 \quad , \tag{6.4}$$

with

$$F = \sqrt{\frac{1 - e^{-\gamma_{z,\text{eff}}\, t_{\text{meas}}}}{\gamma_{z,\text{eff}}\, t_{\text{meas}}}} \tag{6.5}$$

defined as the F-term (sometimes called *fudge factor*) that allows us to calculate an *effective* axial amplitude for the frequency shifts. However, due to the decay of the axial signal, the later data does not carry as much weight in the fit procedure as the earlier data. It can be argued that the F-term simply has to be calculated with $2 \cdot \gamma_{z,\text{eff}}$ instead of $\gamma_{z,\text{eff}}$ to account for this effect, but this has not been studied in detail[3]. Instead, to avoid this problem, the PnP cycles at the FSU trap are taken with a 15 Hz detuning between f_z and f_{det}. This significantly reduces $\gamma_{z,\text{eff}}$ from typically $1/(1\,\text{s})$ to $1/(20\,\text{s})$, so that the frequency change during the measurement is much less severe and the F-term is close to unity. This detuning between f_z and f_{det} has the added benefit of reducing the uncertainty of the coil-pushing shift. While the coil-pushing shift vanishes for $f_z - f_{\text{det}} = 0$, its dependence on $f_z - f_{\text{det}}$ is maximal, so that the $f_z - f_{\text{det}}$ uncertainty leads to a large uncertainty of the coil-pushing shift.

Another relevant shift to f_z is given by the $K_6 \cdot \hat{z}^4$ shift. In principle, one would have to define an equivalent G-term that parameterizes the effective amplitude $\langle \hat{z}^4 \rangle^{1/4}$. However, in practice, this constant is usually so close to F that only F is used.

The F-terms used in the analysis were $F = 0.94(10)$ for the Kr^{2+} ions, $F = 0.91(10)$ for the Xe^{3+} ions, and $F = 0.85(10)$ for the Yb^{4+} ions. The uncertainty was chosen such that it generously encompasses the differences of F, G, or F with twice-increased damping.

6.2.4. Estimating the $B_1 \cdot K_1$-shift

The $B_1 \cdot K_1$-shift is usually estimated by applying an offset potential onto one of the endcap electrodes to shift the center of the axial motion along the z-axis. By observing the resulting shift of the free-space cyclotron frequency f_c, the B_1 gradient can be calculated, and by observing the shift of the axial frequency, the parameter K_1 can, under certain circumstances, also be estimated (see subsection 2.10.4).

The influence of the $B_1 \cdot K_1$-shift on measurements of the cyclotron frequency ratio R can be shown to be proportional to the m/q-difference of the two ions. Since the determination of C_1 is somewhat ambiguous, and to exclude other unknown shifts that are proportional to the m/q-difference, the cyclotron frequency ratio of $^{84}Kr^{2+}/^{84}Kr^{3+}$ was determined using three runs at optimized settings of the inner radii $\hat{\rho}_{+,\text{i}}$ and parking radii $\hat{\rho}_{+,\text{k}}$. The average ratio $\overline{R}$ was

$$\begin{aligned}
\overline{R}\left(^{84}Kr^{2+}/^{84}Kr^{3+}\right)_{\text{uncorr}} &= 0.666\,662\,308\,676\,(30)_{\text{stat}} \\
\overline{R}\left(^{84}Kr^{2+}/^{84}Kr3+\right)_{\text{corr}} &= 0.666\,662\,308\,605\,(30)_{\text{stat}} \\
\overline{R}\left(^{84}Kr^{2+}/^{84}Kr^{3+}\right)_{\text{theo}} &= 0.666\,662\,308\,524 \quad .
\end{aligned}$$

[3] This is a somewhat messy issue, hence the name "fudge factor" for F. It is similar to the lineshape problem at THe-Trap, but not as severe.

The expected value R_{theo} is given by the the inverse of the *ion* mass ratio. The ion masses were calculated from the literature value of $m(^{84}\text{Kr})$ by correcting it for the missing electrons and the total ionization energies:

$$m(\text{ion}) = m(\text{atom}) - x \cdot m_e + \frac{E_{\text{ion}}}{c^2} \quad , \tag{6.6}$$

with m_e as the electron mass, x as the ion's charge state, and E_{ion} as the total ionization energy to reach charge state x. Comparing R_{theo} to $\overline{R}_{\text{uncorr}}$, which has not been corrected for any shifts, the total influence of m/q-dependent ratio shifts can be estimated as

$$\frac{\Delta R}{\Delta(m/q)} = \frac{11\,\text{ppt}}{e/\text{u}} \quad . \tag{6.7}$$

The value of $\overline{R}_{\text{corr}}$ shows that the corrections bring the measured value into better agreement with the expected value. The systematic error was not calculated for this measurement, but can be estimated to be larger than the statistic error. Still, to ensure that no m/q-dependent ratio-shifts are overlooked, the uncertainty of the magnetron angle was increased, such that the value used in the analysis was $\theta = 0.52(5)^\circ$. The influence of the magnetron uncertainty on the systematic error is proportional to m/q, and the increased uncertainty generously includes the $11\,\text{ppt}/(e/\text{u})$ deviation between the *uncorrected* ratio $\overline{R}_{\text{uncorr}}$ and the expected ratio R_{theo}.

Further measurements were performed on the same ion pair, using bigger-than-optimal inner radii $\hat{\rho}_{+,\text{i}}$ and smaller-than-optimal parking radii $\hat{\rho}_{+,\text{k}}$, in order to test the theoretical models of the ion–ion-related shifts and the amplitude-dependent shifts at a large m/q-difference. The measured ratio shifts agreed well with the expected values.

6.2.5. Further trap calibration measurements

Additional measurement to determine the temperature of the detection circuit (which allows to calculate possible shifts due to thermal radii) and the voltage offset between the endcaps had been performed earlier and are described in [71, 114].

6.3. Measurements

All 226 measurement runs[4] were taken with the FSU two-ion technique, in which one ion, the inner ion "i", is investigated in the center of the trap (using a cyclotron radius of $\hat{\rho}_{+,\text{i}}$ for setting the cyclotron phase), and another ion, the parked ion "k", is situated on a large cyclotron radius $\hat{\rho}_{+,\text{k}}$. In a typical measurement run, the cyclotron frequency of the inner ion was determined three times in a row using three 10-minute PnP cycles. Then the inner and outer ion were swapped and the procedure repeated for typically 10 hours. After this time, the LN_2-jacket of the bore cryostat was refilled. Together with the time needed for all relevant surfaces to reach thermal equilibrium again, this resulted in a convenient 12 hour cycle of the measurement runs. A typical example of a measurement run is shown in Figure 6.3.

[4] The vast majority of the measurement runs – 202 – were taken by Raman Rana!

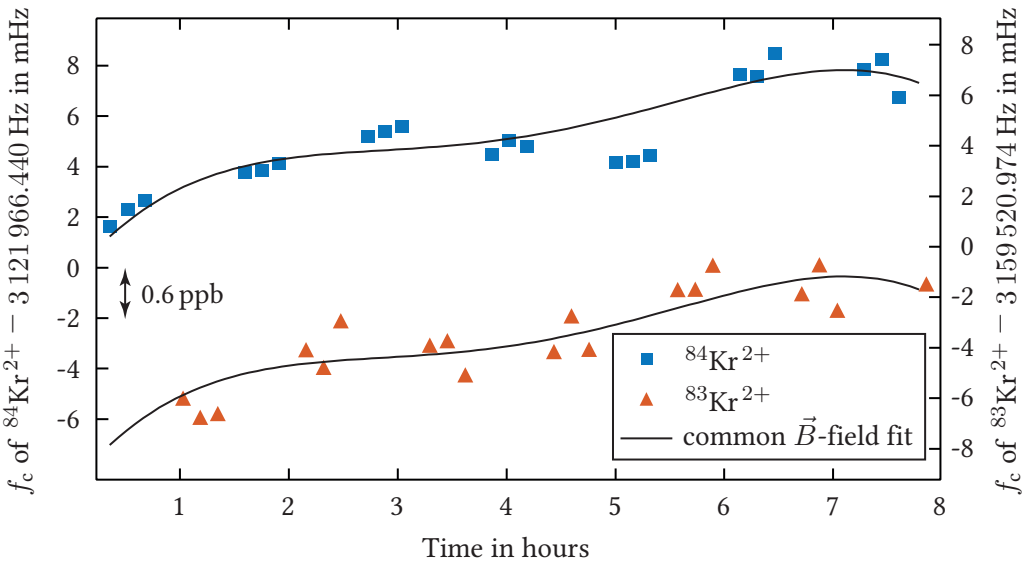

Figure 6.3.: Typical measurement run performed at the FSU trap. In this case, the F-test suggested a fourth-order fit of the f_c drifts.

Of the 226 measurement runs, 111 runs were taken at optimal settings of $\hat{\rho}_{+,i}$ and $\hat{\rho}_{+,k}$ (see Table 6.2). The remaining runs were not used directly in the mass ratio determinations, but instead used for verifying the theoretical models of the systematic shifts.

6.4. Data analysis

The first step of the data analysis — fitting the ring-downs with a decaying sinusoid — is performed by a C subroutine [112] of the program that controls the experiment. The next step of the data analysis consists of using an IGOR Pro routine to semi-automatically[5] *unwrap* the measured phases of the PnP ring-downs and thereby determine f_+. The IGOR Pro routine is further used to combine the measurements of f_+, f_z and θ into f_c values, and to fit the f_c vs. t data of both ions with polynomials of up to 10th degree (see Equation 5.21). The routine identifies the optimal polynomial degree with an F test [115], and repeats the fit of the optimal polynomial using a "robust" fit routine that deweights f_c outliers.

The final step of the analysis consists of recording the results of the standard fit and the robust fit into an Excel file, in which the run-parameters are used to correct the measured R of each run for systematic shifts. The Excel file is further used to find the systematic error, to combine measurements on identical ion pairs into averages, and to calculate the mass differences and

[5] In rare cases, measurement noise causes the unwrapping procedure to add an inappropriate amount of 2π's to the data points. In the f_c vs. t plots, this results in obvious (many σ away from the average) outliers. One can try to manually identify and mask-out the offending ring-down to help the unwrapping procedure find a more sensible result. However, in almost all cases, the outliers were simply discarded.

Table 6.2.: Optimal parameters of $\hat{\rho}_{+,\mathrm{i}}$ and $\hat{\rho}_{+,\mathrm{k}}$ that were used in the mass ratio determinations. These values are averages of the parameters that were used. To prevent systematic shifts caused by differential heating effects (section 4.2), U_{pulse} and t_{pulse} of the cyclotron exciation pulses are set to the same value for both ions in a ratio measurement. Due to the m/q dependence of $\hat{\rho}_{+,\mathrm{cal}}$, the $\hat{\rho}_{+,\mathrm{i}}$ and $\hat{\rho}_{+,\mathrm{k}}$ values of the ions in a ratio measurement will actually be slightly different. This is accounted for in the analysis.

Ratio	$\hat{\rho}_{+,\mathrm{i}}$	$\hat{\rho}_{+,\mathrm{k}}$
Kr^{2+}/Kr^{2+}	65 μm	1850 μm
Xe^{3+}/Xe^{3+}	55 μm	1750 μm
Sr^{2+}/Kr^{2+}	75 μm	2200 μm
Yb^{4+}/Xe^{3+}	50 μm	2200 μm

final masses. In this step of the analysis, 8 runs had to be discarded due to uncovered erroneous settings of the cyclotron-to-axial coupling frequency (6 runs), excessive f_z-drifts (1 run) and unstable resonances caused by a contaminant ion (1 run).

The systematic shifts can be grouped into three categories: Shifts that are caused by trap imperfections, ΔR_{trap}, shifts caused by ion-ion interaction, ΔR_{ii}, and shifts caused by the measurement of the axial frequency, ΔR_{f_z}. The uncertainties of the systematic shifts are combined to form the systematic error δR_{syst}. The statistical error, δR_{stat}, is calculated from the fit-errors of the individual R measurements, and from their scatter around the mean $\overline{R}$ values. The results of this analysis are summarized in Table 6.3. Additional information on the individual shifts are given below.

6.4.1. Trap imperfections: ΔR_{trap}

The relativistic corrections and the trap imperfections, parametrized by K_4, K_6, and B_2, lead to amplitude dependent frequency shifts (section 2.10). During the measurement of f_+ (during the phase evolution time of the PnP), only $\hat{\rho}_+ = \hat{\rho}_{+,\mathrm{i}}$ is above the thermal limit, and during the ring-down measurement of f_z, only $\hat{z}$ is above the thermal limit (assuming perfect cyclotron-to-axial coupling efficiency). Therefore, the most relevant shifts of the cyclotron frequency determination are given by the $\hat{\rho}$-dependent terms of the f_+ shifts, and by the $\hat{z}$-dependent f_z shifts.

The amplitude $\hat{\rho}_{+,\mathrm{i}}$ was calculated using the pulse amplitude, the pulse time, and the calibration factor $\hat{\rho}_{+,\mathrm{cal}}$. The amplitude $\hat{z}$ is given by $\hat{\rho}_{+,\mathrm{i}}$ and the properties of the cyclotron-to-axial coupling pulse. It was calculated using

$$\hat{z} = \eta \cdot F \cdot \sqrt{f_+/f_z}\hat{\rho}_{+,\mathrm{i}} \quad , \tag{6.8}$$

with F as the F-term (Equation 6.5), and η describing the effectiveness of the coupling pulse. The effectiveness was estimated by comparing the amplitude, duration, and frequency of the used coupling pulse to the values of the optimal coupling pulse, using a model of a near-

Table 6.3.: Average cyclotron frequency ratios. The shifts $\Delta\overline{R}_{\mathrm{ii}}$, $\Delta\overline{R}_{f_z}$, and their uncertainties (in parentheses) are given in ppt. The combination of their uncertainties is the systematic error $\delta\overline{R}_{\mathrm{syst}}$, which like $\delta\overline{R}_{\mathrm{stat}}$ is also given in ppt. $\overline{R}$ denotes the corrected frequency ratio, averaged over the N measurements of the respective ion pair.

Ion Pair	N	$\Delta\overline{R}_{\mathrm{trap}}$	$\Delta\overline{R}_{\mathrm{ii}}$	$\Delta\overline{R}_{f_z}$	$\delta\overline{R}_{\mathrm{syst}}$	$\delta\overline{R}_{\mathrm{stat}}$	$\overline{R}$
$^{84}Kr^{2+}/^{83}Kr^{2+}$	4	1(11)	0(1)	−1(25)	27	102	0.988 113 854 714(106)
$^{84}Kr^{2+}/^{82}Kr^{2+}$	7	1(21)	1(1)	5(15)	26	55	0.976 188 689 857(61)
$^{86}Kr^{2+}/^{82}Kr^{2+}$	1	4(42)	5(1)	12(39)	57	93	0.953 472 795 915(109)
$^{131}Xe^{3+}/^{129}Xe^{3+}$	3	−1(15)	6(5)	3(28)	32	64	0.984 719 245 708(72)
$^{132}Xe^{3+}/^{131}Xe^{3+}$	2	0(8)	2(3)	−4(38)	39	102	0.992 425 686 562(109)
$^{134}Xe^{3+}/^{132}Xe^{3+}$	5	0(16)	7(7)	3(16)	23	58	0.985 054 653 174(62)
$^{86}Sr^{2+}/^{84}Kr^{2+}$	5	5(25)	3(10)	6(25)	36	49	0.976 745 365 137(61)
$^{86}Kr^{2+}/^{86}Sr^{2+}$	8	1(6)	−1(10)	−3(30)	31	63	0.999 984 286 726(70)
$^{87}Sr^{2+}/^{84}Kr^{2+}$	4	6(38)	5(10)	9(30)	48	44	0.965 510 800 825(65)
$^{87}Sr^{2+}/^{86}Kr^{2+}$	7	3(13)	2(11)	5(27)	30	49	0.988 513 492 824(57)
$^{88}Sr^{2+}/^{84}Kr^{2+}$	3	8(50)	8(11)	7(24)	56	51	0.954 563 033 516(76)
$^{88}Sr^{2+}/^{86}Kr^{2+}$	6	4(26)	4(11)	4(37)	45	47	0.977 304 901 803(65)
$^{86}Kr^{2+}/^{84}Kr^{2+}$	8	5(24)	4(10)	8(24)	34	33	0.976 730 017 222(48)
$^{129}Xe^{3+}/^{170}Yb^{4+}$	6	−29(10)	−2(7)	−102(51)	51	48	0.988 722 497 571(70)
$^{132}Xe^{3+}/^{170}Yb^{4+}$	6	−26(30)	1(7)	−104(49)	58	50	0.966 239 613 795(76)
$^{129}Xe^{3+}/^{171}Yb^{4+}$	3	−29(6)	−2(7)	−111(45)	45	55	0.994 549 921 376(71)
$^{132}Xe^{3+}/^{172}Yb^{4+}$	6	−27(22)	−1(7)	−93(50)	54	48	0.977 620 857 204(73)
$^{173}Yb^{4+}/^{129}Xe^{3+}$	3	31(8)	5(7)	117(47)	48	59	0.993 840 640 888(75)
$^{132}Xe^{3+}/^{173}Yb^{4+}$	3	−28(15)	−1(8)	−97(47)	50	68	0.983 317 277 812(84)
$^{174}Yb^{4+}/^{129}Xe^{3+}$	7	31(13)	5(8)	113(46)	49	35	0.988 123 111 853(61)
$^{132}Xe^{3+}/^{174}Yb^{4+}$	5	−29(11)	−2(8)	−126(64)	65	70	0.989 006 998 775(95)
$^{176}Yb^{4+}/^{129}Xe^{3+}$	5	33(24)	7(8)	132(59)	66	61	0.976 869 814 901(90)
$^{176}Yb^{4+}/^{132}Xe^{3+}$	4	31(5)	9(9)	120(68)	73	138	0.999 600 046 860(156)

resonant excitation. The parameter η was further used to calculate the remaining, above-thermal amplitude of the cyclotron mode after the coupling pulse.

For the runs taken at optimal settings (the runs summarized in Table 6.3), the K_4-related ratio shifts are negligible, since U_{G} is set close to $U_{\mathrm{G},0}$, which minimizes K_4. However, for runs where the ions had a large m/q difference (larger than 1 u$/e$) , the uncertainty in $U_{\mathrm{G},0}$ led to a relevant (larger than 20 ppt uncertainty) effect on the measured cyclotron frequency ratio.

Since the K_6-coefficient cannot be nulled with the guard voltage, the K_6 shift of f_z was relevant for runs with a large m/q difference. The uncertainty of the shift correction was approximately half as big as the shift itself.

The B_2-shift of f_+ due to $\hat{\rho}_+^2$ were generally at a level below 10 ppt. The shifts and uncertainties due to the remaining K_4, K_6, B_2, and relativistic terms (coupling to the pulsed amplitudes, the thermal amplitudes, or the residual cyclotron amplitude) were all found to be negligible.

Since f_- is not measured in the PnP cycles, but instead calculated from the earlier determination of θ, the uncertainty of θ leads to an amplitude-independent uncertainty of R. It was negligible in all measurements, but nevertheless included in ΔR_{trap}. The possible $B_1 \cdot C_1$ shift was estimated from the $^{84}\mathrm{Kr}^{2+}/^{84}\mathrm{Kr}^{3+}$-measurement and taken into account by increasing the θ-uncertainty (see subsection 6.2.4).

Finally, ΔR_{trap} also includes the image charge shift. This shift is negligible when both ions carry the same charge, but leads to a 30 ppt correction of the $\mathrm{Yb}^{4+}/\mathrm{Xe}^{3+}$ ratios. Thanks to a detailed theoretical model of the image charge shift [91], the uncertainty of the correction is negligible.

6.4.2. Ion-ion interactions: ΔR_{ii}

The resonant ion-ion interaction (subsection 2.10.7) was found to be negligible. The main ratio shift was caused by the average influence that the outer ion has on the K_4 and K_6 parameter of the inner ion. This shift was generally below 10 ppt. The uncertainties of the ion-ion shifts are all below 11 ppt.

In Table 6.3, the quoted ΔR_{ii} uncertainties of the Kr and Xe mass measurements are lower than those of the Sr and Yb measurements. The reason is that they were estimated with two different methods: Some of the uncertainties, especially those of ΔR_{ii}, are notoriously difficult to calculate from first principles. The formulas have lots of terms, and doing Gaussian error-propagation on them is not feasible. Therefore, in the Kr and Xe mass measurements, the uncertainty was calculated with a crude form of Monte-Carlo error estimation. For the Sr and Yb measurements, the Monte Carlo calculation was replaced by a simpler estimate, in which the uncertainty of the ion-ion shift to the *ratio* was generously approximated from the uncertainties of the ion-ion shifts to the *cyclotron frequencies*. The shifts of the cyclotron frequencies are heavily correlated and cancel out in the ratio, and in the Monte Carlo estimate. But even when using the generous overestimation, the uncertainty of the ion-ion shift was at most 11 ppt, and therefore negligible.

6.4.3. Axial detection: ΔR_{f_z}

ΔR_{f_z} consolidates the shifts caused by the f_z determination. The coil-pushing shift is estimated according to Equation (2.40), using a calculated, but corrected (38% lower) value for γ_z. In order to reduce the uncertainty of the coil-pushing shift, all runs that were considered in the final analysis were taken with a 15 Hz detuning between f_z and f_{det}. The coil-pushing shift was therefore generally less than 10 ppt, with an even lower uncertainty. However, in the $\mathrm{Yb}^{4+}/\mathrm{Xe}^{3+}$ ratios, the different charge states of the ions result in a differential coil-pushing shift. For these runs, the coil-pushing correction amounted to typically 110 ppt, with an uncertainty of 40 ppt dominated by the uncertainty in the 38% correction factor. The coil-pushing shift was the biggest correction that had to be applied to the data.

The shift due to a differential voltage drift (subsection 4.5.3) was typically smaller than 10 ppt. It was estimated by fitting the observed drift of f_z with respect to the start of the PnP cycle, averaged over all the PnP cycles for each ion in a run, with various polynomials, in order to estimate f_z at the time of the f_+ measurements. This estimate, however, has a higher uncertainty than the average of the f_z values, which leads to uncertainties in the order of 30 ppt for this shift.

In the Kr and Xe mass measurements, we treated this shift as a random run-to-run variation, which allowed us to add its uncertainty in quadrature when forming the average ratios, reducing the uncertainty of this shift. For the Sr and Yb measurements, we used the safer choice to treat this shift as a true systematic shift, with the drawback that the uncertainty of the shift was not added in quadrature, but instead averaged.

6.4.4. Systematic error: δR_{syst}

The systematic error is given by the combined uncertainty of the ratio shifts. As a first estimate, this combination can be formed by adding the uncertainties of ΔR_{trap}, ΔR_{ii}, and ΔR_{f_z} in quadrature. However, this neglects the correlations of the shifts (for example, both ΔR_{trap} and ΔR_{ii} depend on the calibration of the cyclotron radius, $\hat{\rho}_{+,\mathrm{cal}}$). A better estimate can be found by writing down the total ratio shift as a function of $\hat{\rho}_{+,1}$, $\hat{\rho}_{+,2}$, K_6/K_2, the $U_{\mathrm{G},0}$ fit parameters, the F-terms, ..., and then performing Gaussian error propagation. Due to the length and complexities of the shift-formulas, this is impractical. Instead, a hybrid approach can be used, in which related shifts are combined into a formula that is then analyzed with Gaussian error propagation, and the resulting uncertainties of these combinations are added in quadrature. This removes most, but not all correlations. (ΔR_{trap} and ΔR_{ii} are still infeasible to combine with this method.) A third approach is to calculate the total ratio correction while varying the input parameters within their uncertainties, in order to determine the uncertainty of the total shift correction (Monte Carlo method). In the end, the naive approach, the hybrid approach, and the Monte Carlo approach all yielded approximately the same result for δR_{syst}. If anything, the Monte Carlo estimate tended to be lower than the estimate given by the hybrid approach. In these cases, the uncertainty of the hybrid approach was often retained, in order to be conservative.

6.4.5. Statistic error: δR_{stat}

For each ion pair, the N measurements of the cyclotron frequency ratio were combined into average ratios $\overline{R}$. Since the runs had different statistical errors $R_{\mathrm{stat},i}$ but common systematic error $R_{\mathrm{syst},i}$, the averages were calculated as weighted averages,

$$\overline{R} = \frac{1}{\sum w_i} \sum_{i=1}^{N} w_i R_i \tag{6.9}$$

with w_i formed from the statistical errors as $w_i = 1/\delta R^2_{\mathrm{stat},i}$. The scatter of the R_i around the weighted mean was quantified by calculating the reduced χ^2 value

$$\chi^2_{\mathrm{red}} = \sum_{i=1}^{N} \frac{(R_i - \overline{R})^2}{\delta R^2_{\mathrm{stat},i}} \quad . \tag{6.10}$$

The χ^2_{red} value is expected to be around unity. To be conservative, for those ion pairs where $\chi^2_{\mathrm{red}} > 1$, the statistical error $\delta\overline{R}_{\mathrm{stat}}$ was scaled up by $\sqrt{\chi^2_{\mathrm{red}}}$. This led to slight increases in $\delta\overline{R}_{\mathrm{stat}}$ of 6 investigated ion pairs, and to a twofold-increase in $\delta\overline{R}_{\mathrm{stat}}$ of the ion pair $^{176}\mathrm{Yb}^{4+}/^{132}\mathrm{Xe}^{3+}$.

Since errors of the unwrapping procedure and perturbation of the magnetic field lead to a non-Gaussian distribution of the measured f_c value around the fitted f_c drift, the standard fit procedure was compared to a robust fit-procedure that deweights outliers. This comparison tests if, for example, asymmetrical outliers biased the standard fit. Since it is not immediately obvious which fit result should be trusted more in such a case, the difference between the robust fit result and the standard fit result was averaged for each ion pair, and then added in quadrature to $\delta\overline{R}_{\text{stat}}$. In most cases, the average difference was less than 20 ppt. Only the measurements on $^{84}Kr^{2+}/^{83}Kr^{2+}$ and on $^{132}Xe^{3+}/^{174}Yb^{4+}$ showed significant differences between the robust and standard fit methods, with 46 ppt and 26 ppt respectively.

6.4.6. Additional checks

Out of the 226 measurement runs that were taken, 8 runs had to be discarded, but only 111 runs were included in the mass determinations. The remaining runs were taken at deliberate sub-optimal settings, in order to test the theoretical models of the ratio shifts. On most ion pairs, additional runs with increased $\hat{\rho}_{+,\text{i}}$ or reduced $\hat{\rho}_{+,\text{k}}$ were taken, in order to verify the estimates of the amplitude dependent shifts that are included in δR_{trap}, and the ion-ion dependent shifts δR_{ii}. A total of 5 runs were taken with $f_z - f_{\text{det}} = +15\,\text{Hz}$, instead of the usual $-15\,\text{Hz}$ detuning, and one additional run was taken with $+8.5\,\text{Hz}$ detuning. This confirmed the coil-pushing corrections. 19 runs were performed on the ion pair $^{88}Sr^{2+}/^{12}C^{16}O_2^+$, in order to be able to reference the Sr masses more directly to the masses of ^{12}C and ^{16}O. However, since the singly-charged molecular ion $^{12}C^{16}O_2^+$ requires a larger amplitude for reliable detection, this measurement was not directly included in the mass determination. The cyclotron frequency ratio of the ion pair $^{86}Kr^{2+}/^{84}Kr^{2+}$ was remeasured with 12 runs, in order to check consistency with earlier measurements performed at the FSU trap [48], and as described in subsection 6.2.4, three runs were taken on the ion pair $^{84}Kr^{2+}/^{84}Kr^{3+}$ to measure possible $C_1 \cdot B_1$ shifts.

The supplemental measurements agreed with the expected values within the measurement uncertainties.

6.5. Results and discussion

The cyclotron frequency ratios given in Table 6.3 can be used to calculate linearized mass-differences, which in turn can be used in future mass-evaluations. The mass-differences state the measurement results in units of u while minimizing the dependence on the mass of the reference ion. Using $q_i = x_i \cdot e$ for the charge of ion i, and $m_{\text{i},i}$ for its mass (making it explicit that this is the *ion* mass, not the *atom* mass), we can write the cyclotron frequency ratio R as

$$R = q_1\, m_{\text{i},2}/(q_2\, m_{\text{i},1}) \quad . \tag{6.11}$$

This allows us to state the mass difference equations for the *ion* masses as

$$x_1 \cdot m_{\text{i},2} - x_2 \cdot m_{\text{i},1} \;=\; (\overline{R} - 1) \cdot x_2 \cdot m_{\text{i},1} \tag{6.12}$$

$$x_2 \cdot m_{\text{i},1} - x_1 \cdot m_{\text{i},2} \;=\; \left(\frac{1}{\overline{R}} - 1\right) \cdot x_1 \cdot m_{\text{i},2} \quad . \tag{6.13}$$

The measurement of $\overline{R}$ and the mass of the reference ion are inserted into the right-hand-side of the equation, in order to determine the value of the left-hand-side of the equation. In the first equation, $m_{\mathrm{i},1}$ is used as reference, and in the second equation, $m_{\mathrm{i},2}$. The factors of $(\overline{R}-1)$ and $(1/(\overline{R})-1)$, suppress the uncertainty of the reference masses in the calculation of the mass difference.

Since in typical applications, the value of the *atomic* masses are needed, the mass-difference equations are corrected for the electron masses and for the energies needed to form the ions (see Equation 6.6). This leads to the equations

$$\begin{aligned} & x_1 \cdot m_{\mathrm{a},2} - x_2 \cdot m_{\mathrm{a},1} \\ & \quad = (\overline{R}-1) \cdot x_2 \cdot \left(m_{\mathrm{a},1} - x_1 \cdot m_e + \frac{E_{\mathrm{ion},1}}{c^2} \right) - x_1 \cdot \frac{E_{\mathrm{ion},2}}{c^2} + x_2 \cdot \frac{E_{\mathrm{ion},1}}{c^2} \end{aligned} \tag{6.14}$$

$$\begin{aligned} & x_2 \cdot m_{\mathrm{a},1} - x_1 \cdot m_{\mathrm{a},2} \\ & \quad = \left(\frac{1}{\overline{R}} - 1 \right) \cdot x_1 \cdot \left(m_{\mathrm{a},2} - x_2 \cdot m_e + \frac{E_{\mathrm{ion},2}}{c^2} \right) - x_2 \cdot \frac{E_{\mathrm{ion},1}}{c^2} + x_1 \cdot \frac{E_{\mathrm{ion},2}}{c^2} \quad , \end{aligned} \tag{6.15}$$

with $E_{\mathrm{ion},1}$ and $E_{\mathrm{ion},2}$ as the total ionization energies for forming the ions 1 and 2, respectively. These equations were used to compute the mass differences given in Table 6.4. The electron mass was taken from [38], the ionization energies of Sr and Yb from [131], the ionization energies of Xe and Kr from [132] and [133]. The reference masses used in the Kr and Xe mass measurements were taken from the AME2012 mass evaluation [24]. These values are based on earlier measurements performed at the FSU trap [48]. However, the uncertainties quoted in the AME2012 are more than 40% smaller than the uncertainties quoted in the original measurement, possibly because systematic shifts of the original mass measurements were treated as statistic shifts in the AME2012 evaluation, and thereby averaged in the global fits. In order to be conservative, the originally published (larger) uncertainties were used for the Kr and Xe mass values.

The Sr and Yb mass measurements were analyzed and published before the AME2012 became available. Here, the masses of Kr and Xe are also used as reference masses, and the values and uncertainties of the original FSU measurement [48] were used. Since these mass values were not shifted in the global evaluation of the AME2012, the quoted mass-differences and final masses were not updated in this summary.

Finally, using the same reference mass values as in the mass-difference equations, the mass values of the investigated isotopes were calculated. For masses where more than one mass-difference equation was applicable, the masses were calculated via a weighted average, with the weights formed from the total uncertainties of the mass-differences. The results are summarized in Table 6.5, while Figure 6.4 shows a visual comparison between the computed values and the AME2012.

The new mass determinations that were performed in the context of this thesis agree well with the results of the current AME2012, but with uncertainties of $(0.9-1.3)\cdot 10^{-10}$ they are between 17 and 130 times more precise and accurate. The uncertainty of these masses is now low enough for experiments that use krypton and xenon isotopes as references masses, and for the first generation of h/m_{a} determinations that plan to use strontium and ytterbium isotopes.

Higher accuracies can be achieved, but would benefit from using molecular ions containing carbon and oxygen as reference ions, in order to not be limited by the uncertainty of the krypton and xenon reference ions used in this thesis.

Table 6.4.: Mass differences calculated from the cyclotron frequency ratios in Table 6.3. The systematic, statistical, and total uncertainties are given in parentheses. In the mass-differences, the error due to the reference masses is suppressed by a factor of approximately $(1 - \bar{R})$, and therefore negligible.

Mass difference	Result in u
$m(^{84}\mathrm{Kr}) - m(^{83}\mathrm{Kr})$	0.997 371 212 7(86)(23)(89)
$m(^{84}\mathrm{Kr}) - m(^{82}\mathrm{Kr})$	1.998 016 573 2(46)(22)(51)
$m(^{86}\mathrm{Kr}) - m(^{82}\mathrm{Kr})$	3.997 129 467 8(80)(49)(94)
$m(^{131}\mathrm{Xe}) - m(^{129}\mathrm{Xe})$	2.000 303 279 2(85)(43)(95)
$m(^{132}\mathrm{Xe}) - m(^{131}\mathrm{Xe})$	0.999 070 949 6(134)(51)(144)
$m(^{134}\mathrm{Xe}) - m(^{132}\mathrm{Xe})$	2.001 237 945 6(79)(32)(85)
$m(^{86}\mathrm{Sr}) - m(^{84}\mathrm{Kr})$	1.997 762 999 2(43)(31)(53)
$m(^{86}\mathrm{Kr}) - m(^{86}\mathrm{Sr})$	0.001 349 896 5(54)(27)(60)
$m(^{87}\mathrm{Sr}) - m(^{84}\mathrm{Kr})$	2.997 379 769 9(40)(43)(59)
$m(^{87}\mathrm{Sr}) - m(^{86}\mathrm{Kr})$	0.998 266 865 9(43)(26)(50)
$m(^{88}\mathrm{Sr}) - m(^{84}\mathrm{Kr})$	3.994 114 530 6(47)(52)(70)
$m(^{88}\mathrm{Sr}) - m(^{86}\mathrm{Kr})$	1.995 001 625 6(42)(40)(58)
$m(^{86}\mathrm{Kr}) - m(^{84}\mathrm{Kr})$	1.999 112 899 9(29)(30)(42)
$4m(^{129}\mathrm{Xe}) - 3m(^{170}\mathrm{Yb})$	5.814 821 686 (25)(27)(36)
$4m(^{132}\mathrm{Xe}) - 3m(^{170}\mathrm{Yb})$	17.812 318 642 (26)(31)(40)
$4m(^{129}\mathrm{Xe}) - 3m(^{171}\mathrm{Yb})$	2.810 128 892 (28)(23)(37)
$4m(^{132}\mathrm{Xe}) - 3m(^{172}\mathrm{Yb})$	11.807 460 378 (25)(29)(38)
$3m(^{173}\mathrm{Yb}) - 4m(^{129}\mathrm{Xe})$	3.195 525 184 (31)(25)(39)
$4m(^{132}\mathrm{Xe}) - 3m(^{173}\mathrm{Yb})$	8.801 971 687 (36)(26)(45)
$3m(^{174}\mathrm{Yb}) - 4m(^{129}\mathrm{Xe})$	6.197 479 237 (19)(26)(32)
$4m(^{132}\mathrm{Xe}) - 3m(^{174}\mathrm{Yb})$	5.800 017 795 (37)(34)(50)
$3m(^{176}\mathrm{Yb}) - 4m(^{129}\mathrm{Xe})$	12.208 600 696 (33)(35)(49)
$3m(^{176}\mathrm{Yb}) - 4m(^{132}\mathrm{Xe})$	0.211 103 718 (73)(38)(82)

Table 6.5.: Results of the atomic mass measurements given in Table 6.4. All values are in u. The FSU values include the statistical error, systematic error, reference error, and total uncertainty in parentheses. For the AME2012 values, the total uncertainty is given in parentheses.

Atom	FSU	AME2012
^{82}Kr	81.913 481 158 8(42)(33)(76)(93)	81.913 482 7(9)
^{83}Kr	82.914 126 518 6(86)(23)(80)(119)	82.914 127 2(3)
^{131}Xe	130.905 084 137 1(75)(47)(106)(138)	130.905 084 06(24)
^{134}Xe	133.905 393 031 6(79)(32)(98)(130)	133.905 394 7(9)
^{86}Sr	85.909 260 730 9(35)(29)(79)(91)	85.909 260 6(12)
^{87}Sr	86.908 877 497 0(30)(34)(79)(91)	86.908 877 5(12)
^{88}Sr	87.905 612 257 1(31)(45)(80)(97)	87.905 612 5(12)
^{170}Yb	169.934 767 241 (6)(10)(14)(18)	169.934 766 4(22)
^{171}Yb	170.936 331 514 (9)(8)(15)(19)	170.936 330 2(22)
^{172}Yb	171.936 386 655 (9)(10)(13)(18)	171.936 385 9(22)
^{173}Yb	172.938 216 213 (8)(9)(14)(18)	172.938 215 1(22)
^{174}Yb	173.938 867 539 (6)(10)(14)(18)	173.938 866 4(22)
^{176}Yb	175.942 574 702 (11)(12)(15)(22)	175.942 576 4(24)

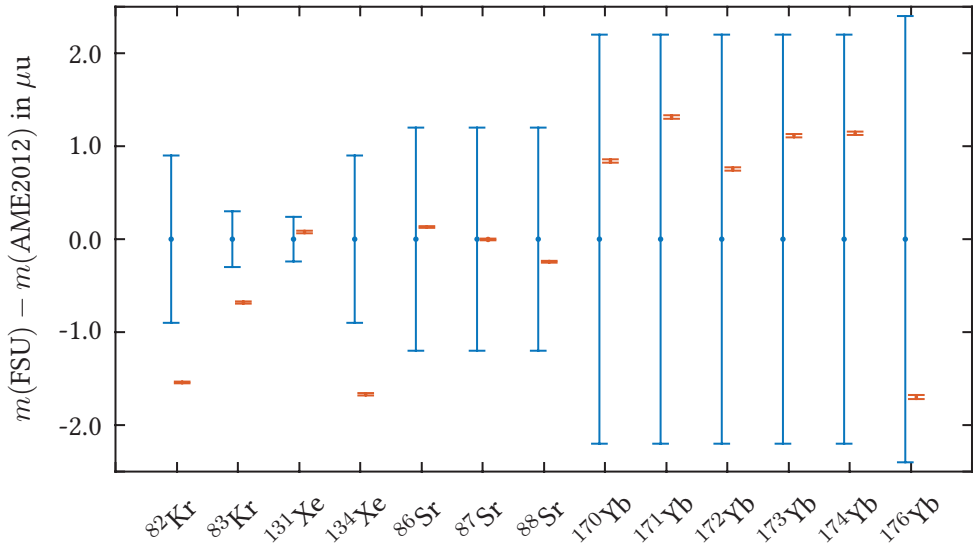

Figure 6.4.: FSU measurements compared to the AME2012. The values given in the AME2012 are shown in blue, with the errorbars corresponding to the uncertainties. At this scale, the error bars of the FSU results (shown in red) reduce to horizontal lines.

7. Conclusion and Outlook

Between the beginning of my time as a diploma student and now, THe-Trap has made tremendous progress. After energizing the magnet, we were almost immediately able to work with small clouds of ions, and we started to continuously refine our techniques. The ion loading, which used to take days of cleaning and still left us with multiple ions in the trap, was reduced to a 20-minute procedure that is fully automated. The sweep width, which during the beginning of my time as a PhD student was several hundred Hertz [52], was gradually narrowed to less than 100 mHz. This enabled us to do cyclotron frequency measurements on $^{12}C^{4+}$ and $^{16}O^{5+}$ ions with a state-of-the-art relative precision of $2 \cdot 10^{-11}$ [53]. By implementing the trap-optimization techniques of the FSU/MIT experiment, we were also able to reduce most systematic errors to a similar level. We developed new models to understand the most relevant frequency shifts [86, 90]. The rotating wave approximation developed in the context of this thesis augments these models by including dynamical and non-rotationally symmetric effects. The PENTATRAP voltage source StaReP was tested successfully at THe-Trap [111]. Due to its larger range ($0 - 100$ V compared to $80 - 90$ V), it was installed as an alternative to the existing high-precision voltage source. A new amplifier, using a design developed at ALPHATRAP, reduced our problems with noise spikes and unwanted amplifier feedback [107]. Overall, the systematic and statistical errors at THe-Trap are now sufficiently controlled to perform mass measurements with relative uncertainties below 10^{-10}.

At the FSU trap, 3 new mass differences were measured, and an additional 20 were analyzed, which resulted in the determination of the masses of 13 isotopes with relative uncertainties between $(0.9 - 1.3) \cdot 10^{-10}$. These mass values have applications in the determination of the fine-structure constant α via the photon-recoil method, and will help to strengthen the backbone of the AME. After my last visit, the FSU trap was modified to optimize it for a measurement of the T$-^3$He mass difference. The superconducting coil of the detection circuit was exchanged for a coil with a higher resonance frequency, and a cryogenic neutral-gas beam collimator was installed in order to reduce the trap contamination when loading tritium. These modifications led to a measurement of the T$-^3$He mass difference that was published in 2015 [32]. This publication included a measurement of the ^{3}He mass with a relative uncertainty of $6.3 \cdot 10^{-11}$. Two months later, the group of Robert Van Dyck published results of measurements that had been taken before the UW-PTMS experiment had moved to Heidelberg [95]. These results also included a measurement of the ^{3}He mass, with an even lower relative uncertainty of only $1.4 \cdot 10^{-11}$. Curiously, these two recent measurements of the ^{3}He mass disagree on a 3.9σ level.

To this end, and in order to be independent of the lineshape problem, the possibilities of PnP-measurements are being investigated at THe-Trap. This will allow us to do a direct comparison of the two leading techniques for mass-measurements with the highest precision, and enable us to investigate the 3.9σ discrepancy.

A. Green's Function Treatment

The Green's function treatment of the Penning trap has been described earlier, but unfortunately either in fairly broad strokes [55, 81] or with advanced techniques that are not easily accessible [56, 57]. This appendix shows that the Green's function treatment does not require advanced mathematical techniques beyond basic properties of the δ-distribution. It could be significantly shortened by using, for example, a Laplace-transform, but in the spirit of our frequency shift calculations [86, 90], foregoing such tricks keeps the treatment accessible to a wider audience.

A.1. Introduction: One-dimensional Green's functions

Consider a one-dimensional, linear differential equation, where the unknown function $f(t)$ has to satisfy

$$Lf(t) = a(t) \quad . \tag{A.1}$$

The symbol L represents a linear differential operator, and the function $a(t)$ the (given) inhomogeneous term. (The equations are usually arranged such that the driving term is given in units of acceleration, which is why I chose the letter a). This type of problem can be solved with the help of the Green's function $G(t, t_0)$. G is a function of two variables, and it is implicitly defined as a function that satisfies the equation

$$L\,G(t, t_0) = \delta(t - t_0) \quad . \tag{A.2}$$

If $G(t, t_0)$ is known, then Equation (A.2) can be multiplied by $a(t_0)$ and integrated over all t_0:

$$\int_{-\infty}^{\infty} dt_0\, L\,G(t, t_0)a(t_0) = \int_{-\infty}^{\infty} dt_0\, \delta(t - t_0)a(t_0) \quad . \tag{A.3}$$

Rearranging the terms (L only acts on t, not t_0, and can be pulled out of the integral) yields

$$L \int_{-\infty}^{\infty} dt_0\, G(t, t_0)a(t_0) = a(t) \quad . \tag{A.4}$$

This solves the initial problem, because we can identify

$$f(t) = \int_{-\infty}^{\infty} dt_0\, G(t, t_0)a(t_0) \tag{A.5}$$

as a particular solution to Equation (A.1). The full solution is given by the particular solution plus the solutions of the homogeneous equation.

The usual Green's function approach consists of guessing a function $G(t, t_0)$ and then proving Equation (A.2), by showing that for all reasonable[1] test functions $h(t)$, the expression $L\,G(t, t_0)$ behaves like a δ-distribution:

$$\int_a^b dt_0\, L\, G(t, t_0) h(t_0) = \begin{cases} h(t) & \text{if } a < t < b \\ 0 & \text{otherwise} \end{cases} \quad . \tag{A.6}$$

A.2. Green's Function of the axial mode

Consider an undamped[2] axial motion $z(t)$ that is forced by the driving term $a(t)$:

$$\ddot{z}(t) + \omega_z^2 z(t) = a(t) \quad . \tag{A.7}$$

Here, the linear operator is

$$L = \frac{d^2}{dt^2} + \omega_z^2 \quad . \tag{A.8}$$

The physical meaning of Equation (A.2), which defines the Green's function $G(t, t_0)$, is exciting the system with a short "bump" at $t = t_0$. Using some intuition, we can guess a solution that has the oscillator resting before the bump, and excited with amplitude $\hat{z}$ after the bump.

$$G(t, t_0) = \begin{cases} 0 & \text{if } t < t_0 \\ \hat{z}\sin(\omega_z(t - t_0)) & \text{if } t \geq t_0 \end{cases} \tag{A.9}$$

$G(t, t_0)$ can also be expressed with the Heaviside step function $\Theta(t)$.

$$G(t, t_0) = \hat{z}\,\Theta(t - t_0)\,\sin(\omega_z(t - t_0)) \tag{A.10}$$

In order to show $LG \equiv \delta$, we need to find the derivatives of $G(t, t_0)$. We'll make use of the fact that $\frac{d}{dt}\Theta(t - t_0) = \delta(t - t_0)$.

$$\frac{d}{dt}G(t, t_0) = \hat{z}\,\delta(t - t_0)\,\sin(\omega_z(t - t_0)) + \hat{z}\,\Theta(t - t_0)\,\omega_z\cos(\omega_z(t - t_0)) \tag{A.11}$$

$$\begin{aligned}\frac{d^2}{dt^2}G(t, t_0) = {} & \hat{z}\tfrac{d}{dt}\delta(t - t_0)\,\sin(\omega_z(t - t_0)) + 2\hat{z}\,\delta(t - t_0)\,\omega_z\cos(\omega_z(t - t_0)) \\ & - \hat{z}\,\Theta(t - t_0)\,\omega_z^2\sin(\omega_z(t - t_0)) \quad .\end{aligned} \tag{A.12}$$

For proving that the proposed Green's function indeed satisfies Equation (A.2), we use Equation (A.6), which includes an integral. But the second derivative of G includes a term with $\frac{d}{dt}\delta(t - t_0)$. How can this be simplified? First, we note that due to symmetry, $\frac{d}{dt}\delta(t - t_0) = -\frac{d}{dt_0}\delta(t - t_0)$. Then, using integration by parts, we can show how this term acts on a test

[1] reasonable for physicists — not obscure functions that mathematicians may find reasonable

[2] This keeps the equations short. Including the damping term is otherwise uncomplicated.

function $h(t)$:

$$
\begin{aligned}
-\int_a^b dt_0 \, \left(\tfrac{d}{dt_0}\delta(t-t_0)\right) \sin(\omega_z(t-t_0)h(t_0) \\
= \; -\delta(t-t_0)\sin(\omega_z(t-t_0))h(t_0)\Big|_{t_0=a}^{t_0=b} \\
+\int_a^b dt_0 \, \delta(t-t_0)\left(-\omega_z\cos(\omega_z(t-t_0))h(t_0) + \sin(\omega_z(t-t_0)\tfrac{d}{dt_0}h(t_0)\right) \quad .
\end{aligned}
\tag{A.13}
$$

The term outside the integral evaluates to zero[3]. The two terms inside the integral only matter at $t_0 = t$, where $\cos(0) = 1$ and $\sin(0) = 0$. Therefore, the integral can be simplified to

$$
\int_a^b dt_0 \, \left(\tfrac{d}{dt}\delta(t-t_0)\right) \sin(\omega_z(t-t_0)h(t_0) = -\int_a^b dt_0 \, \delta(t-t_0)\omega_z h(t_0) \quad . \tag{A.14}
$$

This helps us in simplifying Equation (A.12) to

$$
\frac{d^2}{dt^2}G(t,t_0) = \hat{z}\,\delta(t-t_0)\omega_z - \hat{z}\,\Theta(t-t_0)\omega_z^2\sin(\omega_z(t-t_0)) \quad . \tag{A.15}
$$

Now we have everything we need to test whether our candidate fulfills the required relationship $LG(t,t_0) = \delta(t-t_0)$.

$$
\left(\frac{d^2}{dt^2} + \omega_z^2\right) G(t,t_0) \stackrel{!}{=} \delta(t-t_0) \tag{A.16}
$$

$$
\Leftrightarrow \qquad \hat{z}\,\delta(t-t_0)\omega_z = \delta(t-t_0) \tag{A.17}
$$

$$
\Leftrightarrow \qquad \hat{z} = \frac{1}{\omega_z} \quad . \tag{A.18}
$$

It does, as long as $\hat{z} = 1/\omega_z$. We actually don't need Equation (A.6) anymore to prove this, because we already used it for motivating simplifications that left us with a direct proof of Equation (A.2). In summary, for any forcing function $a(t)$, the harmonic oscillator can be solved using

$$
\begin{aligned}
z(t) &= +\int_{-\infty}^{\infty} dt_0 \, a(t_0)\frac{1}{\omega_z}\Theta(t-t_0)\sin(\omega_z(t-t_0)) \\
&= +\int_{-\infty}^{t} dt_0 \, a(t_0)\frac{1}{\omega_z}\sin(\omega_z(t-t_0)) \quad ,
\end{aligned}
\tag{A.19}
$$

Again, this is only a particular solution, and the homogeneous solutions have to be added to ensure that possible boundary conditions are satisfied. The variable t appears both in the limit of the integral and inside of the integral, which looks a bit awkward, but for the evaluation of the integral, it is simply a constant that happens to appear twice.

[3] To prove this, consider how this particular term acts on another test-function in an additional integral.

To show an application of the Green's function, let us calculate the response of an ion at rest to a sinusoidal drive that is switched on at $t = 0$. This drive can be described with $a(t) = \Theta(t-0)\hat{a}\cos(\omega_{\text{drive}}t)$. The Green's function approach gives the solution as

$$z(t) = \int_{-\infty}^{t} dt_0\, \Theta(t_0)\hat{a}\cos(\omega_{\text{drive}}t_0)\frac{1}{\omega_z}\sin(\omega_z(t-t_0)) \quad . \tag{A.20}$$

The term $\Theta(t_0)$ can be absorbed into the lower limit of the integral. Further, using the trigonometric identity $\cos(a)\sin(b) = (\sin(a+b) - \sin(a-b))/2$, the integral can be transformed to

$$z(t) = \int_{0}^{t} dt_0\, \frac{\hat{a}}{2\omega_z}\Big(\sin\left[(\omega_{\text{drive}} - \omega_z)\, t_0 + \omega_z t\right] - \sin\left[(\omega_{\text{drive}} + \omega_z)\, t_0 - \omega_z t\right]\Big) \quad . \tag{A.21}$$

For $\omega_{\text{drive}} \neq \omega_z$ (and $t > 0$) this integral is readily evaluated to

$$z(t) = \frac{\hat{a}}{\omega_z^2 - \omega_{\text{drive}}^2}\left[\cos\left(\omega_{\text{drive}}t\right) - \cos\left(\omega_z t\right)\right] \quad . \tag{A.22}$$

As can be seen, this particular solution happens to solve the boundary conditions (ion at rest for $t < 0$). The solution displays beating between ω_{drive} and ω_z. When ω_{drive} approaches ω_z, the amplitude of the beating grows. In the limit $\omega_{\text{drive}} = \omega_z$, the solution simplifies to

$$z(t) = \frac{\hat{a}}{2\omega_z}t\sin(\omega_z t) \quad , \tag{A.23}$$

and the amplitude is no longer constant, but increases linearly with time. The phase of the response lags $90°$ behind the phase of the excitation.

A.3. Two-dimensional Green's functions

In order to apply the Green's function formalism to two-dimensional[4] linear differential equations, the operator L must be expressed as a matrix with four components:

$$\begin{pmatrix} L_{xx} & L_{xy} \\ L_{yx} & L_{yy} \end{pmatrix}\begin{pmatrix} x(t) \\ y(t) \end{pmatrix} = \begin{pmatrix} a_x(t) \\ a_y(t) \end{pmatrix} \quad . \tag{A.24}$$

Here, $a_x(t)$ and $a_y(t)$ are the external drives in x and y-direction, respectively.

Because the equation is linear, we can treat the driving terms $a_x(t)$ and $a_y(t)$ separately and solve for

$$\begin{pmatrix} L_{xx} & L_{xy} \\ L_{yx} & L_{yy} \end{pmatrix}\begin{pmatrix} x_x \\ y_x \end{pmatrix} = \begin{pmatrix} a_x \\ 0 \end{pmatrix} \tag{A.25}$$

$$\begin{pmatrix} L_{xx} & L_{xy} \\ L_{yx} & L_{yy} \end{pmatrix}\begin{pmatrix} x_y \\ y_y \end{pmatrix} = \begin{pmatrix} 0 \\ a_y \end{pmatrix} \tag{A.26}$$

[4] This argument can easily be expanded to N dimensions.

independently. The full solution is given by adding these two particular solutions, and then adding the solutions of the homogeneous (undriven) equation to fix the initial conditions.

Having decomposed the problem into two problems where the forces are limited to one dimension, we can now turn to the Green's formalism, by examining the system's response to a δ-pulse. We consider only forces in the x-direction (forces in the y-direction can be treated in the same way) and define the functions G_{xx}, G_{yx} as solutions to the problem

$$\begin{pmatrix} L_{xx} & L_{xy} \\ L_{yx} & L_{yy} \end{pmatrix} \begin{pmatrix} G_{xx}(t,t_0) \\ G_{yx}(t,t_0) \end{pmatrix} = \delta(t-t_0) \begin{pmatrix} 1 \\ 0 \end{pmatrix} \quad . \tag{A.27}$$

G_{xx} and G_{yx} stand for the system's $x(t)$ and $y(t)$ responses to a bump in x-direction. If they are known, then (analogous to the treatment of Equation A.2) we can multiply the top and bottom equations by $a_x(t_0)$ and integrate over all t_0. After rearranging the terms we arrive at

$$L_{xx} \int_{-\infty}^{\infty} G_{xx}(t,t_0) a_x(t_0) dt_0 \; + \; L_{xy} \int_{-\infty}^{\infty} G_{yx}(t,t_0) a_x(t_0) dt_0 \; = \; a_x(t) \tag{A.28}$$

$$L_{yx} \int_{-\infty}^{\infty} G_{xx}(t,t_0) a_x(t_0) dt_0 \; + \; L_{yy} \int_{-\infty}^{\infty} G_{yx}(t,t_0) a_x(t_0) dt_0 \; = 0 \quad , \tag{A.29}$$

and by comparison with Equation (A.25), we can identify

$$x_x(t) = \int_{-\infty}^{\infty} G_{xx}(t,t_0) a_x(t_0) dt_0 \tag{A.30}$$

$$y_x(t) = \int_{-\infty}^{\infty} G_{yx}(t,t_0) a_x(t_0) dt_0 \tag{A.31}$$

as the particular solution of the system being driven in x-direction. The full solution can be obtained as the sum of this solution, the solution to the drive in y-direction, and the homogeneous solution.

A.4. Green's function of the radial modes

Using the standard relationships between ω_c, ω_z, ω_+, and ω_-, the radial equations of motion can be rewritten as

$$\begin{aligned} \ddot{x}(t) \; - \; (\omega_+ + \omega_-)\dot{y}(t) \; - \; \omega_+\omega_- x(t) \; &= \; 0 \\ \ddot{y}(t) \; + \; (\omega_+ + \omega_-)\dot{x}(t) \; - \; \omega_+\omega_- y(t) \; &= \; 0 \quad . \end{aligned} \tag{A.32}$$

As a reminder, the solutions to the undriven equation are (using real-valued functions instead of $e^{i\cdots}$)

$$\begin{aligned} x(t) &= r_+ \sin(\omega_+ t + \varphi_+) + r_- \sin(\omega_- t + \varphi_-) \\ y(t) &= r_+ \cos(\omega_+ t + \varphi_+) + r_- \cos(\omega_- t + \varphi_-) \quad . \end{aligned} \tag{A.33}$$

The matrix representation of the differential operator in Equation (A.32) is

$$\begin{pmatrix} L_{xx} & L_{xy} \\ L_{yx} & L_{yy} \end{pmatrix} = \begin{pmatrix} \frac{d^2}{dt^2} - \omega_+\omega_- & -(\omega_+ + \omega_-)\frac{d}{dt} \\ (\omega_+ + \omega_-)\frac{d}{dt} & \frac{d^2}{dt^2} - \omega_+\omega_- \end{pmatrix} \quad . \tag{A.34}$$

Due to the symmetry of the problem, the solution to a push in the y-direction follows directly from the solution to a push in the x-direction, so we only need to solve for forces in the x-direction. With the operator L of the radial motion, the definition of the Green's function (Equation A.27) becomes

$$\begin{aligned} \ddot{G}_{xx}(t,t_0) \; - \; (\omega_+ + \omega_-)\dot{G}_{yx}(t,t_0) \; - \; \omega_+\omega_- G_{xx}(t,t_0) \; &= \; \delta(t-t_0) \\ \ddot{G}_{yx}(t,t_0) \; + \; (\omega_+ + \omega_-)\dot{G}_{xx}(t,t_0) \; - \; \omega_+\omega_- G_{yx}(t,t_0) \; &= \; 0 \quad . \end{aligned} \tag{A.35}$$

Let us try to do an educated guess of the ion's response to a push in the x-direction at $t_0 = 0$. If the ion rests before the push, intuition tells us that the ion moves in the x-direction right after the push:

$$x(t) \; = \; \Theta(t)\left[r_+ \sin(\omega_+ t) \; + \; r_- \sin(\omega_- t)\right] \quad . \tag{A.36}$$

The parameters r_+, r_- have yet to be determined. Since in a Penning trap there can be no x-motion without y-motion, the y-motion must be

$$y(t) \; = \; \Theta(t)\left[r_+ \cos(\omega_+ t) \; + \; r_- \cos(\omega_- t)\right] \quad . \tag{A.37}$$

But the cos-terms in the y-motion are potentially problematic: It would be unphysical if the push in x-direction made the particle jump to a new y-position. The only combination of r_+, r_- that does not make the y-motion jump at the time of the push is $r_- = -r_+$. This simplifies the educated guess of the Green's functions to

$$\begin{aligned} G_{xx}(t,t_0) \; &= \; \Theta(t-t_0) r\left[\sin(\omega_+(t-t_0)) \; - \; \sin(\omega_-(t-t_0))\right] \\ G_{yx}(t,t_0) \; &= \; \Theta(t-t_0) r\left[\cos(\omega_+(t-t_0)) \; - \; \cos(\omega_-(t-t_0))\right] \quad . \end{aligned} \tag{A.38}$$

Applying this guess to Equation (A.35) is lengthy, but straightforward. The derivatives of G_{xx} are essentially given by Equation (A.11) and Equation (A.15). The derivatives of G_{yx} are similar, except the second derivative includes two $\dot{\delta}(t)$-terms that, for $t = t_0$, cancel each other. Ultimately, the second equation evaluates to true and the first equation reduces to

$$(\omega_+ - \omega_-)\, r\, \delta(t-t_0) = \delta(t-t_0) \quad , \tag{A.39}$$

which proves that the educated guess was correct and that the radius r is given by

$$r = \frac{1}{\omega_+ - \omega_-} \quad . \tag{A.40}$$

We conclude by noting that the Green's function of the radial mode, Equation (A.38), comprises the sum of two terms. Apart from a scaling factor, each term resembles the Green's function of the harmonic oscillator. In the treatment of the harmonic oscillator (Equation A.22), we learned that its response to non-resonant drives is much smaller than the response to resonant drives. Therefore, when the radial Green's function is driven near either resonance, we can neglect the non-resonant term, and the Green's function becomes identical to the Green's function of a one-dimensional harmonic oscillator, except that the response is scaled by a factor of

$$c_+ = +\frac{\omega_+}{\omega_+ - \omega_-} \tag{A.41}$$

for drives near ω_+, and by

$$c_- = -\frac{\omega_-}{\omega_+ - \omega_-} \tag{A.42}$$

for drives near ω_-. This makes it possible to treat the magnetron mode and the cyclotron mode as independent harmonic oscillators. The minus sign of c_- reveals a fundamental property of the magnetron mode: Its response does not lag 90° behind the drive, but instead leads it by 90°. This is also to the reason why dissipative forces, which are proportional to the velocity, lead to an increase of the magnetron radius, instead of a decrease.

A.5. Rotating wave approximation

Calculating the ion response to drives that are nearly resonant is greatly simplified by using the classical version of the rotating wave-approximation. This approximation can be motivated using the Green's function of the one-dimensional harmonic oscillator[5].

Consider a one-dimensional, undamped oscillator that is driven with a resonant pulse of strength $\hat{a}$ and phase φ. The drive is switched on at t_s and switched off at t_f. Using the Green's-function approach (Equation A.19), the ion motion at $t = t_f$, when the pulse is switched off, is given by

$$z(t_f) = z_0(t_f) + \int_{t_s}^{t_f} dt_0\, \hat{a} \cos(\omega_z t_0 + \varphi) \frac{1}{\omega_z} \sin(\omega_z (t_f - t_0)) \quad . \tag{A.43}$$

Here, we explicitly allowed for initial motion of the ion, given by $z_0(t)$. With the help of the identity $\cos(a)\sin(b) = (\sin(a+b) - \sin(a-b))/2$, the integral can be transformed to

$$z(t_f) = z_0(t_f) + \int_{t_s}^{t_f} dt_0\, \frac{\hat{a}}{2\omega_z} \left[\sin(\omega_z t_f + \varphi) - \sin(2\omega_z t_0 - \omega_z t_f + \varphi)\right] \quad . \tag{A.44}$$

The first term inside the integral is constant with respect to t_0, while the second term has a frequency of $2\omega_z$ with respect to t_0. Therefore, when performing the integration, the first term leads to an oscillation with growing amplitude, while the second term leads to oscillating terms with bound amplitude. For times $t_f - t_s \gg \frac{1}{2\omega_z}$, the amplitude of the second term will be much smaller than the amplitude of the first term. We can thus neglect the second term and are left with

$$z(t_f) \approx \hat{z}(t_f) + \frac{\hat{a}}{2\omega_z}(t_f - t_s)\sin(\omega_z t_f + \varphi) \quad . \tag{A.45}$$

The $\sin(\omega_z t + \varphi)$-term can be expanded using a standard trigonometric identity, and the original ion motion $\hat{z}(t)$ can parametrized as

$$\hat{z}(t) = Z_c \cos(\omega_z t) + Z_s \sin(\omega_z t) \quad . \tag{A.46}$$

[5] The name "rotating wave" implies a two-dimensional motion, but we restrict ourselves to a one-dimensional oscillator in this section. The "rotation" refers to treating phasors in a rotating reference frame. The phasor-picture, although more intuitive, is more challenging to treat quantitatively than the Green's function approach.

This leads to the lengthy, but simple expression

$$z(t_f) = Z_c \cos(\omega_z t_f) + Z_s \sin(\omega_z t_f) + \frac{\hat{a}}{2\omega_z}(t_f - t_s)\left[\sin(\varphi)\cos(\omega_z t_f) + \cos(\varphi)\sin(\omega_z t_f)\right] \quad . \tag{A.47}$$

Defining $\Delta t = t_f - t_s$, we can see that the effect of the pulse can interpreted as a change of the coefficients Z_c and Z_s that is proportional to Δt:

$$\begin{aligned} Z_c(t_s + \Delta t) - Z_c(t_s) &= \sin(\varphi)\frac{\hat{a}}{2\omega_z}\Delta t \\ Z_s(t_s + \Delta t) - Z_s(t_s) &= \cos(\varphi)\frac{\hat{a}}{2\omega_z}\Delta t \quad . \end{aligned} \tag{A.48}$$

This leads directly to the full rotating wave approximation: A drive "sufficiently" near resonance can be decomposed into smaller excitations of duration Δt, where each excitation is exactly resonant. Near-resonant excitations with frequency $\omega_{\text{drive}} \neq \omega_z$ can be treated by letting the phase φ vary slowly (so that $\Delta t \gg \frac{1}{2\omega_z}$ is still satisfied), with

$$\frac{\Delta\varphi}{\Delta t} = \omega_{\text{drive}} - \omega_z \quad . \tag{A.49}$$

Each of the short excitations changes the coefficients Z_c and Z_s according to Equation (A.48). Dividing these equations by Δt and expressing Z_c, Z_s, φ, and $\hat{a}$ as slowly varying functions of time, we can finally state the full rotating wave approximation as

$$\begin{aligned} \dot{Z}_c(t) &= \sin[\varphi(t)]\frac{\hat{a}(t)}{2\omega_z} \\ \dot{Z}_s(t) &= \cos[\varphi(t)]\frac{\hat{a}(t)}{2\omega_z} \quad . \end{aligned} \tag{A.50}$$

This is an important simplification, because $Z_c(t)$ and $Z_s(t)$ are now given by integrals that are free of the fast oscillation with ω_z. This helps to find these integrals, especially when they have to be computed numerically.

The rotating wave approximation can also be stated in complex form when defining

$$Z(t) = Z_c(t) - iZ_s(t) \tag{A.51}$$

$$\Rightarrow \quad z(t) = \Re\left(Z(t)e^{i\omega_z t}\right) \quad . \tag{A.52}$$

$Z(t)$ is the complex amplitude of the ion's z-motion. The drive $a(t)$ can be defined in an analogous fashion as

$$D(t) = \hat{a}(t)e^{i\varphi(t)} \tag{A.53}$$

$$\Rightarrow \quad a(t) = \Re\left(D(t)e^{i\omega_z t}\right) \quad . \tag{A.54}$$

Using this notation, the rotating wave approximation can be transformed to

$$\dot{Z}(t) = \frac{1}{2i\omega_z}D(t) \quad . \tag{A.55}$$

This complex form can help to treat certain driving terms in shorter notation. For example, a weak damping term can be treated as a drive $D(t)$ that is proportional to $iZ(t)$:

$$\ddot{z}(t) + \omega_z^2 z(t) = -\gamma_z \dot{z}(t) \approx \Re\left(-i\omega_z\gamma_z Z(t) e^{i\omega_z t}\right) \tag{A.56}$$

$$\Rightarrow \qquad D(t) = -i\omega_z\gamma_z Z(t) \tag{A.57}$$

$$\Rightarrow \qquad \dot{Z}(t) = -\frac{1}{2}\gamma_z Z(t) \tag{A.58}$$

$$\Rightarrow \qquad Z(t) = \hat{Z} e^{-\frac{1}{2}\gamma_z t} \quad . \tag{A.59}$$

As expected, the damping term γ_z causes the amplitude Z to decay with a time-constant of $2/\gamma_z$. However, compared to the full solution, the rotating wave approximation does not show the small frequency shift that is caused by the damping term. This is a valid simplification for $\gamma_z \ll \omega_z$.

The rotating wave approximation can also be used to show that anharmonic terms lead to frequency shifts. For example, an anharmonic term λz^3 leads to a differential equation that can be approximated as

$$\ddot{z}(t) + \omega_z^2 z(t) = -\lambda [z(t)]^3 \tag{A.60}$$

$$= -\lambda \left[\Re\left(Z(t)e^{i\omega_z t}\right)\right]^3 \tag{A.61}$$

$$= -\lambda \left[\frac{1}{2}\left(Z(t)e^{i\omega_z t} + Z^*(t)e^{-i\omega_z t}\right)\right]^3 \tag{A.62}$$

$$\approx -\lambda\, \Re\left(\frac{3}{4}\left|Z(t)\right|^2 Z(t) e^{i\omega_z t}\right) \quad . \tag{A.63}$$

In the last step, we neglected non-resonant terms. The remaining term is an effective drive $D(t)$ that is proportional to $Z(t)$:

$$D(t) = -\frac{3}{4}\lambda \left|Z(t)\right|^2 Z(t) \tag{A.64}$$

$$\Rightarrow \qquad \dot{Z}(t) = -\frac{3}{8i\omega_z}\lambda \left|Z(t)\right|^2 Z(t) \quad . \tag{A.65}$$

The ansatz $Z(t) = \hat{Z}\exp(i\Delta\omega_z t)$ leads to a frequency shift of

$$i\Delta\omega_z = -\frac{3}{8i\omega_z}\lambda|\hat{Z}|^2$$

$$\Rightarrow \qquad \Delta\omega_z = \frac{3}{8}\frac{\lambda|\hat{Z}|^2}{\omega_z} \quad , \tag{A.66}$$

which is the same result that can be obtained using perturbation theory [84, 87]. This approach can also be turned around: When there is a known frequency shift proportional to $\hat{Z}^2$ (for example, caused by special relativity), then Equation (A.66) gives the corresponding λ with which the shift can be included in the rotating wave approximation.

The true advantage of the rotating wave approximation reveals itself when different $D(t)$ (damping, anharmonicities, coupling) are combined. The resulting differential equation for $\dot{Z}(t)$

can generally not be solved analytically, but it can be integrated numerically. While this is also possible for the full differential equation, the integral of the rotating wave approximation is less expensive, because the fast oscillation with ω_z (or ω_- or ω_+) is not present in the approximation.

A.6. Mode coupling

A.6.1. Example: Axial to Cyclotron

Coupling two modes can be achieved by using a weak potential (compared to the main trapping potential) that mixes two dimensions. The lowest order potentials with this property are given by the polynomials $p_{2,1}$, $p_{2,-1}$, and $p_{2,-2}$ (Equation 2.43). For example, consider the potential given by $p_{2,1}$, which leads to the field

$$\vec{E}_{\text{couple}} = c_0 \begin{pmatrix} z \\ 0 \\ x \end{pmatrix} \quad , \tag{A.67}$$

with $c_0 = -D_{2,1}U_d$ as the constant of unit V/m^2 that gives the strength of the field. This particular field can be used to couple the radial modes to the axial mode. When it is static, this field tugs on the ion in x-direction with a force proportional to the ion's z-position, and vice versa. In each mode this tug is non-resonant: The x-mode is wiggled with ω_z, and the z-mode is wiggled with ω_+ and ω_-. However, if c_0 is made explicitly time-dependent,

$$\vec{E}_{\text{couple}}(t) = c_0 \cos\left(\omega_{\text{drive}} t + \varphi\right) \begin{pmatrix} z \\ 0 \\ x \end{pmatrix} \quad , \tag{A.68}$$

the multiplication of $z(t)$, $x(t)$ with the term $\cos(\omega_{\text{drive}} t)$ creates upper and lower sidebands that can be resonant with the radial modes and the axial mode, when $\omega_{\text{drive}} = \omega_+ \pm \omega_z$ or $\omega_{\text{drive}} = \omega_- \pm \omega_z$.

For a qualitative description of the ion-behavior in such a modulated coupling field, one can consider an ion state that has initial cyclotron amplitude, but no initial axial amplitude. The modulated coupling field, together with the ion's x-motion, causes an effective, resonant force in the axial direction, and the axial amplitude grows. But the growing z-motion, together with the coupling field, now also causes an effective, resonant force on the cyclotron mode: The axial motion back-acts on the cyclotron motion. We will show that this back-action is positive when $\omega_{\text{drive}} = \omega_z + \omega_+$, which causes the amplitudes in both modes to grow exponentially, and that it is negative for $\omega_{\text{drive}} = \omega_z - \omega_+$, which causes the amplitudes to oscillate (Rabi oscillations).

In order to show this in detail, we use results of the Green's function treatment and the rotating wave approximation. The Green's function treatment showed that radial forces near ω_+ or ω_- lead to an ion response that can be approximated with two independent, one-dimensional harmonic oscillators. Forces far away from the frequencies ω_+ or ω_- can be neglected.

We will therefore treat all three modes as independent, undamped[6], harmonic oscillators $z(t)$, $x_+(t)$, $x_-(t)$. Also, to set up the rotating wave approximation, we will describe each oscillator

[6] Damping can be incorporated as an additional driving term, as shown in the previous section and in [55].

in terms of the complex amplitudes $Z(t)$, $X_+(t)$, $X_-(t)$ as

$$z(t) = \Re\left(Z(t)e^{i\omega_z t}\right) \tag{A.69}$$
$$x_+(t) = \Re\left(X_+(t)e^{i\omega_+ t}\right) \tag{A.70}$$
$$x_-(t) = \Re\left(X_-(t)e^{i\omega_- t}\right) \quad . \tag{A.71}$$

For the coupling drive, we choose the concrete example of a drive with frequency $\omega_{\text{drive}} = \omega_+ - \omega_z$, complex amplitude D, and a coupling field given by $p_{2,1}$. This changes the time-dependent part in Equation (A.68) to

$$c_0 \cos\left(\omega_{\text{drive}} t + \varphi\right) = \Re\left(Ce^{i\omega_{\text{drive}} t}\right) \quad . \tag{A.72}$$

One word of caution: When using a complex ansatz, the $\Re$-operator is often dropped and the imaginary part of all equations tacitly ignored. In most cases, this is valid, but care has to be taken when multiplying "complexified" components with each other, because $\Re(z_1)\Re(z_2) \neq \Re(z_1 z_2)$. For example, when ω_1, ω_2 are real, then

$$\Re\left(a_1 e^{i\omega_1 t}\right)\Re\left(a_2 e^{i\omega_2 t}\right) = \frac{1}{2}\Re\left(a_1 a_2 e^{i(\omega_1+\omega_2)t} + a_1 a_2^* e^{i(\omega_1-\omega_2)t}\right) \quad . \tag{A.73}$$

Therefore, the x-component of the coupling force $\vec{F} = q\vec{E}_{\text{couple}}$ is

$$\begin{aligned} F_x(t) &= q\,\Re\left(Z(t)e^{i\omega_z t}\right)\Re\left(Ce^{i(\omega_+-\omega_z)t}\right) \\ &= \frac{q}{2}\Re\left(CZ(t)e^{i\omega_+ t} + C^* Z(t)e^{i(2\omega_z-\omega_+)t}\right) \quad . \end{aligned} \tag{A.74}$$

The y-component of the coupling force is zero. The force on the cyclotron *mode* is given by the terms that have a frequency of ω_+ — all other, non-resonant terms can be neglected. Further, the force on the cyclotron mode has to be scaled by $\omega_+/(\omega_+ - \omega_-)$ (Equation A.41), which results in

$$F_+(t) = \frac{q\omega_+}{2(\omega_+ - \omega_-)}\Re\left(CZ(t)e^{i\omega_+ t}\right) \quad . \tag{A.75}$$

For calculating the force on the z-mode, we have to remember that the x-position depends on the magnetron amplitude X_- and the cyclotron amplitude X_+. However, after dropping all non-resonant terms, the force (which does not need to be scaled) can be approximated as

$$F_z(t) = \frac{q}{2}\Re\left(C^* X_+(t)e^{i\omega_z t}\right) \quad . \tag{A.76}$$

From these forces, we can construct the amplitudes of the driving acceleration as

$$\begin{aligned} D_+(t) &= \frac{q}{2m}\frac{\omega_+}{\omega_+ - \omega_-}CZ(t) \\ D_z(t) &= \frac{q}{2m}C^* X_+(t) \quad . \end{aligned} \tag{A.77}$$

Finally, we can use the rotating wave approximation Equation (A.55) to state the time-evolution of the amplitudes $X_+(t)$ and $Z(t)$ as

$$\dot{X}_+(t) = \frac{q}{4im(\omega_+ - \omega_-)} C Z(t) \tag{A.78}$$

$$\dot{Z}(t) = \frac{q}{4im\omega_z} C^* X_+(t) \quad . \tag{A.79}$$

After taking the derivative of the first equation, it can be combined with the second equation to yield

$$\ddot{X}_+(t) + \frac{q^2 C C^*}{16m^2\omega_z(\omega_+ - \omega_-)} X_+(t) = 0 \quad . \tag{A.80}$$

This leads to the solution

$$X_+(t) = A_0 e^{i\Omega t} + A_1 e^{-i\Omega t} \qquad \text{with} \tag{A.81}$$

$$\Omega = \frac{|C|}{4}\frac{q}{m}\frac{1}{\sqrt{\omega_z}\sqrt{\omega_+ - \omega_-}} \quad ,$$

where A_0 and A_1 are given by the initial conditions of the problem. We can plug this solution back into Equation (A.78) to get the solution for $Z(t)$:

$$Z(t) = \frac{|C|}{C}\sqrt{\frac{\omega_+ - \omega_-}{\omega_z}}\left(-A_0 e^{i\Omega t} + A_1 e^{-i\Omega t}\right) \quad . \tag{A.82}$$

A.6.2. Rabi Oscillations

The energy in the x_+-mode is proportional to $|X_+|^2$. When the coupling drive is applied, the energy oscillates over time (Rabi oscillations):

$$\begin{aligned} |X_+(t)|^2 &= \left(A_0 e^{i\Omega t} + A_1 e^{-i\Omega t}\right)\left(A_0^* e^{-i\Omega t} + A_1^* e^{i\Omega t}\right) \\ &= |A_0|^2 + |A_1|^2 + 2\Re(A_0 A_1^* e^{2i\Omega t}) \quad . \end{aligned} \tag{A.83}$$

The frequency of the oscillatory term, 2Ω, is called the *Rabi frequency*. It can also be shown that the total energy for the modes is not conserved: When calculating $\omega_+^2 |X_+|^2 + \omega_z^2 |Z|^2$, the square root of the frequency ratio in Equation (A.82) prevents the oscillating terms from cancelling out. But it can easily be shown that

$$(\omega_+ - \omega_-)|X_+|^2 + \omega_z |Z|^2 = \text{const.} \tag{A.84}$$

has to be a conserved quantity[7]. This quantity can be related to classical *action* [55].

[7] Authors with more foresight put factors of $\sqrt{\omega_+ - \omega_-}$, $\sqrt{\omega_z}$ into the definitions of $X_+(t)$, $Z(t)$. They define $x_+(t) = \Re(\tilde{X}_+(t)\exp(i\omega_+ t))/\sqrt{\omega_+ - \omega_-}$, and $z(t)$ accordingly, and then find that $\left|\tilde{X}_+\right|^2 + \left|\tilde{Z}\right|^2$ is a conserved quantity. Further others set $\omega_+ - \omega_- \approx \omega_+$ to simplify the equations.

A.6.3. Pi-Pulses

The solutions $X_+(t), Z(t)$ contain the complex constants A_0, A_1, which can be related to the amplitudes and phases of the x_+ and z motions at time $t = 0$:

$$X_+(0) = A_0 + A_1 \tag{A.85}$$

$$Z(0) = \frac{|C|}{C}\sqrt{\frac{\omega_+ - \omega_-}{\omega_z}}\,(-A_0 + A_1) \quad . \tag{A.86}$$

These equations are helpful for determining A_0, A_1 in the case where the coupling drive is switched on at $t = 0$, so that the initial conditions of $x_+(t)$ and $Z(t)$ are given by $X_+(0)$ and $Z(0)$. For example, after a time $t_\pi = \frac{\pi}{2}\frac{1}{\Omega}$, the amplitudes have evolved to

$$X_+(t_\pi) = i\,(A_0 - A_1) \tag{A.87}$$

$$Z(t_\pi) = -i\frac{|C|}{C}\sqrt{\frac{\omega_+ - \omega_-}{\omega_z}}\,(A_0 + A_1) \quad , \tag{A.88}$$

which (apart from constant factors) constitutes a swap of the original amplitudes. A pulse with a length t_π is known as a π-pulse, because it causes half a Rabi oscillation (energy oscillation).

A.6.4. The other sideband

When choosing a frequency $\omega_{\text{drive}} = \omega_+ + \omega_z$, the interaction between the cyclotron mode and the axial mode is also resonant. However, the resonant terms lead to the driving-accelerations

$$D_+(t) = \frac{q}{2m}\frac{\omega_+}{\omega_+ - \omega_-}CZ^*(t) \tag{A.89}$$

$$D_z(t) = \frac{q}{2m}CX_+^*(t) \quad , \tag{A.90}$$

which ultimately lead to solutions $X_+(t)$, $Z(t)$ that are almost identical to those that we found for the lower sideband. The only difference is that the oscillating terms are replaced with an exponentially growing and an exponentially decaying term. The growing amplitudes, however, still contain the phase-information of the original motion. This can be used to amplify the ion motion for better signal-to-noise. The usefulness of pulses at this sideband was foreshadowed in an MIT-thesis footnote [84], and it was independently rediscovered at the Mainz bound-electron g-factor experiment [134]. It can be shown that these pulses are especially useful when the ion can be cooled to temperatures below those of the detector.

A.6.5. Coupling other modes, Damping

The other modes can be treated in the same way as the treatment of the cyclotron mode. Coupling the magnetron mode to the axial mode can be done with the same spatial field configuration ($p_{2,1}$ or $p_{2,-1}$), and coupling the radial modes with each other can be done with a field given by $p_{2,-2}$. However, the negative scaling factor of forces acting on the magnetron mode reverses the roles of the sidebands whenever the magnetron mode is involved.

As shown in the previous section, the axial damping can be treated as an additional driving term. This modifies Equation (A.79) to

$$\dot{Z}(t) = \frac{q}{4im\omega_z} C^* X_+(t) - \frac{1}{2}\gamma_z Z(t) \quad , \tag{A.91}$$

while Equation (A.78) is unmodified. The solution can be shown to be a damped Rabi oscillation. When the coupling is strong compared to the damping ($\Omega > \gamma_z/4$), the amplitude decays with a time constant given by $\gamma_z/4$ (instead of $\gamma_z/2$ in the uncoupled case). Therefore, a strong, continuous coupling drive can be used to damp the cyclotron amplitude. The magnetron mode can be damped in the same fashion by using a frequency of $\omega_z + \omega_-$.

B. Computer Code

B.1. Harmonic polynomials in Mathematica

While formulas that generate harmonic polynomials $p_{lm}(x, y, z)$ exist [76], it is more convenient to start with spherical harmonics $Y_l^m(\theta, \phi)$ and transform them to Cartesian coordinates. However, it should be noted that there is no universally accepted numbering scheme, normalization, or even "vector space basis" of the resulting p_{lm}. The polynomials that are used in this thesis were obtained by defining real-valued, non-normalized spherical harmonics $\bar{Y}_l^m$ as

$$\bar{Y}_l^m(\theta, \phi) = \begin{cases} L_l^m(\cos(\theta))\ \cos(m\phi) & \text{for } m \geq 0 \\ L_l^m(\cos(\theta))\ \sin(m\phi) & \text{for } m < 0 \end{cases}, \tag{B.1}$$

where $L_l^m(\cos(\theta))$ denotes associated Legendre polynomials, including the Condon-Shortley phase $(-1)^m$. The harmonic polynomials p_{lm} are then obtained by transforming the expression $r^l \bar{Y}_l^m(\theta, \phi)$ to Cartesian coordinates. This can be done, for example, using *Mathematica*.

```
phase[m_]     := If[m >= 0, Cos[m phi], Sin[m phi]];
ybar[l_, m_] := LegendreP[l, m, Cos[theta]]*phase[m];
p[l_, m_]     := TransformedField["Spherical"->"Cartesian",
    r^l*ybar[l, m], {r, theta, phi} -> {x, y, z}];

(* Example Usage *)
$Assumptions = {Element[{x, y, z}, Reals]};
FullSimplify[p[2,0]]
```

The resulting polynomials are not normalized, but all $p_{l,0}$ satisfy $p_{l,0}(0, 0, 1) \equiv 1$. This convention is traditionally used for calculating the frequency-shifts caused by such imperfections [17, 87]. The other p_{lm} can be normalized over the unit sphere or the unit cube, but this leads to unwieldy factors that are inconsistent with the desired property of $p_{l,0}(0, 0, 1) \equiv 1$. While there is an obscure, but fitting "quasi-normalization" used in the description of geomagnetism [135], I instead resolved to manually picking normalization constants that made the $p_{lm\neq 0}$ in Equation (2.43) as short as possible.

Mathematica does not always simplify the higher order polynomials in a sensible fashion. In these cases, it is better to use a generating formula. Unfortunately, the generating formula in [76] leads to a different vector space base of the polynomials.

B.2. Rotating wave approximation in Matlab

The following Matlab code implements some of the results of the rotating wave approximation. It simulates a cyclotron-to-axial coupling drive that is swept across the coupling resonance of an axially damped, anharmonic ion. The parameters are realistic parameters of a $^{12}C^{4+}$ ion trapped at THe-Trap, except for the guard voltage detuning (the anharmonicity), which is five times larger than usual, in order to show its effect more clearly.

The code is based on the fact that the ion motion can be written as

$$\begin{aligned} x(t) &= \Re\left(\quad X_+(t)e^{i\omega_+ t} + \; X_-(t)e^{i\omega_- t}\right) \\ y(t) &= \Re\left(-iX_+(t)e^{i\omega_+ t} - iX_-(t)e^{i\omega_- t}\right) \\ z(t) &= \Re\left(\quad Z(t)e^{i\omega_z t}\right) \quad , \end{aligned}$$

where $X_+(t)$, $X_-(t)$, $Z(t)$ are the slowly varying amplitudes of the cyclotron, magnetron, and axial modes. The anharmonic term (in this case an electric anharmonicity given by $K_4 \cdot p_{4,0}$) leads to a force of

$$F_{\text{anharm}} = \frac{1}{2} q K_4 \begin{pmatrix} 3x(x^2+y^2) - 12xz^2 \\ 3y(x^2+y^2) - 12yz^2 \\ -12z(x^2+y^2) + 8z^3 \end{pmatrix} \quad . \tag{B.2}$$

After inserting the ion motion into this formula, the terms resonant with the ion modes can be identified. The forces in the y-dimension and the x-dimension act on the ion modes *independently* and have to be added. The forces on the radial modes are scaled by the appropriate factors, and the effective driving terms of the modes are summarized as

$$\begin{aligned} D_{+,\text{anharm}} &= \frac{q}{m} K_4 \frac{-\omega_+}{\omega_+ - \omega_-} X_+ \left(3|X_+|^2 + 6|X_-|^2 - 6|Z|^2\right) \\ D_{-,\text{anharm}} &= \frac{q}{m} K_4 \frac{\omega_-}{\omega_+ - \omega_-} X_- \left(3|X_-|^2 + 6|X_+|^2 - 6|Z|^2\right) \\ D_{z,\text{anharm}} &= \frac{q}{m} K_4 \, Z \left(6|X_+|^2 + 6|X_-|^2 - 3|Z|^2\right) \end{aligned}$$

These driving terms are added to the driving terms of the cyclotron-to-axial coupling (Equation A.77) and the axial damping (Equation A.57). Finally, the rotating wave approximation

$$\begin{aligned} \dot{X}_+ &= \frac{1}{2i\omega_+} D_{+,\text{total}} \\ \dot{X}_- &= \frac{1}{2i\omega_-} D_{-,\text{total}} \\ \dot{Z} &= \frac{1}{2i\omega_z} D_{z,\text{total}} \end{aligned}$$

is solved through numerical integration. The following code is meant as an educational, extensible example. It is neither optimized for speed nor for numerical precision, and the magnetron mode is not included. However, the code can be modified to also simulate the magnetron mode, as well as trap tilt, ellipticity, higher-order electrostatic imperfections, magnetic inhomogeneities, image charge shift, relativistic shifts, simultaneous excitations, and other phenomena that can be approximated as effective, resonant driving terms.

```
function [t,y] = trap_sim(ion, t_interval)
  % Numerically solves cyc to ax coupling using RWA. Input "ion"
  % must be struct with fields m, q, wp, wm, wz, k4, gamma,
  % C, Xp0, and Z0. The latter two are complex start conditions,
  % and "ion.C" a function handle for the coupling strength C(t).
  min_steps = 2e4;
  options = odeset('MaxStep', diff(t_interval)/min_steps, ...
                   'AbsTol', 1e-10);
  y_start = [ion.Xp0; ion.Z0];
  [t, y] = ode113(@go_function, t_interval, y_start, options);
  function y_prime = go_function(t,y)
      Xp = y(1); Z = y(2);
      D_p_k4   = -ion.q*ion.k4*ion.wp/(ion.m*(ion.wp-ion.wm))*...
                  Xp*(3*abs(Xp)^2 -6*abs(Z)^2);
      D_z_k4   = ion.q*ion.k4/ion.m*3*Z*(2*abs(Xp)^2 - abs(Z)^2);
      D_p_coup = ion.q*ion.wp/(2*ion.m*(ion.wp-ion.wm))*ion.C(t)*Z;
      D_z_coup = ion.q*ion.wz/(2*ion.m*ion.wz)*conj(ion.C(t))*Xp;
      D_z_damp = -1i*ion.wz*ion.gamma*Z;
      Xp_prime = 1/(2i*ion.wp)*(D_p_k4 + D_p_coup);
      Z_prime  = 1/(2i*ion.wz)*(D_z_k4 + D_z_coup + D_z_damp);
      y_prime = [Xp_prime; Z_prime];
  end
end
```

Example usage of the `trap_sim` function:

```
ion.m   = 12*1.6605e-27; % 12 u, all units SI
ion.q   = 4*1.6022e-19;  % 4 e
ion.wp  = 2*pi*27e6;
ion.wm  = 2*pi*300e3;
ion.wz  = sqrt(2*ion.wm*ion.wp);
ion.Xp0 = 100e-6;
ion.Z0  = 1e-6;
sweep_rate = 2*pi*10;          % 10 Hz/s upsweep
w_start = 2*pi*(-50);          % negative for upsweep
delta_Vg = 1;                  % guard voltage offset
b_G_4_0 = -5.34e-4/(1e-3)^4;  % see master thesis of Marc Schuh
ion.k4 = delta_Vg*b_G_4_0;
ion.gamma = 2*pi*0.2;     % 0.2 Hz ion width
% Anonymous function for coupling field strength.
ion.C =  @(t) 100*exp(1i*(w_start*t + (sweep_rate/2)*t.^2));
[t, y] = trap_sim(ion, [0, 10]);
plot(t, abs(y(:,1)),t,abs(y(:,2)))
legend('Cyclotron mode', 'Axial mode')
```

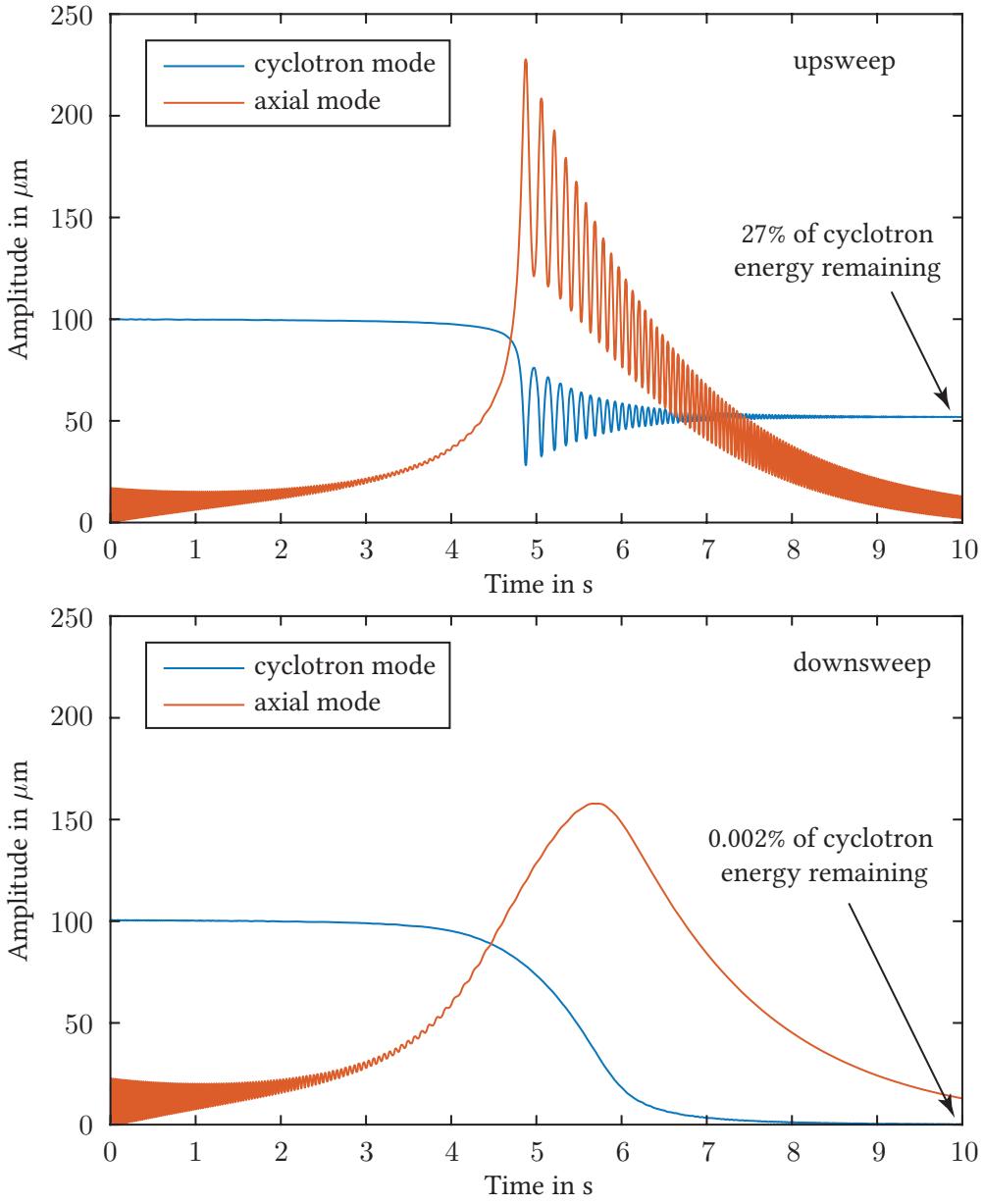

Figure B.1.: Simulated ion amplitudes during upsweep (top) and downsweep (bottom) of a strong coupling drive in an anharmonic trap. The axial damping parameter was set to 0.2 Hz (typical), and the guard voltage offset, which determines the anharmonicity $p_{4,0}$, was set to 1 V (five times larger than usual). The anharmonicity causes the coupling frequency to shift down during the energy transfer, which makes the downsweep more adiabatic and therefore more effective. Not included are the effects of noise, relativity, magnetic imperfections, or the electrostatic imperfection $p_{6,0}$. These relatively weak effects do not change the qualitative behavior of a coupling sweep.

Bibliography

[1] K. S. Sharma. Mass spectrometry – the early years. *International Journal of Mass Spectrometry*, 349–350:3–8, 2013. ISSN 1387-3806. URL http://dx.doi.org/10.1016/j.ijms.2013.05.028.

[2] G. Audi. The history of nuclidic masses and of their evaluation. *International Journal of Mass Spectrometry*, 251(2-3):85–94, 2006. URL http://dx.doi.org/10.1016/j.ijms.2006.01.048.

[3] E. G. Myers. The most precise atomic mass measurements in Penning traps. *International Journal of Mass Spectrometry*, 349–350:107–122, 2013. ISSN 1387-3806. URL http://dx.doi.org/10.1016/j.ijms.2013.03.018.

[4] K. Blaum. High-accuracy mass spectrometry with stored ions. *Physics Reports*, 425(1):1 – 78, 2006. ISSN 0370-1573. URL http://dx.doi.org/10.1016/j.physrep.2005.10.011.

[5] G. Gabrielse, A. Khabbaz, D. S. Hall, C. Heimann, H. Kalinowsky, and W. Jhe. Precision mass spectroscopy of the antiproton and proton using simultaneously trapped particles. *Physical Review Letters*, 82:3198–3201, 1999. URL http://dx.doi.org/10.1103/PhysRevLett.82.3198.

[6] S. Ulmer, C. Smorra, A. Mooser, K. Franke, H. Nagahama, G. Schneider, T. Higuchi, S. Van Gorp, K. Blaum, Y. Matsuda, et al. High-precision comparison of the antiproton-to-proton charge-to-mass ratio. *Nature*, 524(7564):196–199, 2015. URL http://dx.doi.org/10.1038/nature14861.

[7] J. J. Thomson. Bakerian lecture: Rays of positive electricity. *Proceedings of the Royal Society of London. Series A, Containing Papers of a Mathematical and Physical Character*, 89(607):pp. 1–20, 1913. ISSN 09501207. URL http://www.jstor.org/stable/93452.

[8] F. W. Aston. A positive ray spectrograph. *Philosophical Magazine Series 6*, 38(228):707–714, 1919. URL http://dx.doi.org/10.1080/14786441208636004.

[9] F. W. Aston. Bakerian lecture: A new mass-spectrograph and the whole number rule. *Proceedings of the Royal Society of London. Series A, Containing Papers of a Mathematical and Physical Character*, 115(772):pp. 487–514, 1927. ISSN 09501207. URL http://www.jstor.org/stable/94803.

[10] J. Mattauch. A double-focusing mass spectrograph and the masses of N^{15} and O^{18}. *Physical Review Series II*, 50:617–623, 1936. URL http://dx.doi.org/10.1103/PhysRev.50.617.

[11] A. O. Nier and T. R. Roberts. The determination of atomic mass doublets by means of a mass spectrometer. *Physical Review Series II*, 81:507–510, 1951. URL http://dx.doi.org/10.1103/PhysRev.81.507.

[12] L. G. Smith. Measurements of six light masses. *Physical Review C*, 4(1):22–31, 1971. URL http://dx.doi.org/10.1103/PhysRevC.4.22.

[13] G. Gärtner and E. Klempt. A direct determination of the proton-electron mass ratio. *Zeitschrift für Physik A*, 287(1):1–6, 1978. ISSN 0939-7922. URL http://dx.doi.org/10.1007/BF01408352.

[14] G. Gräff, H. Kalinowsky, and J. Traut. A direct determination of the proton electron mass ratio. *Zeitschrift für Physik A*, 297(1):35–39, 1980. ISSN 0939-7922. URL http://dx.doi.org/10.1007/BF01414243.

[15] R. S. Van Dyck, Jr., F. L. Moore, D. L. Farnham, and P. B. Schwinberg. Number dependency in the compensated Penning trap. *Physical Review A*, 40(11):6308–6313, 1989. ISSN 0556-2791. URL http://dx.doi.org/10.1103/PhysRevA.40.6308.

[16] E. A. Cornell, R. M. Weisskoff, K. R. Boyce, R. W. Flanagan, G. P. Lafyatis, and D. E. Pritchard. Single-ion cyclotron resonance measurement of $m(CO^+)/m(N_2^+)$. *Physical Review Letters*, 63:1674–1677, 1989. URL http://dx.doi.org/10.1103/PhysRevLett.63.1674.

[17] S. Rainville, J. K. Thompson, and D. E. Pritchard. An Ion Balance for Ultra-High-Precision Atomic Mass Measurements. *Science*, 303(5656):334–338, 2004. URL http://dx.doi.org/10.1126/science.1092320.

[18] R. S. Van Dyck, Jr., D. B. Pinegar, S. Van Liew, and S. L. Zafonte. The UW-PTMS: Systematic studies, measurement progress, and future improvements. *International Journal of Mass Spectrometry*, 251(2-3):231–242, 2006. URL http://dx.doi.org/10.1016/j.ijms.2006.01.038.

[19] V. N. Aseev, A. I. Belesev, A. I. Berlev, E. V. Geraskin, A. A. Golubev, N. A. Likhovid, V. M. Lobashev, A. A. Nozik, V. S. Pantuev, V. I. Parfenov, A. K. Skasyrskaya, F. V. Tkachov, and S. V. Zadorozhny. Upper limit on the electron antineutrino mass from the Troitsk experiment. *Physical Review D*, 84:112003, 2011. URL http://dx.doi.org/10.1103/PhysRevD.84.112003.

[20] K. Olive and P. D. Group. Review of particle physics. *Chinese Physics C*, 38(9):090001, 2014. URL http://stacks.iop.org/1674-1137/38/i=9/a=090001.

[21] Y. Fukuda, T. Hayakawa, E. Ichihara, K. Inoue, K. Ishihara, H. Ishino, Y. Itow, T. Kajita, J. Kameda, S. Kasuga, K. Kobayashi, Y. Kobayashi, Y. Koshio, M. Miura, M. Nakahata, S. Nakayama, A. Okada, K. Okumura, N. Sakurai, M. Shiozawa, Y. Suzuki, Y. Takeuchi, Y. Totsuka, S. Yamada, M. Earl, A. Habig, and E. Kearns. Evidence for oscillation of atmospheric neutrinos. *Physical Review Letters*, 81(8):1562–1567, 1998. URL http://dx.doi.org/10.1103/PhysRevLett.81.1562.

[22] Q. R. Ahmad, et al. (SNO Collaboration). Direct evidence for neutrino flavor transformation from neutral-current interactions in the Sudbury Neutrino Observatory. *Physical Review Letters*, 89(1):011301, 2002. URL http://dx.doi.org/10.1103/PhysRevLett.89.011301.

[23] E. Giusarma, R. de Putter, S. Ho, and O. Mena. Constraints on neutrino masses from Planck and Galaxy clustering data. *Physical Review D*, 88:063515, 2013. URL http://dx.doi.org/10.1103/PhysRevD.88.063515.

[24] M. Wang, G. Audi, A. Wapstra, F. Kondev, M. MacCormick, X. Xu, and B. Pfeiffer. The AME2012 atomic mass evaluation. *Chinese Physics C*, 36(12):1603, 2012. URL http://stacks.iop.org/1674-1137/36/i=12/a=003.

[25] E. W. Otten and C. Weinheimer. Neutrino mass limit from tritium β-decay. *Reports on Progress in Physics*, 71(8):086201, 2008. ISSN 0034-4885. URL http://dx.doi.org/10.1088/0034-4885/71/8/086201.

[26] L. I. Bodine, D. S. Parno, and R. G. H. Robertson. Assessment of molecular effects on neutrino mass measurements from tritium β decay. *Physical Review C*, 91:035505, 2015. URL http://dx.doi.org/10.1103/PhysRevC.91.035505.

[27] E. W. Otten, J. Bonn, and C. Weinheimer. The Q-value of tritium β-decay and the neutrino mass. *International Journal of Mass Spectrometry*, 251(2-3):173–178, 2006. URL http://dx.doi.org/10.1016/j.ijms.2006.01.035.

[28] C. Kraus et al. Final results from phase II of the Mainz neutrino mass search in tritium β-decay. *European Physical Journal C*, 40:447–468, 2005. URL http://dx.doi.org/10.1140/epjc/s2005-02139-7.

[29] M. Beck et al. (KATRIN collaboration). The KATRIN experiment. *Journal of Physics: Conference Series*, 203(1):012097, 2010. URL http://stacks.iop.org/1742-6596/203/i=1/a=012097.

[30] S. Bauer, R. Berendes, F. Hochschulz, H. W. Ortjohann, S. Rosendahl, T. Thümmler, M. Schmidt, and C. Weinheimer. Next generation KATRIN high precision voltage divider for voltages up to 65 kV. *Journal of Instrumentation*, 8(10):P10026, 2013. URL http://dx.doi.org/10.1088/1748-0221/8/10/P10026.

[31] S. Nagy, T. Fritioff, M. Björkhage, I. Bergström, and R. Schuch. On the Q-value of the tritium β-decay. *Europhysics Letters*, 74:404–410, 2006. URL http://dx.doi.org/10.1209/epl/i2005-10559-2.

[32] E. G. Myers, A. Wagner, H. Kracke, and B. A. Wesson. Atomic masses of tritium and helium-3. *Physical Review Letters*, 114:013003, 2015. URL http://dx.doi.org/10.1103/PhysRevLett.114.013003.

[33] G. Audi, M. Wang, A. H. Wapstra, F. G. Kondev, M. MacCormick, X. Xu, and B. Pfeiffer. The AME2012 atomic mass evaluation. *Chinese Physics C*, 36(12):1287, 2012. URL http://stacks.iop.org/1674-1137/36/i=12/a=002.

[34] B. N. Taylor, W. H. Parker, and D. N. Langenberg. Determination of $\frac{e}{h}$, using macroscopic quantum phase coherence in superconductors: Implications for quantum electrodynamics and the fundamental physical constants. *Reviews of Modern Physics*, 41:375–496, 1969. URL http://dx.doi.org/10.1103/RevModPhys.41.375.

[35] D. Hanneke, S. Fogwell, and G. Gabrielse. New measurement of the electron magnetic moment and the fine structure constant. *Physical Review Letters*, 100(12):120801, 2008. URL http://dx.doi.org/10.1103/PhysRevLett.100.120801.

[36] R. Bouchendira, P. Cladé, S. Guellati-Khélifa, F. Nez, and F. Biraben. New determination of the fine structure constant and test of the quantum electrodynamics. *Physical Review Letters*, 106:080801, 2011. URL http://dx.doi.org/10.1103/PhysRevLett.106.080801.

[37] A. Wicht, J. M. Hensley, E. Sarajlic, and S. Chu. A preliminary measurement of the fine structure constant based on atom interferometry. *Physica Scripta*, 2002(T102):82, 2002. URL http://stacks.iop.org/1402-4896/2002/i=T102/a=014.

[38] P. J. Mohr, B. N. Taylor, and D. B. Newell. CODATA recommended values of the fundamental physical constants: 2010. *Reviews of Modern Physics*, 84:1527–1605, 2012. URL http://dx.doi.org/10.1103/RevModPhys.84.1527.

[39] J. Verdú, S. Djekić, S. Stahl, T. Valenzuela, M. Vogel, G. Werth, T. Beier, H.-J. Kluge, and W. Quint. Electronic g factor of hydrogenlike oxygen $^{16}O^{7+}$. *Physical Review Letters*, 92(9):093002, 2004. URL http://dx.doi.org/10.1103/PhysRevLett.92.093002.

[40] S. Sturm, F. Köhler, J. Zatorski, A. Wagner, Z. Harman, G. Werth, W. Quint, C. H. Keitel, and K. Blaum. High-precision measurement of the atomic mass of the electron. *Nature*, 506(7489):467–470, 2014. ISSN 0028-0836. URL http://dx.doi.org/10.1038/nature13026.

[41] M. Hori, A. Soter, D. Barna, A. Dax, R. Hayano, S. Friedreich, B. Juhasz, T. Pask, E. Widmann, D. Horvath, L. Venturelli, and N. Zurlo. Two-photon laser spectroscopy of antiprotonic helium and the antiproton-to-electron mass ratio. *Nature*, 475:484–488, 2011. URL http://dx.doi.org/10.1038/nature10260.

[42] D. L. Farnham, R. S. Van Dyck, Jr., and P. B. Schwinberg. Determination of the electron's atomic mass and the proton/electron mass ratio via Penning trap mass spectroscopy. *Physical Review Letters*, 75(20):3598–3601, 1995. URL http://dx.doi.org/10.1103/PhysRevLett.75.3598.

[43] B. J. Mount, M. Redshaw, and E. G. Myers. Atomic masses of ^{6}Li, ^{23}Na, ^{39,41}K, ^{85,87}Rb, and ^{133}Cs. *Physical Review Letters*, 82:042513, 2010. URL http://dx.doi.org/10.1103/PhysRevA.82.042513.

[44] R. Rana, M. Höcker, and E. G. Myers. Atomic masses of strontium and ytterbium. *Physical Review A*, 86:050502, 2012. URL http://dx.doi.org/10.1103/PhysRevA.86.050502.

[45] R. Barlow. Systematic errors: Facts and fictions. In *Advanced Statistical Techniques in Particle Physics. Proceedings, Conference, Durham, UK, March 18-22, 2002*, pages 134–144. 2002. URL http://www.ippp.dur.ac.uk/Workshops/02/statistics/proceedings//barlow.pdf.

[46] R. S. Van Dyck, Jr., S. L. Zafonte, S. Van Liew, D. B. Pinegar, and P. B. Schwinberg. Ultraprecise atomic mass measurement of the α particle and ^{4}He. *Physical Review Letters*, 92(22):220802/1–4, 2004. URL http://dx.doi.org/10.1103/PhysRevLett.92.220802.

[47] D. B. Pinegar. *Tools for a precise tritium to helium-3 mass comparison.* Ph.D. thesis, University of Washington, Seattle, 2007. URL http://search.proquest.com/docview/304796368/abstract.

[48] M. Redshaw, B. J. Mount, and E. G. Myers. Improved atomic masses of ^{84,86}Kr and ^{129,132}Xe. *Physical Review A*, 79:012506, 2009. URL http://dx.doi.org/10.1103/PhysRevA.79.012506.

[49] J. K. Thompson, S. Rainville, and D. E. Pritchard. Cyclotron frequency shift arising from polarization forces. *Nature*, 430(6995):58–61, 2004. ISSN 0028-0836. URL http://dx.doi.org/10.1038/nature02682.

[50] M. Höcker. *Ion Transfer Studies in the UW/MPIK Double-Penning Trap Experiment.* Diplomarbeit, Universität Heidelberg, Heidelberg, 2010. URL http://hdl.handle.net/11858/00-001M-0000-0011-72BA-F.

[51] M. Höcker, R. Rana, and E. G. Myers. Atomic masses of ^{82,83}Kr and ^{131,134}Xe. *Physical Review A*, 88:052502, 2013. URL http://dx.doi.org/10.1103/PhysRevA.88.052502.

[52] C. Diehl, K. Blaum, M. Höcker, J. Ketter, D. B. Pinegar, S. Streubel, and R. S. Van Dyck, Jr. Progress with the MPIK/UW-PTMS in Heidelberg. *Hyperfine Interactions*, 199(1-3):291–300, 2011. ISSN 0304-3843. URL http://dx.doi.org/10.1007/s10751-011-0324-6.

[53] S. Streubel, T. Eronen, M. Höcker, J. Ketter, M. Schuh, R. Van Dyck, Jr., and K. Blaum. Toward a more accurate Q value measurement of tritium: Status of THe-Trap. *Applied Physics B*, 114(1-2):137–145, 2014. ISSN 0946-2171. URL http://dx.doi.org/10.1007/s00340-013-5669-x.

[54] C. Diehl. *First Mass Measurements with the MPIK/UW-PTMS*. Ph.D. thesis, University of Heidelberg, 2011. URL http://www.ub.uni-heidelberg.de/archiv/12038.

[55] E. A. Cornell, R. M. Weisskoff, K. R. Boyce, and D. E. Pritchard. Mode coupling in a Penning trap: π pulses and a classical avoided crossing. *Physical Review A*, 41:312–315, 1990. URL http://dx.doi.org/10.1103/PhysRevA.41.312.

[56] R. M. Weisskoff. *Detecting Single, Trapped Ions*. Ph.D. thesis, MIT, 1988. URL http://hdl.handle.net/1721.1/68230.

[57] L. S. Brown and G. Gabrielse. Geonium theory: Physics of a single electron or ion in a Penning trap. *Reviews of Modern Physics*, 58(1):233–311, 1986. URL http://dx.doi.org/10.1103/RevModPhys.58.233.

[58] R. S. Van Dyck, Jr., D. L. Farnham, S. L. Zafonte, and P. B. Schwinberg. Ultrastable superconducting magnet system for a Penning trap mass spectrometer. *Review of Scientific Instruments*, 70(3):1665–1671, 1999. URL http://dx.doi.org/10.1063/1.1149649.

[59] L. D. Landau and E. M. Lifshitz. *The Classical Theory of Fields*. Pergamon Press, 1971. URL https://archive.org/details/TheClassicalTheoryOfFields.

[60] G. Gabrielse. Relaxation calculation of the electrostatic properties of compensated Penning traps with hyperbolic electrodes. *Physical Review A*, 27(5):2277–2290, 1983. URL http://dx.doi.org/10.1103/PhysRevA.27.2277.

[61] S. Van Liew. *An ultra-precise determination of the mass of helium-3 using Penning trap mass spectrometry*. Ph.D. thesis, University of Washington, Seattle, 2004. URL http://search.proquest.com/docview/305108183.

[62] J. Ketter. *Verbesserungen der Ionennachweissysteme des Präzisions-Penningfallen-Massenspektrometers Triga-Trap*. Diplomarbeit, Johannes Gutenberg Universität Mainz, 2009. URL http://hdl.handle.net/11858/00-001M-0000-0011-767C-C.

[63] L. S. Brown and G. Gabrielse. Precision spectroscopy of a charged particle in an imperfect Penning trap. *Physical Review A*, 25(4):2423–2425, 1982. URL http://dx.doi.org/10.1103/PhysRevA.25.2423.

[64] G. Gabrielse. Why is sideband mass spectrometry possible with ions in a Penning trap? *Physical Review Letters*, 102(17):172501, 2009. URL http://dx.doi.org/10.1103/PhysRevLett.102.172501.

[65] G. Bollen, R. B. Moore, G. Savard, and H. Stolzenberg. The accuracy of heavy-ion mass measurements using time of flight-ion cyclotron resonance in a Penning trap. *Journal of Applied Physics*, 68(9):4355–4374, 1990. URL http://dx.doi.org/10.1063/1.346185.

[66] S. Eliseev, K. Blaum, M. Block, C. Droese, M. Goncharov, E. Minaya Ramirez, D. A. Nesterenko, Y. N. Novikov, and L. Schweikhard. Phase-imaging ion-cyclotron-resonance measurements for short-lived nuclides. *Physical Review Letters*, 110(8):5, 2013. URL http://dx.doi.org/10.1103/PhysRevLett.110.082501.

[67] H. G. Dehmelt and F. L. Walls. "Bolometric" technique for the RF spectroscopy of stored ions. *Physical Review Letters*, 21(3):127–131, 1968. URL http://dx.doi.org/10.1103/PhysRevLett.21.127.

[68] W. Shockley. Currents to conductors induced by a moving point charge. *Journal of Applied Physics*, 9(10):635–636, 1938. URL http://dx.doi.org/10.1063/1.1710367.

[69] G. Gabrielse. Detection, damping, and translating the center of the axial oscillation of a charged particle in a Penning trap with hyperbolic electrodes. *Physical Review A*, 29:462–469, 1984. URL http://dx.doi.org/10.1103/PhysRevA.29.462.

[70] M. Schuh. *Simulations of the electrostatic and magnetic field properties and tests of the Penning-ion source at THe-Trap.* Master's thesis, Max-Planck-Institut für Kernphysik, Heidelberg, 2014. URL http://hdl.handle.net/11858/00-001M-0000-0024-46A3-7.

[71] M. Redshaw. *Precise Measurements of the Atomic Masses of ^{28}Si, ^{31}P, ^{32}S, $^{84,86}Kr$, $^{129,132,136}Xe$, and the Dipole Moment of PH^+ using Single-Ion and Two-Ion Penning Trap Techniques.* Ph.D. thesis, Florida State University, 2007. URL http://purl.flvc.org/fsu/fd/FSU_migr_etd-1915.

[72] D. J. Wineland and H. G. Dehmelt. Principles of the stored ion calorimeter. *Journal of Applied Physics*, 46(2):919–930, 1975. URL http://dx.doi.org/10.1063/1.321602.

[73] M. Bradley. *A Sub-ppb Measurement of the Mass of Cesium for a New Determination of the Fine-Structure Constant.* Ph.D. thesis, Massachusetts Institute of Technology, 2000. URL http://hdl.handle.net/1721.1/28222.

[74] M. Kretzschmar. Single particle motion in a Penning trap: Description in the classical canonical formalism. *Physica Scripta*, 46(6):544–554, 1992. URL http://stacks.iop.org/1402-4896/46/544.

[75] M. Kretzschmar. Theoretical investigations of different excitation modes for Penning trap mass spectrometry. *International Journal of Mass Spectrometry*, 349–350:227 – 239, 2013. ISSN 1387-3806. URL http://dx.doi.org/10.1016/j.ijms.2013.03.023.

[76] E. J. Brändas and E. S. Kryachko, editors. *Fundamental World of Quantum Chemistry.* Kluwer Academic Publishers, 2003.

[77] K. R. Boyce. *Improved Single Ion Cyclotron Resonance Mass Spectroscopy.* Ph.D. thesis, MIT, 1992. URL http://hdl.handle.net/1721.1/42551.

[78] J. Tan and G. Gabrielse. Parametrically pumped electron oscillators. *Physical Review A*, 48:3105–3122, 1993. URL http://dx.doi.org/10.1103/PhysRevA.48.3105.

[79] L. J. Lapidus. *Synchronization and Stochastic Behavior of Electrons in a Penning Trap.* Ph.D. thesis, Harvard University, 1998. URL http://search.proquest.com/docview/304435208/.

[80] A. Dörr. *PENTATRAP: A novel Penning-trap system for high-precision mass measurements*. Ph.D. thesis, University of Heidelberg, 2015. URL http://www.ub.uni-heidelberg.de/archiv/18090.

[81] T. P. Heavner. *A precision measurement of the atomic mass of ^{6}Li using a Penning ion trap mass spectrometer*. Ph.D. thesis, University of Colorado, Boulder, 1998.

[82] B. W. Shore, M. V. Gromovyy, L. P. Yatsenko, and V. I. Romanenko. Simple mechanical analogs of rapid adiabatic passage in atomic physics. *American Journal of Physics*, 77(12):1183–1194, 2009. URL http://dx.doi.org/10.1119/1.3231688.

[83] G. Gabrielse. The true cyclotron frequency for particles and ions in a Penning trap. *International Journal of Mass Spectrometry*, 279(2–3):107 – 112, 2009. ISSN 1387-3806. URL http://dx.doi.org/10.1016/j.ijms.2008.10.015.

[84] J. K. Thompson. *Two-ion control and polarization forces for precise mass comparisons*. Ph.D. thesis, Massachusetts Institute of Technology, Cambridge, MA, 2003. URL http://hdl.handle.net/1721.1/17011.

[85] C. Gerz, D. Wilsdorf, and G. Werth. A high precision Penning trap mass spectrometer. *Nuclear Instruments and Methods in Physics Research Section B: Beam Interactions with Materials and Atoms*, 47(4):453 – 461, 1990. ISSN 0168-583X. URL http://dx.doi.org/10.1016/0168-583X(90)90626-6.

[86] J. Ketter, T. Eronen, M. Höcker, S. Streubel, and K. Blaum. First-order perturbative calculation of the frequency-shifts caused by static cylindrically-symmetric electric and magnetic imperfections of a Penning trap. *International Journal of Mass Spectrometry*, 358:1 – 16, 2014. ISSN 1387-3806. URL http://dx.doi.org/10.1016/j.ijms.2013.10.005.

[87] J. Ketter. *Theoretical treatment of miscellaneous frequency-shifts in Penning traps with classical perturbation theory*. Ph.D. thesis, Universität Heidelberg, 2015. URL http://www.ub.uni-heidelberg.de/archiv/18227.

[88] J. L. V. Galiana. *Ultrapräzise Messung des elektronischen g-Faktors in wasserstoffähnlichem Sauerstoff*. Ph.D. thesis, Johannes Gutenberg-Universität Mainz, 2003.

[89] S. Ulmer, C. C. Rodegheri, K. Blaum, H. Kracke, A. Mooser, W. Quint, and J. Walz. Observation of spin flips with a single trapped proton. *Physical Review Letters*, 106:253001, 2011. URL http://dx.doi.org/10.1103/PhysRevLett.106.253001.

[90] J. Ketter, T. Eronen, M. Höcker, M. Schuh, S. Streubel, and K. Blaum. Classical calculation of relativistic frequency-shifts in an ideal Penning trap. *International Journal of Mass Spectrometry*, 361:34 – 40, 2014. ISSN 1387-3806. URL http://dx.doi.org/10.1016/j.ijms.2014.01.028.

[91] J. V. Porto. Series solution for the image charge fields in arbitrary cylindrically symmetric Penning traps. *Physical Review A*, 64(2):023403, 2001. URL http://dx.doi.org/10.1103/PhysRevA.64.023403.

[92] M. Redshaw, J. McDaniel, W. Shi, and E. G. Myers. Mass ratio of two ions in a Penning trap by alternating between the trap center and a large cyclotron orbit. *International Journal of Mass Spectrometry*, 251(2–3):125 – 130, 2006. ISSN 1387-3806. URL http://dx.doi.org/10.1016/j.ijms.2006.01.015.

[93] R. S. Van Dyck, Jr., S. L. Zafonte, and P. B. Schwinberg. Ultra-precise mass measurements using the UW-PTMS. *Hyperfine Interactions*, 132(1–4):163–175, 2001. URL http://dx.doi.org/10.1023/A:1011914310458.

[94] S. Streubel. *Kontrolle der Umwelteinflüsse auf THe-Trap am Beispiel der Bestimmung des Massenverhältnisses von Kohlenstoff-12 zu Sauerstoff-16*. Ph.D. thesis, Universität Heidelberg, 2014. URL http://www.ub.uni-heidelberg.de/archiv/16870.

[95] S. L. Zafonte and R. S. V. D. Jr. Ultra-precise single-ion atomic mass measurements on deuterium and helium-3. *Metrologia*, 52(2):280, 2015. URL http://stacks.iop.org/0026-1394/52/i=2/a=280.

[96] M. Tremer. *Untersuchung und Optimierung des externen Ladens von Ionen*. Diplomarbeit, University of Heidelberg, 2011. URL http://hdl.handle.net/11858/00-001M-0000-0012-2FBD-2.

[97] G. Gabrielse and J. Tan. Self-shielding superconducting solenoid systems. *Journal of Applied Physics*, 63(10):5143–5148, 1988. ISSN 0021-8979. URL http://dx.doi.org/10.1063/1.340416.

[98] D. L. Farnham. *A determination of the proton/electron mass ratio and the electron's atomic mass via Penning trap mass spectroscopy*. Ph.D. thesis, University of Washington, Seattle, 1995.

[99] P. W. Anderson. Theory of flux creep in hard superconductors. *Physical Review Letters*, 9(7):309, 1962. URL http://link.aps.org/abstract/PRL/v9/p309.

[100] F. Hibberd. The geomagnetic s_q variation – annual, semi-annual and solar cycle variations and ring current effects. *Journal of Atmospheric and Terrestrial Physics*, 47(4):341 – 352, 1985. ISSN 0021-9169. URL http://dx.doi.org/10.1016/0021-9169(85)90014-5.

[101] J. W. Ekin. *Experimental Techniques for Low-Temperature Measurements*. Oxford University Press (OUP), 2006.

[102] J. Repp. *The setup of the high-precision Penning-trap mass spectrometer PENTATRAP and first production studies of highly charged ions*. Ph.D. thesis, University of Heidelberg, 2012. URL http://www.ub.uni-heidelberg.de/archiv/13994.

[103] Z. Anđelkovič. *Setup of a Penning trap for precision laser spectroscopy at HITRAP*. Ph.D. thesis, Johannes Gutenberg-Universität Mainz, 2012. URL http://ubm.opus.hbz-nrw.de/volltexte/2012/3132/.

[104] M. A. Levine, R. E. Marrs, J. R. Henderson, D. A. Knapp, and M. B. Schneider. The electron beam ion trap: A new instrument for atomic physics measurements. *Physica Scripta*, 1988(T22):157, 1988. URL http://stacks.iop.org/1402-4896/1988/i=T22/a=024.

[105] R. S. Van Dyck, Jr. private communication, 2010.

[106] S. L. Zafonte. *A Determination of the Mass of the Deuteron*. Ph.D. thesis, University of Washington, 2012. URL http://hdl.handle.net/1773/20247.

[107] A. Weigel. *Entwicklung des kryogenen Nachweissystems für ALPHATRAP und THe-Trap*. Master's thesis, Universität Heidelberg, 2014. URL http://hdl.handle.net/11858/00-001M-0000-0024-469B-E.

[108] S. Sturm. *The g-factor of the electron bound in $^{28}Si^{13+}$: The most stringent test of bound-state quantum electrodynamics.* Ph.D. thesis, Johannes Gutenberg-Universität Mainz, 2011. URL http://ubm.opus.hbz-nrw.de/volltexte/2012/3108/.

[109] R. S. Van Dyck, Jr., P. B. Schwinberg, and H. G. Dehmelt. Electron magnetic moment from geonium spectra: Early experiments and background concepts. *Physical Review D*, 34(3):722–736, 1986. URL http://dx.doi.org/10.1103/PhysRevD.34.722.

[110] F. L. Moore. *High resolution mass spectroscopy in a quadring Penning trap.* Ph.D. thesis, University of Washington, 1989.

[111] C. Böhm, S. Sturm, A. Rischka, A. Dörr, S. Eliseev, M. Höcker, J. Ketter, F. Köhler, D. Marschall, J. Martin, D. Obieglo, J. R. R. Roux, R. Schüssler, M. Steigleder, S. Streubel, T. Wagner, J. Westermann, V. Wieder, R. Zirpel, J. Melcher, and K. Blaum. An ultra-stable voltage source for precision Penning-trap experiments. *Nuclear Instruments and Methods in Physics Research A*, 828:125–131, 2016. URL http://dx.doi.org/10.1016/j.nima.2016.05.044.

[112] V. Natarajan. *Penning Trap Mass Spectroscopy at 0.1 ppb.* Ph.D. thesis, MIT, 1993. URL http://hdl.handle.net/1721.1/28017.

[113] E. A. Cornell. *Mass Spectroscopy Using Single Ion Cyclotron Resonance.* Ph.D. thesis, Massachusetts Insitute of Technology, 1990. URL http://hdl.handle.net/1721.1/13562.

[114] B. J. Mount. *High Precision Atomic Mass Spectrometry with Application to Neutrino Physics, Fundamental Constants and Physical Chemistry.* Ph.D. thesis, Florida State University, 2010. URL http://purl.flvc.org/fsu/fd/FSU_migr_etd-2217.

[115] F. DiFilippo. *Precise Atomic Masses for Determining Fundamental Constants.* Ph.D. thesis, MIT, 1994. URL http://hdl.handle.net/1721.1/26860.

[116] R. M. Weisskoff, G. P. Lafyatis, K. R. Boyce, E. A. Cornell, R. W. Flanagan, and D. E. Pritchard. rf SQUID detector for single-ion trapping experiments. *Journal of Applied Physics*, 63(9):4599–4604, 1988. URL http://dx.doi.org/10.1063/1.340137.

[117] E. A. Cornell, K. R. Boyce, D. L. K. Fygenson, and D. E. Pritchard. Two ions in a Penning trap: Implications for precision mass spectroscopy. *Physical Review A*, 45:3049–3059, 1992. URL http://dx.doi.org/10.1103/PhysRevA.45.3049.

[118] J. Ketter. Mysteriöses Feintuning - Calculations on the modulation shift. Private communication, February 2011.

[119] C.-E. Roux. *High-Resolution Mass Spectrometry: The Trap Design and Detection System of Pentatrap and New Q-Values for Neutrino Studies.* Ph.D. thesis, Universität Heidelberg, 2012. URL http://www.ub.uni-heidelberg.de/archiv/14006.

[120] N. Metropolis and S. Ulam. The Monte Carlo method. *Journal of the American Statistical Association*, 44(247):335–341, 1949. ISSN 01621459. URL http://www.jstor.org/stable/2280232.

[121] M. Schuh. *to be anounced.* Ph.D. thesis, University of Heidelberg, 2019.

[122] F. Terranova and G. M. Tino. Testing the a_μ anomaly in the electron sector through a precise measurement of h/m. *Physical Review A*, 89:052118, 2014. URL http://dx.doi.org/10.1103/PhysRevA.89.052118.

[123] G. Ferrari, N. Poli, F. Sorrentino, and G. M. Tino. Long-lived Bloch oscillations with bosonic Sr atoms and application to gravity measurement at the micrometer scale. *Physical Review Letters*, 97:060402, 2006. URL http://dx.doi.org/10.1103/PhysRevLett.97.060402.

[124] N. Poli, F.-Y. Wang, M. G. Tarallo, A. Alberti, M. Prevedelli, and G. M. Tino. Precision measurement of gravity with cold atoms in an optical lattice and comparison with a classical gravimeter. *Physical Review Letters*, 106:038501, 2011. URL http://dx.doi.org/10.1103/PhysRevLett.106.038501.

[125] A. O. Jamison, B. Plotkin-Swing, and S. Gupta. Advances in precision contrast interferometry with Yb Bose-Einstein condensates. *Physical Review A*, 90:063606, 2014. URL http://dx.doi.org/10.1103/PhysRevA.90.063606.

[126] M. Redshaw, E. Wingfield, J. McDaniel, and E. G. Myers. Mass and double-beta-decay Q value of ^{136}Xe. *Physical Review Letters*, 98:053003, 2007. URL http://dx.doi.org/10.1103/PhysRevLett.98.053003.

[127] M. Redshaw, B. J. Mount, E. G. Myers, and F. T. Avignone. Masses of ^{130}Te and ^{130}Xe and double-β-decay Q value of ^{130}Te. *Physical Review Letters*, 102:212502, 2009. URL http://dx.doi.org/10.1103/PhysRevLett.102.212502.

[128] J. Hakala, J. Dobaczewski, D. Gorelov, T. Eronen, A. Jokinen, A. Kankainen, V. S. Kolhinen, M. Kortelainen, I. D. Moore, H. Penttilä, S. Rinta-Antila, J. Rissanen, A. Saastamoinen, V. Sonnenschein, and J. Äystö. Precision mass measurements beyond ^{132}Sn: Anomalous behavior of odd-even staggering of binding energies. *Physical Review Letters*, 109:032501, 2012. URL http://dx.doi.org/10.1103/PhysRevLett.109.032501.

[129] N. D. Scielzo, S. Caldwell, G. Savard, J. A. Clark, C. M. Deibel, J. Fallis, S. Gulick, D. Lascar, A. F. Levand, G. Li, J. Mintz, E. B. Norman, K. S. Sharma, M. Sternberg, T. Sun, and J. Van Schelt. Double-β-decay Q values of ^{130}Te, ^{128}Te, and ^{120}Te. *Physical Review C*, 80:025501, 2009. URL http://dx.doi.org/10.1103/PhysRevC.80.025501.

[130] S. Naimi, G. Audi, D. Beck, K. Blaum, C. Böhm, C. Borgmann, M. Breitenfeldt, S. George, F. Herfurth, A. Herlert, M. Kowalska, S. Kreim, D. Lunney, D. Neidherr, M. Rosenbusch, S. Schwarz, L. Schweikhard, and K. Zuber. Critical-point boundary for the nuclear quantum phase transition near $A = 100$ from mass measurements of ^{96,97}Kr. *Physical Review Letters*, 105:032502, 2010. URL http://dx.doi.org/10.1103/PhysRevLett.105.032502.

[131] W. M. Haynes, editor. *CRC Handbook of Chemistry and Physics*. CRC Press/Taylor and Francis, Boca Raton, FL, 92nd. edition, 2012.

[132] E. B. Saloman. Energy levels and observed spectral lines of xenon, Xe I through Xe LIV. *Journal of Physical and Chemical Reference Data*, 33(3):765–921, 2004. URL http://dx.doi.org/10.1063/1.1649348.

[133] E. B. Saloman. Energy levels and observed spectral lines of krypton, Kr I through Kr XXXVI. *Journal of Physical and Chemical Reference Data*, 36(1):215–386, 2007. URL http://dx.doi.org/10.1063/1.2227036.

[134] S. Sturm, A. Wagner, B. Schabinger, and K. Blaum. Phase-sensitive cyclotron frequency measurements at ultralow energies. *Physical Review Letters*, 107:143003, 2011. URL http://dx.doi.org/10.1103/PhysRevLett.107.143003.

[135] D. E. Winch, D. J. Ivers, J. P. R. Turner, and R. J. Stening. Geomagnetism and Schmidt quasi-normalization. *Geophysical Journal International*, 160(2):487–504, 2005. ISSN 1365-246X. URL http://dx.doi.org/10.1111/j.1365-246x.2004.02472.x.

Acknowledgments

I had a tremendous amount of fun working on my thesis — all of it due to the amazing people that I got to meet and work with! In no particular order, I would like to thank:

Klaus Blaum for offering me a position as a diploma-, and later as a PhD-student. Klaus Blaum is an amazing group leader who has established a wonderful work environment. He grants his students a lot of freedom in their research, but also provides round-the-clock support for any and all questions that may arise — certainly not easy on the busy schedule of a Max-Planck-Institute director! Working in the Blaum group is a wonderful experience that I cannot recommend highly enough!

Edmund Myers for visiting us at THe-Trap and for inviting me to the FSU trap. His patient explanations of the FSU trap techniques were of tremendous help to us in Heidelberg. In fact, THe-Trap is incorporating more and more FSU trap features. I also have to thank Ed and Lisa for showing me the beautiful areas around Tallahassee!

Markus Oberthaler for his readiness to act as a second referee.

Robert Van Dyck for building this beautiful experiment, and for his continuing support in answering all of our questions.

David Pinegar† for introducing me to Matlab, Adobe Illustrator, and to experimental physics in general. David was an amazing person to work with and a wonderful friend. Shortly after returning to the United States, he died in a tragic climbing accident. David, you are sorely missed.

THe-Trappers (and THe-Trap alumni): Christoph Diehl for his work in setting up the lab and getting us started, Sebastian Streubel for taking care of the stabilization system and the LabWindows CVI programming, Jochen Ketter for investigating the theory and for fixing and developing our electronics, Marius Tremer for his work on the ion source, Tommi Eronen for his Linux enthusiasm and being a truly all-around experimental physicist, Marc Schuh for his finite element simulations, and finally Marc Schuh (again!) and Tom Segal for their excellent work in taking over the experiment. I learned a lot from all you guys and thoroughly enjoyed working with you!

Our Strahlenschutz for enabling us to work with tritium, even if that means having to respond to false-alarms at 3 a.m. on Saturday mornings... Radiation safety is a complicated matter, and I have to thank Ralf Lackner, Jochen Schreiner, Andreas Sold, and Elmar Scheurich for making it easy for us!

Our Technicians for their support in all mechanical or electrical matters. I would like to thank Ralph Zilly in particular for his assistance in the many day-to-day matters!

James Carolan and Bert Heise for their assistance in getting the magnet working again after the quench and subsequent failure of the bore-tube glue-joint. I had found James Carolan — retired founder of Nalorac (Carolan spelled backwards) — through the DNS-records of his photography website, and sent him and email to find out if he knew any technicians experienced with Nalorac magnets. He offered to serve as a consultant himself, and his insight into the magnet's design and fabrication process enabled us to repair the magnet without having to take too much apart. Here I also have thank Sebastian Streubel, Jochen Ketter, Tom Segal, and Marc Schuh for carrying out

the crucial parts of the repair while I focused on writing this thesis. Bert Heise was indispensable for energizing and shimming the magnet.

Our administration, especially Frau Dücker, Gabi Weese, and the HGSFP-Sekretariat for helping me every step of the way, even when I was (again) misinterpreting the necessary formalities. The administrative staff at the MPIK is always eager to help and extraordinarily cheerful, which plays a big role in making the work environment at the MPIK as wonderful as it is.

MATSlers from PENTATRAP, FT-ICR, ALPHATRAP, PROTON, bound-electron g-factor, and other experiments, for the wonderful and enlightening discussions about physics, life, and everything. In particular, I would like to thank Sergey Eliseev and Andreas Dörr for showing me the new PI-ICR method, Sven Sturm for his incredibly deep insights and refreshing new ideas about Penning-traps, and Alexander Rischka for his continued support of the voltage source and his enthusiasm in trying new ideas. But most importantly, I would like to thank the MATSlers for their kindness and friendship!

Yuri Novikov for being the best person to share an office with you can hope for! Gmahd-lohbt!

Leslie for her proof-reading skills and all her help in the last weeks of writing this thesis. Also, thanks again to Jochen Ketter, Sebastian Streubel, Marc Schuh, and Tom Segal for the insightful comments on the earlier drafts.

My parents, my brother, and my in laws for their continued love and support — I am immensely grateful for having such amazing people to rely on.

My wife Hermine who supported me every step of the way and who is the most wonderful person that I know.

Anni for being the cutest, most easy-going, and happy baby I have ever seen.